Real-time estimation and diagnosis of vehicle's dynamics states with low-cost sensors in different driving condition

Kun Jiang

Par **Kun JIANG**

Real-time estimation and diagnosis of vehicle's dynamics states with low-cost sensors in different driving condition

Thèse présentée
pour l'obtention du grade
de Docteur de l'UTC

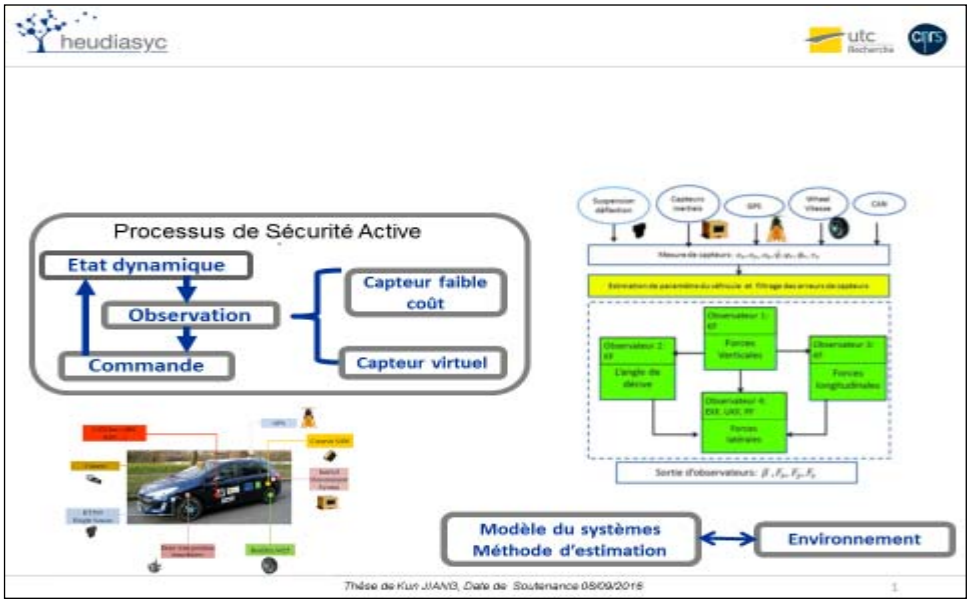

Soutenue le 08 septembre 2016
Spécialité : Information Technologies and Systems

D2292

University of Technology of Compiègne

Thesis

Submitted of the requirements for the degree of
Doctor

Area of specialization: Information Technologies and Systems

by

Kun JIANG

Real-time estimation and diagnosis of vehicle's dynamics states with low-cost sensors in different driving condition

Estimation et diagnostic de la dynamique du véhicule en interaction avec l'environnement

Heudiasyc Laboratory, UMR UTC/CNRS 7253

Defence date: the Eighth of September, 2016

Thesis Committee:

Reviewers:	Dominique Meizel	Université de Limoge - ENSIL
	Houcine Chafouk	ESIGELEC
Examiners:	Ahmed El Hajjaji	Université de Picardie Jules Vernes
	Reine Talj	Université de Technologie de Compiègne
Supervisors:	Ali Charara	Université de Technologie de Compiègne
	AlessandroCorrêaVictorino	Université de Technologie de Compiègne

“As far as the laws of mathematics refer to reality, they are not certain; and as far as they are certain, they do not refer to reality.”

— Albert Einstein

Acknowledgments

Life is full of uncertainty, that is why life is full of hope. In this unpredictable world, it is very lucky for me to keep my curiosity and enthusiasm about the unknown territory of both academic life and personal life. I am very grateful to the people I met in the three years of my PhD study. It is with their help that I could be able to make the impossible possible.

Firstly, I would like to express my special thanks to my supervisor, professor Ali Charara and Alessandro Corrêa Victorino at Universite de Technologie de Compiegne. Their instructive advices and fully support are the sources of energy for me to overcome the difficulties during my PhD study. Their insightful criticism and constant patience have pointed out the correct direction of research for me and has made it possible for me to complete my thesis with some interesting contributions.

I also sincerely appreciate the help of professor Dominique Meizel and professor Houcine Chafouk. Thanks for accepting being my reporters to check this dissertation. They have provided lots of helpful advises to improve the quality of this dissertation. At the same time, I feel very indebted to their encouragement and kindness during the review of this thesis. Their positive comments about my work has encouraged me to move further in the academic road in the future. Thanks for all the members of the thesis committee. Professor Ahmed El Hajjaji and Reine Talj have examined the results of this work and pointed out promising topics that could be my future research interests.

Thank you for the engineers in our team, Gerald Dherbomez, Thierry Monglon. They had made a great effort on the implementation of the embedded system and the arrangement of the experimental validation at CERAM. Without their help, the experimental part is impossible to be completed. I would like to show sincere gratitude for my colleague, Bin, Yue, Danilo, Phuc, Zui, Giovani, Ning, Chunlei, Qiaochu, Hafida, Kahoula. Thank you for your support and consolation in my life. The beautiful memories with all of you will never be forgotten, they will accompany me till forever. Besides, I would like to express my gratitude to all my friends both in China and France. Thank you for your support and encouragement.

Last but not the least, I would like to send special acknowledgments to my family. Even though I was far from my families, but their love, care and miss are the only reasons that I could keep smiling no matter what happens.

Abstract

Enhancing road safety by developing active safety system is the general purpose of this thesis. A challenging task in the development of active safety system is to get accurate information about immeasurable vehicle dynamics states. More specifically, we need to estimate the vertical load, the lateral frictional force and longitudinal frictional force at each wheel, and also the sideslip angle at center of gravity. These states are the key parameters that could optimize the control of vehicle's stability. The estimation of vertical load at each tire enables the evaluation of the risk of rollover. Estimation of tire lateral forces could help the control system reduce the lateral slip and prevent the situation like spinning and drift out. Tire longitudinal forces can also greatly influence the performance of vehicle. The sideslip angle is one of the most important parameter to control the lateral dynamics of vehicle. However, in the current market, very few safety systems are based on tire forces, due to the lack of cost-effective method to get these information.

For all the above reasons, we would like to develop a perception system to monitor these vehicle dynamics states by using only low-cost sensor. In order to achieve this objective, we propose to develop novel observers to estimate unmeasured states. However, construction of an observer which could provide satisfactory performance at all condition is never simple. It requires: 1, accurate and efficient models; 2, a robust estimation algorithm; 3, considering the parameter variation and sensor errors. As motivated by these requirements, this dissertation is organized to present our contribution in three aspects: vehicle dynamics modelization, observer design and adaptive estimation.

In the aspect of modeling, we propose several new models to describe vehicle dynamics. The existent models are obtained by simplifying the vehicle motion as a planar motion. In the proposed models, we described the vehicle motion as a 3D motion and considered the effects of road inclination. Then for the vertical dynamics, we propose to incorporate the suspension deflection to calculate the transfer of vertical load. For the lateral dynamics, we propose the model of transfer of lateral forces to describe the interaction between left wheel and right wheel. With this new model, the lateral force at each tire can be calculated without sideslip angle. Similarly, for longitudinal dynamics, we also propose the model of transfer of longitudinal forces to calculate the longitudinal force at each tire.

In the aspect of observer design, we propose a novel observation system, which is consisted of four individual observers connected in a cascaded way. The four observers

are developed for the estimation of vertical tire force, lateral tire force and longitudinal tire force and sideslip angle respectively. For the linear system, the Kalman filter is employed. While for the nonlinear system, the EKF, UKF and PF are applied to minimize the estimation errors.

In the aspect of adaptive estimation, we propose the algorithms to improve sensor measurement and estimate vehicle parameters in order to stay robust in presence of parameter variation and sensor errors. Furthermore, we also propose to incorporate the digital map to enhance the estimation accuracy. The utilization of digital map could also enable the prediction of vehicle dynamics states and prevent the road accidents.

Finally, we implement our algorithm in the experimental vehicle to realize real-time estimation. Experimental data has validated the proposed algorithm.

Keywords: vehicle dynamics, state observer, tire road contact force, adaptive estimation

Résumé

Le développement des systèmes intelligents pour contrôler la stabilité du véhicule et éviter les accidents routier est au cœur de la recherche automobile. L'expansion de ces systèmes intelligents à l'application réelle exige une estimation précise de la dynamique du véhicule dans des environnements diverses (dévers et pente). Cette exigence implique principalement trois problèmes: i), extraire des informations non mesurées à partir des capteurs faible coût; ii), rester robuste et précis face aux les perturbations incertaines causées par les erreurs de mesure ou de la méconnaissance de l'environnement; iii), estimer l'état du véhicule et prévoir le risque d'accident en temps réel. La motivation de cette thèse est de résoudre ces trois problèmes afin d'assurer le fonctionnement du système de sécurité en cas de situation critique. L'originalité de cette thèse par rapport à l'existant, consiste dans le développement des nouveaux algorithmes, basés sur des nouveaux modèles du véhicule et des différentes techniques d'observation d'état, pour estimer des variables ou des paramètres incertains de la dynamique du véhicule en temps réel. Le structure de notre observateur est montré dans le Figure 1.

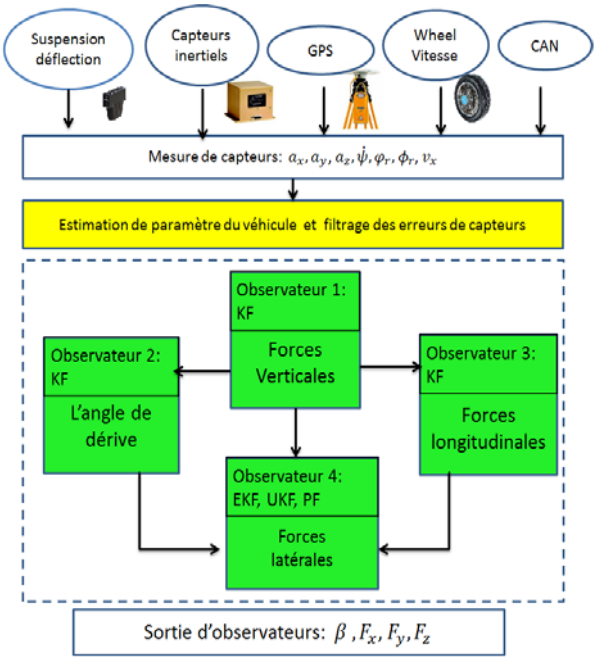

Figure 0.1: Les observateurs pour estimer les forces par pneu et l'angle de dérive au centre de gravité

La première étape de notre étude est le développement de nouveaux modèles pour mieux décrire le comportement du véhicule dans des différentes situations. Nous proposons trois nouveaux modèles pour décrire la dynamique verticale, latérale et longitudinale. L'avantage de ces nouveaux modèles est de considérer l'influence de la géométrie de la route, ce qui ce qui résulte dans une amélioration de la performance des observateurs dans des routes avec dévers et pente. De plus, comparés avec le modèle de Dugoff et le modèle de Pacejka, ces nouveaux modèles sont plus efficaces et précises lors de fortes sollicitations latérales, car ils permettent de reconstruire les efforts par pneu sans besoin de l'angle de dérive ou du taux de glissement.

Pour minimiser les erreurs de modèle, un système d'estimation composé de quatre observateurs est proposé pour estimer les forces verticales, longitudinales et latérales par pneu, ainsi que l'angle de dérive, représentés par les bloc verts dans Figure 1. Pour l'estimation des forces latérales, trois techniques d'observation non linéaires (EKF, UKF et PF) sont appliqués pour tenir compte des non-linéarités du modèle. Pour valider la performance de nos observateurs, nous avons implémenté en C++ des modules temps-réel qui, embarqué sur le véhicule, estiment la dynamique du véhicule pendant le mouvement. Le véhicule expérimental et la piste d'essais sont montrés dans le Figure 2.

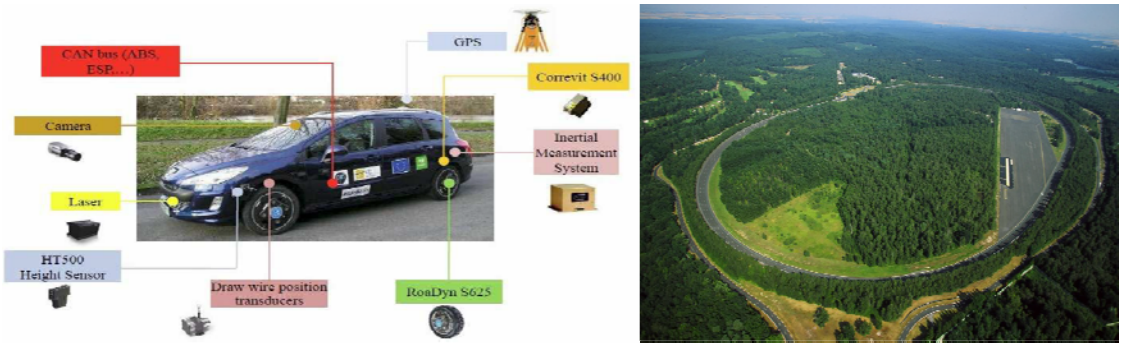

Figure 0.2: Véhicule expérimental DYNA et la piste d'essais de UTAC CERAM

En fin, nous proposons aussi des algorithmes pour estimer des paramètres physiques (la masse, la rigidité de dérive, l'angle de la route, etc). Limité par la qualité de mesure, l'estimation temps réel de ces paramètres n'est pas très précise. Afin d'améliorer l'estimation, nous proposons de récupérer des informations géométriques de la route à partir d'une carte numérique. De plus, basé sur les informations sur la route devant le véhicule, un système de prédiction est développé pour prévoir les forces par pneu et évaluer le risque potentiel d'un accident imminent.. Les données expérimentales sont utilisées pour valider l'algorithme proposé.

Mots-clés : Dynamique du véhicule; Efforts au contact pneumatique/chaussée; Observateur d'état; Anticipation de risque de conduite; Validation expérimentale.

Contents

1 Introduction **1**

1.1 Motivation 1
1.2 Objectives And Contribution 5
1.3 Work Frame 8
1.4 Dissertation Outline 9

2 Vehicle Dynamics Model **11**

2.1 Introduction 11
2.2 Tire Models 12
2.2.1 Tire Fundamentals 14
2.2.2 Mechanism Of Tire Forces 16
2.2.3 Steady State Tire Models 20
2.2.3.1 Linear Tire Model 20
2.2.3.2 Brush Tire Model 21
2.2.3.3 Dugoff's Tire Model 24
2.2.3.4 Magic Tire Model 24
2.2.4 Transient State Tire Models 28
2.3 Dynamic Models Of A Rigid Car 29
2.3.1 Vehicle Coordinate Frame 29
2.3.2 Vehicle Dynamics At 2D Environment 31
2.3.3 Vehicle Dynamics At 3D Environment 32
2.3.4 External Forces And Moments Applied On The Vehicle 34
2.4 Dynamics Models Of A Real Vehicle 37
2.4.1 Dynamics Models For Vehicle Vertical Motion 38
2.4.1.1 Vertical Forces Of A Rigid Car 39
2.4.1.2 Vertical Forces Of A Soft-suspension Car 40
2.4.1.3 The contribution proposed for vertical dynamics model . 41
2.4.2 Dynamics Models For Vehicle Lateral Motion 45
2.4.2.1 Steering Geometry 46
2.4.2.2 Bicycle Model 49
2.4.2.3 Double Track Model 51
2.4.2.4 The contribution proposed for Lateral Dynamics Models 52

2.4.3 Dynamics Models For Vehicle Longitudinal Motion 55
2.4.3.1 Wheel rotational dynamics 56
2.4.3.2 The contribution proposed for longitudinal tire forces model 56
2.5 Conclusion 58

3 Observer Theory 60
3.1 Introduction 60
3.2 Basic Estimation Methods 61
3.2.1 Minimum Variance Unbiased (MVU) Estimator 62
3.2.2 Minimum Mean Square Estimator (MMSE) 63
3.2.3 Sequential MMSE 64
3.2.4 Estimator for non linear observation model 65
3.3 Observer of Dynamic System States 66
3.3.1 Linear system and linear Kalman Filter 66
3.3.2 Non linear system and Extended Kalman Filter 68
3.3.3 Unscented Kalman Filter 70
3.3.4 The Particle Filter Algorithm 72
3.3.4.1 Sequential Importance Sampling: 73
3.3.4.2 Resampling 74
3.4 Conclusion 76

4 Observers For Estimation Of Tire Forces And Sideslip Angle 78
4.1 Introduction 78
4.2 Implementation of Embedded System 80
4.2.1 Embedded sensors 80
4.2.2 Software Modules 83
4.3 Open-loop Estimation Of Vehicle Dynamics States 84
4.3.1 Vertical tire force open-loop estimation 85
4.3.2 lateral tire force open-loop estimation 87
4.3.3 longitudinal tire force open-loop estimation 90
4.3.4 Sideslip angle open-loop estimation 92
4.4 Observer Design 94
4.4.1 Cascaded Kalman observers for estimation of vehicle dynamics states 95
4.4.2 Filter settings 99
4.4.3 Communication between the four observers 101
4.4.4 Particle filter based observer 102
4.5 Experimental Validation Of The Observers 102
4.5.1 Intense slalom test at 50 km/h at level ground 104
4.5.2 Moderate slalom test at 30 km/h at level ground 109

4.5.3 Chicane test at 20 km/h at level ground . . . 113
4.5.4 Chicane test at 100 km/h at level ground . . . 117
4.5.5 Circling test at 40 km/h at level ground . . . 121
4.5.6 Slalom test at 40 km/h at slippery road . . . 125
4.5.7 Slalom test at 140 km/h at banked road . . . 129
4.6 Conclusion . . . 133

5 Adaptive Estimation In Presence Of Parameter Variation 134
5.1 Introduction . . . 134
5.2 Improvement Of Sensor Measurement . . . 134
5.2.1 Multiple measurement models . . . 135
5.2.2 Observer design . . . 137
5.2.3 Experimental validation . . . 140
5.2.3.1 Validation of different kinematic models . . . 140
5.2.3.2 Fusion of multiple models to correct sensor errors . . . 142
5.3 Vehicle Physical Parameters . . . 143
5.3.1 Parameters and models . . . 143
5.3.2 Observer Design . . . 145
5.3.3 Experimental Validation . . . 146
5.4 Prediction Based On The Use Of OpenStreetMap . . . 149
5.4.1 Introduction . . . 149
5.4.2 Road Geometry Estimation . . . 149
5.4.3 Risk assessment . . . 154
5.4.4 Prediction Algorithm . . . 155
5.4.5 Experimental Validation . . . 156
5.5 Conclusion . . . 160

6 Conclusion And Perspectives 161
6.1 Conclusions . . . 161
6.2 Future work . . . 163

Bibliography 163

List of Figures

0.1 Les observateurs pour estimer les forces par pneu et l'angle de dérive au centre de gravité v
0.2 Véhicule expérimental DYNA et la piste d'essais de UTAC CERAM . . . vi

1.1 Accidents data provided by [ONISR, 2015]: a) Evolution of the annual mortality in France; b)Prime causes of fatal accidents 2
1.2 Structure of an active safety system 5
1.3 Heudiasyc laboratory experimental vehicle: DYNA 9

2.1 Illustration of terminology in tire models 13
2.2 Illustration of a sample tire interior components and arrangement [Reza, 2007] 15
2.3 Illustration of tire structure a) Tire effective radius R_{eff} compared to tire radius R_o and loaded height R_{load} b) Tire camber angle 16
2.4 Deformation of tire under longitudinal force and lateral force 17
2.5 Vertical, longitudinal, and lateral stiffness curves[Reza, 2007] 17
2.6 Longitudinal tire force as a function of tire slip ratio [Rajamani, 2012] . . 19
2.7 Lateral force behavior of a sample tire for different normal loads as a function of slip angle α [Rajamani, 2012] 19
2.8 The brush tire model. Left: the deformation of bristle during turning, Right: the tire at different slip condition (pure side slip, pure brake slip and combined slip) [Pacejka, 2006] 21
2.9 Bottom view of a deflected tire. Left: illustration of adhesion region and sliding region during longitudinal deflection; Right: illustration of adhesion region and sliding region during lateral deflection. [Reza, 2007] 22
2.10 Explanation of magic formula parameters [Rajamani, 2012] 26
2.11 The characteristics of Magic tire model for longitudinal force, lateral force and aligning moment 27
2.12 Vehicle body coordinate frame [Reza, 2007] 30
2.13 Illustration of cruise angle, yaw angle and side slip angle 31
2.14 Description of motion in body frame and global frame 32
2.15 A rigid car running at irregular road 33
2.16 Projection of tire forces into the vehicle body frame 35
2.17 Illustration of the vertical dynamics of a vehicle parked on level pavement 39

2.18 A quarter vehicle suspension system 40
2.19 Illustration of errors of measured acceleration: the measured lateral acceleration is not parallel to the road surface 42
2.20 a) Full-car automotive suspension model [Baffet, 2007] b) the proposed pitch-roll suspension model 44
2.21 Lane departure caused by the failure of lateral dynamics control 46
2.22 Ackerman geometry [Reza, 2007] 47
2.23 Effect of E/L on the Ackerman condition for front-wheel-steering geometry 48
2.24 The position of rotation center in real driving condition 49
2.25 Bicycle model 49
2.26 Double track model 51
2.27 Tire test equipment: providing different speeds and different vertical loads [Otso et al., 2016] 53
2.28 Double track model 57

3.1 Hidden Markov-chain Model 73
3.2 Illustration of Sampling Importance Resampling algorithm 75
3.3 Illustration of Stratified Resampling algorithm 76

4.1 Heudiasyc laboratory experimental vehicle: DYNA 80
4.2 a) Kistler wheel force transducers at front left wheel; b) The Correvit installed at place of the spare wheel 81
4.3 a) MEMS sensor for inertial parameters and gyroscope; b) Laser sensor for chassis height measurement 81
4.4 a) Laser sensor installed at front bumper; b) Embedded electronics and computer in the trunk 82
4.5 The structure of the acquisition system 83
4.6 Software architecture of PACPUS 83
4.7 Software architecture of acquisition system and estimation system 84
4.8 Maneuver time history of the slalom test 85
4.9 Open-loop estimation of lateral load transfer $T_{Fz,lat} = F_{z11} - F_{z12} + F_{z21} - F_{z22}$ 86
4.10 Open-loop estimation of longitudinal load transfer $T_{Fz,lon} = F_{z11} + F_{z12} - F_{z21} - F_{z22}$ 86
4.11 Open-loop estimation of vertical force at each tire 87
4.12 Open-loop estimation of resultant lateral force at front axle $F_{y,f} = F_{y11} + F_{y12}$ and at rear axle $F_{y,r} = F_{y21} + F_{y22}$ 88
4.13 Open-loop estimation of transfer of lateral force at front axle $T_{Fy,f} = F_{y11} - F_{y12}$ and at rear axle $T_{Fy,r} = F_{y21} - F_{y22}$ 89
4.14 Open-loop estimation of lateral force at each tire 89

4.15 Open-loop estimation of resultant longitudinal force at front axle $F_{x,f} = F_{x11} + F_{x12}$ and at rear axle $F_{x,r} = F_{x21} + F_{x22}$ 90
4.16 Open-loop estimation of transfer of longitudinal force at front axle $T_{Fx,f} = F_{x11} - F_{x12}$ and at rear axle $T_{Fx,r} = F_{x21} - F_{x22}$ 91
4.17 Open-loop estimation of longitudinal force at each tire 91
4.18 Open-loop estimation of sideslip angle during steady turning test 93
4.19 Open-loop estimation of sideslip angle during slalom test 94
4.20 Overall algorithm of the estimation of vehicle dynamics states 96
4.21 Selective communication between the four observers 102
4.22 The trajectory of road circuit on plan 103
4.23 Maneuver time history of Test 1: Intense slalom test 104
4.24 Test 1 (intense slalom test): Estimation of vertical force at each tire . . . 104
4.25 Test 1 (intense slalom test): Estimation of longitudinal force at each tire 105
4.26 Test 1 (intense slalom test): left) Results and error bounds of the new observer for estimation of sideslip angle at CoG; right) Comparison of the estimation results of sideslip angle at CoG obtained by different observers 106
4.27 Test 1 (intense slalom test): left) Results and error bounds of the new observer for estimation of sideslip angle at rear axle; right) Comparison of the estimation results of sideslip angle at rear axle obtained by different observers 107
4.28 Test 1 (intense slalom test): Results and error bounds of the new observer for estimation of lateral forces at each tire 107
4.29 Test 1 (intense slalom test): Comparison of the estimation results of tire lateral forces obtained by different observers 108
4.30 Maneuver time history of Test 2: Moderate slalom test 109
4.31 Test 2 (moderate slalom): estimation results of vertical force at each tire 110
4.32 Test 2 (moderate slalom): estimation results of F_x at each tire 110
4.33 Test 2 (moderate slalom test): left) Results and error bounds of the new observer for estimation of sideslip angle at CoG; right) Comparison of the estimation results of sideslip angle at CoG obtained by different observers 111
4.34 Test 2 (moderate slalom test): left) Results and error bounds of the new observer for estimation of sideslip angle at rear axle; right) Comparison of the estimation results of sideslip angle at rear axle obtained by different observers 111
4.35 Test 2 (moderate slalom test): Results and error bounds of the new observer for estimation of lateral tire forces 112
4.36 Test 2 (moderate slalom test): Comparison of different observers for the estimation of lateral tire forces 112
4.37 Maneuver time history of Test 3: Low-speed chicane test 113

4.38 Test 3 (low speed chicane test): Comparison of the estimation results of vertical force at each tire 114
4.39 Test 3 (low speed chicane test): Comparison of the estimation results of longitudinal force at each tire 114
4.40 Test 3 (low speed chicane test): left) Results and error bounds of the new observer for estimation of sideslip angle at CoG; right) Comparison of the estimation results of sideslip angle at CoG obtained by different observers 115
4.41 Test 3 (low speed chicane test): left) Results and error bounds of the new observer for estimation of sideslip angle at rear axle; right) Comparison of the estimation results of sideslip angle at rear axle obtained by different observers 115
4.42 Test 3 (low-speed chicane test): Results and error bounds of the new observer for estimation of lateral forces at each tire 116
4.43 Test 3 (low-speed chicane test): Comparison of the estimation results of tire lateral forces obtained by different observers 116
4.44 Maneuver time history of Test 4: High-speed chicane test 117
4.45 Test 4 (high speed chicane test): Comparison of the estimation results of vertical force at each tire 118
4.46 Test 4 (high speed chicane test): Comparison of the estimation results of longitudinal force at each tire 118
4.47 Test 4 (high speed chicane test): left) Results and error bounds of the new observer for estimation of sideslip angle at CoG; right) Comparison of the estimation results of sideslip angle at CoG obtained by different observers 119
4.48 Test 4 (high speed chicane test): left) Results and error bounds of the new observer for estimation of sideslip angle at rear axle; right) Comparison of the estimation results of sideslip angle at rear axle obtained by different observers 119
4.49 Test 4 (high speed chicane test): Results and error bounds of the new observer for estimation of lateral forces at each tire 120
4.50 Test 4 (high-speed chicane test): Comparison of the estimation results of tire lateral forces obtained by different observers 120
4.51 Maneuver time history of Test 5: Circling test 121
4.52 Test 5 (circling test): Comparison of the estimation results of vertical force at each tire 122
4.53 Test 5 (circling test): Comparison of the estimation results of longitudinal force at each tire 122
4.54 Test 5 (circling test): left) Results and error bounds of the new observer for estimation of sideslip angle at CoG; right) Comparison of the estimation results of sideslip angle at CoG obtained by different observers . . . 123

4.55 Test 5 (circling test): left) Results and error bounds of the new observer for estimation of sideslip angle at rear axle; right) Comparison of the es- timation results of sideslip angle at rear axle obtained by different observers 123
4.56 Test 5 (circling test): Results and error bounds of the new observer for estimation of lateral forces at each tire 124
4.57 Test 5 (circling test): Comparison of the estimation results of tire lateral forces obtained by different observers 124
4.58 Maneuver time history of Test 6: Low adhesion slalom test 125
4.59 Test 6 (low adhesion slalom test): Comparison of the estimation results of vertical force at each tire 126
4.60 Test 6 (low adhesion slalom test): Comparison of the estimation results of longitudinal force at each tire 126
4.61 Test 6 (low adhesion slalom test): left) Results and error bounds of the new observer for estimation of sideslip angle at CoG; right) Comparison of the estimation results of sideslip angle at CoG obtained by different observers 127
4.62 Test 6 (low adhesion slalom test): left) Results and error bounds of the new observer for estimation of sideslip angle at rear axle; right) Compar- ison of the estimation results of sideslip angle at rear axle obtained by different observers 127
4.63 Test 6 (low adhesion slalom test): Results and error bounds of the new observer for estimation of lateral forces at each tire 128
4.64 Test 6 (low adhesion slalom test): Comparison of the estimation results of tire lateral forces obtained by different observers 128
4.65 Maneuver time history of Test 7: Banked road slalom test 129
4.66 Test 7 (banked road slalom test): Comparison of the estimation results of vertical force at each tire 130
4.67 Test 1 (banked road slalom test): Comparison of the estimation results of longitudinal force at each tire 130
4.68 Test 7 (banked road slalom test): left) Results and error bounds of the new observer for estimation of sideslip angle at CoG; right) Comparison of the estimation results of sideslip angle at CoG obtained by different observers 131
4.69 Test 7 (banked road slalom test): left) Results and error bounds of the new observer for estimation of sideslip angle at rear axle; right) Comparison of the estimation results of sideslip angle at rear axle obtained by different observers 131
4.70 Test 7 (banked road slalom test): Results and error bounds of the new observer for estimation of lateral forces at each tire 132

4.71 Test 7 (banked road slalom test): Comparison of the estimation results of tire lateral forces obtained by different observers 132

5.1 Roll and pitch movement of vehicle body 137
5.2 Algorithm overview: Estimation based on the fusion of multiple sensors 138
5.3 Description of slalom test 140
5.4 Validation of four models for estimating longitudinal velocity: "Rear right wheel" refers to $v_{x,rr}$, "Rear left wheel" refers to $v_{x,rl}$,"GPS" refers to $v_{x,GPS}$ 140
5.5 Validation of four models for estimating yaw rate: "Gyroscope" represents direct measurement, "Wheel speed model" refers to equation 5.5, "Steering model" refers to equation 5.6, "Heading angle model" refers to equation 5.7 141
5.6 Estimation of vehicle roll and pitch angle. In this figure, the red lines are vehicle's accelerations which could indicate the roll and pitch motion of vehicle. "Fusion" represents the results obtained by the fusion of integration method and suspension method. 142
5.7 Estimation of vehicle longitudinal speed and yaw rate based on sensor fusion. 142
5.8 Comparison of the estimated variation of vehicle weight with real data. "suspension" corresponds to the estimated value by suspension deflection. 146
5.9 Experimental results of the estimator for position of CoG. "suspension" corresponds to the value estimated with suspension deflection. 147
5.10 Estimation results of the cornering stiffness: a) slalom test at dry road; b) slalom test at wet slippery road 147
5.11 Estimation results of the road angles 148
5.12 Topological representation of vehicle path 152
5.13 Overall structure of vehicle safety prediction system 155
5.14 Vehicle's trajectory and maneuver time history: at $t = 150s$, the vehicle is at the point of black circle, $t = 250s$, the vehicle is at the point of black star. 156
5.15 The value of curvature stored in each Critical Point 157
5.16 Comparison of lateral dynamics states estimated by inertial sensors and OSM 158
5.17 a) Estimation of of vertical forces at each tire; b) Estimation of lateral forces at each tire: comparison between sensor measurement and estimation 159
5.18 Prediction of vehicle safety in the following 300 meters road 159

List of Tables

4.1 Summary of vehicle vertical dynamics models 85
4.2 Summary of vehicle lateral dynamics models 88
4.3 Summary of vehicle longitudinal dynamics models 90
4.4 Summary of Vehicle longitudinal dynamics models 93

5.1 parameters of the vehicle 143
5.2 Tags attributed to Critical Points 150
5.3 Tags attributed to Corridors 150
5.4 The construction of Critical points and corridors 157

Nomenclature

a_x	Longitudinal acceleration (m/s^2)
a_y	Lateral acceleration (m/s^2)
a_z	Vertical acceleration (m/s^2)
a_{xm}	Measured Longitudinal acceleration (m/s^2)
a_{ym}	Measured lateral acceleration (m/s^2)
C_α	Cornering stiffness (N/rad)
C_s	Longitudinal slip stiffness (N/rad)
C_β	Average Cornering stiffness of each tire (N/rad)
C_f	Cornering stiffness of the front axle (N/rad)
C_r	Cornering stiffness of the rear axle (N/rad)
C_ϕ	Total damping coefficient of roll motion ($N.m.s/rad$)
C_θ	Total damping coefficient of pitch motion ($N.m.s/rad$)(N/rad)
d_w	Tire damping ($N.s/m$)
d_u	Suspension damping ($N.s/m$)
E	Vehicle average track width (m)
E_1, E_2	Vehicle front and rear track width(m)
F_x	Longitudinal force (N)
F_y	Lateral force (N)
F_z	Vertical force (N)
h	Height of the center of gravity (m)
I_{xx}	Moment of inertial about roll axis ($kg.m^2$)
I_{yy}	Moment of inertial about pitch axis ($kg.m^2$)
I_{zz}	Moment of inertial about yaw axis ($kg.m^2$)
ij	Front left(11) or rear right(22)
k_u	Suspension spring (N/m)
k_w	Tire spring (N/m)
K_ϕ, K_θ	Total spring coefficient of roll motion and pitch motion($N.m/rad$)
L	Wheel base (m)
L_1, L_2	Distance from the cog to the front and rear axles respectively (m)

Nomenclature

m_v, m_s	Vehicle total mass and vehicle sprung mass (kg)
M_x	Roll moment ($N.m$)
M_y	Pitch moment ($N.m$)
M_z	Yaw moment ($N.m$)
$M_F x$	Yaw moment caused by the longitudinal force($N.m$)
$R_e ff$	Effective tire radius (m)
R_o	unloaded tire radius (m)
$R_l oad$	Tire radius under load(m)
s	Slip ratio
τ	time delay the tire need to develop force
$T_F x, f$	Transfer of longitudinal force at front axle(N)
$T_F x, r$	Transfer of longitudinal force at rear axle(N)
$T_F y, f$	Transfer of lateral force at front axle ($N.m$)
$T_F y, r$	Transfer of lateral force at rear axle ($N.m$)
$T_F z, f$	Transfer of vertical force at front axle ($N.m$)
$T_F z, r$	Transfer of vertical force at rear axle ($N.m$)
v_g	Vehicle speed at COG (m/s)
v_x, v_y	Vehicle longitudinal and lateral speed (m/s)
ψ	Yaw angle (rad)
$\dot{\psi}$	Yaw rate (rad/s)
$\ddot{\psi}$	Yaw acceleration (rad/s^2)
ϕ	Roll angle (rad)
$\dot{\phi}$	Roll rate (rad/s)
$\theta, \dot{\theta}$	Pitch angle and pitch rate(rad)
γ	Camber angle (rad)
μ_x	Longitudinal friction coefficient
μ	Friction coefficient
θ_r, ϕ_r	Road slope angle and bank angle (rad)
ξ	Percentage of the sprung mass
ρ_{ij}	Suspension position (m)

Glossary

ADAS	Advanced Driver Assistance System
ACC	Adaptive Cruise Control
CAN	Controller Area Network
CoG	Center of Gravity
CP	Critical Point
CWS	Curve Warning System
ECU	Electronic Control Unit
ESC	Electronic Stability Control
INS	Inertial Navigation System
LDW	Lane Departure Warning
LSR	Lateral Skid Ratio
LTR	Lateral Load Transfer
OSM	OpenStreetMap
PACPUS	Perception et Assistance pour une Conduite Plus Sûre
RLS	Recurisve Least Square
RMF	Rollover Mitigation Functions
ROR	Run Of Road
SD	Stopping Distance
SIS	Sequential Importance Sampling
SIR	Sequential Importance Resampling
VSC	Vehicle Stability Control

Publications

1. Kun Jiang, Adina Pavelescu, Alessandro Corrêa Victorino, Ali Charara. Estimation of vehicle's vertical and lateral tire forces considering road angle and road irregularity. 17th International IEEE Conference on Intelligent Transportation Systems (ITSC 2014), Oct 2014, Qingdao, China. pp.342-347. 2014

2. Kun Jiang, Alessandro Corrêa Victorino, Ali Charara. Adaptive Estimation of Vehicle Dynamics Through RLS and Kalman Filter Approaches. 18th IEEE International Conference on Intelligent Transportation Systems (ITSC 2015), Sep 2015, Canary Islands, Spain. pp.1741-1746, 2015

3. Kun Jiang, Alessandro Corrêa Victorino, Ali Charara. Estimation de l'état dynamique du véhicule sur routes avec dévers et pentes. 6èmes Journées Doctorales / Journées Nationales MACS, Juin 2015, Bourges, France.

4. Kun Jiang, Alessandro Corrêa Victorino, Ali Charara. Real-Time Estimation of Vehicle's Lateral Dynamics at Inclined Road Employing Extended Kalman Filter. 11th IEEE conference on Industrial Electronics and Applications (ICIEA 2016), Jun 2016, Hefei, China.

5. Kun Jiang, Alessandro Corrêa Victorino, Ali Charara. Estimation and prediction of vehicle dynamics states based on fusion of OpenStreetMap and vehicle dynamics models. IEEE Intelligent Vehicles Symposium (IV 2016), Jun 2016, Göteborg, Sweden.

6. Kun Jiang, Alessandro Corrêa Victorino, Ali Charara. Robust estimation of vehicle dynamic states based on a parameter-variable EKF observer. 19th IEEE International Conference on Intelligent Transportation Systems (ITSC 2016)

Publication submitted or under preparation:

1. Kun Jiang, Alessandro Corrêa Victorino, Ali Charara, Multi-model based estimation of tire forces and sideslip angle at irregular road. [preparation]

1 Introduction

1.1 Motivation

Man's mode of land transportation does not change too much until the advent of automobile. In 1768, the first steam-powered automobile capable of human transportation was built by a French inventor, Nicolas-Joseph Cugnot [Eckermann, 2001]. One source states that it has seated four passengers and moved at a speed of 3.6 km/h [Manwaring, 1966]. The desire of a higher speed and a greater power has continuously pushed forward the development of automobile. In 1807, François Isaac de Rivaz designed the first car powered by an internal combustion engine fueled by hydrogen. In 1886, the first petrol-powered automobile, was invented by Karl Benz. The maximum speed is said to reach at 30 km/h. Since then, the industry of automobile has entered a period of rapid development.

Now, in 21st century, the manufacturers of automobile use new technologies to make the vehicles capable of accelerating easily and running faster. Lots of commercialized passenger cars are capable of accelerating to the speed of more than 200 km/h. The fast transportation provides convenience in people's daily life and promotes the development of human society. On the contrary, the high speed transportation also brings critical problems to the society. The increasing road accidents has caused uncountable losses of people's lives and properties every year all over the world. According to the latest statistics report in ONISR (Observatoire National Internministriel de la Sécurité Routière), 56,109 accidents occurred in France in 2015, resulting in 70,442 injured and 3464 fatalities [ONISR, 2015]. Improving road safety at high speed is the key challenges posed to road traffic today.

According to the statistical data illustrated in Figure 1, the excessive speed is considered as the prime reason of accidents. Consequently, many governments have established laws to put a limit on the maximum vehicle speed. However, limiting the speed is not the best way to eliminate road accidents. Firstly, it is very hard to define the limit of speed. Many accidents happened at low speed. A dangerous speed is not a speed surpassing a specific value but a speed that will cause the instability of vehicle. It can be influenced by many factors, such as the road geometry, road surface condition and even weather condition. When the vehicle is passing an icy roundabout, it could be dangerous even at low speed. To the contrast, when the vehicle is on an empty straight highway, it is

a)

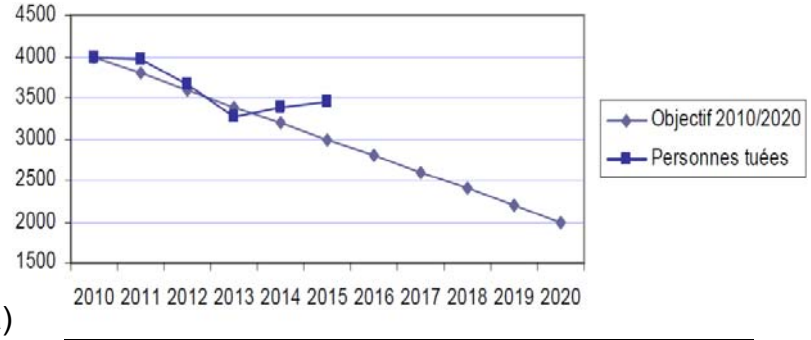

b)

The first cause of fatal accidents during 15 months	*metropolitan France*
Speed	*23%*
Alcohol	*18%*
No respect of priority	*12%*
Inattention	*6%*
Narcotic	*3%*
Discomfort	*3%*
Dangerous overtaking	*3%*
Fatigue	*2%*
Wrong way	*2%*
Lane changing	*2%*
Telephone	*1%*
Obstacles on the road	*1%*
Equipment factors	*1%*
Non respect of distances	*1%*
Other causes	*12%*
Cause unclear	*9%*

Figure 1.1: Accidents data provided by [ONISR, 2015]: a) Evolution of the annual mortality in France; b)Prime causes of fatal accidents

safe to drive at a very high speed. Secondly, it is a fact that a considerable number of drivers has exceeded the speed limit, intentionally or unintentionally. It is necessary to emphasis the importance of respect the speed limit, meanwhile it is also necessary to ensure the safety of the drivers who has exceeded the speed limit. Thirdly, limiting the speed is just a temporary solution to enhance road safety. The desire of a higher speed is motivated by the development of human society. The limit of speed has reduced the efficiency of transportation and wasted the potential power of engines. In long term, the best solution to the traffic problem is to ensure the safety at high speed rather than limiting the vehicle to a low speed.

A further study of accident data has uncovered the real reason of accidents. The study states that it is the human errors that account for over 90% of all road accidents [NHTSA, 2013]. Human errors could be caused by many reasons, such as the tiredness or the bad visibility. These errors will possibly cause the drivers to take wrong actions responding to the emergency situation, resulting in the lost of control of vehicle dynamics and then accidents. Thanks to the development of embedded systems high-tech sensors, observation and control techniques, many intelligent systems has designed to help the drivers to reduce the human errors. These intelligent systems are capable of providing a better perception of the environment and a better control of the vehicle in critical situation. These intelligent systems are commonly named Advanced Driver Assistance Systems (ADAS).

The ADAS systems can be classified according to whether they are vehicle based systems or infrastructure related systems which require interaction between the vehicle and the infrastructure aiming at sending, receiving, processing and storing various information (telematic systems). Here we introduce several ADAS systems that are already in the market [Liu and Ye, 2011]. Systems from 1 to 6 are the vehicle based systems, while 7-9 are the infrastructure realted systems.

1. ABS, Anti-Lock Breaking System: it is the system that prevents the blocking of the wheels when breaking and thus allowing the car to stay on track. It is first taken in use in cars in late 1970's. Now ABS are required on all new passenger cars sold in the EU since 2004.

2. ESP, Electronic Stability Program: system stabilising the vehicle and preventing skidding in critical situations. ESP is integrated with the vehicle braking system to guarantee vehicle stability in critical condition. It is designed to automatically control the brakes at each tire to correct the slide and prevent spinning. It could minimize the loss of control during a already happened danger. It is reported that the European Commission has confirmed a proposal for the mandatory introduction of ESP on all new cars and commercial vehicle models sold in the EU from 2012.

3. Obstacle and collision warning: system detecting potential collisions with other vehicles or obstacles based on current speed. Available as an option in several European models.

4. Lane departure warning system: system warning the driver when unintentionally leaving the lane. Available for commercial vehicles as an extra fitment for several years, for passenger vehicles some models available in 2005.

5. Monitoring the state of vigilance of the driver: system warning the driver in case of drowsiness, distraction or carelessness.

6. Adaptive Head Lights: system moving headlights when turning into bends and adjusting the luminous intensity in order to avoid dazzling. Available as an option in several European Models.

7. eCall, Emergency call system: system automatically calling the local emergency authorities and instantly transferring to them accurate vehicle position and other accident related data when the vehicle is involved in a serious accident and thus reducing the time for the rescue services to arrive. The aim is to equip all new vehicles with eCall system starting 2010.

8. Real time traffic and travel information: system providing real time information about the road network such as traffic jams and weather conditions allowing drivers to choose an alternative itinerary.

9. Speed Alert: system detecting local speed limits on all types of roads and warning driver if they exceed these.

These intelligent systems are proved to be efficient at enhancing the road safety. According to the report of U.S Department of Transportation [NHTSA, 2013], for the vehicles equipped with both ABS and ESC, 7.5 percent ran off the road, while for the vehicles equipped with neither ABS nor ESC, 14.6 percent ran off the road. In the next few years, many other intelligent systems are going to appear to warn and assist the human driver in case of critical maneuvers. The development of a vehicle safety system can be generally divided into three steps: measurement (perception), decision(analysis) and action(control), as illustrated in Figure 1.2. This research concentrates on the task of perception. All intelligent systems need accurate information about the vehicle dynamics. Actually, the safety systems are based on basic information about vehicle dynamics, which could be directly measured by some low-cost sensors, such as the wheel speed sensor, the gyroscopes and the accelerometers. These systems are widely employed in the automobile industry, due to the simplicity and robustness. But further developed safety systems and other high-level decision systems need more detailed information about the vehicle dynamics state like tire/road forces and sideslip angle. This needs us to have a better perception of all available vehicle dynamics states. One method to improve the perception is to add new sensors. Another method is to develop “virtual sensors” to reconstruct or estimate the unknown variables without using new sensors. In this thesis, we prefer the second method, in order to develop a safety system which has high potential for real applications. As a conclusion, the methodology of this thesis is to extract as more information about vehicle dynamics states as we can by using only the sensors which are already available in the currently standard vehicles. Studying vehicle

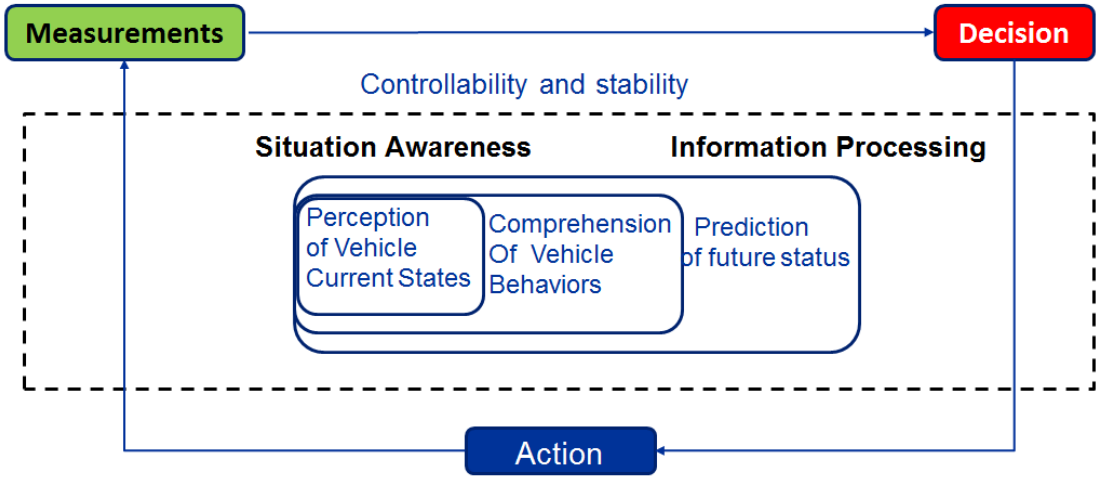

Figure 1.2: Structure of an active safety system

dynamics models and building robust observers are the kernel of this thesis.

1.2 Objectives And Contribution

Enhancing road safety by developing active safety system is the general purpose of this thesis. A challenging task in the development of this system is to get accurate information about immeasurable vehicle dynamics states. More specifically, we need to estimate the vertical load, the lateral frictional force and longitudinal frictional force at each wheel, and also the sideslip angle at center of gravity. These states are the key parameters that could optimize the control of vehicle's stability. However, in the current market, very few safety systems are based on tire forces, due to the lack of cost-effective method to get these information. The current safety systems rely on information obtained through basic measurements and integration of inertial sensors, which may be prone to error and uncertainty [Fukada, 1999], [Van Zanten, 2002]. The accurate estimation of all vehicle dynamics states could greatly improve the performance of vehicle's safety system [Doumiati et al., 2009]. The estimation of vertical load at each tire enables the evaluation of the risk of rollover. Estimation of tire lateral forces could help the control system reduce the lateral slip and prevent the situation like spinning and drift out. Tire longitudinal forces can also greatly influence the performance of vehicle. The sideslip angle is one of the most important parameter to control the lateral dynamics of vehicle. For all the above reason, lots of research have been conducted to get accurate information about these vehicle dynamics states.

In the literature, many dynamics models and observers have been proposed. When applying these existent models and observers in our research, we encountered several

problems that are rarely discussed in the literature. Our research is started by the task to estimate vertical tire forces. In the literature, many authors assume the vertical forces as constant values. However, in the experiments, a significant variation of vertical load at each wheel is perceived during cornering or braking. Some simple models are proposed in the literature to calculate the vertical load at each tire during dynamics maneuvers. These models are developed with the assumption that the road is level and flat. In real environment, road condition is complex and may vary a lot during a journey. It is a challenging task to accurately estimate the vertical forces in all terrain. In the subsequent research, we found that the lateral dynamics and longitudinal dynamics are also greatly affected by the road condition. The currently widely-used vehicle dynamics models (the bicycle model and double track model) failed to take into account the influence of road irregularities. They are obtained through an oversimplification of the real situation, approximating the vehicle dynamics by planar rigid body dynamics. Consequently, the estimation based on the current models are less accurate at inclined road. In order to make our observer capable of operating safely at different road conditions, we have to modify the vehicle dynamics models to take into account the influence of road condition. However, even with the modified vehicle models, the estimation errors are still significant due to the sensor noises and model incertitude. Thus the techniques to obtain the optimal estimation in presence of sensor noises and model errors are quite meaningful to our research. Different observer techniques are going to be studied and compared in this thesis. Then based on these observer techniques, we develop robust observers to provide accurate estimation during critical dynamics maneuvers. Another remark of our work is to estimate the parameters of the vehicle. In the literature, the vehicle parameters, like mass, position of center of gravity and stiffness of sideslip, are usually considered as known constants. In our research, these parameters are regarded as unknown variables and needed to be identified. Consideration of these challenging problems is motivated by the attempt to expand the active safety system from the research stage into useful real-world applications. We are trying to consider all possible variation in real conditions and make our observers realistic. In this context, all our theoretical development will be implemented in our experimental vehicle and evaluated by tests in real condition. In order to realize the real-time estimation, a balance point should be found between the accuracy of estimation and the computing efficiency. Finally, as an application of the vehicle dynamics observer, we are going to develop a risk prediction system to advise the safe speed.

Directed by the objectives described above, we have conducted studies in both theoretical way and experimental way. Compared with the state-of-the-art of knowledge in this field, the new contribution in this dissertation could be concluded with the following points:

- Development of novel models to better describe the vehicle dynamics in different

road conditions. Vehicle dynamics models have been studied since long time ago, but these models are either oversimplified or computationally expensive. We proposed some novel models to efficiently describe vehicle dynamics. In the aspect of vertical dynamics, we integrated the deflections of suspension and the inertial sensors to take into account the pitch and roll motion of suspension. In the aspect of lateral dynamics, we employ the three-dimensional dynamics rather than the planar dynamics to describe the vehicle's motion. In this way, we can consider the additional liberty of motion caused by the road irregularity. Furthermore, we proposed the model of transfer of lateral forces, which enables us to estimate the tire lateral force without the need of sideslip angle. In the aspect of longitudinal dynamics, we proposed the model of transfer of longitudinal forces.

- Development of a set of observers devoted to estimate the tire forces and the sideslip angle in real-time. A system consisting of four individual observers, connected in a cascaded structure, is proposed in order to improve the robustness and efficiency of the overall estimation process. For the linear estimation problems, the observers are developed based on classic Kalman filter. For the non linear estimation problem, three nonlinear observer techniques (EKF, UKF and PF) are addressed to cope to the nonlinearity of vehicle model. Compared with the previous work in our laboratory and in the literature, the observers proposed in this thesis are more robust and accurate due to the fusion of different models. Both the new proposed models and the classic models are incorporated to estimate the vehicle states. We developed an algorithm to change the model uncertainty according to the vehicle dynamics state. Experimental validations demonstrate the performance of our observer in various road environments and driving maneuvers.
- Development of observers to filter out the bias of sensor measurement. In the literature, the sensor measurement (inertial sensors, GPS, wheel speed sensor) is regarded as always available and accurate. Nevertheless, during the experiments in real condition, we found that the unpredictable sensor errors or sensor failures could happen at any moment. To improve the accuracy of sensor measurement, we proposed to combine multiple models and sensors to estimate each dynamic state, making the estimation insensitive to the sensor failure.
- Development of the RLS algorithm to estimate the vehicle parameters, including the vehicle mass, road cornering stiffness and position of CoG. These parameters are important to the estimation of vehicle dynamics and are usually regarded as constants. Adaptive estimation of these parameters could improve the accuracy and robustness of our observer.
- Development of a risk prediction system by incorporating digital road map and vehicle dynamics models. The existing observers are only capable of estimating

vehicle dynamics states at a current instant but not to predict the potential dangers in a future instant. In order to make time for correcting drive behaviors, especially when driving at high speed, it seems very appealing for us to predict an impending dangerous event and react before the danger occurs. The geometry of the upcoming path ahead of vehicle, obtained through the digital map, could be employed to predict the future dynamics states. The OpenStreetMap is employed to create the database of the road information, like road curvature, road bank angle or slope angle. Experimental data validates that the digital map can effectively predict the vehicle dynamics states.

- Implementation of software modules consisting of data processing and embedded application. Experimental implementation is also significant in this work. It should be highlighted that above-mentioned observers for estimation of vehicle dynamics states are realized and validated through on-line real-time test.

1.3 Work Frame

The entire work is completed at the HeuDiaSyc ("Heuristic et Diagnostic des Systèmes Complexes") UMR 7253 CNRS Laboratory at the Computer Science Department of Université de Technologie de Compiègne (UTC) in France, under the supervision of Prof. Ali Charara and Alessandro Corrêa Victorino. This Ph.D funding is provided in part by China Scholarship Council (CSC).

The works on this thesis were developed in relation to a Franco-German cooperation between the CNRS-UTC in Compiègne (Picardie, France) and TU Ilmenau (Thuringia, Germany), in the context of the latest European Project VERVE (Novel Vehicle Dynamics Control Technique for Enhancing Active Safety and Range Extension of Intelligent Electric Vehicles) .

Both simulation software and experimental vehicle are employed to test and validate our observers. Certain theoretical tests are performed by using Simulator CALLAS software developed by OKTAL society [www.callasprosper.com]. It is an advanced vehicle dynamics simulator validated by many research laboratories and vehicle manufacturers. The experimental tests are conducted with the vehicle which is fully developed by our laboratory HEUDIASYC UMR 7253 CNRS at Compiègne, France. As illustrated in in Figure 1.3, we employ a Peugeot 308sw to install all the necessary sensors and other embedded systems. The equipped sensors and in-vehicle systems are devoted to vehicle dynamics research and real-time application test. In this work, Matlab environment is used for theoretical development and off-line validation. Real-time applications are implemented in C++ language combining with Qt cross-platform development framework. More details are introduced in the section 4.2.

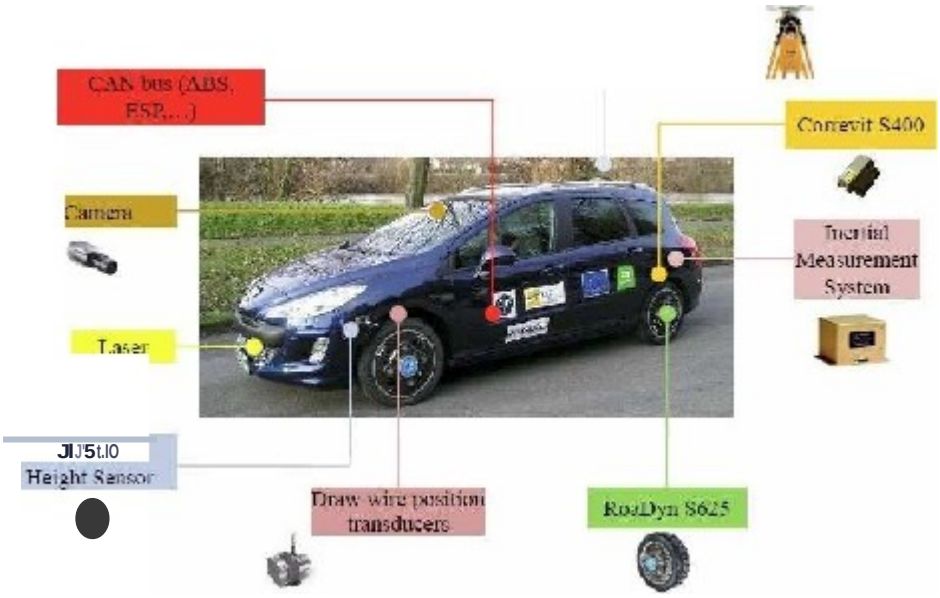

Figure 1.3: Heudiasyc laboratory experimental vehicle: DYNA

1.4 Dissertation Outline

In order to better present the contribution of our research, the remainder of this dissertation is divided into three principal parts, organized as follows:

Theoretical development of vehicle dynamics models and observer theory
In the first part of this ths;is, we introduce the vehicle dynamics theory and the basic concepts of the observation theory. This part provides solid theoretical foundation for the construction of the observers. Both the classic vehicle dynamics models and the proposed novel models are introduced and compared in this part. Moreover, the

- *Chapter 2: Vehicle Dynamics Models*

The state of art of the vehicle and tire dynamics theory is briefly reviewed in this chapter. We first introduce the pneumatic tire/road interaction characteristics. The well-known brush tire mode!, the Pacejka's Magic tire mode!are compared with its own features. Afterwards, we present the classic vehicle dynamics theory, which employs the planar rigid body dynamics to describe the vehicle behaviors. In order to consider the road irregularities, we propose to extend vehicle's planar motion into 3D motion. Then we discuss in details about the vertical dynamics, lateral dynamics and longitudinal dynamics of the vehicle. It is highlighted that the models proposed in this chapter are capable of estimating each individual tire's forces in ali three direction. This chapter provides the models needed for observer construction in Chapter 4.

- *Chapter 3: Observer theory*

This chapter provides a brief summary of the linear/nonlinear observation techniques. Firstly, the estimation problem of a constant parameter is discussed. The minimum variance unbiased estimator and the minimum mean square estimator are reviewed and compared. Then the estimation techniques for a dynamics system, the observers, are reviewed. The algorithms of Kalman Filter, Extended Kalman filter, Unscented Kalman Filter and Particle Filter are reviewed and compared in this chapter.

Construction and experimental validation of observers for estimation of tire forces and sideslip angle

In the second part of this thesis, we present the details about the observers we developed for estimation of tire forces and sideslip angle.

- ***Chapter 4: Observers for estimation of tire forces and sideslip angle***

The target of this chapter is to estimate 13 dynamics states: the vertical, lateral and longitudinal forces at each tire and the sideslip angle at center of gravity. This target is quite ambitious as no such system can be found in the literature. Most observers found in the literature are developed to estimate only the sideslip angle. Some other observers are developed to estimate the forces at each axle rather than at each tire. The novel observers are inspired by the previous work of our laboratory but have some further advantages. First of all, we employed more dynamics models to estimate more information about the vehicle dynamics with a higher accuracy. Secondly, we proposed a more complicate structure of observers to stay robust and accurate against sensor errors. Furthermore, the implementation of experimental vehicle is also presented in this chapter. The experimental data in several critical tests is presented to validate the performance of our observers.

Fusion of multiple sensors and digital map to enhance the road safety

In the third part of this thesis, we present the supplementary methods to further improve the accuracy of our observers.

- ***Chapter 5: Adaptive estimation in presence of parameter variation and sensor errors***

This chapter considers the estimation problem in a more realistic context. During the experiments in real condition, we find the performance of observers is very sensitive to the quality of sensor measurements and the quality of vehicle parameter configuration. We developed the algorithms to automatically identify the vehicle parameters and filter out the sensor errors, called the adaptive estimation. Furthermore, we propose to incorporate the digital map to predict the future dynamic states of vehicle. A risk prediction system aiming at enhancing road safety is developed based on the predicted tire forces . Experimental data is used to validate the proposed algorithms.

Finally in Chapter 6, we give a conclusive summary of our work and outline some directions for the future work.

2 Vehicle Dynamics Model

2.1 Introduction

Comprehension of vehicle's behavior is fundamental for improvement of vehicle's stability and security. For a standard ground vehicle, the overall vehicle motion is supposed to be controlled by steering wheel, accelerator and brakes. Unfortunately, in some situation, for example on slippery road, the steering wheel cannot effectively change the direction of vehicle and this usually leads to accidents. In addition, when the vehicle is driving on the inclined road, the vehicle dynamics is easier to enter the dangerous region leading to the instability of vehicle. To eliminate these dangerous situations and predict vehicle motion, the awareness of tire forces is needed. The tire forces that are meaninful for the safety systems include the longitudinal force, lateral force and vertical force. For technical and economic reasons, it is not possible for a standard passenger car to directly measure these tire forces. Therefore, we propose to construct observers, or the so-called virtual sensors, to provide a robust estimation of tire forces based on those low-cost sensors. A full comprehension of vehicle dynamics models is the key to develop an accurate virtual sensor.

A vehicle is a highly complex system bringing together a large number of mechanical, electronic and mechatronics elements. The complexity of vehicle modeling representation depends on the desired objectives. For the purpose of global location, the vehicle can be simply represented by a vector indicating the location and direction. To the contrast, for a simulator design for instance, complex finite element methods are employed to reproduce as exactly as possible the behavior of each individual vehicle components. Simulations of such complex models are computationally expensive and time consuming. In our case, the modeling issues are associated to two critical objectives : completeness and complexity. In a side, our model must represent as closer as possible the real behavior of the vehicle, this is completeness. On the other side, this model is used in an state-observer system that must be on-boarded on the vehicle working in a real-time application (estimation of tire forces and evaluation of risk in real-time). Due to the limited calculation capacity of embedded system on vehicle, model simplifications have to be made, this is related to complexity. Developing vehicle models that describe accurately all dynamics of interest while as simple as possible is the main challenge for the so far developed vehicle state observers, completeness versus complexity. This

chapter briefly reviews the vehicle dynamics theory. Furthermore, the limitation of the existent vehicle dynamics models and our proposed models will also be introduced in this chapter.

We remember that the global problem we are considering in our thesis project: developing state observer to describe the dynamics of the vehicle in a precise and robust way, even when the vehicle is navigating in a unleveled road (banked or sloped). This problematic was considered with a constraint: precisely estimating the geometry of the road (bank and slop angles) is not an objective in this work. What we are searching for is to build observers that reconstruct the dynamics of the vehicle in level or unlevel roads, without searching to estimate the precise geometry of the road. To achieve this ambitious objective, the first point is to revisit the proposed vehicle dynamics modeling approaches, proposing our contributions. That is the objective of this chapter. Vehicle dynamics is a intense research subject for more than a hundred years. Many references on the subject are available. We can refer to [Rajamani, 2012][Rajamani, 2012] [Reza, 2007] [Thomas, 1997] [Schiehlen, 2009] [Kiencke and Nielsen, 2005] [Popp and Schiehlen, 2010] and [Wong, 2008]. To begin with, we would like to review the theory of tire road interaction in section 2.2. The tire-road interaction is more of a contact mechanics problem. The principle factors affecting the generation of tire forces will be discussed in this section. Then in section 2.3, the rigid body dynamics are reviewed. Simplifying the car as a rigid body is an efficient method to capture the major features of vehicle dynamics. Most of the existent vehicle dynamics models are based on the theory of rigid body dynamics. Normally, the vehicle motion is simplified as a planar(2D) motion. However, when the road is irregular (banked or sloped or even curved), the vehicle motion has more liberty. In order to take into account the road irregularity , the 3D dynamics models of a rigid car is introduced in section 2.3. Tire dynamics and rigid body dynamics are the two most important elements to understand vehicle behaviors, but they still cannot represent all the features of a vehicle. Suspensions, steering systems and other subsystem can also greatly influence the vehicle's dynamics. In section 2.4, the tire dynamics, rigid body dynamics and subsystem's characteristics are combined together to have a more detailed description of a real vehicle's dynamics. The vertical dynamics, lateral dynamics and longitudinal dynamics are discussed in this section. Finally, in section 2.5, we present a conclusion about our contribution in the modeling of vehicle dynamics.

2.2 Tire Models

Tires are the only vehicle components generating external forces that can be effectively manipulated to control vehicle motions. This important role of tires make tire force modeling a crucial topic for vehicle control. The tire-road contact can generate longitudinal force, lateral force and vertical force (F_{wx}, F_{wy} F_{wz}), and moments along three

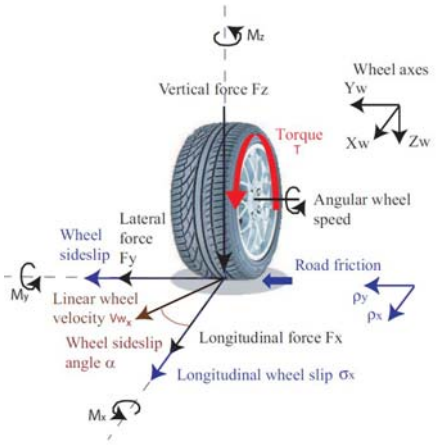

Figure 2.1: Illustration of terminology in tire models

direction (M_{wx}, M_{wy} M_{wz}) allowing the car to accelerate/brake and to turn. The forces and moments generated at the tire-road contact point are illustrated in the Figure 2.1.

The coordinate frame of the wheel is a local coordinate attached to the tire. The origin point of wheel frame is at the center of tire contact patch *w*. The *wz*-axis of wheel frame is always perpendicular to the road surface. The *wy*-axis is orthogonal to the tire direction and towards the left side of vehicle. The *xw*-axis is orthogonal to both *yw* and *zw* axis and parallel to the tire direction. One important parameter illustrated in Figure 2.1 is the tire slip angle α.

- Tire slip angle α: Tire slip angle is the angular difference between the direction of tire contact patch and the direction of the wheel. Positive slip angle delegate right orientation as it moves in the forward direction.

In order to guarantee the optimal driving maneuvers in different road condition including slippery roads, it is important to be aware of the actual tire forces and the maximum attainable tire forces. In this way, we can decide whether the tire is at the imminence of losing control and whether the protection process should be activated. Actually, there is no available sensors for ordinary passenger cars to directly measure tire forces for technical and economical reasons. Consequently, several types of mathematical models of the tire have been developed during the last half century to reconstruct these forces. The developed model of tire forces are function of tire properties (material, tread pattern, tread depth and profile), the vertical load, and the velocities experienced by the tire. The relationship between these factors are extremely nonlinear and complex. As concluded in the book of [Pacejka, 2006], the mathematical models can be divided into four categories:

- Models based on experimental data only: fitting full scale tire test data by regression techniques, the so-called empirical model.

- Models using similarity method: distorting, rescaling and combining basic characteristics.
- Models through simple physical model: using simple mechanical representation.
- Models though complex physical model: describing tire in greater detail, using computer simulation or finite-elements method.

Finite-elements models of the tires are of particular use when considering the distribution of forces and the irregularity of road [Svendenius, 2007]. Models based on similarity method were useful early but have found less use recently as they are replaced by other models. Such models are discussed in [Pacejka, 2006]. These two models are not considered in our research due to the limited computation capacity of embedded system. The two remaining model categories, empiric models and simple physical models are the two models most widely used in the literature for estimating and predicting tire forces. The empiric models are based on a curve-fitting approach and are able to describe the highly nonlinear behavior of the tires. The the parameters of the empirical models sometimes do not have a specific physical meaning. To the contrast, the simple physical models are based on the physical interpretation of the tire and are extremely useful to get a better understanding of tire behavior.

In this section, first of all we will introduce the basic structure of pneumatic tires and the terminologies in tire modeling. Then the basic mechanism of tire forces and moments are discussed. In this thesis, four different tire models are presented, which are the Brush model, the Dugoff's model, the linear model and the Pacejka's Magic tire model.

2.2.1 Tire Fundamentals

Pneumatic tire is a flexible structure made of rubber and a series of synthetic materials. Thanks to its flexibility, the tire is able to reduce vibrations caused by the irregularity of road and to achieve a high friction coefficient in the interaction with the road surface. Both the materials and structure of the tires can greatly influence the tire characteristics. In order to make the tire able to hold the pressure of the inflated air and support the weight of vehicle, multiple layer structure is employed, including the body plies, bead bundle, belts, sidewalls and tire inner liner (combined by fiber, textile, and steel cords). The function of each layer is described in details in [Reza, 2007]. The mentioned interior components are illustrated in Figure 2.2.

Depending on the desired working condition, the tire structure could be particularly designed to ensure a high performance. The tread pattern, the tire pressure, the tire radius, tire temperature and the camber angle are the important parameters to describe the tire's operating conditions.

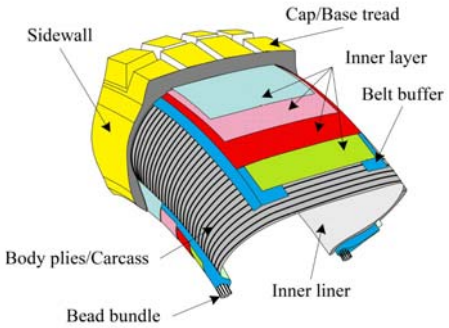

Figure 2.2: Illustration of a sample tire interior components and arrangement [Reza, 2007]

The tread pattern is made up of tread lugs (also called blocks) and tread voids (also called grooves). The lugs are the sections of rubber that make contact with the road and voids are the spaces that are located between the lugs. Tire's traction ability and noise level are greatly influenced by the tire tread pattern of block-groove configurations. Tires with wide and longitudinal grooves have a lower noise level and high lateral friction. More lateral grooves could increase traction ability and noise levels. Both longitudinal and lateral grooves are necessary for the passenger car tires. Without such grooves, the rain water on the road would be compressed into the grooves and not be able to escape out to the sides of the wheel. This will lead to a dramatic decrease of tire friction, which is very dangerous. However, for driving only on a dry road, the tire treads are not not necessary because they reduce the contact area between the rubber and the road. This is the reason for using treadless or slick tires at smooth and dry race tracks. As a contrast, the mud-terrain tire is characterized by large blocks and large grooves, allowing the tire to grasp deeper in the mud and clean itself easily. The tread pattern is an important factor of the actual friction coefficient of the tire.

Tire pressure can effectively change the stiffness of tire and influence the generation of tire forces. Recently, interesting results have been obtained to improve break and confort caracteristics by controlling the tire pressure in real-time [Savitski et al., 2015]. Decreasing the tire pressure causes the tire to be more flexible so the contact patch area becomes bigger, which increases the friction and the tire's traction ability. Lower tire pressure also helps the tire grip small obstacles and make contact with the object in more places. However, the low tire pressure will increase tire temperature and fuel consumption [Reza, 2007].

Tire loaded radius R_{load} is the distance between wheel center and the tire contact center in the road plane. The tire load radius is determined by the stiffness of tire or the tire pressure. When the tire is rolling, the effective radius R_{eff} is between the unloaded radius R_o and loaded radius R_{load}, as illustrated in the Figure 2.3. The effective tire

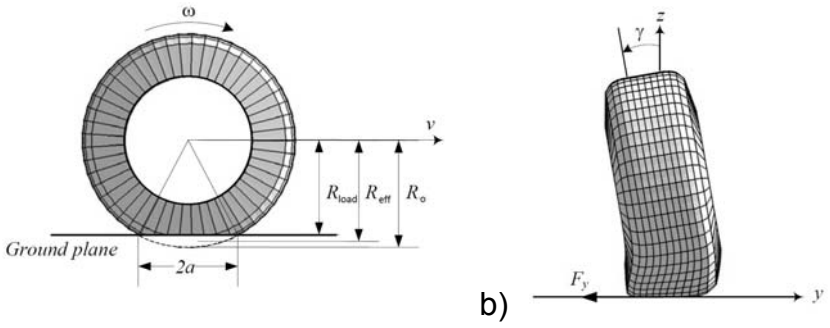

a) b)

Figure 2.3: Illustration of tire structure a) Tire effective radius R_{eff} compared to tire radius R_o and loaded height R_{load} b) Tire camber angle

radius R_{eff} shows the relation between its angular velocity and the linear velocity.

$$\begin{array}{rcl} R_{eff} & = & \frac{v_x}{\omega_w} \\ R_o > & R_{eff} & > R_{load} \end{array} \tag{2.1}$$

where v_x is the forward velocity, and ω_w is the angular velocity of the wheel. It is approximately equal to

$$R_{eff} = R_o - \frac{R_o - R_{load}}{3} \tag{2.2}$$

During each rotation, the tire has experienced the compressing and releasing process, transforming the mechanical energy into thermal energy. That's why the tire temperature is increasing while driving at high speed. The influence of tire temperature is not discussed in this thesis. Therefore, during the experimentation with our test car, the duration of each test is limited to several minutes, in this way the tire temperature will not vary too much.

Another important parameter to describe the tire operation condition is the camber angle γ. The camber angle is the angle between the tire-plane and the vertical plane, as illustrated in Figure 2.3 b). Camber angle generates a lateral tire force called camber trust or camber force. The camber force is proportional to γ at low camber angles and depends directly on the wheel load F_{zw} [Reza, 2007].

$$F_y = -C_\gamma \gamma \tag{2.3}$$

where C_γ is called the camber stiffness of tire. The camber angle γ is positive when the tire leans to the right.

2.2.2 Mechanism Of Tire Forces

In this section, we briefly explain the mechanism and the most important factors in generating tire forces, allowing us to better understand the physical meaning of different

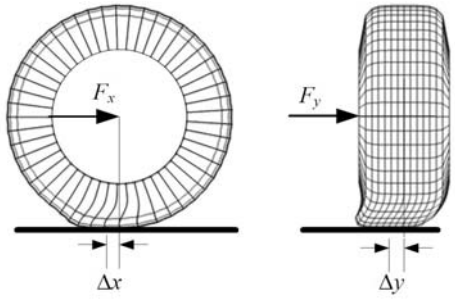

Figure 2.4: Deformation of tire under longitudinal force and lateral force

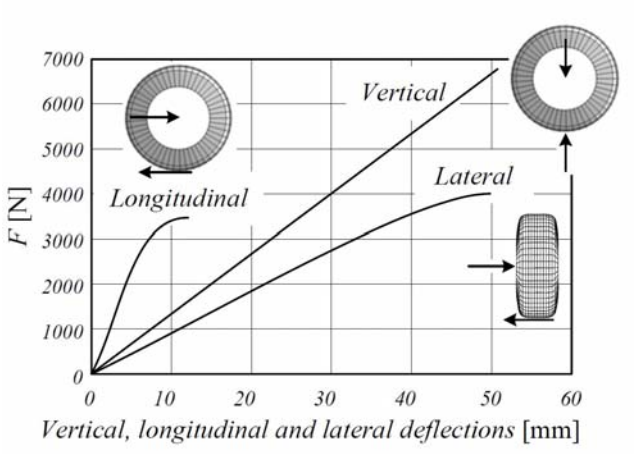

Figure 2.5: Vertical, longitudinal, and lateral stiffness curves[Reza, 2007]

tire models. It is also based on the comprehension of how tire generates forces that we proposed a novel simplified tire model to estimate tire forces, which is introduced in the section 2.4.

The tire-road contact forces are not applied at a point, but are the resultant from normal and shear stresses distributed in the contact patch. In [Thomas, 1997], the author explains clearly that the tractive force and lateral force of tire are equal to the integration of the shear stress at each tire tread. In [Reza, 2007], the author considers that the deformation behavior of tires in three directions x, y, and z is the first important tire characteristics in tire dynamics, as illustrated in Figure 2.4. For a tire on a stiff and flat ground, the tire forces are the function of its deformation in each direction, x, y, z :

$$\begin{aligned} F_{wx} &= f(x) \\ F_{wy} &= f(y) \\ F_{wz} &= f(z) \end{aligned} \tag{2.4}$$

An example of tire stiffness curves is illustrated in Figure 2.5.

From the Figure 2.5, we can see that during small deformation, the tire forces are approximately proportional to the deflections. While during large deformation, the relations become nonlinear. Generally, the tire is most stiff in the longitudinal direction and least stiff in the lateral direction. The maximum lateral and longitudinal forces are limited by tire friction coefficient and vertical load.

The deformation theory could intuitively explain the characteristic of tire forces, but it is not practical for real application in an ordinary car. It is due to the difficulty of directly measuring the tire tread deformation while the vehicle is running. To overcome the difficulty, the concept of longitudinal slip ratio s and tire slip angle α are employed to represent the tire deformation in wx-axis and wy-axis respectively.

The longitudinal slip ratio s is defined as:

$$s = \frac{\omega_w R_{eff} - v_x}{\omega_w R_{eff}} \quad during\ acceleration \tag{2.5}$$

$$s = \frac{\omega_w R_{eff} - v_x}{v_x} \quad during\ braking \tag{2.6}$$

where v_x is the longitudinal velocity of tire, R_{eff} is the effective tire radius, ω_w is the wheel rotational speed. The slip ratio is positive when accelerating and negative when braking.

The tire lateral slip angle α is defined as:

$$\alpha = \arctan(\frac{v_y}{|v_x|}) \tag{2.7}$$

where v_y is the lateral speed of the tire. The lateral slip angle is positive when slipping to the left side and negative when slipping to the right side.

In ISO 8855:1991, the units of longitudinal slip and lateral slip are changed into [%] and [°]: $100s$ [%] and α [deg]. The evolution of the longitudinal force with respect to the longitudinal slip ratio s is illustrated in the Figure 2.6. The relation between lateral forces, vertical load and tire slip angle is illustrated in Figure 2.7.

The longitudinal force reaches a peak value at $s \approx 0.1$. At this moment the tire starts to undergo a pure sliding. When $s > 0.1$, the longitudinal ratio can no longer represent the tire tread deformation and the longitudinal force converges to a constant.

According to the experimental data shown in Figure 2.7, the lateral force vary with respect to the lateral slip α, reaching its maximal value in a given value of α, beyond which the tire will completely skid. In this figure, we can also find the lateral force is affected by the vertical load applied to the tire. The nonlinear characteristic of tire's behavior can be explained by the existence of both kinetic friction and static tire tread deformation during the motion of tire. As explained in [Rajamani, 2012], the tire forces come from two sources: siding region and static region. The slip ratio s or slip angle α

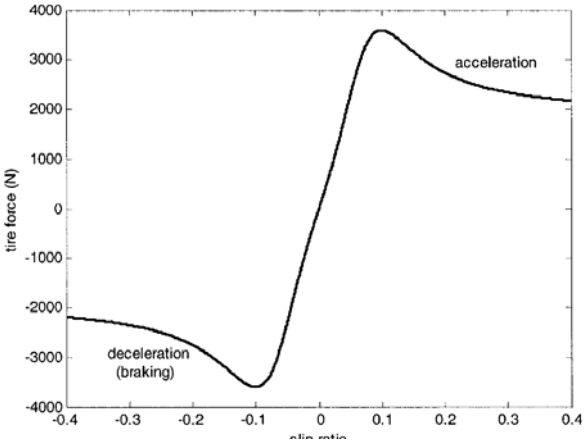

Figure 2.6: Longitudinal tire force as a function of tire slip ratio [Rajamani, 2012]

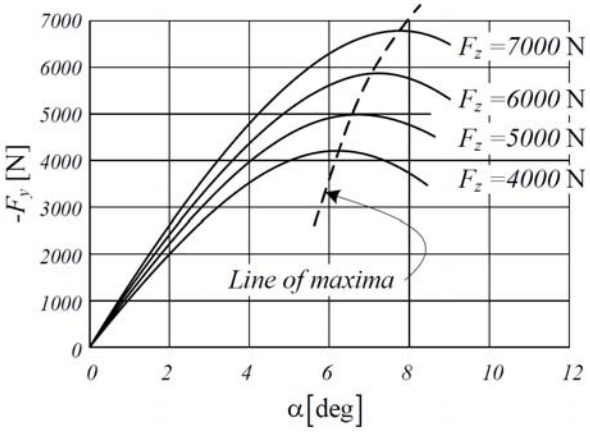

Figure 2.7: Lateral force behavior of a sample tire for different normal loads as a function of slip angle α [Rajamani, 2012]

can be viewed as an indicator of the percentage of static region. When they are small, most of the contact region is the static region.

As a conclusion, the tire forces are mainly decided by the following three factors.

- Vertical load F_{wz}
- Friction coefficient μ
- Slip ratio s or slip angle α

Therefore, generally the tire forces can be represented by the following function:

$$\begin{aligned} F_{wx} &= f_{Tire}(F_{wz}, \mu, s) \\ F_{wy} &= f_{Tire}(F_{wz}, \mu, \alpha) \end{aligned} \tag{2.8}$$

In this section, we have roughly explained the mechanism of tire forces. Tire deformation is the main cause of pneumatic tire forces. The tire slip ratio and tire slip angle are employed to represent the deformation of a rolling tire. Besides the tire slip ratio and slip angle, vertical load and road friction are also important factors to affect the generation of tire forces. It is noted that tire forces depend on many other parameters such as pressure, temperature, humidity and so on. In this thesis, limited by the number of sensors installed on the vehicle and the intention of simplicity, only the tire slip (s or α), vertical load F_{wz} and road friction condition μ are considered in the tire model. This simplification has neglected many details but it is validated by many authors in the literature to represent the major features of tire behaviors.

Even the input variables of tire model are already chosen (s or α, F_{wz} , μ), it is still challenging to propose a precise model to fit the non-linearity of the curve illustrated in Figure 2.6 and 2.7. In the following section, we will introduce the four widely accepted steady state tire models: the Linear tire model, the Brush tire model, the Dugoff's tire model and the Magic tire model.

2.2.3 Steady State Tire Models

2.2.3.1 Linear Tire Model

The strategy of using linear tire model is to simplify the calculation and concentrate on the major cause of tire forces: the tire slip (s or α). Under normal driving, the tires are well away from saturation (maximal points on the curves of figures 2.6 and 2.7) and have small deformation and slip angle values. According to the work of [Lechner, 2002], the linear tire model can represent real tire behavior for vehicle accelerations under 0.4g. As a result, during small tire slip, it is common to use this linear approximation for the tire forces:

$$\begin{aligned} F_{wx} &= C_s s \\ F_{wy} &= C_\alpha \alpha \end{aligned} \tag{2.9}$$

where C_s is called the longitudinal slip stiffness, C_α is the cornering stiffness.

The advantages of linear tire model mainly relies on the simplicity. The linear model is widely employed in the observer of vehicle dynamics and the controller of vehicle motion. However, the simplicity of model leads to a new challenging problem, which is to identify the value of longitudinal stiffness and cornering stiffness. As one can see on the curves of figures 2.6 and 2.7, the values of longitudinal and cornering stiffness, C_s and C_α, depend essentially on the road friction and on the tire load. Moreover, the linear tire model has neglected the effects of combined slip. Due to the negligence of the efforts saturation, the tire forces tend to be over estimated by the linear model, especially when the tire slip is excessive. When using these linear approximations, it is

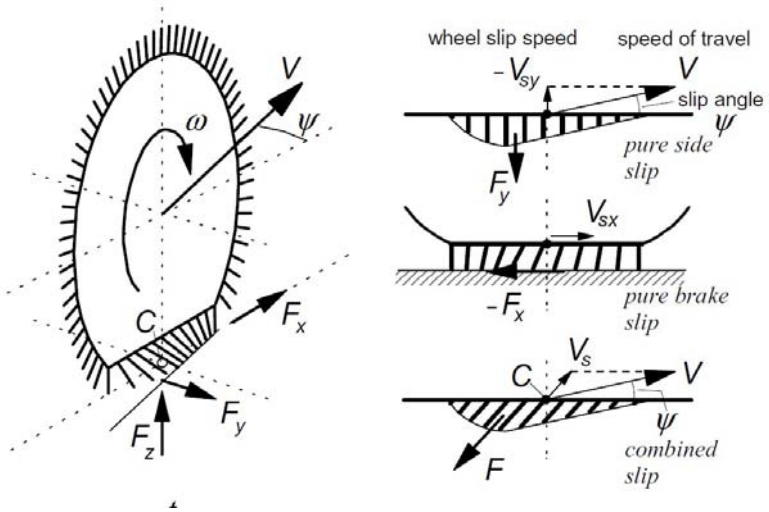

Figure 2.8: The brush tire model. Left: the deformation of bristle during turning, Right: the tire at different slip condition (pure side slip, pure brake slip and combined slip) [Pacejka, 2006]

important to understand the operating region of the tires for the specific application. Otherwise, the accuracy of tire model is not guaranteed.

2.2.3.2 Brush Tire Model

To compensate the errors caused by the over simplification in linear model, some physical models are proposed to describe the tire behaviors with more details, such as the spring model and the brush model [Pacejka, 2006]. The brush model is a further explanation of the tire deformation. It consists of a row of elastic bristles that touches the road and can deflect in a direction parallel to the road surface. These bristles are the simplified representation of tread elements. Their compliance represents the elasticity of the combination of different tire components (carcass, belt, tread etc). The Brush tire model is illustrated by the Figure 2.8.

In real driving situation, especially when the tire slip is large, the tire-road contact patch is divided into adhesion region and sliding region, as illustrated in Figure 2.9. In adhesion region, the tire treads are static, while in the sliding region, the tire treads are undergoing pure slip. The force distribution in each region is different.

In adhesion region, the longitudinal deformation u_{bx} and lateral deformation u_{by} of each bristle along the contact patch can be approximated with a linear distribution, expressed by [Pacejka, 2006]:

$$\begin{aligned} u_{bx} &= (a - x)_{1+s}^{s} \\ u_{by} &= (a - x)\tan\alpha \end{aligned} \tag{2.10}$$

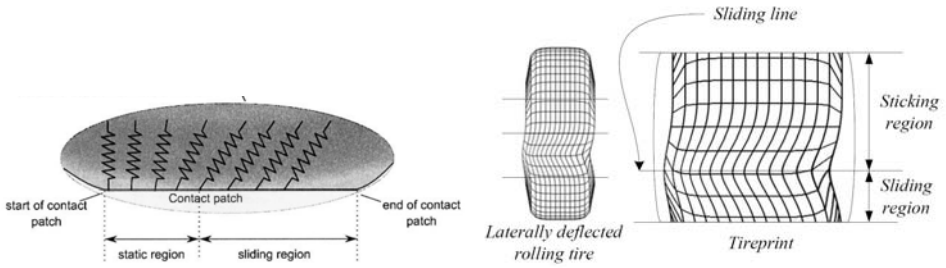

Figure 2.9: Bottom view of a deflected tire. Left: illustration of adhesion region and sliding region during longitudinal deflection; Right: illustration of adhesion region and sliding region during lateral deflection. [Reza, 2007]

where a denotes half length of the contact length, x denotes the position of the bristle in the contact patch, $x \in [-a, a]$, $x = 0$ means the center of contact patch.

With the assumption of linear elasticity, the longitudinal and lateral force distribution ($q_{x,ad}$ and $q_{y,ad}$) can be represented by:

$$\begin{aligned} q_{x,ad} &= c_{px}(a - x)\frac{s}{1+s} \\ q_{y,ad} &= c_{py}(a - x)\tan\alpha \end{aligned} \tag{2.11}$$

where c_{px}, c_{py} are the longitudinal and lateral stiffness of each bristle respectively.

In the siding region, the lateral force of each bristle is equal to the maximum possible friction force. For the purpose of simplicity, we suppose the vertical load distribution per unit length q_z varies according to a parabola, expressed by:

$$q_z = \frac{3F_{wz}}{4a}\left(1 - \left(\frac{x}{a}\right)^2\right) \tag{2.12}$$

As a result, the distribution of the largest possible friction force in longitudinal and lateral direction ($q_{x,max}$, $q_{y,max}$) can be expressed by :

$$\begin{aligned} q_{x,max} &= \mu_x q_z = \frac{3}{4}\mu_x F_{wz}\frac{a^2 - x^2}{a^3} \\ q_{y,max} &= \mu_y q_z = \frac{3}{4}\mu_y F_{wz}\frac{a^2 - x^2}{a^3} \end{aligned} \tag{2.13}$$

where μ_x, μ_y are the friction coefficient in longitudinal and lateral direction respectively.

Then the total longitudinal and lateral forces are the integration of the force distribution along the contact patch. The resulting formula for the lateral force is provided by [Pacejka, 2006] as:

$$F_{wy} = \begin{cases} 3\mu F_{wz}\theta_y\sigma_y\left(1 - |\theta_y\sigma_y| + \frac{1}{3}(\theta_y\sigma_y)^2\right) & \textit{if } |\sigma_y| < \frac{1}{\theta_y} \\ \mu_y F_{wz}\,sgn\alpha & \textit{if } |\sigma_y| \geq \frac{1}{\theta_y} \end{cases} \tag{2.14}$$

where

$$\begin{aligned} \theta_y &= \frac{2c_{py}a^2}{3\mu_y F_{wz}} \\ \sigma_y &= \tan\alpha \end{aligned} \tag{2.15}$$

Similarly, the tire force at pure longitudinal slip can be computed by the following equations [Pacejka, 2006]:

$$F_{wx} = \begin{cases} 3\mu F_{wz}\theta_x\sigma_x \left(1 - |\theta_x\sigma_x| + \frac{1}{3}(\theta_x\sigma_x)^2\right) & \textit{if } |\sigma_x| < \frac{1}{\theta_x} \\ \mu_x F_{wz}\, sgn\sigma_x & \textit{if } |\sigma_x| \geq \frac{1}{\theta_x} \end{cases} \tag{2.16}$$

where

$$\begin{aligned} \theta_x &= \frac{2c_{py}a^2}{3\mu_x F_{wz}} \\ \sigma_x &= \frac{s}{1+s} \end{aligned} \tag{2.17}$$

The equation 2.14 and 2.16 are obtained based on the assumption that the vehicle is undergoing pure side or longitudinal slip. However, in the real driving condition, the tire is possible to operate in presence of both side and longitudinal slip. In this situation, the coupling effect between longitudinal and lateral force has to be considered, as the sum of tire force should not exceed the total friction force of tire μF_{wz}.

During combined slip behavior, the total tire slip is expressed as [Rajamani, 2012]:

$$\sigma_t = \sqrt{\sigma_x^2 + \sigma_y^2} \tag{2.18}$$

The longitudinal force and lateral force during combined slip ($F_{wt,x}$, $F_{wt,y}$) are the two components of total tire forces:

$$\begin{aligned} F_{wt,x} &= \frac{\sigma_x}{\sigma_t} F_{wt} \\ F_{wt,y} &= \frac{\sigma_y}{\sigma_t} F_{wt} \end{aligned} \tag{2.19}$$

where F_{wt} is the total tire-road contact force.

It is noted that the Brush model introduced here is based on the steady state assumption, which means the tire forces can react to the slip variation without time delay. In fact, for a real tire, it need time to develop the deformation when the slip occurs. The models which considered the dynamic process of the generation of tire forces are called the transient tire model. We will briefly introduce the transient model at section 2.2.4.

2.2.3.3 Dugoff's Tire Model

The Brush tire model introduced above is a simplified analytical model, it could represent both the linear and non-linear characteristic of tire. However the inconvenient point of this kind of models is the need of three parameters during application: the cornering stiffness, friction coefficient and the length of contact patch. Compared to the Brush model, the Dugoff's model offers a simpler formula, as it synthesizes all the tire property parameters into two constants, C_σ and C_α, referred to as longitudinal slip stiffness and cornering stiffness of the tire. Furthermore, the relation for combined slip is clearly expressed in Dugoff's model [Dugoff et al., 1969]. The coupling effect of friction in different direction is also called the "Friction Ellipse". More details about the importance of "Friction Ellipse" can be found in many literature [Pacejka, 2006]. Another significant advantage of Dugoff's tire model is that it has considered the influence of the vertical load on the generation of tire forces. Hence, in extensive literature such as [Zhang et al., 1998] [Dakhlallah et al., 2008] [Boyden and Velinsky, 1994] [Smith, 2004], the Dugoff model is adopted for its simplicity and efficiency. This model is one of the three models usually referred to as the HSRI-models developed at the Highway Safety Research Institute [Dugoff et al., 1969]. The Dugoff's model is also an analytical model that assumes a uniform vertical pressure distribution on the tire contact patch.

The Dugoff tire model can be used for calculation of lateral and longitudinal forces, either for pure-slip or combined-slip conditions. The longitudinal tire force is obtained by

$$\overline{F_x} = -C_\sigma \frac{\sigma_x}{1+\sigma_x} f(\lambda) \tag{2.20}$$

and the lateral tire force is given by:

$$\overline{F_y} = -C_\alpha \frac{\tan\alpha}{1+\sigma_x} f(\lambda) \tag{2.21}$$

and $f(\lambda)$ is given by:

$$f(\lambda) = \begin{cases} (2-\lambda)\lambda & if\ \lambda < 1 \\ 1 & if\ \lambda \geq 1 \end{cases} \tag{2.22}$$

$$\lambda = -\frac{\mu F_{wz}(1+\sigma_x)}{2[(C_\sigma \sigma_x)^2 + (C_\alpha \tan\alpha)^2]^{1/2}} \tag{2.23}$$

2.2.3.4 Magic Tire Model

The brush model and the Dugoff's model are physically intuitive and appear quite realistic, however these analytical models are not always accurate compared with experimental measurement [Pacejka, 2006]. Especially at large slip and at combined slip, the

difference between model prediction and measurement is not negligible. The following important features which are not included in the simple brush model may be responsible for these differences [Rajamani et al., 2006]

- unequal stiffness in x and y directions,
- non-symmetric and non-constant pressure distribution
- non-constant friction coefficient, including a difference between static and kinetic friction coefficients

It is possible to introduce these factors into the physical model, but this will highly increase the model complexity. Besides using analytical physical model, the empirical modeling based on experimental data is an alternate way to obtain a more accurate tire model. A very flexible empirical tire model is proposed by Holmes (1968) for curve fitting. The model is a polynomial equation of speed and side slip angle, expressed as [Holmes and Stone, 1969]:

$$F_{0y} = a_0 + a_1 v_x + a_1 v_x^2 + a_3 \alpha + a_4 \alpha^2 + a_5 \alpha^3 + a_6 R + a_7 P \tag{2.24}$$

where P is a tire -pattern constant and R is a tire-tread constant. The coefficients $a_{1\ldots7}$ are the empirical constant and have no physical interpretation. However, the idea to treat the dependence of the velocity as an additional contribution was not really accepted by the other researchers in the field.

Many other empirical tire models are also proposed to optimize the curve fitting for combined slip situation. More details about these models can be found in [Kiencke and Nielsen, 2005].

The paper [Pacejka et al., 1987] present the “Magic Formula”, which was quickly widely accepted and became the best known empirical model. Compared with the model of Holmes, the Magic tire model is also referred to as semi-empirical, because the model is based on measured data but also uses physical models. This model was developed as a joint venture between Volvo Car Corporation and the Delft University of Technology.

The basic formula for this model is:

$$y = D \sin[C \arctan\{Bx - E(Bx - \arctan Bx)\}] \tag{2.25}$$

with

$$\begin{aligned} Y(x) &= y(x) + S_v \\ x &= X + S_h \end{aligned} \tag{2.26}$$

In these formulas Y is the output variable: it could be longitudinal force F_{wx} or lateral force F_{wy} or aligning moment M_{wz}. X is the input variable, it stands for lateral slip angle α or longitudinal slip σ_x. Therefore the following equations are deduced:

$$\overline{F_{wx}}(\sigma_x + S_{hx}) = D_x \sin[C_x \arctan\{B_x\sigma_x - E_x(B_x\sigma_x - \arctan(B_x\sigma_x))\}] + S_{vx} \tag{2.27}$$

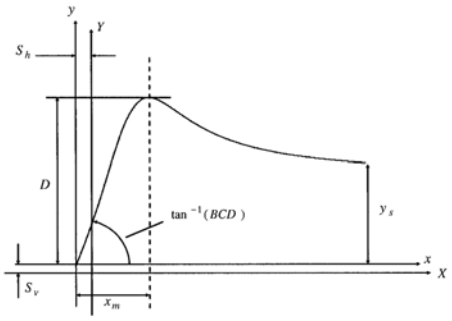

Figure 2.10: Explanation of magic formula parameters [Rajamani, 2012]

$$\overline{F_{wy}}(\alpha + S_{hy}) = D_y \sin[C_y \arctan\{B_y\sigma_y - E_y(B_y\sigma_y - \arctan(B_y\sigma_y))\}] + S_{vy} \quad (2.28)$$

The parameters B, C, D, E, S_v, S_h of this formula have their physical interpretations, as illustrated in the Figure 2.10.

B : the stiffness factor. This factor determines the slope at the origin; C : the shape factor that controls the resulting curve; D: the peak factor; E : the curvature factor, it controls the value of the slip at which the peak of the curve occurs; $B \times C \times D$: this product corresponds to the slope at the origin . For lateral force, this factor corresponds to the cornering stiffness. S_h, S_v are the horizontal shift and vertical shift respectively, which are possibly caused by the rolling resistance and make the curves not to pass through the origin.

In 1991, Pacejka proposed a detailed method to calculate the values of these parameters [Pacejka and Sharp, 1991], which has taken into account the camber angle, the cornering stiffness and the load variations . To visualize the Magic formula, the longitudinal, lateral and self-aligning moment evolution for different vertical loads are illustrated in the Figure 2.11. When the wheel load increases, the tire can better stick to the road and thus the maximum tire forces increase.

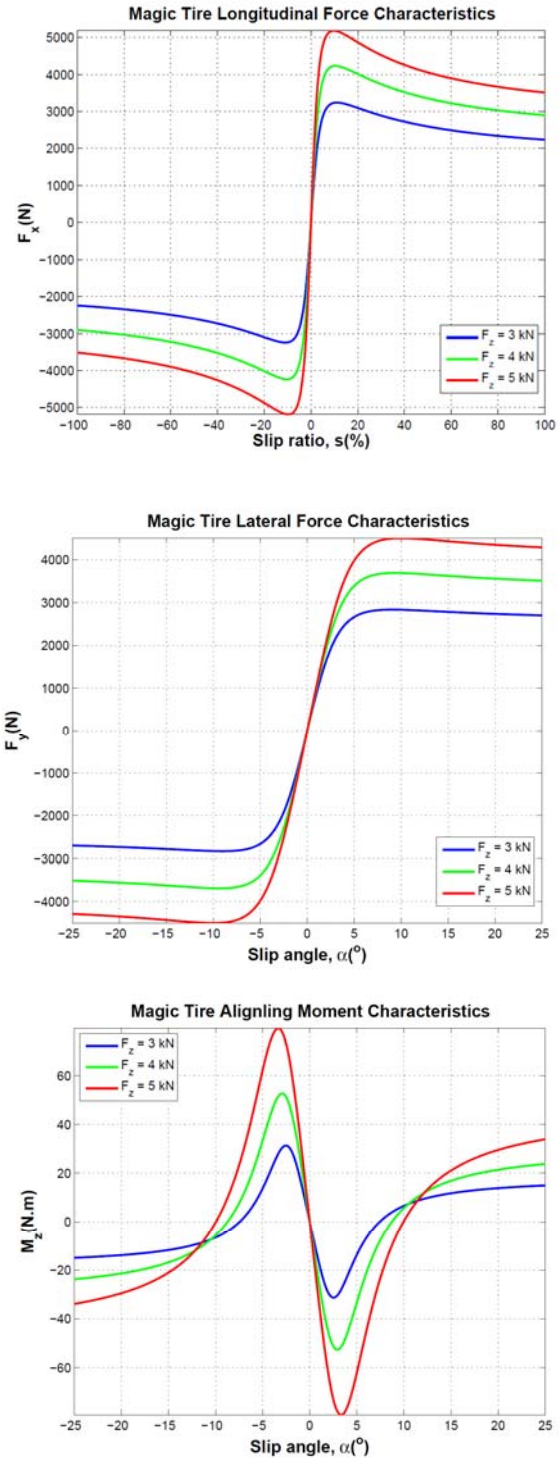

Figure 2.11: The characteristics of Magic tire model for longitudinal force, lateral force and aligning moment

2.2.4 Transient State Tire Models

Transient state tire model is developed to analyze the dynamic behavior of tire. Due to pneumatic tire's flexible structure, tire forces do not develop instantaneously at maneuvering actions, but require a short period of time to build up. In steady state tire model, we assume the tire slip can effectively represent the deformation of tire. However, in real situation, the tire works like a damping system, a sudden change of slip angle will not instantaneously lead to the deformation of tire. The difference between steady state tire model and transient tire model may occurs when the vehicle's dynamics states change quickly, especially at high speed. It has also been shown that experimentally measured lateral tire forces have under-damped characteristics at high speeds [Heydinger et al., 1991]. Therefore, the transient tire model has lately gained a large interest.

A simple way to model this transient behavior of tire dynamics, was described and validated in [Clark, 1981]. The model represented by a first-order transfer function, describes the relation between the measured slip, $\bar{\lambda}$, and the effective slip, λ, which generates the tire forces and corresponds to the real deformation of tire:

$$\frac{\sigma_{rel}\, d\lambda}{v_x\ dt} = \lambda - \bar{\lambda} \tag{2.29}$$

where σ_{rel} is the relaxation length, which is the rolling distance needed to buildup tire deformation. v_x is the longitudinal speed, σ/v_x is the time constant of the system.

The equation 2.29 shows that the tire deformation needs time to build up when the tire slip occurs. A typical first order model that can describe the tire force dynamics is presented by [Rajamani, 2012]:

$$\tau \dot{F}_y + F_y = \overline{F_y} \tag{2.30}$$

where τ is the relaxation time constant, F_y is the dynamics lateral force and $\overline{F_y}$ is the lateral tire force calculated from a steady state tire model.

The time constant τ can be approximated by

$$\tau = \frac{\sigma_{rel}}{v_x} \tag{2.31}$$

where σ_{rel} is the length the tire need to develop the tire force, called as the relaxation length,

The dynamic model is employed only in high velocity. At low velocities, the "damping effect" is not obvious and thus the transient tire model is not valid.

2.3 Dynamic Models Of A Rigid Car

The rigid body dynamics studies the movement of systems of interconnected bodies under the action of external forces. The vehicle can be regarded as a system of vehicle body and vehicle chassis, while the vehicle body and chassis are connected by the suspensions. In this section, we neglected the flexible interaction between the two parts of vehicle, considering the entire vehicle as one rigid body. In this way, we can concentrate on the relationship between the external forces and vehicle's movement, without studying the internal forces. In order to better describe the dynamics of a moving vehicle, the fundamental step is to clearly define the vehicle coordinate frame, as introduced in the section 2.3.1. Then the planar rigid vehicle kinematics is describe in details in Section 2.3.2. The planar kinematics studies the vehicle behaviors at level pavement. In reality, the road can be irregular (banked or sloped). Consequently, the vehicle motion is no longer a planar motion but a three-dimensional motion. The 3D vehicle kinematics is discussed in Section 2.3.3. The relation between vehicle's motion and vehicle's external forces are explained in Section 2.3.4.

2.3.1 Vehicle Coordinate Frame

Generally there are two widely used coordinate frames in the research of vehicle dynamics, the vehicle body fixed coordinate frame $B_{(C\,xyz)}$ and the grounded fixed coordinate frame $G_{(OXYZ)}$ as shown in Figure 2.12. The vehicle coordinate frame is called the body frame or vehicle frame, and the grounded frame is called the global frame. The body frame is attached to the vehicle at the mass center C, and it is static related to the vehicle and passengers. In the frame of $B_{(C\,xyz)}$, the x-axis is a longitudinal axis passing through mass center C and directed forward. The y-axis goes laterally to the left from the driver's viewpoint. The z-axis is perpendicular to the ground, which makes the coordinate system a right-hand triad. The equations of motion in vehicle dynamics are usually expressed in body coordinate frame $B_{(C\,xyz)}$.

The forces applied on the vehicle are vectors defined according to the body coordinate frame. The resultant of external forces and moments, that the vehicle receives from the ground and environment, makes the vehicle force system ($^{B}\mathbf{F}$, $^{B}\mathbf{M}$), as shown in equation 2.32.

$$ {}^{B}\mathbf{F} = \begin{bmatrix} F_x \\ F_y \\ F_z \end{bmatrix}, \quad {}^{B}\mathbf{M} = \begin{bmatrix} M_x \\ M_y \\ M_z \end{bmatrix} \tag{2.32} $$

where F_x, F_y,F_z are the resultant longitudinal, lateral and vertical forces of the vehicle, M_x, M_y ,M_z are the resultant moments about the x, y and z axis. In this thesis, $F_x < 0$ if the vehicle is braking, $F_y > 0$ if it is leftward from the driver's viewpoint, $F_z > 0$ if it

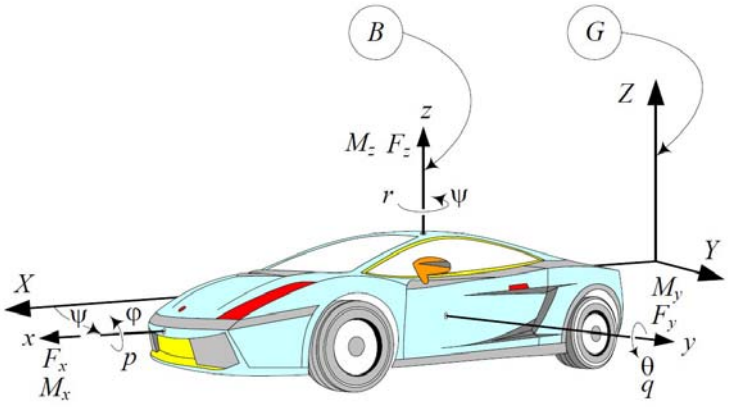

Figure 2.12: Vehicle body coordinate frame [Reza, 2007]

is upward, $M_x > 0$ if the vehicle tends to turn anti-clockwise about the x-axis, $M_y > 0$ if the vehicle tends to turn about the y-axis and move the head down, $M_z > 0$ if the tire tends to turn anti-clockwise about the z-axis.

Besides the resultant forces, we also define the kinematic parameters according to the body frame. The roll angle ϕ_v describes the rotation of vehicle body about the x-axis, pitch angle θ_v is the rotation about the y-axis, and yaw angle ψ_v is about the z-axis. The rate of the rotation angles are called as roll rate ω_x, pitch rate ω_y, and yaw rate ω_z respectively. v_x, v_y, v_z are the velocities referred to the body frame. a_x, a_y, a_z are the accelerations in the three corresponding directions.

The vehicle's motion is usually described in body frame, due to the velocities and accelerations measured by vehicle's local perception system are parallel to the body frame. However, sometimes it is necessary to employ the global frame to describe vehicle's motion. A typical example is the application of GPS and digital map. When we want to locate the vehicle on the digital map and visualize its trajectory, it is necessary to transform the motion into global frame.

The transformation of speed vector can be obtained by equation 2.33.

$$^{G}\mathbf{v} = \mathbf{R}_{B}^{GB}\mathbf{v} \tag{2.33}$$

Similarly, the angular velocity, angular accelerations and linear accelerations measured in body frame can be transferred into global frame with equation 2.34.

$$\begin{aligned} ^{G}\boldsymbol{\omega} &= \mathbf{R}_{B}^{GB}\boldsymbol{\omega} \\ ^{G}\dot{\boldsymbol{\omega}} &= \mathbf{R}_{B}^{GB}\dot{\boldsymbol{\omega}} \\ ^{G}\boldsymbol{a} &= \mathbf{R}_{B}^{GB}\boldsymbol{a} \end{aligned} \tag{2.34}$$

Besides the six degree of motion, the heading angle, side slip angle of vehicle center and

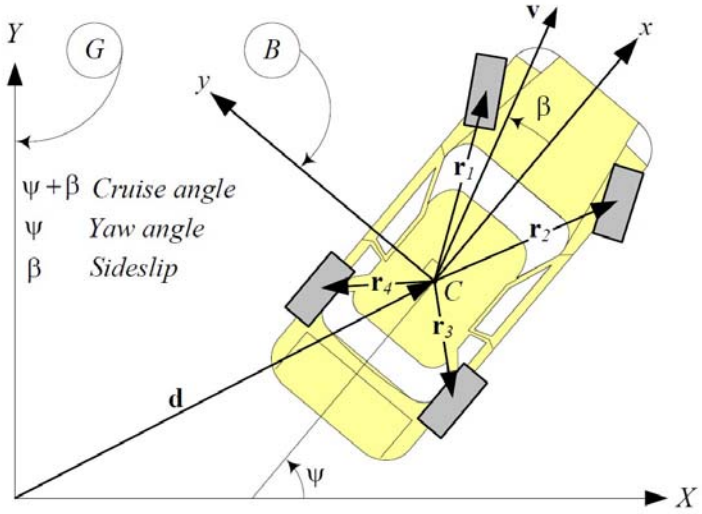

Figure 2.13: Illustration of cruise angle, yaw angle and side slip angle

cruise angle are also important parameters to describe vehicle's behaviors. As illustrated in the Figure 2.13, the heading angle ψ is defined as the Cx-axis direction in global frame. It is noted that the heading direction is different with the velocity direction, when the vehicle is turning. The velocity of the vehicle v makes an angle β with the Cx-axis, which is called as attitude angle or side slip angle. In addition, the vehicle's velocity vector v makes an angle $\beta + \psi$ with the global OX-axis that is called the cruise angle.

2.3.2 Vehicle Dynamics At 2D Environment

When the vehicle is regarded as a rigid body and it is moving at horizontal and flat ground, the z-axis in body frame is always parallel to the Z-axis in global frame, as illustrated in Figure 2.14. Moreover, the roll movement and pitch movement could be ignored. .

The rotation matrix at level ground is given by equation 2.35.

$$\mathbf{R}_B^G = \begin{bmatrix} \cos\psi & -\sin\psi & 0 \\ \sin\psi & \cos\psi & 0 \\ 0 & 0 & 1 \end{bmatrix} \tag{2.35}$$

where ψ is the yaw angle.

The dynamics relationship between the motion and the forces can be expressed by [Rajamani et al., 2006]:

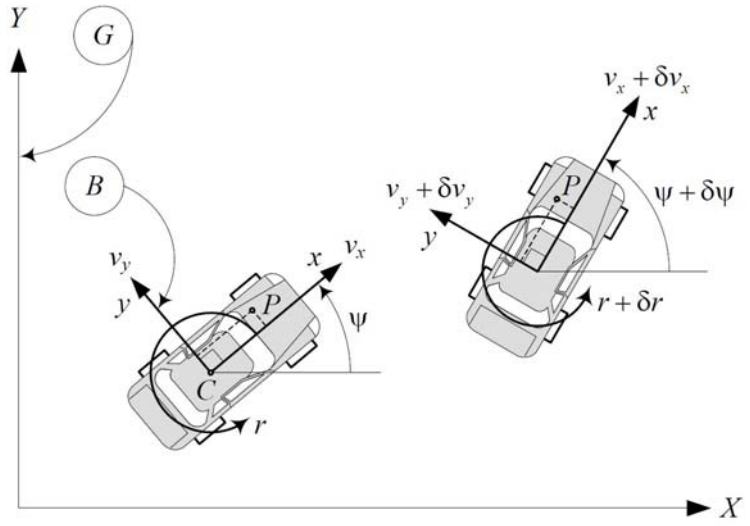

Figure 2.14: Description of motion in body frame and global frame

$$\begin{bmatrix} F_x \\ F_y \\ F_z \end{bmatrix} = \begin{bmatrix} m(\dot{v}_x - \dot{\psi} v_y) \\ m(\dot{v}_y + \dot{\psi} v_x) \\ 0 \end{bmatrix}$$
$$\begin{bmatrix} M_x \\ M_y \\ M_z \end{bmatrix} = \begin{bmatrix} 0 \\ 0 \\ I_z \ddot{\psi} \end{bmatrix} \tag{2.36}$$

where v_x, v_y, $\dot{\psi}$ are the measured longitudinal speed, lateral speed and the yaw velocity, I_z is vehicle's moment of inertia around z-axis, g is the standard gravity on earth.

The equation 2.36 is valid under the assumption that the road is level and horizontal, which is a simplification of the real road condition. In order to improve the accuracy of vehicle dynamics models, the road inclination (bank angle and slope angle) should be considered. In the next section, we will discuss the vehicle dynamics at irregular road, the so called 3D environment.

2.3.3 Vehicle Dynamics At 3D Environment

When we consider the irregularity of the road, the z-axis in body frame is no longer parallel to the Z-axis in global frame. The axis of body frame make an angle with the axis of global frame, as illustrated in Figure 2.15.

Compared with the planar motion, the vehicle's 3D motion has three additional degree of freedom, the pitch motion, the roll motion and the vertical motion. By neglecting the

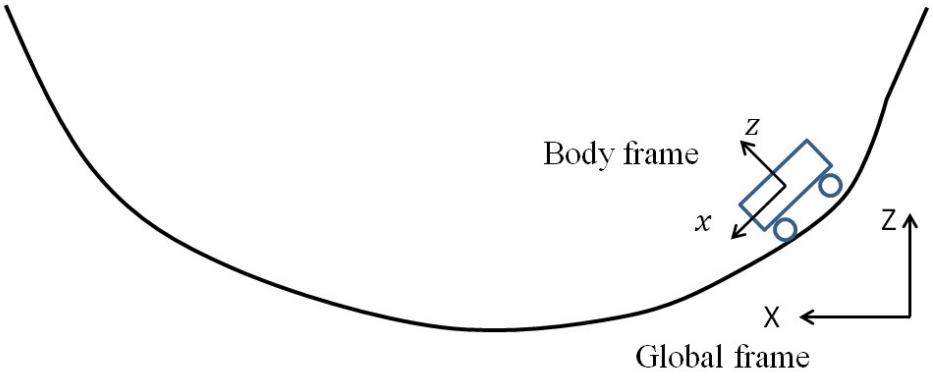

Figure 2.15: A rigid car running at irregular road

coupling effects between each rotation, we can consider the orientation of the vehicle is obtained by realizing three basic rotations: firstly rotate the vehicle along X axis with an angle ϕ, then rotate along Y axis with an angle θ, finally rotate along Z axis with an angle ψ. The final rotation matrix at irregular road is given by equation 2.37.

$$R_B^G = R_X R_Y R_Z \tag{2.37}$$

where R_X, R_Y, R_Z are the three basic rotation matrix which rotate vectors along X, Y, Z axis.

$$R_X = \begin{bmatrix} 1 & 0 & 0 \\ 0 & \cos\phi & -\sin\phi \\ 0 & \sin\phi & \cos\phi \end{bmatrix} \tag{2.38}$$

$$R_Y = \begin{bmatrix} \cos\theta & 0 & \sin\theta \\ 0 & 1 & 0 \\ -\sin\theta & 0 & \cos\theta \end{bmatrix} \tag{2.39}$$

$$R_Z = \begin{bmatrix} \cos\psi & -\sin\psi & 0 \\ \sin\psi & \cos\psi & 0 \\ 0 & 0 & 1 \end{bmatrix} \tag{2.40}$$

If we consider the vehicle as a rigid body, the vehicle's rotation about the global frame is only caused by the road angle. If we consider the deflection of suspension, the each rotation consists of two components: rotation motion caused by deflection of suspension (ϕ_v, θ_v, ψ_v) and rotation motion caused by the road inclination (ϕ_r, θ_r, ψ_r).

$$\begin{aligned} \theta_g &= \theta_v + \theta_r \\ \phi_g &= \phi_v + \phi_r \\ \psi_g &= \psi_v + \psi_r \end{aligned} \tag{2.41}$$

The force system in global frame is obtained with the Newton's law, expressed by:

$$\begin{bmatrix} F_X \\ F_Y \\ F_Z \end{bmatrix} = m \begin{bmatrix} \dot{v}_X \\ \dot{v}_Y \\ \dot{v}_Z \end{bmatrix}$$
$$\begin{bmatrix} M_X \\ M_Y \\ M_Z \end{bmatrix} = \begin{bmatrix} I_X & 0 & 0 \\ 0 & I_Y & 0 \\ 0 & 0 & I_Z \end{bmatrix} \begin{bmatrix} \dot{\omega}_X \\ \dot{\omega}_Y \\ \dot{\omega}_Z \end{bmatrix} \tag{2.42}$$

Then the force system expressed in the body frame can be obtained by the transformation process, as shown in the following equations:

$$\begin{bmatrix} F_x \\ F_y \\ F_z \end{bmatrix} = (R_X R_Y R_Z)^{-1} \begin{bmatrix} F_X \\ F_Y \\ F_Z \end{bmatrix} = \begin{bmatrix} m(\dot{v}_x - \dot{\psi} v_y) \\ m(\dot{v}_y + \dot{\psi} v_x) \\ -m v_x \dot{\theta} + m v_y \dot{\phi} \end{bmatrix}$$
$$\begin{bmatrix} M_x \\ M_y \\ M_z \end{bmatrix} = (R_X R_Y R_Z)^{-1} \begin{bmatrix} M_X \\ M_Y \\ M_Z \end{bmatrix} = \begin{bmatrix} I_x \dot{\omega}_x + (I_z - I_y)\dot{\theta}\dot{\psi} \\ I_y \dot{\omega}_y + (I_x - I_z)\dot{\phi}\dot{\psi} \\ I_z \dot{\omega}_z + (I_y - I_x)\dot{\theta}\dot{\phi} \end{bmatrix} \tag{2.43}$$

2.3.4 External Forces And Moments Applied On The Vehicle

The forces acting on a system of connected rigid body can be divided into internal and external forces. Internal forces are acting between connected bodies, and external forces are acting from outside of the system. According to the principle of Newton, the motion of vehicle is controlled by external forces. The force systems obtained in the former section represent the resultant external forces and the resultant external moments applied on the vehicle. For a standard vehicle, the external forces and moments come from the tire-road contact, the gravity and the air.

$$^{B}\mathbf{F} = \mathbf{F}_{\mathbf{gravity}} + \mathbf{F}_{\mathbf{wheel}} + \mathbf{F}_{\mathbf{air}} \tag{2.44}$$

$$^{B}\mathbf{M} = \mathbf{M}_{\mathbf{gravity}} + \boldsymbol{M}_{\text{wheel}} + \mathbf{M}_{\mathbf{air}} \tag{2.45}$$

Air resistance

The air resistance is neglected in our development:

$$\begin{aligned} \mathbf{F}_{\mathbf{air}} &= [0\ 0\ 0]^T \\ \mathbf{M}_{\mathbf{air}} &= [0\ 0\ 0]^T \end{aligned} \tag{2.46}$$

Gravity force

The gravity forces is determined by road geometry and vehicle mass.

$$\mathbf{F_{gravity}} = m(R_B^G)^T \begin{bmatrix} 0 \\ 0 \\ g \end{bmatrix} = mg \begin{bmatrix} -\sin\theta \\ -\cos\theta\sin\phi \\ -\cos\theta\cos\phi \end{bmatrix} \qquad \mathbf{M_{gravity}} = [0\ 0\ 0]^T \tag{2.47}$$

where the moment generated by gravity forces is zero, due to the moment center is at the gravity center.

Tire-road contact force

The tire-road contact forces $\mathbf{F_{wheel}}$ are generated by the interaction between the road and tire. Tires affect a vehicle's handling, traction, ride comfort, and fuel consumption. The performance of a vehicle is mainly influenced by the characteristics of its tires. The mathematical models for calculating tire forces are already introduced in the section 2.2. In this section, we will explain how tire forces can affect vehicle's motion.

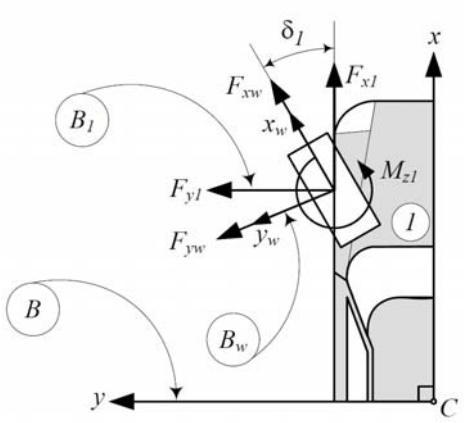

Figure 2.16: Projection of tire forces into the vehicle body frame

The force system generated at the tire print can be expressed in the wheel frame with equation 2.48

$$\begin{aligned} {}^{w}\mathbf{F_{11}} &= F_{x11}\vec{i}_{11} + F_{y11}\vec{j}_{11} + F_{z11}\vec{k}_{11} \\ {}^{w}\mathbf{F_{12}} &= F_{x12}\vec{i}_{12} + F_{y12}\vec{j}_{12} + F_{z12}\vec{k}_{12} \\ {}^{w}\mathbf{F_{21}} &= F_{x21}\vec{i}_{21} + F_{y21}\vec{j}_{21} + F_{z21}\vec{k}_{21} \\ {}^{w}\mathbf{F_{22}} &= F_{x22}\vec{i}_{22} + F_{y22}\vec{j}_{22} + F_{z22}\vec{k}_{22} \end{aligned} \tag{2.48}$$

where the index $_{ij}$ means the identity of each wheel, $_{11}$ means the front left wheel, $_{12}$ represents the front right wheel, $_{21}$ means rear left wheel and $_{22}$ stands for rear right wheel.

In order to describe the wheel forces in the body frame, we should rotate the wheel

frame along *wz*-axis until it becomes parallel to the body frame, as illustrated in the Figure 2.16. The rotation matrix needed is given by equation 2.49.

$$R^{\mathbf{B}}_{\mathbf{W},\mathbf{ij}} = \begin{bmatrix} \cos\delta_{ij} & -\sin\delta_{ij} & 0 \\ \sin\delta_{ij} & \cos\delta_{ij} & 0 \\ 0 & 0 & 1 \end{bmatrix} \tag{2.49}$$

where δ_{ij} is the steering angle of the indicated tire.

Hence, the forces of each tire are given by equation 2.50.

$$\begin{aligned} {}^{\mathbf{B}}\mathbf{F}_{\mathbf{ij}} &= R^{\mathbf{B}}_{\mathbf{W},\mathbf{ij}}\,{}^{\mathbf{w}}\mathbf{F}_{\mathbf{ij}} \\ \begin{bmatrix} F_{xij} \\ F_{yij} \\ F_{zij} \end{bmatrix} &= \begin{bmatrix} F_{xij}\cos\delta_{ij} - F_{yij}\sin\delta_{ij} \\ F_{xij}\sin\delta_{ij} + F_{yij}\cos\delta_{ij} \\ F_{zij} \end{bmatrix} \end{aligned} \tag{2.50}$$

$$\begin{aligned} {}^{\mathbf{B}}\mathbf{M}_{\mathbf{ij}} &= R^{\mathbf{B}}_{\mathbf{W},\mathbf{ij}}\,{}^{\mathbf{w}}\mathbf{M}_{\mathbf{ij}} \\ \begin{bmatrix} M_{xij} \\ M_{yij} \\ M_{zij} \end{bmatrix} &= \begin{bmatrix} 0 \\ 0 \\ M_{zij} \end{bmatrix} \end{aligned} \tag{2.51}$$

where the tire moment at the tire print M_{xij}, M_{yij} are regarded as zero to simplify the equations.

The resultant forces and moments generated by the tire-road contact are represented by equation 2.52 and 2.53.

$$\mathbf{F}_{\mathbf{wheel}} = \sum {}^{\mathbf{B}}\mathbf{F}_{\mathbf{ij}} \tag{2.52}$$

$$\mathbf{M}_{\mathbf{wheel}} = \sum {}^{\mathbf{B}}\mathbf{M}_{\mathbf{ij}} + \sum \mathbf{P}_{\mathbf{ij}} \times {}^{\mathbf{B}}\mathbf{F}_{\mathbf{ij}} \tag{2.53}$$

$$\begin{aligned} \mathbf{P_{11}} &= \begin{bmatrix} L_1 \\ \frac{E_1}{2} \\ -h \end{bmatrix} & \mathbf{P_{12}} &= \begin{bmatrix} L_1 \\ -\frac{E_1}{2} \\ -h \end{bmatrix} \\ \mathbf{P_{21}} &= \begin{bmatrix} -L_2 \\ \frac{E_2}{2} \\ -h \end{bmatrix} & \mathbf{P_{22}} &= \begin{bmatrix} -L_2 \\ -\frac{E_2}{2} \\ -h \end{bmatrix} \end{aligned} \tag{2.54}$$

where P_{ij} is the position of each wheel in the body frame, h is the height of gravity center, E_1 and E_2 are the length of front axle and rear axle respectively, L_1 is the distance from front axle to the gravity center and L_2 is the distance from the rear axle to the gravity center.

If we only consider the planar motion of vehicle, then the relation between the tire

forces and vehicle motion can be represented by equation 2.55.

$$\begin{bmatrix} m(\dot{v}_x - \dot{\psi}v_y) \\ m(\dot{v}_y + \dot{\psi}v_x) \\ 0 \end{bmatrix} = mg \begin{bmatrix} -\sin\theta \\ -\sin\phi\cos\theta \\ -\cos\theta\cos\phi \end{bmatrix} + \sum_{ij} \begin{bmatrix} F_{xij}\cos\delta_{ij} - F_{yij}\sin\delta_{ij} \\ F_{xij}\sin\delta_{ij} + F_{yij}\cos\delta_{ij} \\ F_{zij} \end{bmatrix}$$
$$\begin{bmatrix} 0 \\ 0 \\ I_z\ddot{\psi} \end{bmatrix} = \sum_{ij} \begin{bmatrix} y_{ij}F_{zij} - z_{ij}(F_{xij}\sin\delta_{ij} + F_{yij}\cos\delta_{ij}) \\ -x_{ij}F_{zij} + z_{ij}(F_{xij}\cos\delta_{ij} - F_{yij}\sin\delta_{ij}) \\ M_{zij} + x_{ij}(F_{xij}\sin\delta_{ij} + F_{yij}\cos\delta_{ij}) - y_{ij}(F_{xij}\cos\delta_{ij} - F_{yij}\sin\delta_{ij}) \end{bmatrix} \tag{2.55}$$

If we consider the irregularity of the road and the 3D motion of the vehicle, then the relation between the tire forces and the vehicle motion can be represented shown by equation 2.56.

$$\begin{bmatrix} m(\dot{v}_x - \dot{\psi}v_y) \\ m(\dot{v}_y + \dot{\psi}v_x) \\ -mv_x\dot{\theta} + mv_y\dot{\phi} \end{bmatrix} = mg \begin{bmatrix} -\sin\theta \\ -\sin\phi\cos\theta \\ -\cos\theta\cos\phi \end{bmatrix} + \sum_{ij} \begin{bmatrix} F_{xij}\cos\delta_{ij} - F_{yij}\sin\delta_{ij} \\ F_{xij}\sin\delta_{ij} + F_{yij}\cos\delta_{ij} \\ F_{zij} \end{bmatrix}$$
$$\begin{bmatrix} I_x\dot{\omega}_x + (I_z - I_y)\dot{\theta}\dot{\psi} \\ I_y\dot{\omega}_y + (I_x - I_z)\dot{\phi}\dot{\psi} \\ I_z\dot{\omega}_z + (I_y - I_x)\dot{\theta}\dot{\phi} \end{bmatrix} = \sum_{ij} \begin{bmatrix} y_{ij}F_{zij} - z_{ij}(F_{xij}\sin\delta_{ij} + F_{yij}\cos\delta_{ij}) \\ -x_{ij}F_{zij} + z_{ij}(F_{xij}\cos\delta_{ij} - F_{yij}\sin\delta_{ij}) \\ M_{zij} + x_{ij}(F_{xij}\sin\delta_{ij} + F_{yij}\cos\delta_{ij}) - y_{ij}(F_{xij}\cos\delta_{ij} - F_{yij}\sin\delta_{ij}) \end{bmatrix} \tag{2.56}$$

As a conclusion of section 2.3, our objective is to describe the relationship between the tire forces and the vehicle motion. In section 2.3.1, we have introduced two coordinate frame to describe the vehicle motion: the vehicle body frame and the global frame. In section 2.3.2, we employ the planar rigid dynamics to calculate the total external forces received by the vehicle. To generalize the vehicle dynamics model for different road geometry, we have developed the 3D vehicle dynamics models in section 2.3.3. In 3D motion, the vehicle has the liberty of pitch and roll motion, which makes our model valid even on the banked road or sloped road. The section 2.3.4 explains that the tire forces and gravity force are the main sources of the external forces. Then the relationship between the tire forces and the vehicle's motion is concluded in the end of section 2.3.4.

2.4 Dynamics Models Of A Real Vehicle

The main objective of developing vehicle dynamics models in this thesis is to observe the tire forces at three directions: longitudinal tire force F_{xij}, lateral tire force F_{yij} and vertical tire force F_{zij}. The models introduced in the section 2.3 are simplified description of tire forces, they are not able to describe the forces at each tire. In order to obtain more information about the tire forces, this section will consider the subsystems of vehicle, such as the suspension system, steering system and driveline system. In a real vehicle, the tire forces are greatly influenced by these subsystems. In [Reza, 2007] [Doumiati, 2009] [Wang, 2013], the authors have also emphasized the importance of an-

alyzing these subsystems. They propose to decompose the overall description of vehicle dynamics into three relatively separate components, the model of vertical dynamics (suspension dynamics), the model of lateral dynamics (steering dynamics) and the model of longitudinal dynamics (driveline dynamics). In the following sections, we will introduce the state of art in the modeling of these subsystems. Furthermore, we will present our proposed models for the description of tire's vertical, lateral and longitudinal forces.

2.4.1 Dynamics Models For Vehicle Vertical Motion

Awareness of vertical load at each tire is fundamental to understand the vehicle's behaviors. The vertical load can affect the maximum braking (longitudinal) forces and turning (lateral) forces that a tire can generate. Experimental data in [Lechner, 2002] has also confirmed the importance of vertical load in tire's performance. A simple model for computing vertical force of each tire can be obtained by assuming the vehicle as a rigid car. However, in a real car, the vertical dynamics is mainly affected by the suspension system. The suspension links the wheels to the vehicle body and allows relative motion. The automotive suspension on a vehicle typically has the following basic tasks:

1. To isolate a car body from road disturbances in order to provide good ride quality. Ride quality in general can be quantified by the vertical acceleration of the passenger locations. The presence of a well-designed suspension provides isolation by reducing the vibratory forces transmitted from the axle to the vehicle body.

2. To keep good road holding. The road holding performance of a vehicle can be characterized in terms of its cornering, braking and traction abilities. Improved cornering, braking and traction are obtained if the variations in normal tire loads are minimized. This is because the lateral and longitudinal forces generated by a tire depend directly on the normal tire load.

3. To provide good handling. The roll and pitch accelerations of a vehicle during cornering, braking and traction are measures of good handling. A good suspension system should ensure that roll and pitch motion are minimized.

4. To support the vehicle static weight. This task is performed well if the rattle space requirements in the vehicle are kept small.

To better accomplish the first two tasks, the suspension should be soft or flexible. It is the flexibility of suspension that reduces the transference of vibration and improves the comfort of vehicle. More information about the vehicle vibration dynamics can be found in [Reza, 2007]. Meanwhile, to accomplish the other two tasks, the suspension is better to be rigid. For a car, the suspension system should be neither too soft nor too rigid. During the design of suspension system, a compromise between being soft

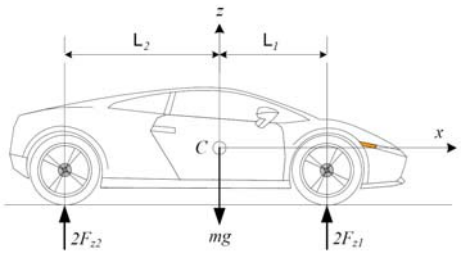

Figure 2.17: Illustration of the vertical dynamics of a vehicle parked on level pavement

or rigid has to be made. Another approach to improve the performance of suspension is to develop the active suspension. The concept of active suspension system refers to the suspension which can generate additional moments to control the suspension motion [Fischer and Isermann, 2004]. The active control of suspension motion is equivalent to control the rigidity of suspension. When the objective is to reduce vertical vibration, the active control is closed and suspension is soft. When the vehicle is undergoing a rapid turning, the active suspension control is activated to provide good handling. For more details about active suspension control, the readers can refer to [Rajamani, 2012].

In literature, the authors have already proposed some models for the vertical tire force. Both the existent models and our contribution will be introduced in the following subsections.

2.4.1.1 Vertical Forces Of A Rigid Car

The vertical forces at each tire is affected by many factors: the mass distribution, the suspension dynamics and the wheel interactions. To model all these factors will result in a set of complex non-linear equations with a lot of unknown parameters. To simplify the calculation, in the literature, authors propose a solid car model, in which we suppose the vehicle is rigid and driving on level pavement, as shown in Figure 2.17.

When the vehicle is accelerating or driving on a sloped road, the vertical forces at front wheels and rear wheels vary a lot. In the literature [Doumiati et al., 2008], this phenomenon is explained by the theory of “virtual mass”. The vehicle mass is divided into two part: the front part m_f and the rear part m_r.

$$\begin{aligned} m_f &= m\frac{L_2}{L} - m\frac{ha_x}{Lg} \\ m_r &= m\frac{L_1}{L} + m\frac{ha_x}{Lg} \end{aligned} \tag{2.57}$$

Then the vertical force of each tire can be obtained by the following equations:

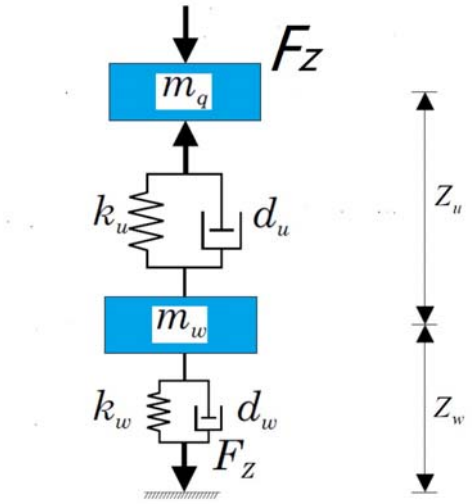

Figure 2.18: A quarter vehicle suspension system

$$\begin{aligned} F_{z11} &= \tfrac{1}{2}mg\tfrac{L_2}{L} - \tfrac{1}{2}m\tfrac{h}{L}a_x - m\tfrac{hL_2}{e_1L}a_y + m\tfrac{h^2L_2}{e_1Lg}a_xa_y \\ F_{z12} &= \tfrac{1}{2}mg\tfrac{L_2}{L} - \tfrac{1}{2}m\tfrac{h}{L}a_x + m\tfrac{hL_2}{e_1L}a_y - m\tfrac{h^2L_2}{e_1Lg}a_xa_y \\ F_{z21} &= \tfrac{1}{2}mg\tfrac{L_1}{L} + \tfrac{1}{2}m\tfrac{h}{L}a_x - m\tfrac{hL_1}{e_2L}a_y - m\tfrac{h^2L_1}{e_2Lg}a_xa_y \\ F_{z22} &= \tfrac{1}{2}mg\tfrac{L_1}{L} + \tfrac{1}{2}m\tfrac{h}{L}a_x + m\tfrac{hL_1}{e_2L}a_y + m\tfrac{h^2L_1}{e_2Lg}a_xa_y \end{aligned} \tag{2.58}$$

where a_x, a_y are the longitudinal and lateral accelerations of vehicle motion.

2.4.1.2 Vertical Forces Of A Soft-suspension Car

When the vehicle suspension is very soft, the rigid car dynamics is no longer valid. To study the suspension behaviors, the authors in the literature have proposed quarter car suspension model [Rajamani, 2012], as shown in Figure 2.18. In the figure, the quarter of car is divided into sprung mass m_q and unsprung mass m_w. The suspension connects the sprung mass and unsprung mass and it is characterized as a spring of stiffness k_u, and a damper with viscous damping coefficient d_u. The unsprung mass m_w is in direct contact with the ground through a tire, which is also represented by a spring k_w and damper d_w. According to the D'Alembert's principle, the vehicle's suspension system is governed by the following relations:

$$\begin{aligned} m_q\ddot{Z}_u + d_u(\dot{Z}_u - \dot{Z}_w) + k_u(Z_u - Z_w) + m_qg &= 0 \\ m_w\ddot{Z}_w - d_u(\dot{Z}_u - \dot{Z}_w) - k_u(Z_u - Z_w) + d_w(\dot{Z}_w - \dot{Z}_r) + k_w(Z_w - Z_r) + m_wg &= 0 \\ F_{wz} + d_w(\dot{Z}_w - \dot{Z}_r) + k_w(Z_w - Z_r) &= 0 \end{aligned} \tag{2.59}$$

where Z_u, Z_w are the positions of sprung mass and unsprung mass respectively, in the global coordinate frame. Z_r is the height of road surface which describes the undulation of road.

To simplify the calculation, we consider the total vehicle mass is supported by the suspension, which means $m_w = 0$. Then we can get

$$F_{zij} = d_u\dot{\sigma}_{ij} + k_u\sigma_{ij} \tag{2.60}$$

where σ_{ij} is the deflection of a quarter of vehicle suspension, then $\sigma_{ij} = Z_w - Z_u$.

2.4.1.3 The contribution proposed for vertical dynamics model

In the following paragraph, we will propose a new mathematical model for the vertical tire forces. To begin with, we'd like to compare the models presented above.

- The first model we introduced is the most widely used vertical dynamics model, represented by equation 2.58, noted as $M^1_{vertical}$. This model is based on the rigid car assumption, which means all the vehicle mass can be regarded as unsprung mass.

- The second model is the quarter-car suspension model as shown in equation 2.60, noted as $M^2_{vertical}$. It uses directly the suspension deflection to calculate vertical forces. The deflection of suspension at each wheel is relatively independent and could represent the mass distribution. However, the forces calculated with $M^2_{vertical}$ is easily affected by the sensor noises when the vehicle is moving. Therefore, the model $M^2_{vertical}$ is usually employed at static situation.

To improve the accuracy of the vertical dynamics model at banked or sloped roads, we propose three modifications:

1. Calibration of measured accelerations;
2. Calculation of the transfer of vertical force by using the pitch and roll angle;
3. Combination of the rigid car model and the soft car model.

Calibration of the measured accelerations

The rigid car model is not accurate especially at banked road, as it doesn't take into account the roll and pitch angle of vehicle body. In a real situation, as illustrated in Figure 2.19, The inertial sensors are installed at the vehicle body and thus will rotate with vehicle body.The measured accelerations are not parallel to the ground, which will result in the errors of rigid car model. In order to eliminate the errors caused by the rotation of inertial sensors, we propose to project the measurement into the vehicle body

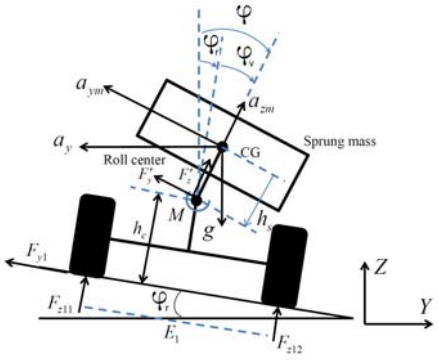

Figure 2.19: Illustration of errors of measured acceleration: the measured lateral acceleration is not parallel to the road surface

frame. When both the pitch and roll motion are considered, the calibration process is represented by the following equations:

$$\begin{bmatrix} a_{xm,c} \\ a_{ym,c} \\ a_{zm,c} \end{bmatrix} = R_\phi R_\theta \begin{bmatrix} a_{xm} \\ a_{ym} \\ a_{zm} \end{bmatrix} \tag{2.61}$$

where $[a_{xm,c},\ a_{ym,c},\ a_{zm,c}]$ are the calibrated accelerations, $R_\phi,\ R_\theta$ are the rotation matrix.

$$R_\phi = \begin{bmatrix} 1 & 0 & 0 \\ 0 & \cos\phi_v & -\sin\phi_v \\ 0 & \sin\phi_v & \cos\phi_v \end{bmatrix},\quad R_\theta = \begin{bmatrix} \cos\theta_v & 0 & \sin\theta_v \\ 0 & 1 & 0 \\ -\sin\theta_v & 0 & \cos\theta_v \end{bmatrix} \tag{2.62}$$

where ϕ_v, θ_v are the roll angle and pitch angle of vehicle body.

Modeling of transfer of vertical load

Different with the virtual mass theory, we propose to use the transfer of vertical load to explain the difference between the vertical force of each tire. The transfer of vertical load at front and rear axle ($T_{Fz,f}$ and $T_{Fz,r}$) are defined as the load difference between left wheels and right wheels:

$$\begin{aligned} T_{Fz,f} &= F_{z11} - F_{z12} \\ T_{Fz,r} &= F_{z21} - F_{z22} \end{aligned} \tag{2.63}$$

With the definition of transfer of vertical load, the vertical dynamics of a rigid car, expressed in equation 2.58, can be equally transformed to the following equations.

$$\begin{aligned} 0 &= L_1 F_{zf} - L_2 F_{zr} + mha_x \\ 0 &= F_{zf} + F_{zr} - mg \\ 0 &= \tfrac{e_1}{2} \cdot T_{Fz,f} + \tfrac{e_2}{2} \cdot T_{Fz,r} + mha_y \\ 0 &= \frac{e_1 \cdot T_{Fz,f}}{e_2 \cdot T_{Fz,r}} - \frac{F_{zf}}{F_{zr}} \end{aligned} \tag{2.64}$$

where e_1, e_2 are the width of front and rear axles, F_{zf} and F_{zr} are the resultant vertical force at front and rear axle.

Inspired by the work of [Wang, 2013], we propose to use the roll angle and pitch angle to describe the transfer of vertical load, rather than using the accelerations. Note that the deformation of suspension already contains the information of gravity force. Therefore when using the suspension to calculate tire vertical load, it is not necessary to develop an additional item to represent the road inclination. The pitch and roll motion of suspension can be represented by the full car suspension model, as illustrated in Figure 2.20.

The full car model consists of four quarter-car suspension models and takes into account the interaction between each part of the suspension, as illustrated in Figure 2.20 a). The full car model could describe more details about the suspension motion but has too many parameters to configure. To facilitate the computation, we propose to simplify the full car suspension model as illustrated in Figure 2.20 b). In the simplified suspension model (pitch-roll model), we only consider the pitch and roll motion of the suspension. The pitch angle and roll angle of suspension are noted as θ_b, ϕ_b. Usually, the roll center varies according to the vehicle movement, here we assumed that the vehicle roll center keeps constant and it is coincident with the center of gravity in the top view [Milliken et al., 2003]. The suspension system's property is represented by the roll stiffness K_ϕ, the pitch stiffness K_θ, the roll damping coefficient C_ϕ and the pitch damping coefficient C_θ. Then according to the torque balance in the roll axis, the roll dynamics of the vehicle body can be described by the following differential equation:

$$I_{xx}\ddot{\phi}_b + C_\phi \dot{\phi}_b + K_\phi \phi_b = ma_{ym} h_s \tag{2.65}$$

where $I_{xx}$is the inertia moment of the vehicle with respect to the roll axis, while I_{yy} is respect to the pitch axis and h_s is the distance between the mass center and the roll axis.

Similarly, we can have the pitch dynamics expressed as:

$$I_{yy}\ddot{\theta}_b + C_\theta \dot{\theta}_b + K_\theta \theta_b = ma_{xm} h_s \tag{2.66}$$

For a soft-suspension car, the roll-pitch motion of suspension will transfer torques to

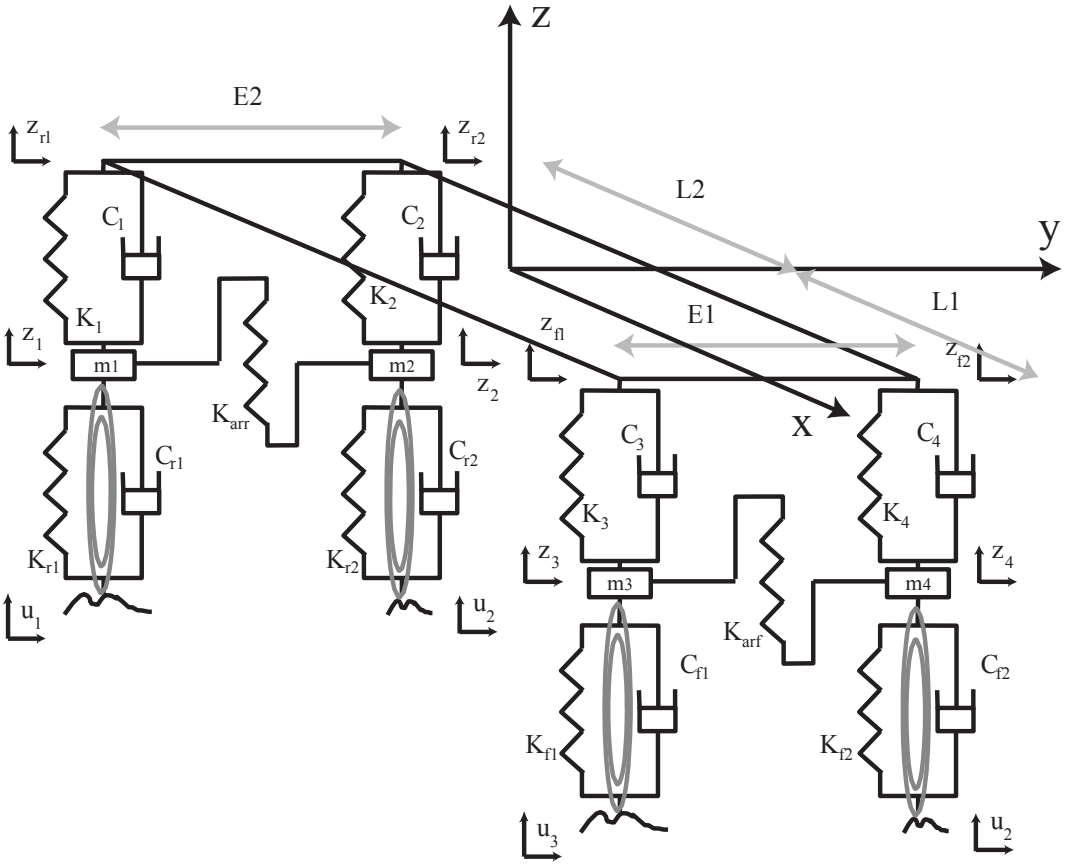

a)

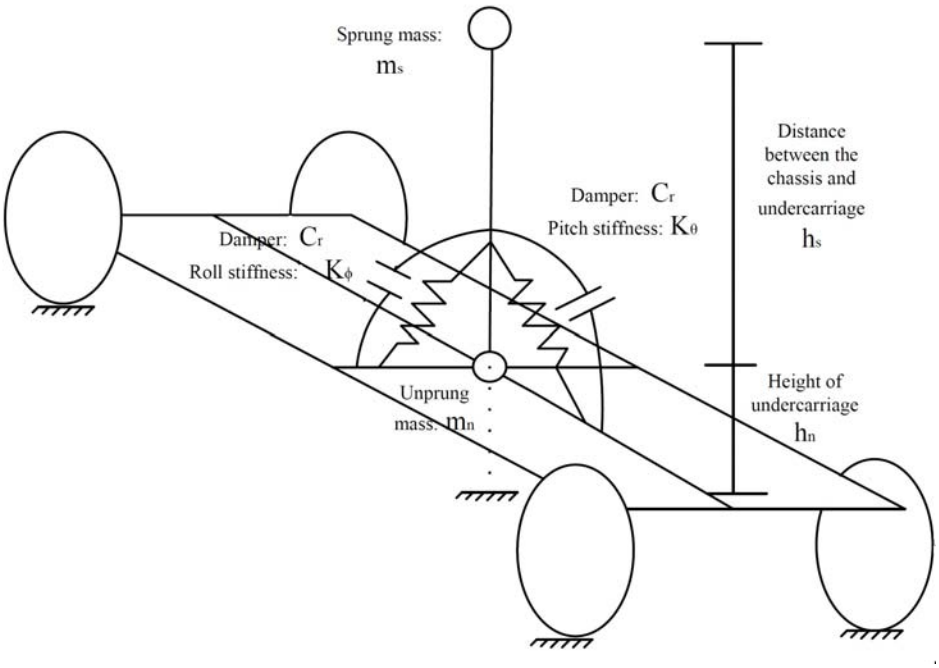

b)

Figure 2.20: a) Full-car automotive suspension model [Baffet, 2007] b) the proposed pitch-roll suspension model

the axles and wheels.

$$\begin{aligned} M_{x,sus} &= C_\phi \dot{\phi}_b + K_\phi \phi_b \\ M_{y,sus} &= C_\theta \dot{\theta}_b + K_\theta \theta_b \end{aligned} \tag{2.67}$$

where $M_{x,sus}$, $M_{y,sus}$ are the torque about x-axis and y-axis respectively.

Different with the quarter-suspension model, the pitch-roll model focus on the motion of the whole suspension. The vertical force obtained through the pitch-roll model is noted as $M^3_{vertical}$, as shown in the following equations.

$$\begin{aligned} 0 &= L_1 F_{zf} - L_2 F_{zr} + M_{y,sus} \\ 0 &= F_{zf} + F_{zr} - ma_z \\ 0 &= \tfrac{e_1}{2} \cdot T_{Fz,f} + \tfrac{e_2}{2} \cdot T_{Fz,r} + M_{x,sus} \\ 0 &= \frac{e_1 \cdot T_{lat,f}}{e_2 \cdot T_{lat,r}} - \frac{F_{zf}}{F_{zr}} \end{aligned} \tag{2.68}$$

Using the pitch angle and roll angle instead of deflection to calculate the vertical force can make the model sensible to the suspension motion. The biggest advantage of this model is that it doesn't need the lateral or longitudinal accelerations. It could work when the inertial sensor is absent.

Combination of the rigid car model and the pitch-roll model

The rigid car model $M^1_{vertical}$ neglects the dynamics of suspension motion. Meanwhile, the pitch-roll model $M^3_{vertical}$ captures the features of suspension dynamics but it suppose all masses as unsprung. In a real car, neither the sprung mass nor the unsprung mass could be neglected. Only the combination of the two models could provide a more accurate model. Then we propose an new model $M^4_{vertical}$ to compute the tire vertical forces, which is the combination of $M^1_{vertical}$ and $M^3_{vertical}$.

$$\begin{aligned} 0 &= L_1 F_{zf} - L_2 F_{zr} + \xi M_{y,sus} + (1-\xi) mha_x \\ 0 &= F_{zf} + F_{zr} - ma_z \\ 0 &= \tfrac{e_1}{2} \cdot T_{Fz,f} + \tfrac{e_2}{2} \cdot T_{Fz,r} + \xi M_{x,sus} + (1-\xi) mha_y \\ 0 &= \frac{e_1 \cdot T_{lat,f}}{e_2 \cdot T_{lat,r}} - \frac{F_{zf}}{F_{zr}} \end{aligned} \tag{2.69}$$

where ξ is the interpolation coefficient, it is decided by the percentage of sprung mass in the total vehicle mass:

$$\xi = \frac{m_{sprung}}{m} \tag{2.70}$$

Having presented our contribution to the vertical dynamics, we consider in the next section the lateral vehicle dynamics.

2.4.2 Dynamics Models For Vehicle Lateral Motion

Vehicle lateral motion control is quite important for the vehicle security. A failure in the lateral motion control will cause the lane departure, which is the number one cause of fatal accidents in the United States, and account for more than 39% of crash-related

fatalities [NHTSA, 2013]. Many advanced driver assistance systems (ADAS) have been developed to automatically keep the vehicle in its lane and follow the lane as it curves around. In the researches, the development of lane keeping systems focus on the improvement of lane mark localization and vehicle localization. In [Guldner et al., 1996], the authors demonstrated a lane keeping system based on the use of cylindrical magnets embedded in the center of the highway lane. In the work of research groups at Berkeley [Taylor et al., 1999], vision cameras were employed to realize the lateral position measurement.

The common point of all these technology is to measure the lateral position of vehicle and then control the steering to keep vehicle in lane. This strategy of control works when the steering can actually control the lateral motion of vehicle. Unfortunately, in real driving situation, it is quite possible to find that the vehicle is slipping and the steering operation is not able to reach the desired target, as illustrated in Figure 2.21.

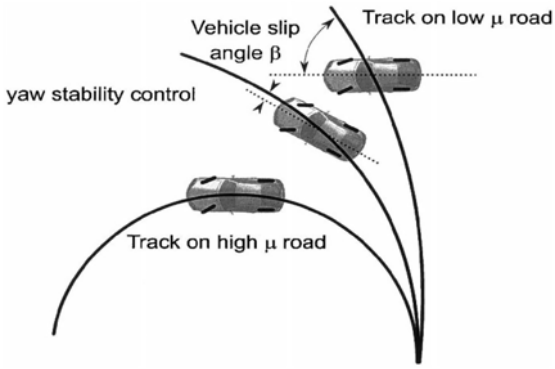

Figure 2.21: Lane departure caused by the failure of lateral dynamics control

To avoid this dangerous situation, we should be aware of the lateral dynamics states and evaluate the safety of steering operation. The kinematic relationship between each tire is introduced in the section of steering geometry. Then the lateral forces at each tire during the steering operation are analyzed with the widely accepted vehicle models: bicycle model and the double track model. After presenting these classical models, we will explain our contribution in the modeling of vehicle lateral forces.

2.4.2.1 Steering Geometry

In this subsection, we will study the kinematic model of steering behavior, which is used for computing the velocity vector of each wheel during steering. In the previous section, we have emphasized the suspension's flexibility. However, in the study of steering kinematics, the vehicle is regarded as rigid in the longitudinal and lateral directions. It is mainly for two reasons.

1. The suspension system only enables the vertical motion of vehicle body.
2. Even if the tire or suspension is deflected, the deformation is negligible compared with tire's global displacement.

Let us consider a front-wheel-steering vehicle that is rotating about a ground point *O*, as shown in Figure 2.22. The four wheels of the vehicle are marked as A, B, C, D in the figure. The steering system is designed to control the wheel direction to facilitate the turning operation. One important factor of designing a steering system is to avoid excessive or unnecessary tire slip. The undesired sideslip of tire could generate huge lateral forces which would not facilitate but resist the turning behavior. Furthermore, large tire side slip will cause damage to the tire and reduce the tire life. Therefore, in a perfect steering system, the velocities at each wheel should be parallel to its wheel direction so that the tire side slip approximates to zero.

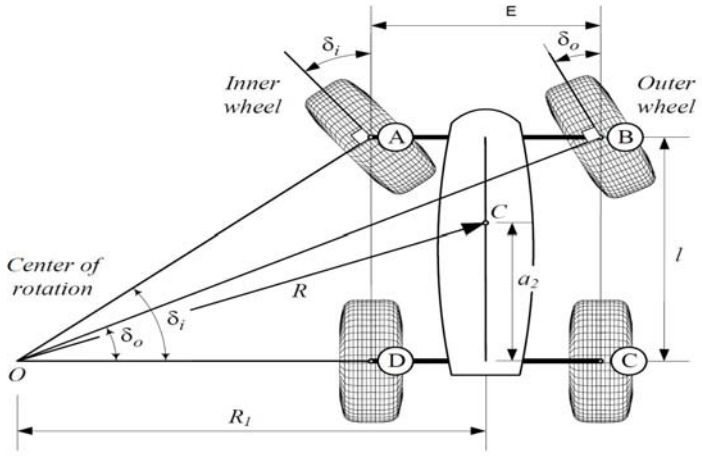

Figure 2.22: Ackerman geometry [Reza, 2007]

For an ordinary car, the steering geometry can be approximated by the Ackerman geometry and is expressed by

$$\tan \delta_i = \frac{L}{R - E/2} \tag{2.71}$$

$$\tan \delta_o = \frac{L}{R + E/2} \tag{2.72}$$

where δ_i is the steer angle of the inner wheel, and δ_o is the steer angle of the outer wheel. The inner and outer wheels are defined based on the turning center *O*. *L* is the distance between front axle and rear axle, called as the wheelbase, *E* is the track width, *R* is the rotation radius.

Then the relation between δ_i and δ_o is expressed by

$$cot\delta_o - cot\delta_i = \frac{E}{L} \tag{2.73}$$

The E/L is the ratio between vehicle width and length. Figure 2.23 illustrates the Ackerman geometry for different values of E/L. The inner and outer steer angles get closer to each other by decreasing E/L.

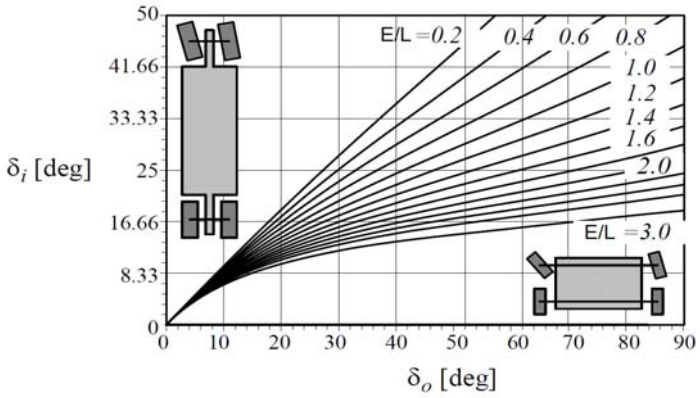

Figure 2.23: Effect of E/L on the Ackerman condition for front-wheel-steering geometry

The rotation radius R could be obtained by the following equation:

$$R = \sqrt{L_2^2 + L^2 cot^2\delta} \tag{2.74}$$

where δ is the cot-average of the inner and outer steer angles.

$$cot\delta = \frac{cot\delta_o + cot\delta_i}{2} \tag{2.75}$$

A device that provides steering according to the Ackerman condition (2.143) is called Ackerman steering or Ackerman mechanism. There is no four-bar linkage steering mechanism that can provide the Ackerman condition perfectly. However, we may design a multi-bar linkages to work close to the condition and be exact at a few angles [Reza, 2007]. It is noted that the Ackerman geometry can represent the real steering kinematic only when the vehicle is moving very slowly. Normally, during the real steering operation, the rotation center O is not on the line $\overline{CD}$ and the side slip angle of rear wheel is not negligible, as illustrated in Figure 2.24.

Suppose the longitudinal velocity is v_x and the side slip angle at center of gravity is β. Then the lateral velocity at the gravity center is obtained by

$$v_y = v_x\beta \tag{2.76}$$

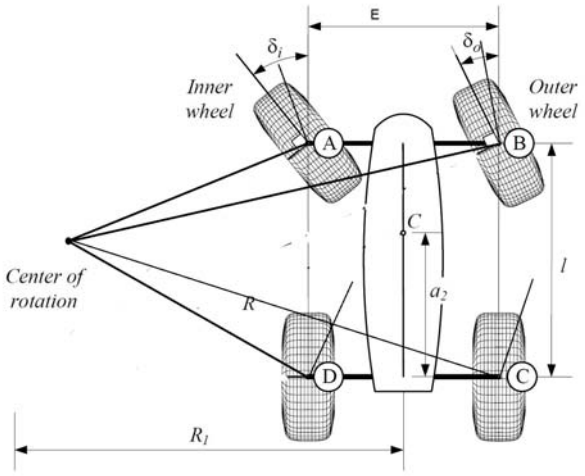

Figure 2.24: The position of rotation center in real driving condition

According to the kinematic relationship between the wheel speeds and the speed at CoG, the sideslip angle at each wheel can be obtained by:

$$\begin{aligned}
\alpha_{11} &= -\delta_{11} + \arctan\left(\frac{v_y + L_1\dot{\psi}}{v_x - \frac{E_1}{2}\dot{\psi}}\right) \\
\alpha_{12} &= -\delta_{12} + \arctan\left(\frac{v_y + L_1\dot{\psi}}{v_x + \frac{E_1}{2}\dot{\psi}}\right) \\
\alpha_{21} &= \arctan\left(\frac{v_y - L_2\dot{\psi}}{v_x - \frac{E_1}{2}\dot{\psi}}\right) \\
\alpha_{22} &= \arctan\left(\frac{v_y - L_2\dot{\psi}}{v_x + \frac{E_1}{2}\dot{\psi}}\right)
\end{aligned} \tag{2.77}$$

2.4.2.2 Bicycle Model

The bicycle model is a simplified expression of basic vehicle lateral dynamics, as shown in Figure 2.25.

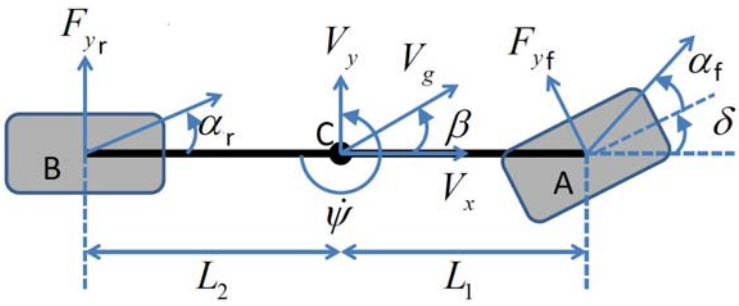

Figure 2.25: Bicycle model

In the bicycle model, the left and right front wheels are represented by one single wheel at point A. Similarly the rear wheels are represented by one single rear wheel at point B. The gravity center of the vehicle is at point C. For the front-wheel-steering vehicle, the steering angle of the front wheels is represented by δ, the steering angle of rear wheels is considered as zero. The tire slip angle of front wheels and rear wheels are represented as α_f and α_r. With these simplification, the vehicle dynamics can be represented by the following functions

$$\begin{aligned} \dot{v}_x &= \frac{1}{m}(F_{xf}\cos(\delta) - F_{yf}\sin(\delta) + F_{xr}) \\ \dot{v}_y &= \frac{1}{m}(F_{xf}\sin(\delta) + F_{yf}\cos(\delta) + F_{yr}) - \dot{\psi}v_x \\ \ddot{\iota} &= \frac{1}{I_z}[L_1(F_{yf}\cos(\delta) + F_{xf}\sin(\delta)) - L_2F_{yr}] \end{aligned} \tag{2.78}$$

where F_{xf} and F_{yf} are the resultant longitudinal and lateral forces at point A. F_{xr} and F_{yr} are the resultant longitudinal and lateral forces at point B.

The bicycle model can be found in many literature, some detailed derivations are given in [Rajamani, 2012]. It is noted that in the literature, the road inclination (bank or slope) is neglected.

In the above formulas, the vehicle lateral motion is represented by the lateral velocity, v_y. However, in the field of vehicle control, researchers prefer to use the sideslip angle β to describe the vehicle lateral motion. In order to directly appear the side slip angle β in the formula, the authors in the literature have proposed another equivalent formula of bicycle dynamics model.

$$\begin{aligned} \dot{V}_g &= \frac{1}{m}(F_{xf}\cos(\delta-\beta) + F_{xr}\cos(\beta) - F_{yf}\sin(\delta-\beta) + F_{yr}\sin(\beta)) \\ \dot{\beta} &= \frac{1}{mV_g}(F_{xf}\sin(\delta-\beta) - F_{xr}\sin(\beta) + F_{yf}\cos(\delta-\beta) + F_{yr}\cos(\beta)) - \dot{\psi} \\ \ddot{\iota} &= \frac{1}{I_z}[L_1(F_{yf}\cos(\delta) + F_{xf}\sin(\delta)) - L_2F_{yr}] \end{aligned} \tag{2.79}$$

where V_g is the linear speed of vehicle, $V_g = \sqrt{v_x^2 + v_y^2}$.

The bicycle model can be also employed to calculate the sideslip angle at point A and point B, as expressed by the following equations:

$$\alpha_f = -\delta_f + \beta + \frac{L_1\dot{\psi}}{v_x} \tag{2.80}$$

$$\alpha_r = \beta - \frac{L_2\dot{\psi}}{v_x} \tag{2.81}$$

Obviously, the difference of left and right tire dynamics is not considered in the above equations. Thus, the bicycle model can only be employed to calculate the lateral force per axle, while it is not able to distinguish the lateral force of each wheel. A more complete vehicle model contains four wheels will be introduced in the following section,

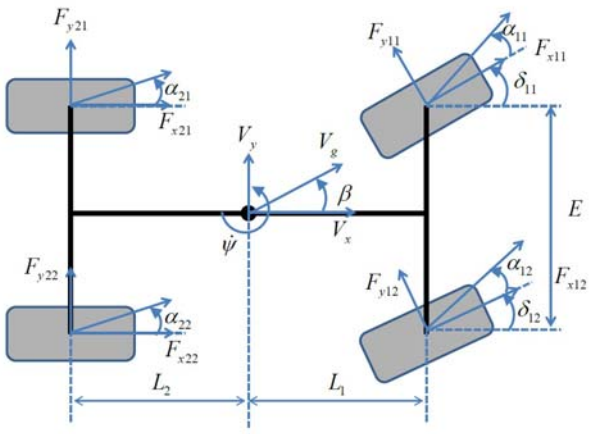

Figure 2.26: Double track model

which can give more precise description of vehicle dynamics.

2.4.2.3 Double Track Model

The four wheels vehicle model represented in Figure 2.26 is discussed in[Reza, 2007] [Doumiati, 2009]. It is able to describe the vehicle planar dynamics with more details compared with the bicycle model, thus it can be found in plenty of applications aimed for vehicle state estimation and control strategy.

The double track model is based on the planar rigid dynamics, as introduced in section 2.3.2. The full detailed function of the double track model is shown in equation 2.82.

$$\begin{aligned}
\dot{V}_g &= \tfrac{1}{m}[F_{x11}\cos(\delta_{11}-\beta)+F_{x12}\cos(\delta_{12}-\beta)+F_{x21}\cos(\beta)+F_{x22}\cos(\beta) \\
&\quad -F_{y11}\sin(\delta_{11}-\beta)-F_{y12}\sin(\delta_{12}-\beta)+F_{y21}\sin(\beta)+F_{y22}\sin(\beta)] \\
\dot{\beta} &= -\dot{\psi}+\tfrac{1}{mV_g}[F_{y11}\cos(\delta_{11}-\beta)+F_{y12}\cos(\delta_{12}-\beta)+F_{y21}\cos(\beta)+F_{y22}\cos(\beta) \\
&\quad +F_{x11}\sin(\delta_{11}-\beta)+F_{x12}\sin(\delta_{12}-\beta)+F_{x21}\sin(\beta)+F_{x22}\sin(\beta)] \\
\ddot{\iota} &= \tfrac{1}{I_z}\{L_1[F_{y11}\cos(\delta_{11})+F_{y12}\cos(\delta_{12})+F_{x11}\sin(\delta_{11})+F_{x12}\sin(\delta_{12})] \\
&\quad -L_2[-F_{y21}+F_{y22}] \\
&\quad +\tfrac{E_1}{2}[F_{y11}\sin(\delta_{11})-F_{y12}\sin(\delta_{12})-F_{x11}\cos(\delta_{11})+F_{x12}\cos(\delta_{12})] \\
&\quad +\tfrac{E_2}{2}[-F_{x21}+F_{x22}]
\end{aligned} \tag{2.82}$$

where δ_{11}, δ_{12} are the steering angles at front left wheel and front right wheel respectively.

When $\delta_{11} = \delta_{12}$, the double track model and bicycle model are equivalent. The advantage of double track model over the bicycle model is the ability to distinguish the different steering angles of outer wheel and inner wheel during turning. Furthermore, in the double track model, the description of tire slip angle is more accurate than in the

bicycle model. The tire slip angle of each wheel is obtained by the equation 2.77. Then the lateral force of each tire can be obtained with the tire models.

$$\begin{aligned} F_{y11} &= f_{Tire}(\alpha_{11},\ F_{z11}) \\ F_{y12} &= f_{Tire}(\alpha_{12},\ F_{z12}) \\ F_{y21} &= f_{Tire}(\alpha_{21},\ F_{z21}) \\ F_{y22} &= f_{Tire}(\alpha_{22},\ F_{z22}) \end{aligned} \tag{2.83}$$

where $f_{Tire}(\,)$ is the tire model, it could be the linear tire model, Dugoff's model or other non-linear tire model, according to the required accuracy.

2.4.2.4 The contribution proposed for Lateral Dynamics Models

There are two principle limitations in the existent vehicle models for calculating the tire lateral forces.

- Firstly, the road inclination is not considered. The banked road or sloped road will make the gravity force act on the lateral direction, which may cause model errors.
- Secondly, there is no efficient method to calculate the lateral forces at each tire. The commonly used tire model requires an accurate measurement of tire slip angle which is difficult to realize with low-cost sensors.

Solution to the first limitation

In order to eliminate the first limitation, we propose to consider the 3D dynamics of vehicle, as we introduced in the section 2.3.3. The components of gravity force in longitudinal and lateral direction are taken into account in the modified model, expressed by

$$\begin{aligned} \dot{v}_x + \dot{\psi} v_y &= \tfrac{1}{m}(F_{xf}\cos(\delta) - F_{yf}\sin(\delta) + F_{xr} - mg\sin\theta_r) \\ \dot{v}_y + \dot{\psi} v_x &= \tfrac{1}{m}(F_{xf}\sin(\delta) + F_{yf}\cos(\delta) + F_{yr} - mg\sin\phi_r) \\ I_z\ddot{\psi} + (I_y - I_x)\dot{\theta}\dot{\phi} &= [L_1(F_{yf}\cos(\delta) + F_{xf}\sin(\delta)) - L_2F_{yr}] \end{aligned} \tag{2.84}$$

where $\dot{\theta}$, $\dot{\phi}$ are the measured roll rate and pitch rate, they are caused by the suspension motion and the road irregularity.

Solution to the second limitation

In order to eliminate the second limitation, we proposed an original model to calculate tire force. The common method to calculate tire force is to employ the tire models. For instant, the linear tire model, $F_{wy} = C_\alpha\alpha$, normally the cornering stiffness $C_\alpha \in [10000,\ 100000]$. The tire model has been studied by many researcher for many years, as introduced in section 2.1. The common point of these tire models is to study the

performance of a single tire under different condition. The tire is individually analyzed in the test, as shown in Figure 2.27.

Figure 2.27: Tire test equipment: providing different speeds and different vertical loads [Otso et al., 2016]

In this thesis, we propose a new strategy to calculate the tire forces, which is to calculate the value of transfer of lateral force ($F_{y11} - F_{y12}$, $F_{y21} - F_{y22}$). The motivation of proposing this new model is to consider the interaction between the wheels. When the vehicle is moving, the force of each tire is not only decided by its own working condition, but also influenced by the interaction between the four wheels. The lateral force per axle (F_{yf}, F_{yr}) are available by using the bicycle model. The force at each wheel could be obtained if we have information about the difference between the left and right wheel ($F_{y11} - F_{y12}$, $F_{y21} - F_{y22}$). This difference in the lateral force is called the "Transfer of lateral force" in this thesis. The transfer of lateral force at front axle and at rear axle are noted as $T_{Fy,f}$ and $T_{Fy,r}$ respectively, and expressed by

$$\begin{aligned} T_{Fy,f} &= F_{y11} - F_{y12} \\ T_{Fy,r} &= F_{y21} - F_{y22} \end{aligned} \tag{2.85}$$

The model we proposed for the calculation of transfer of lateral force is represented by the following equations:

$$\begin{aligned} T_{Fy,f} &= \frac{T_{Fz,f}}{F_{zf}} F_{yf} + a_1 F_{zf}\delta + a_2 \ddot{\psi} v_x \\ T_{Fy,r} &= \frac{T_{Fz,r}}{F_{zr}} F_{yr} + a_3 \ddot{\psi} v_x \end{aligned} \tag{2.86}$$

where $a_{1,2,3}$ are constant parameters, influenced by the road friction.

The advantage of this model is to calculate the tire forces without tire slip angle, which could greatly reduce the difficulty of estimating tire forces. In the following paragraphs, we will provide the details of the development of the model.

Proof:

The proposed model is a further development based on the Brush model. The value of $T_{Fy,f}$ and $T_{Fy,r}$ can be obtained by employing the Brush model.

$$\begin{aligned} T_{Fy,f} &= f_{Tire}(\alpha_{11}, F_{z11}) - f_{Tire}(\alpha_{12}, F_{z12}) \\ T_{Fy,r} &= f_{Tire}(\alpha_{21}, F_{z21}) - f_{Tire}(\alpha_{22}, F_{z22}) \end{aligned} \tag{2.87}$$

According to the experimentation data of many researchers [Pacejka, 2006] [Lechner, 2002], the vertical load have great impact on the generation of tire forces. Therefore, the tire model $f_{Tire}(\cdot)$ we used here is the Brush model, which has considered the impact of load transfer. To simplify the calculation, we have generalized the representation of the non-linear tire model as

$$f_{Tire}(\alpha, F_{wz}) = b_1 F_{wz}(b_2\alpha + b_3\alpha^2 + b_4\alpha^3) \tag{2.88}$$

where α is the slip angle of the corresponding wheel, F_{wz} is the vertical load at this wheel, $b_{1...4}$ are the model coefficients to represent the non-linearity of the model.

Then this generalized tire model is employed to compute the transfer of lateral force, $T_{Fy,f}$ and $T_{Fy,r}$.

$$T_{Fy,r} = b_1 F_{z12}(b_2\alpha_{21} + b_3\alpha^2 \quad {}_{4}{}_{21}) - b_1 F_{z22}(b_2\alpha_{22} + b_3\alpha^2{}_{22} + b_4\alpha^3_{22}) \tag{2.89}$$

To further simplify the calculation, we can have the following assumption: the vehicle is at a high speed so that

$$\begin{aligned} \alpha_{21} &= \alpha_{22} = \alpha_r \\ \alpha_{11} - \alpha_{12} &= \delta_{12} - \delta_{11} \end{aligned} \tag{2.90}$$

Then the transfer of lateral force at rear axle $T_{Fy,r}$ is computed by the following equations:

$$T_{Fy,r} = \frac{T_{Fz,r}}{F_{zr}} F_{yr} \tag{2.91}$$

Similarly, the transfer of lateral force at front axle $T_{Fy,f}$ is computed by the following equations:

$$\begin{aligned} T_{Fy,f} &= b_1 F_{z11}(b_2\alpha_{11} + b_3\alpha^2 \quad {}_{4}{}_{11}) - b_1 F_{z12}(b_2\alpha_{12} + b_3\alpha^2_{12} + b_4\alpha^3_{12}) \\ &\text{c:::} \quad \frac{T_{Fz,f}}{F_{zf}} F_{yf} + a_1 F_{zf}\delta \end{aligned} \tag{2.92}$$

where $a_1 F_{zf}\delta$ represents the force difference caused by the steering angle, $\frac{T_{Fz,f}}{F_{zf}} F_{yf}$ represents the force difference caused by the load transfer.

With the proposed tire force model, the side slip angle is no longer needed for computing tire forces. Instead, the tire forces are computed with vertical load transfer, velocity and yaw rate, which can be easily obtained with low cost sensors. Another advantage of the proposed model is to take into account the first order dynamics of the tire behavior. The additional items $a_2\ddot{\psi}v_x$, $a_3\ddot{\psi}v_x$ in equation 2.86 represent the lateral tire forces caused by quick maneuvers.

2.4.3 Dynamics Models For Vehicle Longitudinal Motion

Longitudinal dynamics has a direct impact on vehicle's driving quality, thus it has been studied by many researchers and automotive manufacturers. The vehicle's longitudinal dynamics states can determine the maximum attainable accelerating force and braking force, which are important for developing advanced longitudinal control system. In the modern cars, many intelligent system have been installed to improve the vehicle security, such as the anti-lock braking system, radar based collision avoidance system, adaptive cruise control and the individual wheel torque control system. The two major elements of longitudinal dynamics are the driveline dynamics and the longitudinal force system. The driveline dynamics studies the engine and transmission performance. The torque received by the drive wheel is determined by the torque generated by the engine and the efficiency of transmission system. In this thesis, the driveline dynamics is not discussed. For more details, the readers can refer to [Rajamani, 2012]. Our work focus on the development of mathematical model for the longitudinal tire dynamics.

In the literature, the tire longitudinal forces can be obtained through following approaches.

1. the planar rigid dynamics, which is already introduced in the bicycle model and double track model. The longitudinal dynamics of the vehicle is expressed by

$$ma_x = F_{xf}\cos(\delta) - F_{yf}\sin(\delta) + F_{xr} - mg\sin\theta_r \tag{2.93}$$

   Note that the tire rolling resistance force and air dragging force are included into the tire longitudinal forces. We can also employ the rigid dynamics to analyze the forces at each wheel, expressed by

$$m_{wij}a_{xij} = F_{wxij} + F_{x,axle} - m_{wij}g\sin\theta_r \tag{2.94}$$

   where m_{wij} is the mass of wheel (ij), $F_{x,axle}$ is the interaction force between the wheel and the axle, which is unavailable in most vehicles.

2. the tire models. The longitudinal force is a function of tire longitudinal slip, as explained in the section 2.2. Typically, it can be computed with the linear tire model:

$$F_{wx} = C_s s \tag{2.95}$$

   where C_s is the longitudinal slip stiffness.

3. the wheel rotational dynamics. The details will be introduced in the following section.

In this thesis, we propose a new model to calculate the longitudinal tire forces, which will be introduced in section 2.4.3.2.

2.4.3.1 Wheel rotational dynamics

For the driving wheels, the dynamic equation for the wheel rotational dynamics is expressed as

$$T_{ij} - T_b - R_{eff} F_{wxij} - M_{resis} = I_{wij} \dot{\omega}_{ij} \tag{2.96}$$

where T_{ij} is the transmitted wheel torque, T_b is the braking torque, R_{eff} is the effective wheel radius, I_{wij} is the moment of inertia of wheel ij, $\dot{\omega}_{ij}$ is the angular acceleration. M_{resis} is the wheel rolling resistant moment.

For an ordinary passenger car, the tire force can be obtained by

$$F_{wxij} \approx \frac{T_{ij} - T_b - M_{resis} - I_{wij} \dot{\omega}_{ij}}{R_{eff}} \tag{2.97}$$

For a front drive vehicle, the front wheel drive torque can be obtained by the torque sensor, while the rear wheel drive torque is equal to zero. The braking torque is a function of the brake pressure, which is available in most modern vehicles. Then the accuracy of using equation 2.97 relies on the estimation of wheel resistance moment. The tire road contact is a complex process which produce both forces and moments. When the vehicle is moving in a straight line in a quasi-static way, the resistant moment can be regarded as a constant. However, when the vehicle is turning, the resistant moment becomes significant and should be taken into account. In the following section, we will propose a new model to calculate the tire longitudinal forces.

.

2.4.3.2 The contribution proposed for longitudinal tire forces model

The slip ratio based tire models have clearly explained the physical relationship between tire forces and tire deformation. However, in the industrial application, it is very difficult to employ this sort of model, due to the large noise in the measurement of slip ratio. In order to overcome this problem, we would like to propose a new tire model for computing the longitudinal force without using the slip ratio.

Similar to the modeling of lateral dynamics, here we would like to introduce the concept of transfer of longitudinal force T_{Fx}. The transfer of longitudinal force at front axle and at rear axle are represented by $T_{Fx,f}$ and $T_{Fx,r}$ respectively, expressed by

$$\begin{aligned} T_{Fx,f} &= F_{x11} - F_{x12} \\ T_{Fx,r} &= F_{x21} - F_{x22} \end{aligned} \tag{2.98}$$

The model we proposed for the calculation of transfer of longitudinal force is repre-

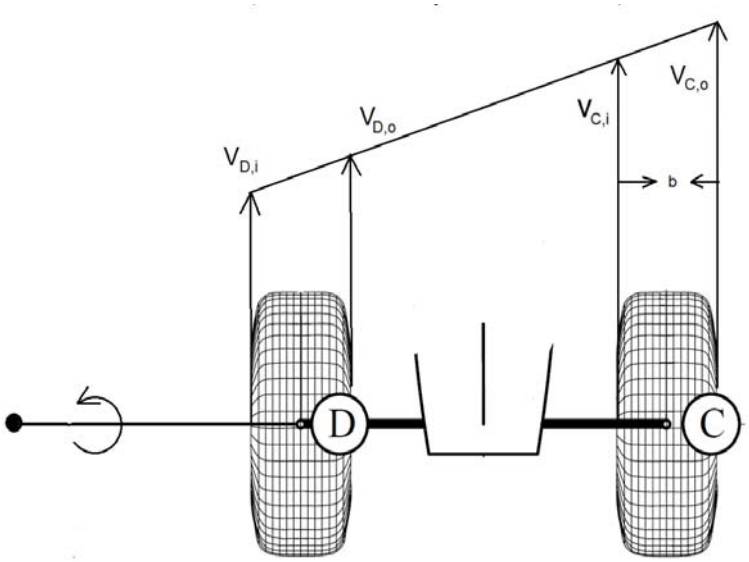

Figure 2.28: Double track model

sented by the following equations:

$$\begin{aligned} T_{Fx,f} &= a_4 \frac{T_{Fz,f}}{F_{zf}} F_{xf} + a_5 F_{zf} \delta \\ T_{Fx,r} &= a_6 T_{Fz,f} \end{aligned} \tag{2.99}$$

For the rear wheels, the longitudinal force is normally simplified as zero. However, when the vehicle is turning, this simplification is not valid, as the tire's longitudinal deformation is significant. It is due to the self-locking phenomenon during turning: the outer side of the wheel generates more deformation than the inner side of the wheel, as illustrated in the Figure 2.28. For an axle, the outer wheel moves faster than the inner wheel. Similarly, for a wheel, the outer tread moves faster than the inner tread. Thus when the vehicle is turning, the outer tread will generates an additional deformation besides the deformation generated when it is driving straight ahead. The speed difference between the inner side and outer side of wheel is equal to $\omega_z b$. According to the definition of slip ratio, the slip ratio at outer side of wheel is computed with

$$s = \frac{\omega_w R_{ef f} - v_x + \omega_z b}{v_x} = s_a + s_r \tag{2.100}$$

where b is the width of contact patch, ω_z is the vehicle's yaw rate, v_x is the wheel speed.

Then the longitudinal slip ratio of the tire can be divided into two elements: the average longitudinal slip s_a, and the additional longitudinal slip caused by vehicle's rotation motion s_r.

$$s_r = \frac{\omega_z b}{v_x} \tag{2.101}$$

According to the tire models, during the turning, the transfer of longitudinal force can be obtained by

$$\begin{aligned} T_{Fy,f} &= f_{Tire}(s_{11}, F_{wz11}) - f_{Tire}(s_{12}, F_{wz12}) \\ T_{Fy,r} &= f_{Tire}(s_{21}, F_{wz21}) - f_{Tire}(s_{22}, F_{wz22}) \end{aligned} \tag{2.102}$$

Similar to the lateral force model, we also use a generalized mathematical model to represent the non-linear model for longitudinal tire forces.

$$f_{Tire}(s, F_{wz}) = b_1 F_{wz}(b_2 s + b_3 s^2 + b_4 s^3) \tag{2.103}$$

Combining equation 2.102 and 2.103 generates the proposed model.

2.5 Conclusion

This chapter provides a brief introduction to the state of art in the field of vehicle dynamics modeling. Furthermore, this chapter has also proposed some original contributions to the modeling of vehicle dynamics for the purpose of efficiency and accuracy. The study of vehicle dynamics generally consists of two major subjects: the dynamics of road-tire contact and the dynamics of vehicle motion. The former subject covers the dynamic modeling of the road/tire system, it explains how the tire forces are generated. The second subject places an emphasis on the relationship between the tire forces and the vehicle's kinematic motion. Therefore, in the organization of this chapter, we firstly introduced the tire models and then the rigid body dynamics.

In the section of tire models, the linear tire model, the Brush model, the Dugoff's model and the quasi-static Magic tire formula are presented and compared. The linear tire model captures the principle relation between tire slip and tire forces, but it ignores the impact of the tire vertical load. The Magic Formula is the most widely used semi-empirical model. It takes into account the tire load and the combined slip and conforms very well to the experimental data. However, it requires a large number of tire-specific parameters that are usually difficult to be configured. The Brush model and Dugoff tire model are developed based on simplified physical tire model. They are not as accurate as the magic formula, but they have successfully represented the non-linear relationship between the tire slip and tire forces, moreover, they have considered the impact of tire vertical load on the generation of tire forces. The Brush model is more intuitive, while the Dugoff's tire model is more suitable for calculation. The transient behavior of the tire is presented according to a relaxation tire model.

In the section of rigid body dynamics, planar rigid dynamics is firstly presented. In

the literature, the vehicle motion is usually simplified as a planar motion, as it could captures the major features of vehicle motion. However, the planar rigid dynamics has ignored the irregularity of the road. When the road is banked or sloped, the vehicle's lateral motion and longitudinal motion will be influenced by the gravity force. In order to consider the road irregularity, we have developed a 3D vehicle dynamics model which could describe the 3D motion.

The tire dynamics models and rigid body dynamics models are the physical explanation of vehicle's dynamics behaviors. Comprehension of the two dynamics models is fundamental for further development of vehicle model. However, the two models cannot represent all details of the vehicle dynamics. For the purpose of simplicity, in the industrial application, the description of vehicle dynamics are divided into three aspects: longitudinal dynamics, lateral dynamics and vertical dynamics. In fact, the dynamics models in the three directions can be regarded as an equivalent transformation of the tire models and rigid body dynamics models. For the study of vertical dynamics, the vehicle can be simplified as a rigid car or two rigid body connected by soft suspension. For the study of lateral dynamics, we usually employ the bicycle model and double track model.

In the classical vehicle dynamics models, there are two limitations which could greatly reduce the accuracy of calculation.

1. the road irregularity is not considered, while in real condition it is quite possible to drive on the banked road or sloped road
2. the tire forces are calculated with tire slip (slip ratio or slip angle), while the tire slip is a very small quantity and very difficult to be accurately measured.

To overcome these two limitations, we proposed two original modifications.

1. applying the 3D rigid dynamics in the development of vertical dynamics model, longitudinal dynamics model and lateral dynamics model.
2. introducing the concepts of "transfer of lateral force" T_{Fy} and "transfer of longitudinal force" T_{Fx}. We develop the mathematical model of T_{Fy}, T_{Fx} based on the Brush model. However, in the final formula of calculation, the slip ratio s or slip angle α is eliminated. Instead, the tire forces are calculated with accelerations, velocities, which are easy to be measured.

In order to clearly present our contributions, in each aspect of vehicle dynamics, the classical model is firstly presented and followed by the modified model. In this way, we can make a comparison between the classical model and the modified model. The entire chapter lays a solid theoretical foundation for the construction of the observers of vehicle dynamics states. The experimental validation of the dynamics models proposed in this chapter will be presented in the chapter 4.

3 Observer Theory

3.1 Introduction

Estimation is to extract useful information of a unknown or unmeasured parameter θ from a collection of observation data y. An accurate estimation is quite challenging due to the model imperfection, sensor inaccuracies, signal distortion, additive noises, unaccounted source variability and multiple interfering signals. Modern estimation theory, which help find the best estimation, can be found at the heart of many electronic signal processing systems designed to extract information. The target parameter can be a constant value or a signal of a dynamic system. Specifically, the estimation of a time-varying signal of a dynamics system is referred as the observer. The behavior of a dynamics system could be characterized and described by a set of states, the more details you want to describe about the system, the more states you have to observe. It is often unrealistic to measure all the states of interest, due to the technical and economic reasons. In fact, even the measurement of a state is available, the real value of the dynamic state is still unknown. That's because the perfect measurement is unrealistic. All the measurement should be considered as the resultant of real value and the noises. The real values of the states are called the internal states of the system, and the available measurement is referred as the external information. The objective of an observer is to extract internal information from external measurements. Another feature of observer is that it usually deal with real time estimation, therefore the sequential estimation algorithm is required. The need of observer can be motivated by various purposes: to monitor the process, to evaluate the performance or to control the system.

The observer technology is widely employed in the development of the advanced driver assistant system. In order to obtain the feedback signals for the control system, the detailed information about the vehicle dynamics states should be provided. Some of the states (speed, yaw rate, accelerations) are directly measured, as the related sensors are sufficiently accurate and successfully commercialized. However, some other states are still immeasurable in ordinary passenger cars. Therefore, the construction of observers of vehicle dynamics states is of great interest to both the researchers and the automobile manufacturer. The standard approach for development of a vehicle dynamics state observer consists of a two-step procedure: firstly, a vehicle dynamics model is identified and successively an observer is designed using observation techniques. The previous

chapter provided suitable vehicle/tire models, in this chapter observation techniques will be discussed.

In general, a dynamic system can be divided into two categories: linear system and nonlinear system. For the linear system, the estimation tools of states have been well developed by Luenberger and Kalman. The Kalman filter is widely used in the industry for the estimation of linear system. However for the nonlinear system, the classic Kalman filter is non longer valid because of the difficulties involved in dealing with nonlinear model. In order to accurate estimation results for nonlinear systems, the extended Kalman filter (EKF), unscented Kalman filter (UKF), particle filter (PF), sliding-mode filter etc. are developed in the literature. The vehicle dynamics system consists of many sub-systems, including both linear and nonlinear systems. To observe all these vehicle dynamics states, both linear observer and non linear observer are of great interest to our research. This chapter is organized as follows: at the beginning, we introduce the basic estimation methods in the domain of parameter estimation, including the classical estimation method and the Bayesian estimation method. Typically, the minimum variance unbiased estimator (MVU) and the minimum mean square estimator (MMSE) are reviewed and compared. Then, the Kalman filter and state-space representation is presented to provide an effective solution for the estimate of linear system. To extend to a larger field, the nonlinear system, the theory of extended Kalman filter is expounded with the complete operation steps. Moreover, considering the highly nonlinearity system and non-Gaussian noises perturbed within the system, the Unscented Kalman filter and the particle filter are also presented. Finally, it is presented the conclusion of the observer theory description.

3.2 Basic Estimation Methods

Generally, the estimation problem is to find a function of the available data (a N-point data set $\boldsymbol{y}$), which could provide an estimate of the real value of the parameter θ.

$$\hat{\theta} = g(\boldsymbol{y}) \tag{3.1}$$

where $\hat{\theta}$ is the estimated value, $g(\boldsymbol{y})$ is known as the estimator function.

It is very easy to find a candidate $g(\boldsymbol{y})$, but obviously, not all of the candidates can provide the best estimation. A natural optimal criterion is to minimize the mean square error:

$$\begin{aligned} mse(\hat{\theta}) &= E[(\theta - \hat{\theta})^2] \\ &= var(\hat{\theta}) + (E(\hat{\theta}) - \theta)^2 \end{aligned} \tag{3.2}$$

A candidate of the $g(\boldsymbol{y})$ can be developed by satisfying $E(\hat{\theta}) - \theta = 0$ and minimizing

the $var(\hat{\theta})$. This generates the Minimum Variance Unbiased Estimator.

3.2.1 Minimum Variance Unbiased (MVU) Estimator

As indicated by its name, the MVU estimator has to satisfy two criterion: to be unbiased and to have the minimum variance, which could be represented by the following equations:

$$E(\hat{\theta}) = \theta$$
$$\hat{\theta}_{MVU} = \arg\min_{\theta}\{E((E(\hat{\theta}) - \hat{\theta})^2)\} \tag{3.3}$$

Let us assume that the probabilistic density function (PDF) of the data is known and expressed as $p(\boldsymbol{y}; \theta)$. Then according to the Cramer-Rao Lower Bound (CLRB) theorem [Cramér, 1947], the MVU estimator can be found by the following equation:

$$\frac{\partial \ln p(\boldsymbol{y}; \theta)}{\partial \theta} = \boldsymbol{I}(\theta)(g(\boldsymbol{y}) - \theta) \tag{3.4}$$

If the PDF of the data can be transformed into the above format, the MVU estimator is obtained by

$$\hat{\theta}_{MVU} = g(\boldsymbol{y}) \tag{3.5}$$

and the minimum variance is $\boldsymbol{I}^{-1}(\theta)$.

Now consider the situation that the parameter $\boldsymbol{\theta}$ is not directly measured but observed with a linear observation model, where the observation data follows a standard normal distribution, expressed as

$$\boldsymbol{y} = \boldsymbol{H}\boldsymbol{\theta} + \boldsymbol{\omega} \tag{3.6}$$

where $\boldsymbol{y}$ is a $N \times 1$ observation data vector, $\boldsymbol{H}$ is a $m \times N$ observation matrix, $\boldsymbol{\theta}$ is a $m \times 1$ vector of parameters to be estimated, $\boldsymbol{\omega}$ is a $N \times 1$ noise vector with $\boldsymbol{N}(0, \sigma^2\boldsymbol{I})$.

Then the MVU estimator of linear system can be obtained through equation 3.4 and the result is expressed as

$$\hat{\boldsymbol{\theta}}_{MVU} = (\boldsymbol{H}^T\boldsymbol{H})^{-1}\boldsymbol{H}^T\boldsymbol{y} \tag{3.7}$$

and the covariance of the estimation is

$$\boldsymbol{P}_M = \sigma^2(\boldsymbol{H}^T\boldsymbol{H})^{-1} \tag{3.8}$$

To obtain a MVU estimator for more general cases, we assume the variance of different measurement are different. And the covariance of these measurement can be represented by $\boldsymbol{P}_{\boldsymbol{y}}$. Then the general MVU estimator for linear model is

$$\hat{\boldsymbol{\theta}}_{MVU} = (\boldsymbol{H}^T\boldsymbol{P}_{\boldsymbol{y}}{}^{-1}\boldsymbol{H})^{-1}\boldsymbol{H}^T\boldsymbol{P}_{\boldsymbol{y}}{}^{-1}\boldsymbol{y} \tag{3.9}$$

where the estimation covariance is $\boldsymbol{P}_M = (\boldsymbol{H}^T \boldsymbol{P}_{\boldsymbol{y}}{}^{-1} \boldsymbol{H})^{-1}$.

Observability Analysis

Observability is a measure for how well internal states of a system can be inferred by knowledge of its external outputs. The observability and controllability of a system are mathematical duals. The concept of observability was introduced by Kalman for linear dynamic systems [Kalman et al., 1960]. Here we employ the concept of observability to describe whether the measurement $\boldsymbol{y}$ has enough information to calculate the value of parameter θ. The observability of a MVU estimator is determined by the following equation

$$k_O = rang(\boldsymbol{H}) \tag{3.10}$$

If $k_O = m$, the observer is observable.

3.2.2 Minimum Mean Square Estimator (MMSE)

The MVU estimator is based on the classic probabilistic approach, which regards the parameter θ as unknown but deterministic. Thus the PDF of the measurement is a function of the data but parameterized by a constant θ, noted as $p(\boldsymbol{y}; \theta)$. As a contrast to the classical approach, the Bayesian philosophy, treated the θ as a random variable with a known prior PDF, $p(\theta)$. Thus the PDF of the measurement is a joint PDF of both data $\boldsymbol{y}$ and θ, referred as $p(\boldsymbol{y}, \theta)$. The calculation of minimum mean square in Bayesian approach is different with the classic *mse* and is expressed as

$$Bmse(\hat{\theta}) = E[(\theta - \hat{\theta})^2] = \int\int (\theta - \hat{\theta})^2 p(\boldsymbol{y}, \theta) d\boldsymbol{y} d\theta \tag{3.11}$$

The estimator which minimize the $Bmse(\hat{\theta})$ is called the Minimum Mean Square Estimator (MMSE), noted as $\hat{\theta}_B$. The formula of $\hat{\theta}_B$ is derived by differentiating $Bmse(\hat{\theta})$ with respect to $\hat{\theta}$ and setting it to zero. The general form of the MMSE is expressed as

$$\hat{\theta}_B = \int \theta p(\theta|\boldsymbol{y}) d\theta \tag{3.12}$$

where the posterior PDF, $p(\theta|\boldsymbol{y})$ is given by:

$$p(\theta|\boldsymbol{y}) = \frac{p(\boldsymbol{y}, \theta)}{p(\boldsymbol{y})} = \frac{p(\boldsymbol{y}, \theta)}{\int p(\boldsymbol{y}, \theta) d\theta} = \frac{p(\boldsymbol{y}|\theta) p(\theta)}{\int p(\boldsymbol{y}|\theta) p(\theta) d\theta} \tag{3.13}$$

Now consider a Bayesian linear model:

$$\boldsymbol{y} = \boldsymbol{H}\boldsymbol{\theta} + \boldsymbol{\omega} \tag{3.14}$$

where $\boldsymbol{y}$ is a $N \times 1$ observation data vector, $\boldsymbol{H}$ is a $N \times m$ observation matrix, $\boldsymbol{\theta}$ is a

$m \times 1$ vector of parameters to be estimated with prior PDF $\boldsymbol{N}(\boldsymbol{\mu_\theta}, \boldsymbol{P_\theta})$, $\boldsymbol{\omega}$ is a $N \times 1$ noise vector with $\boldsymbol{N}(0, \boldsymbol{P_\omega})$.

The MMSE for the linear system is expressed as

$$\begin{aligned} \hat{\boldsymbol{\theta}}_B &= \boldsymbol{\mu}_\theta + \boldsymbol{P}_\theta \boldsymbol{H}^T (\boldsymbol{H}\boldsymbol{P}_\theta \boldsymbol{H}^T + \boldsymbol{P}_\omega)^{-1} (\boldsymbol{y} - \boldsymbol{H}\boldsymbol{\mu}_\theta) \\ \boldsymbol{P}_{\theta|y} &= \boldsymbol{P}_\theta - \boldsymbol{P}_\theta \boldsymbol{H}^T (\boldsymbol{H}\boldsymbol{P}_\theta \boldsymbol{H}^T)^{-1} \boldsymbol{H}\boldsymbol{P}_\theta^T \end{aligned} \tag{3.15}$$

Observability Analysis

For a MMSE estimator, the final estimation result is also influenced by the prior information of the parameter. The parameter can be updated by the measurement, even though the measurement is not complete, $rang(\boldsymbol{H}) < m$. However, to simplify the analysis, we suppose all the parameters are independent from each other. Then the covariance matrix $\boldsymbol{P}_\theta$ is a diagonal matrix. In this case, the estimator is observable when $rang(\boldsymbol{H}) = m$.

3.2.3 Sequential MMSE

In the previous sections, the observation data is usually a stream of data. The estimation strategy is to wait for N samples to arrive and then form our estimate based on these samples. Theoretically, the more samples we take into account, the more accurate the estimation is. However, the delay in waiting for these samples will be considerable. Furthermore, each time the data arrives we have to repeat the calculation of the former data. It will lead to a growing burden for calculation and buffer. One solution is to use the sequential mode of processing. The estimate at moment $t = n$, $\boldsymbol{\theta}[n]$ is derived from the previous estimate $\boldsymbol{\theta}[n-1]$. The Bayesian linear model can be expressed as

$$\boldsymbol{y}[n] = \boldsymbol{H}[n]\boldsymbol{\theta}[n] + \boldsymbol{\omega}[n] \tag{3.16}$$

The covariance of $\boldsymbol{\theta}[n-1]$ is noted as $\boldsymbol{P}_\theta[n-1]$. The covariance of noise $\boldsymbol{\omega}[n]$ is $\boldsymbol{P}_\omega[n]$. As the $\boldsymbol{\theta}[n-1]$ is close to $\boldsymbol{\theta}[n]$ and we ignore the dynamics behavior of $\boldsymbol{\theta}$, we could assume a prior information about $\boldsymbol{\theta}[n]$, which is

$$\begin{aligned} E(\boldsymbol{\theta}[n]) &= \boldsymbol{\theta}[n-1] \\ var(\boldsymbol{\theta}[n]) &= \boldsymbol{P}_\theta[n-1] \end{aligned} \tag{3.17}$$

Then the MMSE of $\boldsymbol{\theta}[n]$ could be developed by combining equation 3.15 and 3.17:

$$\boldsymbol{\theta}[n] = \boldsymbol{\theta}[n-1] + \boldsymbol{K}[n](\boldsymbol{y}[n] - \boldsymbol{H}[n]\boldsymbol{\theta}[n-1]) \tag{3.18}$$

$$\boldsymbol{K}[n] = \boldsymbol{P}_\theta[n-1]\boldsymbol{H}^T[n](\boldsymbol{H}[n]\boldsymbol{P}_\theta[n-1]\boldsymbol{H}^T[n] + \boldsymbol{P}_\omega[n])^{-1} \tag{3.19}$$

$$\boldsymbol{P}_{\theta}[n] = (\boldsymbol{I} - \boldsymbol{K}[n]\boldsymbol{H}[n])\boldsymbol{P}_{\theta}[n-1] \tag{3.20}$$

Observability
The observability of sequential MMSE is the same with the MMSE. When all the parameters to be estimated are independent and $rang(H)$ equals to the number of the parameters, the estimator is observable.

3.2.4 Estimator for non linear observation model

When the observation model is non-linear, shown as

$$\boldsymbol{y}[n] = \boldsymbol{h}(\boldsymbol{\theta}[n]) + \boldsymbol{\omega}[n] \tag{3.21}$$

it is very difficult to get the mathematical formula of MMSE estimator by minimizing the $Bmse(\hat{\theta})$ expressed in equation 3.11. In order to simplify the problem, the non-linear model is usually approximated by a linear model at point $\boldsymbol{\theta} = \boldsymbol{\theta}_k$

$$\boldsymbol{h}(\boldsymbol{\theta}) \approx \boldsymbol{h}(\boldsymbol{\theta}_k) + \frac{\partial \boldsymbol{h}(\boldsymbol{\theta})}{\partial \boldsymbol{\theta}}_{\boldsymbol{\theta}=\boldsymbol{\theta}_k} (\boldsymbol{\theta} - \boldsymbol{\theta}_k) \tag{3.22}$$

Then substituting the equation 3.22 into 3.18-2.21 provides the approximate MMSE for non linear model.

$$\boldsymbol{\theta}[n] = \boldsymbol{\theta}[n-1] + \boldsymbol{K}[n](\boldsymbol{y}[n] - \boldsymbol{h}(\boldsymbol{\theta}[n-1])) \tag{3.23}$$

$$\boldsymbol{K}[n] = \boldsymbol{P}_{\theta}[n-1]\boldsymbol{H}^{T}[n](\boldsymbol{H}[n]\boldsymbol{P}_{\theta}[n-1]\boldsymbol{H}^{T}[n] + \boldsymbol{P}_{\omega}[n])^{-1} \tag{3.24}$$

$$\boldsymbol{P}_{\theta}[n] = (\boldsymbol{I} - \boldsymbol{K}[n]\boldsymbol{H}[n])\boldsymbol{P}_{\theta}[n-1] \tag{3.25}$$

where $\boldsymbol{H}[n] = \frac{\partial \boldsymbol{h}(\boldsymbol{\theta})}{\partial \boldsymbol{\theta}}|_{\boldsymbol{\theta}=\boldsymbol{\theta}[n-1]}$

Observability analysis
For non-linear observation model, the observation matrix $H[n]$ is not a constant and should be calculated at each point $x[n]$. If we assume the parameters are independent, the observability of the estimator can be examined by $rang(\boldsymbol{H}[n])$. When $rang(\boldsymbol{H}[n]) = m$, the estimator is observable.

3.3 Observer of Dynamic System States

In the previous section, we briefly introduced the theory for estimation of constant parameters. Here we would like to introduce the observer techniques for estimation of dynamics states. The state of a dynamic system is a set of physical quantities which could describe the transient evolution of this system. In a dynamics system, the states are varying with time. The estimation of dynamic states is based on two models: first, a model describing the evolution with time (the dynamic model), and second, a model projecting measurements into the state space (the observation model). More physical interpretation of a such representation has been discussed in detail in [Kalman et al., 1960]. The two models are usually expressed in the state space as shown in equation 3.26.

$$\begin{cases} \dot{x}(t) = f(x(t), u(t)) \\ y(t) = h(x(t)) \end{cases} \tag{3.26}$$

where $f(.)$ is the time evolution model, $h(.)$ is the observation model, $x(t)$ is the dynamic states to be estimated, $u(t)$ is the input of observer.

3.3.1 Linear system and linear Kalman Filter

When both the dynamics model and the observation model are linear, the continuous time system in 3.32 can be formatted as:

$$\begin{cases} \dot{x}(t) = A_c x(t) + B_c u(t) + q \\ y(t) = C_c x(t) + r \end{cases} \tag{3.27}$$

For the discrete time system, the state space can be expanded as

$$\begin{cases} x_{k+1} = Ax_k + Bu_k + q \\ y_{k+1} = Cx_k + r \end{cases} \tag{3.28}$$

where $x \in R^m$ is the state vector, $y \in R^n$ is the vector of measurement, $u \in R^p$ is the input vector. A and C are the state evolution matrix and observation matrix respectively. $q \in R^m$ and $r \in R^n$ are the noise vector of the evolution model and the observation model respectively. Q and R are the covariance matrix corresponding to the noise q and r.

The observer of linear system is well developed in the literature. Among all these observers, the Kalman filter is widely accepted as the most effective method to filter a linear system. R. E. Kalman first published his famous statistical estimation theory in 1960. It is described as a recursive solution to estimate the instantaneous state of the process, in a way that the mean squared error could be minimized. The Kalman filter

can be viewed as an extension of the sequential LMMSE, presented in section 3.2.3, to the case where the parameter θ varies with time. In the following paragraph, we will explain how to obtain the Kalman filter based on the algorithm of sequential MMSE.

Now, we suppose that our target of estimation is the state at instant $t = k + 1$, x_{k+1}. The prior (predicted) PDF of state x_{k+1} could be represented by $N \sim (\mu_{k+1|k}, P_{k+1|k})$, where $\mu_{k+1|k}$ and $P_{k+1|k}$ are obtained through the dynamics model, expressed as

$$\begin{aligned} \mu_{k+1|k} &= Ax_k + Bu_k \\ P_{k+1|k} &= AP_{k|k}A^T + Q \end{aligned} \tag{3.29}$$

After getting the prior PDF of x_{k+1}, the sequential MMSE of x_{k+1} can be obtained by substituting equation 3.29 into 3.18-2.20.

$$x_{k+1} = Ax_k + Bu_k + K_{k+1}(y_{k+1} - Cx_k) \tag{3.30}$$

$$K_{k+1} = P_{k+1}C^T(CP_{k+1}C^T + R)^{-1} \tag{3.31}$$

$$P_{k+1|k+1} = (I - K_{k+1}C)P_{k+1} \tag{3.32}$$

In the literature, the Kalman filter is interpreted as a physical process consisted of model prediction and measurement update.

$$\begin{aligned} &\textit{Prediction from models}: \\ &\hat{x}_{k+1|k} = A\hat{x}_{k|k} + Bu_{k+1} \\ &P_{k+1|k} = AP_{k|k}A^T + Q_{k+1} \\ &\textit{Update from measurements}: \\ &K_{k+1} = P_{k+1|k}C^T(CP_{k+1|k}C^T + R_{k+1|k})^{-1} \\ &x_{k+1|k+1} = \hat{x}_{k+1|k} + K_{k+1}(z_{k+1} - C\hat{x}_{k+1|k}) \\ &P_{k+1|k+1} = (I - K_{k+1}C)P_{k+1|k} \end{aligned} \tag{3.33}$$

where $\hat{x}_{k+1|k}$ and $P_{k+1|k}$ are the predicted value of state and predicted covariance of state based on the data at moment k.

Observability Analysis

When all the states are independent from each other, the observability is determined by the observation matrix. If $rang(C) = m$, the system is observable. However, in a dynamics system, the states are usually highly correlated. Therefore, the observability is not only determined by the observation model C but also influenced by the update model A. The validation of observability of such discrete time system is given in the

matrix as follows:

$$O = \begin{bmatrix} C \\ CA \\ CA^2 \\ \vdots \\ CA^{m-1} \end{bmatrix} \tag{3.34}$$

where m is the dimension of the state vector x.

The system is observable with the condition that the rank of above observability matrix is equal to the dimension of the state vector x.

$$rang(O) = m \tag{3.35}$$

3.3.2 Non linear system and Extended Kalman Filter

As discussed in section 3.2.4, it is not practical to develop a non-linear MMSE, due to the computational difficulty. A first-order linear approximation is usually employed to simplify the problem. The discrete-time state space representation of the system can be formed as

$$\begin{cases} x(k+1) = f(x(k), u(k)) + q \\ y(k+1) = h(x(k+1)) + r \end{cases} \tag{3.36}$$

The linear approximation is given by

$$x(k+1) \approx x(k) + \frac{\partial f(x)}{\partial x}|_{x=x(k)}(x(k+1) - x(k)) \tag{3.37}$$

$$y(k+1) \approx y(k) + \frac{\partial h(x)}{\partial x}|_{x=x(k)}(x(k+1) - x(k)) \tag{3.38}$$

Then the state of non-linear system is observed with the linear Kalman algorithm. The combination of the linear approximation and linear Kalman filter is called the Extended Kalman Filter. The overall process of the EKF can be also interpreted as two steps of

estimation: prediction with model and update with measurement.

$$
\begin{aligned}
&\textit{Prediction with models}: \\
&\hat{x}_{k+1|k} = \boldsymbol{f}(x_{k|k},\, u_{k+1}) \\
&P_{k+1|k} = F P_{k|k} F^T + Q_{k+1} \\
&\textit{Update with measurements}: \\
&K_{k+1} = P_{k+1|k} H^T (H P_{k+1|k} H^T + R_{k+1|k})^{-1} \\
&x_{k+1|k+1} = \hat{x}_{k+1|k} + K_{k+1}(z_{k+1} - \boldsymbol{f}(x_{k|k},\, u_{k+1})) \\
&P_{k+1|k+1} = (I - K_{k+1} H) P_{k+1|k}
\end{aligned}
\tag{3.39}
$$

where

$$
\begin{aligned}
F &= \frac{\partial \boldsymbol{f}(x)}{\partial x}\Big|_{x=x(k)} = \begin{bmatrix} \frac{\partial \boldsymbol{f}_1}{\partial x_1} & \frac{\partial \boldsymbol{f}_1}{\partial x_2} & \cdots & \frac{\partial \boldsymbol{f}_1}{\partial x_n} \\ \vdots & \vdots & \ddots & \vdots \\ \frac{\partial \boldsymbol{f}_n}{\partial x_1} & \frac{\partial \boldsymbol{f}_n}{\partial x_2} & \cdots & \frac{\partial \boldsymbol{f}_n}{\partial x_n} \end{bmatrix} \\
H &= \frac{\partial h(x)}{\partial x}\Big|_{x=x(k)} = \begin{bmatrix} \frac{\partial h_1}{\partial x_1} & \frac{\partial h_1}{\partial x_2} & \cdots & \frac{\partial h_1}{\partial x_n} \\ \vdots & \vdots & \ddots & \vdots \\ \frac{\partial h_n}{\partial x_1} & \frac{\partial h_n}{\partial x_2} & \cdots & \frac{\partial h_n}{\partial x_n} \end{bmatrix}
\end{aligned}
\tag{3.40}
$$

Although the EKF is widely used to solve the nonlinear dynamic system due to its simple conception and fast operation, it is also accused of being unstable when dealing with extreme non linear model. The errors of EKF is caused by the linear approximation process. More specifically, when we look into the entire process of EKF as shown in equation 3.39, we can find the errors of EKF mainly come from the items like $FP_{k|k}F^T + Q_{k+1}$, $HP_{k+1|k}H^T$ and $P_{k+1|k}H^T$. These terms are obtained through the linear approximation process. To reduce the errors in these terms, the Unscented Kalman Filter and Particle Filter are introduced in the next sections.

Observability Analysis

The observability of nonlinear systems is also defined to represent how well the system output could indicate the internal states of the system. However, it is non longer possible to construct a constant observability matrix for nonlinear system. Usually, the observability of nonlinear system is presented with local observability. The global consideration [Hermann and Krener, 1977][Khalil, 2002] is not refereed in this section. Local observability can be verified by using the Lie derivative. The Lie derivative of

function $h(x)$, at $r+1$ order, is defined as:

$$\begin{aligned} L_{\boldsymbol{f}}^{r+1}(h(x)) &= \tfrac{\partial}{\partial x}[L_{\boldsymbol{f}}^{r}(h(x))] \cdot \boldsymbol{f}(x) \\ L_{\boldsymbol{f}}^{0}(h(x)) &= \boldsymbol{h}(x) \end{aligned} \tag{3.41}$$

It is noted that $\dot{h} = \dfrac{\partial h \partial x}{\partial x \, \partial t} = \dfrac{\partial h}{\partial x}\boldsymbol{f} = L_{\boldsymbol{f}}^{1}(h(x))$. The observability matrix is given as:

$$O = \begin{bmatrix} dh(x) \\ dL_{\boldsymbol{f}}^{1}(h(x)) \\ dL_{\boldsymbol{f}}^{2}(h(x)) \\ \vdots \\ dL_{\boldsymbol{f}}^{n-1}(h(x)) \end{bmatrix} \tag{3.42}$$

where the operator d means:

$$dh(x) = \left(\frac{\partial h(x)}{\partial x_1}, \frac{\partial h(x)}{\partial x_2}, \cdots, \frac{\partial h(x)}{\partial x_n}, \right) \tag{3.43}$$

The system is observable with the condition that the rank of matrix O is equal to the dimension of state vector x.

$$rang(O) = m \tag{3.44}$$

It is noted that the $h(x)$ can be a vector, when there is multi measures $[h_1, h_2, \cdots, h_p]^T$.

3.3.3 Unscented Kalman Filter

Both the EKF and UKF are MMSE estimators. The general form of a MMSE-based observer could be represented by the following function:

$$\begin{aligned} \hat{x}_{k+1|k+1} &= E(\boldsymbol{f}(x_k, u_{k+1})) + P_{xy,\,k+1|k} P_{yy,\,k+1}^{-1}[y - E(h(x_k))] \\ P_{xx,\,k+1|k+1} &= P_{xx,\,k+1|k} - P_{xy,\,k+1|k} P_{yy,\,k+1}^{-1} P_{xy,\,k+1|k}^{T} \end{aligned} \tag{3.45}$$

where the operator $E(.)$ means the expected value.

The development of a MMSE-based observer is equivalent to find a method to calculate the $E(\boldsymbol{f}(x_k, u_{k+1}))$, $E(h(x_k))$, $P_{xx,\,k+1|k}$, $P_{yy,k+1}$ and $P_{xy,\,k+1|k}$. For the sake of abbreviation, they are noted as μ_{prior}, μ_y, P_{prior}, P_{yy} and P_{xy} respectively.

To deal with the non-linear estimation problem, the EKF employs the linear approximation method, which would introduce errors to the estimation. Different with the EKF, the UKF employs the sampling techniques to approximate the covariance. The detailed derivation of UKF is already given in [Haykin et al., 2001]. Here we directly

present the principle steps to calculate the needed variables (μ_{prior}, μ_y, P_{prior}, P_{yy} and P_{xy}).

1. Creation of sigma points. Generally speaking, the UKF is to use the weighted sample mean and covariance to approximate the needed variables. Therefore the first step is to create sample points. Given the estimation result of state and its variance at instant $t = k$, $\hat{x}_{k|k}$ and $P_{xx,k|k}$, we can represent the PDF of x_k with a number of $2N_\lambda + 1$ points ,$\chi \in R^{1\times 2N_\lambda+1}$. These sample points are expressed by

$$\chi^i = \begin{cases} \hat{x}_{k|k} & i = 0 \\ \hat{x}_{k|k} + (\sqrt{(N_\lambda + \kappa)P_{xx}[k|k]})_i & i = 1 \cdots N_\lambda \\ \hat{x}_{k|k} - (\sqrt{(N_\lambda + \kappa)P_{xx}[k|k]})_{i-N_\lambda} & i = N_\lambda + 1 \cdots 2N_\lambda \end{cases} \tag{3.46}$$

   The $\sqrt{(N_\lambda + \kappa)P_1})_i$ means the *ith* column of the square root matrix. κ and ε are constant parameters, more details can be found in [Haykin et al., 2001]. When we compute the mean value of sample points, the weight of each sample is obtained by equation 3.47. When we compute the covariance of sample points, the weight is obtained by equation 3.48.

$$W^m[i] = \begin{cases} \frac{\kappa}{N_\lambda+\kappa} & i = 0 \\ \frac{1}{2(N_\lambda+\kappa)} & i = 1 \cdots 2N_\lambda \end{cases} \tag{3.47}$$

$$W^c[i] = \begin{cases} \frac{\kappa}{N_\lambda+\kappa} + \varepsilon & i = 0 \\ \frac{1}{2(N_\lambda+\kappa)} & i = 1 \cdots 2N_\lambda \end{cases} \tag{3.48}$$

2. Calculate the prior PDF of state x_{k+1}, which is to find the mean value μ_{prior} and variance P_{prior} of x_{k+1}.

$$\begin{aligned} \mu_{prior} &= \sum_0^{2N_\lambda} W^m[i] f(\chi^i, u_{k+1}) \\ P_{prior} &= \sum_0^{2N_\lambda} W^c[i](f(\chi^i, u_{k+1}) - \mu_{prior})(f(\chi^i, u_{k+1}) - \mu_{prior})^T + Q \end{aligned} \tag{3.49}$$

   where Q is the additive noise of the dynamic model.

3. Calculate the prior PDF of the external measurement y_{k+1}, which is to find μ_y, P_{yy}. And then calculate the cross correlation matrix P_{xy}

$$\begin{aligned} \mu_y &= \sum_0^{2N_\lambda} W^m[i] h(\chi[i]) \\ P_{yy} &= \sum_0^{2N_\lambda} W^c[i](h(\chi[i], u_{k+1}) - \mu_y)(h(\chi[i], u_{k+1}) - \mu_y,)^T + R \\ P_{xy} &= \sum_0^{2N_\lambda} W^c[i](f(\chi[i], u_{k+1}) - \mu_{prior})(h(\chi[i], u_{k+1}) - \mu_y,)^T + R \end{aligned} \tag{3.50}$$

where R is the additive noise of the measurement.

4. Calculate the posterior PDF of x_{k+1} after the measurement update.

$$\begin{aligned} x[k+1] &= \mu_{prior} + P_{xy}P_{yy}^{-1}(y-\mu_y) \\ P_{xx}[k+1|k+1] &= P_{prior} - P_{xy}P_{yy}^{-1}P_{xy}^T \end{aligned} \tag{3.51}$$

3.3.4 The Particle Filter Algorithm

We remind that the Bayesian estimation of a parameter θ is previously presented by equation 3.12 as

$$\hat{\theta}_B = \int \theta p(\theta|y)d\theta$$

where $p(\theta|y)$ is the posterior PDF of θ after the measurement.

Here in the context of sequential estimation of a dynamic state, the Bayesian estimation of state x_{k+1} is given by

$$\hat{x}_{k+1} = \int x_{k+1} p(x_{k+1}|y_{0:k+1})dx_{k+1} \tag{3.52}$$

where $y_{0:k+1}$ means all the measurements from the initial instant to the current instant $t = k+1$.

According to the Monte Carlo method, the integral calculation can be approximated by a series of sample points $\chi^{0:N}$.

$$E(\theta) = \int \theta q_s(\theta)d\theta \approx \begin{cases} \frac{1}{N}\sum_{i=1}^{N} \chi^i & (a) \\ \sum \chi^i q_s(\chi^i) & (b) \end{cases} \tag{3.53}$$

When the sample points are strictly taken over the designed probabilistic distribution $q_s(\theta)$, the expectation is obtained through equation 3.53(a). Alternatively, when the analytical expression of $q_s(\theta)$ is not available, or it is hard to sample over $q_s(\theta)$, the expectation can be obtained with equation 3.53(b). The $q_s(\chi^i)$ physically means the weight of this sample.

The particle filtering is based on the sampling theory and Monte Carlo method, where the system model can be extremely non-linear while without the need of linear approximation and the noises are not limited to the Gaussian processes noises. There are many tutorials for the methods of the Particle filter in [Beadle and Djuric, 1997] [Candy, 2007]. The overall goal of Particle Filter is to directly implement the Bayesian estimation, by recursively approximating the complete posterior PDF $p(x_{k+1}|y_{0:k+1})$ with sampling points. In the particle filtering process, the system dynamic model is viewed as a Hidden Markov Model (HMM), as illustrated in Figure 3.1. The $p(x_0)$ is the initial probability of a state, $p(x_{k+1|k})$ is the likelihood of current state given the previous state. The PDF

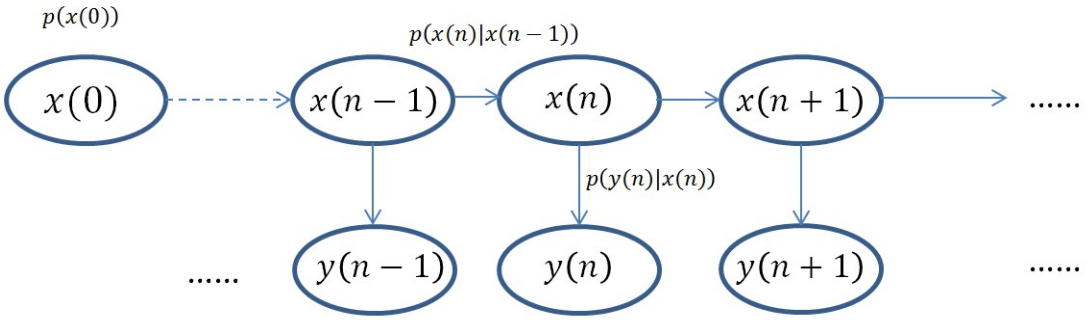

Figure 3.1: Hidden Markov-chain Model

of the measurement is expressed by $p(y_{k+1}|x_{k+1})$. For a modeled dynamic system, the three PDF $p(x[0])$, $p(x_{k+1|k})$, $p(y_{k+1}|x_{k+1})$ are regarded as known. Generally, according to the Particle Filter theory, the posterior PDF $p(x_{k+1}|y_{0:k+1})$ is obtained by two steps, just like the operation of Kalman Filter. The two steps work in a recursive framework:

Step 1: the prediction of the posterior PDF, $p(x_{k+1}|y_{0:k})$, based on the former measurements;

$$p(x_{k+1}|y_{0:k}) = \int p(x_{k+1}|x_k)p(x_k|y_{0:k})dx_k \tag{3.54}$$

Step 2: the correction of the prediction, $p(x_{k+1}|y_{0:k+1})$, with the new measurements;

$$p(x_{k+1}|y_{0:k+1}) = \frac{p(y_{k+1}|x_{k+1})p(x_{k+1}|y_{0:k})}{p(y_{k+1}|y_{0:k})} \tag{3.55}$$

where

$$p(y_{k+1}|y_{0:k}) = \int p(y_{k+1}|x_{k+1})p(x_{k+1}|y_{0:k})dx_{k+1} \tag{3.56}$$

Due to the integral operation involved in the algorithm, it is quite difficult to obtain an analytical solution in the prediction and correction step. Hence the Monte Carlo method is introduced to numerically approximate the posterior PDF $p(x_{k+1}|y_{0:k+1})$ with a set of sample points (particles). The tricky problem here is how to sample these particles. In the literature [Haykin et al., 2001], the Sequential Importance Sampling (SIS) algorithm and the resampling algorithm are employed to facilitate the process of sampling.

3.3.4.1 Sequential Importance Sampling:

Suppose a number of N sample points, $\chi_{k+1} \in R^{1\times N}$, are taken over a known PDF, also called the proposal distribution, $q_{sis}(x_{k+1})$. The estimation of x_{k+1} expressed in

equation 3.52 can be transformed into the following equation

$$\hat{x}_{k+1} = \int x_{k+1} \frac{p(x_{k+1}|y_{0:k+1})}{q_{sis}(x_{k+1})} q_{sis}(x_{k+1})\, dx_{k+1} \tag{3.57}$$

Then substituting equation 3.53-3.56 into 3.57 generates the estimation of x_{k+1} through SIS algorithm:

$$\hat{x}_{k+1} \approx \frac{\sum_{i=1}^{N} X_{k+1}^{i} w_{k+1}[i]}{\sum_{i=1}^{N} w_{k+1}[i]} \tag{3.58}$$

where the variable $w_{k+1}[i]$ is known as the unormalized importance weights of particle X_{k+1}^{i}. The detailed definition of $w_{k+1}[i]$ can be found in [Haykin et al., 2001], here we directly give its recursive form of definition :

$$\begin{aligned} w_{k+1}[i] &= w_k[i] \frac{p(y_{k+1}|X_{k+1}^{i}) p(X_{k+1}^{i}|x_k)}{q_{sis}(X_{k+1}^{i})} \\ w_0[i] &= w_0 \end{aligned} \tag{3.59}$$

In our research, the initial particles are simply obtained through a uniform distribution, thus $w_0[i] = \frac{1}{N}$. The proposal distribution $q_{sis}(x_{k+1})$ is set as equal to $p(x_{k+1}|x_k)$. As a result, the sampling process can be greatly simplified as

$$\begin{aligned} w_{k+1}[i] &= w_k[i] p(y_{k+1}|X_{k+1}^{i}) \\ w_0[i] &= \frac{1}{N} \end{aligned} \tag{3.60}$$

The sequential importance sampling algorithm has a serious limitation: the variance of the importance weights increases stochastically over time. Typically, after a few iterations, one of the normalized importance weights tends to unity, while the remaining weights tend to zero. A large number of samples are thus effectively removed from the sample set because their importance weights become numerically insignificant. To avoid this degeneracy, a resampling process is used to eliminate samples with low importance weights and multiply samples with high importance weights.

3.3.4.2 Resampling

In the literature, several algorithms are proposed to correctly select the good samples, including sampling-importance resampling, residual resampling algorithm and the stratified resampling algorithm [Haykin et al., 2001]. These algorithms can make each particle

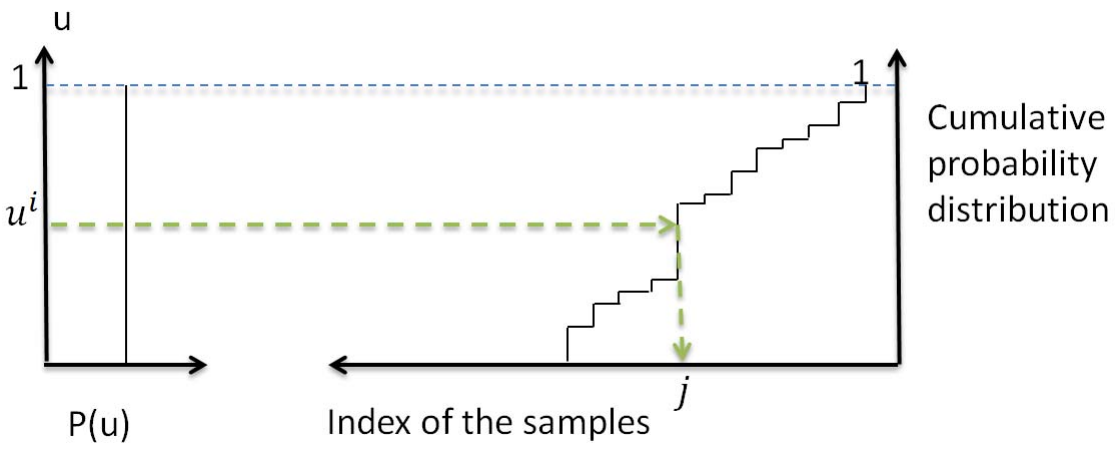

Figure 3.2: Illustration of Sampling Importance Resampling algorithm

has a equal importance weight.

Sampling Importance Resampling

Generally, the SIR process is to generate N_i copies of each sample x^i_{k+1}, while $\sum_{i=1}^{N} N_i = N$. The new set of samples is the assemble of all these copies. The role of the resampling algorithm is to decide the value of N_i. This can be accomplished by generating N independent random variables $\{u^i; i = 1, \cdots N\}$ according to the uniform distribution on interval $(0, 1]$ and for each u^i, one sample x^j will be selected according to the inverse of the cumulative probability distribution. For $u^i \in (\sum_{i=1}^{j-1} w_{k+1}[i], \sum_{i=1}^{j} w_{k+1}[i])$, the corresponding sample x^j_{k+1} will be selected, as illustrated in the Figure 3.2. After the SIR process, the original samples $\{x^i_{k+1}, w_{k+1}[i]; i = 1, \cdots N\}$ is mapped into a set of uniformly distributed samples $\{x^i_{k+1}, \frac{1}{N}; i = 1, \cdots N\}$. When the number of samples is very big, the computational cost of the SIR algorithm is significant. In order to make the resampling process more efficient, the residual resampling and stratified resampling algorithms are proposed.

Residual resampling algorithm

In the residual resampling algorithm, the value of N_i is decided with a two-step process: $N_i = N_i^A + N_i^B$.

- In the first step, the number of copies are deterministicly obtained using the floor function, $N_i^A = \lfloor N w_{k+1}[i] \rfloor$. Then there still remains $N_{res} = N - \sum_{i=1}^{N} \lfloor N w_{k+1}[i] \rfloor$ particles to be sampled.
- In the second step, the remaining samples are taken through the SIR method. The

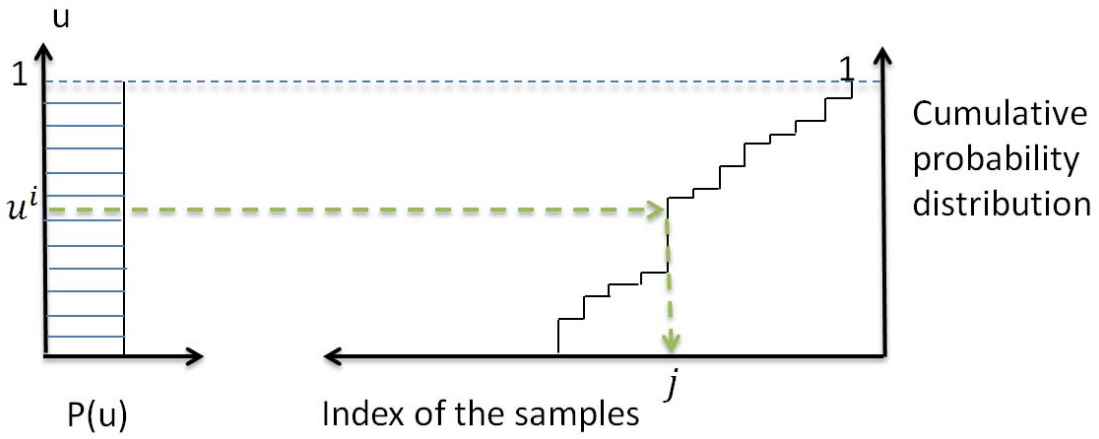

Figure 3.3: Illustration of Stratified Resampling algorithm

new importance weight after the first step is noted as $w^{res}_{k+1}[i]$ and obtained by

$$w^{res}_{k+1}[i] = \frac{Nw_{k+1}[i] - Nw_{k+1}[i]}{N_{res}} \tag{3.61}$$

This procedure is computationally cheaper than the pure SIR.

Stratified resampling algorithm

The stratified resampling algorithm is firstly proposed in [Kitagawa, 1996], and thus it is also called the Kitagawa resampling algorithm.

Different with the SIR method, the stratified resampling is to partition the interval $(0, 1]$ into N disjoint sets, $(0, 1] = (0, 1/n] \cup (1/n, 2/n] \cup \cdots \cup (n-1, n]$. The u^i are drawn independently in each of these sub-intervals. It has cheaper computational cost as every time it take sample over a small interval instead of the whole interval $(0, 1]$. Furthermore, it has improved the sample variety.

3.4 Conclusion

This chapter provides a brief summary of the linear/nonlinear observation techniques. Firstly, the estimation problem of a constant parameter is discussed. The minimum variance unbiased estimator and the minimum mean square error estimator are reviewed and compared. The MVU is based on the assumption that the parameter to be estimated is a deterministic constant value and we do not know any information about it until the measurement arrives. While the MMSE estimator is based on the Bayesian philosophy, which considers the parameter as a random variable with a prior distribution. The role of estimation is to update the distribution of the random variable after the measurement.

Then the estimation techniques for a dynamics system, the observers, are reviewed. All the observers introduced in this section are based on the Bayesian philosophy. For the estimation of linear dynamics system, the classic Kalman filter is widely employed. Different with the classic explanation in the literature, we interpret the Kalman filter as a recursive LMMSE estimator. Furthermore, we also introduced the the observation techniques for nonlinear dynamics systems. The Extended Kalman filter employs the first order linear approximation method to simplify the problem. The drawback of the extended Kalman filter is that it introduces additional errors to the estimation due to the linear approximation. In order to overcome the shortcoming of EKF, the Unscented Kalman filter and Particle filter are introduced. The unscented Kalman filter is another extension of Kalman Filter. It also assumes that the model errors follow a normal distribution, however it uses sampling techniques to approximate the covariance instead of the “first-order” linearization. Therefore, the Unscented Kalman filter is suitable for highly nonlinear systems. To further extend the observer for a larger field, the particle filter is presented for highly nonlinear system with non-Gaussian noise. The PF directly approximates the posterior distribution of the estimates with the sample points (particles). We have briefly deduced the PF based on the Monte-Carlo method and the MMSE theory. The performance of PF is greatly influenced by sampling process. The classic sequential importance sampling may lead to the degeneracy problem. To overcome this shortcoming, different resampling techniques are introduced, such as the sampling-importance resampling, the residual resampling and the stratified resampling.

4 Observers For Estimation Of Tire Forces And Sideslip Angle

4.1 Introduction

Tires are the only vehicle components which could generate external forces to control vehicle motion. The engines, brakes, steering systems are supposed to always be able to control the tire forces. Unfortunately, when the tire is undergoing excessive slip, the driving operation (steering or braking) will not reach its intended target. This possibly results in the over-steering or under-steering situation, which is very dangerous for the vehicle. In such an emergent situation, the drivers usually are not able to make a good decision and control the vehicle back to the safe state. Many advanced driver assistance systems (ADAS) have been developed to ensure the vehicle stay in control in dangerous situation, such as the anti-lock braking system (ABS) and electric stability program (ESP). These safety systems are activated only when the dangerous tire slip has already happened. It is more interesting for us to detect the potential excessive tire slip and avoid the accidents from happening. Monitoring tire forces could help the drivers or the intelligent system to evaluate the safety of tires. Therefore, awareness of tire forces becomes very important for the further development of active safety system. These dynamics states could be obtained by two methods: *measurement* and *observers*.

Direct measurement method

Many high tech sensors have been developed to directly measure the dynamics states of the vehicle. The task of measuring sideslip angle is very challenging due to the difficulty of measuring vehicle speed in the absolute coordinate system. However, through the use of the high-tech optical sensor or the high-performance multiple-antenna Global Positioning System (GPS) [Ryu et al., 2002] [Chen and Hsieh, 2008][Klomp et al., 2014], the vehicle's over-ground speed can be measured directly. Meanwhile, the shortcomings of direct measurement method is also very obvious. Firstly, this sort of sensor is too expensive for ordinary car. The wheel transducers that measures the 6-components (three forces and three torques in the longitudinal, lateral and vertical direction) of road-tire contact force system, is about 100,000 euros. Secondly, limited by the physical mechanism of the sensor, they are sensitive to the variation of the environment and can only work in some particular condition.

State observer based method

The state observer, also called as virtual sensor, is able to estimate the non-measured dynamics states based on the available measurement. The observer technique can be further classified into two categories: the liner observer and non-linear observer. The linear observer deals with the linear model, such as the Luenberger Observers, Recursive least squares algorithms and the Kalman filters [Nam et al., 2013]. In order to deal with the non-linear vehicle dynamics models, many non-linear observers are also developed in the literature. The extended Kalman filter is employed to estimate the sideslip angle at low friction road [Li et al., 2014a]. A fuzzy observer that utilizes fuzzy model with T–S fuzzy rules to represent the nonlinear vehicle model was proposed to estimate vehicle slip angle [Dahmani et al., 2013]. The sliding mode observer is employed to estimate the tire forces in [Baffet, 2007]. The unscented Kalman filter is employed to estimate the tire forces and side slip angle in [Doumiati, 2009].

Generally, the existent observers for estimation of vehicle dynamics can be improved in two aspects:

1. further development of vehicle models, which accurately describe all dynamics behaviors of interest while as simple as possible.
2. creative construction of observers, which reduce the model errors and sensor errors to the maximum extent.

In this thesis, we propose contributions in both of the two aspects. In the aspect of vehicle modeling, we propose several new vehicle dynamics models as introduced in the Chapter 2. We consider the vehicle motion as a three-dimensional motion rather than a planar motion. The pitch-roll motion of suspension is taken into account to calculate the vehicle load transfer. As a result, the vehicle model would be accurate even when the vehicle is driving on the inclined road (road with bank angle or slope angle). In addition, we have also propose the models to calculate the transfer of lateral forces T_{Fy} and transfer of longitudinal forces T_{Fx}. The biggest advantage of our proposed model is to enable the estimation of tire frictional forces without the tire slip (tire sideslip angle or tire slip ratio). Besides the proposed models, we also developed an robust observer to combine all existent models. The estimation of vehicle dynamics states is obtained through the fusion of multiple models and multiple sensors, which makes the observer robust in different driving condition. Our observer is developed according to the Kalman filter algorithm (including linear KF, Extend KF and Unscented KF). In order to further adapt to the non-linear system, we also develop an observers based on the Particle filter.

In general, the contribution of the work in this chapter is to develop a robust observer for estimation of tire forces and sideslip angle. The estimation of tire forces is already widely discussed in the literature [Wang, 2013]. However, we consider the problem in the following view points, which make the estimation more challenging and also more realistic.

1. considering the highly non-linear tire model;
2. estimating the vertical , longitudinal and lateral forces of each tire;
3. considering the road inclination;
4. using only low-cost sensors;
5. implementing the observers in the experimental vehicle for real-time estimation.

This chapter is organized as follows. Section 4.2 presents the implementation of embedded system on the experimental vehicle. Section 4.3 demonstrates experimental data to validate the proposed models. Section 4.4 introduces the observer design. Then, the performance of the new observers are evaluated by several critical tests. The analysis of experimental results are presented in Section 4.5. Finally, concluding remarks and future perspectives are given in Section 4.6.

4.2 Implementation of Embedded System

In this section, we will mainly present implementation of the experimental vehicle in our laboratory, including the embedded sensors and the software modules [Dherbomez et al., 2013a]. Our experimental vehicle DYNA is instrumented by the laboratory HEUDIASYC UMR 7253 CNRS at Compiègne, France, as shown in Figure 4.1.

Figure 4.1: Heudiasyc laboratory experimental vehicle: DYNA

4.2.1 Embedded sensors

Plenty of sensors are equipped in our vehicle. They could be generally classified as two categories, sensors used for validation and sensors used for input of the estimator.

Sensors used for validation:

- Kistler RoaDyn S625 wheel force transducers: It's able to measure all the tire-road contact forces and wheel torques in three dimensions. Four wheel force sensors are

fixed at each wheel. These sensors are very expensive for ordinary cars. It is noted that they are used only for reference.(see Figure 4.2.a)

- CORREVIT S-400: Non-Contact Optical Sensor for measurement of lateral speed and sideslip angle. The sensor is installed at place of the spare wheel under the car.(see Figure 3.5.b)
- A scenario record camera is used to register the vehicle trajectory.

a)  b) 

Figure 4.2: a) Kistler wheel force transducers at front left wheel; b) The Correvit installed at place of the spare wheel

Sensors used for input measures:

- CROSSBOW VG700AB: It combines MEMSIC's high performance fiber optic gyros with silicon micro-machined (MEMS) accelerometer technology. It could provide a highly accurate measurement of Vertical Gyro (VG) and Inertial parameters. (see Figure 4.3.a)

a) 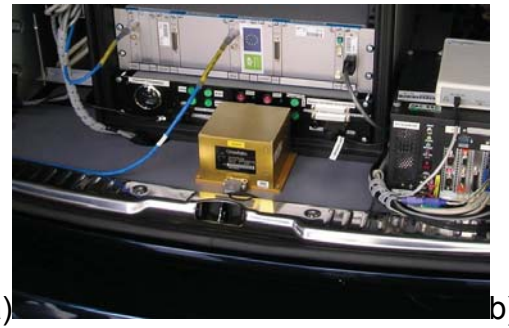 b) 

Figure 4.3: a) MEMS sensor for inertial parameters and gyroscope; b) Laser sensor for chassis height measurement

- CORRSYS-DATRON HT500: it is a non contact distance sensor. It provides measurement of the deflection between chassis and ground. They are installed respectively at four corners of vehicle body. (see Figure 4.3.b)

- Available data on CAN bus: wheel rotation velocity, engine speed, yaw rate, brake pressure, lateral acceleration from the ESP, steering wheel angle.
- GPS receiver operating in RTK mode locates the vehicle with centimetric accuracy.
- Mobileye system: it is able to provide a list of detected obstacles (pedestrians, vehicles, ...) and the position of the vehicle relative to the ground side markings on the vehicle CAN bus in real-time.
- Ibeo Standard (8L) Eight Layer/Multi-Echo LUX Sensor (Ibeo LUX 8L): the sensor is installed at front bumper to track the object on top 4 layers and raw data ground scanning/ profiling (see Figure 4.4.a).

These devices are located in the trunk of the car with the electric circuit system as shown in Figure 4.4.b. The monitoring equipment is located on the back left seat. The operator can manipulate the configuration of the system with a monitor and keyboard.

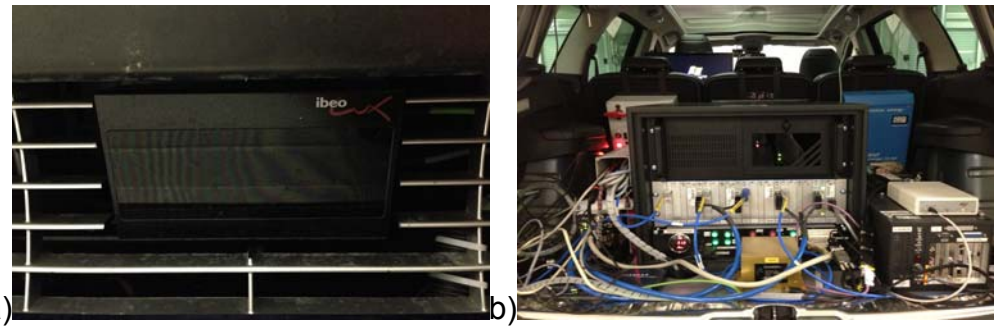

a) b)

Figure 4.4: a) Laser sensor installed at front bumper; b) Embedded electronics and computer in the trunk

Sensor data should be sent to a computer which has installed the estimation algorithm. However, some of these sensors cannot be directly connected to the computer. Therefore we developed an acquisition system based on the UEI PowerDNA Ethernet DAQ Cube to fulfill the task. It is capable of acquiring 48 analog channels using a 24-bit converter. It consists of a computer UEI powered by a 200 MHz PowerPC processor running a real-time operating system Xenomai. The Xenomai is a real-time development framework cooperating with the Linux kernel. The software provides data acquisition by using the analog cards AI-217, shown in Figure 4.5. Digital filters with different cut-off frequency are installed in the cube to cut off high frequency noise. The acquisition frequency of the cube is 4 kHz, while the data is sent back in 200 Hz.

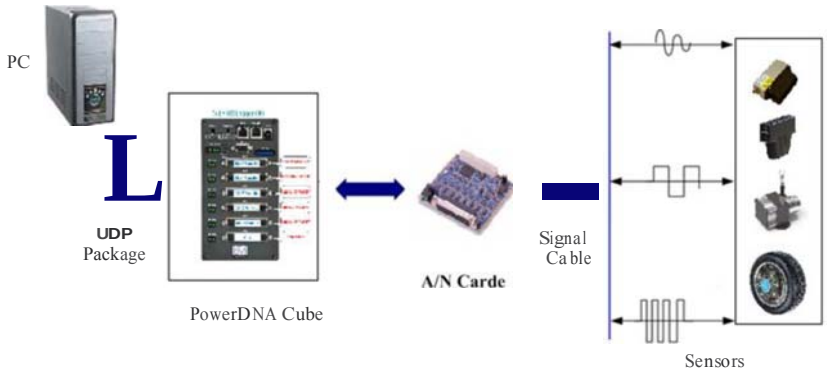

Figure 4.5: The structure of the acquisition system

4.2.2 Software Modules

This car is equipped with an industrial PC in the trunk. A particular prototyping environment, PACPUS[1](Perception et Assistance pour une Conduite Plus Sûre), is developed in C/C++ for the real time estimation system. The framework of PACPUS is illustrated in Figure 4.6. Following the principle of component-oriented design, PAC-

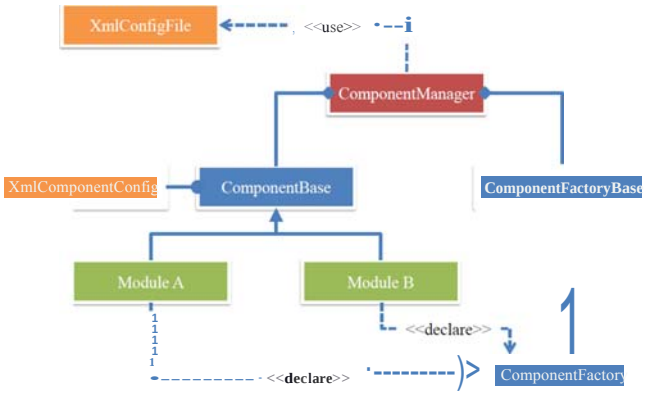

Figure 4.6: Software architecture of PACPUS

PUS provides users more versatility in their developments. Different components of PACPUS are developed in our work to fulfill different tasks. For instance, we develop the component "CubeClient" for the task of communication between the cube and the PC. The component is devoted to the task of sending the request, receiving the UDP packet and then decoding the UDP packet. Then the data is sent to the component of vehicle dynamics estimation. Similarly, the components for management of the other

[1]The framework PACPUS is an open source with free license CeCILL-C. It is available at https://devel.hds.utc.fr/softwarejpacpus/wiki

sensors are also constructed in our work. The estimation algorithm is developed in the .DLL form as a real-time application. The framework PACPUS employs the Qt API for graphical interfaces and can be integrated with other development environment for multi-sensor fusion. The schema of PACPUS is shown in Figure 4.7.

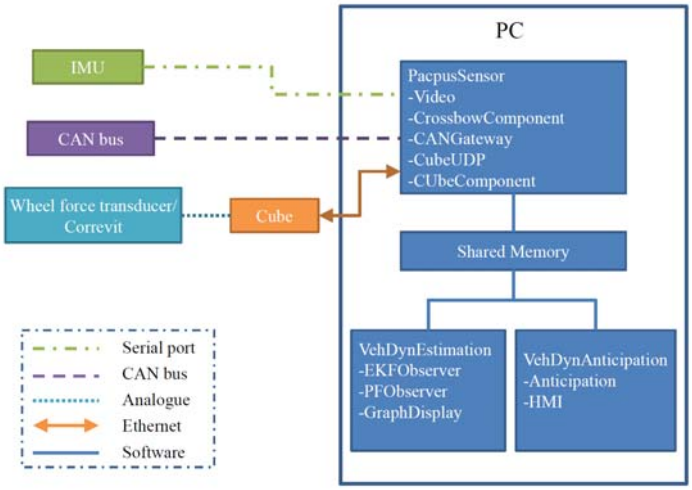

Figure 4.7: Software architecture of acquisition system and estimation system

4.3 Open-loop Estimation Of Vehicle Dynamics States

The model quality can greatly influence the performance of the observers. In this section, we will present the experimental data to validate the dynamics models introduced in Chapter 2. In order to better demonstrate the quality of each model, the estimation results illustrated in this section are obtained by the open-loop method without any filtering techniques or observer techniques. Therefore, the accuracy of the estimation result is completely dependent on the model quality and the sensor quality. The experimental vehicle is equipped with the inertial sensors, wheel speed sensors, which provide the input data for the estimation. Meanwhile, the wheel force transducers and optic sensor are employed to directly measure the tire forces and sideslip angle and only used as the ground truth to evaluate the open-loop estimation.

A slalom test is performed to analyze the property of the different vehicle dynamics models. The maneuver time history of the slalom test is given in Figure 4.8. The vehicle is firstly accelerating to the speed of $70km/h$, then following with a slalom maneuver with the lateral acceleration $-10m/s^2 < a_y < 10m/s^2$ at constant speed $70km/s$. This slalom test with high value of lateral acceleration is able to create obvious lateral load transfer, which will lead to great variation on vehicle's dynamics states. Note that the experimental data in section 4.3.1-4.3.3 are the same set of data taken from this test.

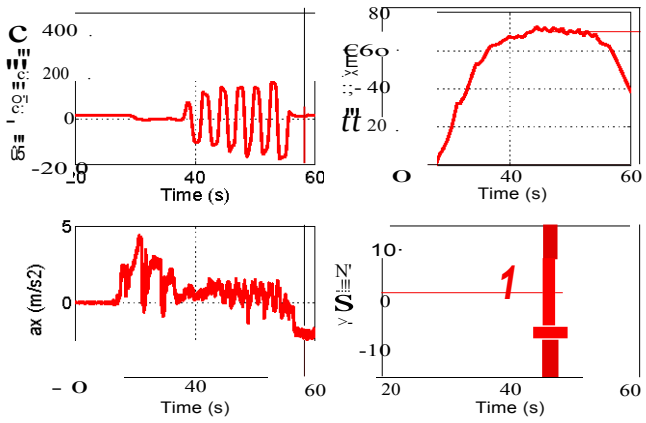

Figure 4.8: Maneuver time history of the slalom test

4.3.1 Vertical tire force open-loop estimation

The models for estimation of vertical forces can be summarized with table 4.1.

Table 4.1: Summary of vehicle vertical dynamics models

Model symbol	Model name	equation
$F_{z,model1}$	Rigid car model	More details in equation 2.58 $M_x = mayhjE$ $M_y = maxh/L$
$F_{z,model2}$	Quarter suspension model	More details in equation 2.60 $F_{zij} = d,/r_{ij} + k_{uCTij}$
$F_{z,model3}$	Pitch-roll model	More details in equation 2.67 $M_{x,sus} = C<py)b + K.p'Pb$ $M_{y,sus} = Ceéb + KeBb$
$F_{z,model4}$	Proposed model	More details in equation 2.69 $F_{z,model4} = (1 - Ç)F_{z,model1} + /;F_{z,model3}$

As introduced in the Section 2.4.1, the key to estimate the vertical force at each tire is to find an accurate model for computing the transfer of vertical load. Figure 4.9 illustrates the open-loop estimation of the lateral load transfer $T_{pz,lat} = F_{z11} - F_{z12} + F_{z21} - F_{z22}$. The red lines are the measurement of the force transducers on-boarded on the experimental vehicle DYNA. Generally, all the four models in Table 4.1 provided good estimation of the lateral load transfer. By comparing the estimation of different models, we can find the rigid car model was less accurate at the peak points, while the proposed new model (dotted dark lines in figure 4.9) could tightly follow the measurements. The limitation of the proposed model is the need of measurement of suspension deflection. In our experimental vehicle, laser sensors have measured the distances between the road surface and the vehicle body. When the road is well paved, the variation of this distance

can be approximated as the defiection of suspension. However, in the experiment, the road was not always perfectly even, and it caused the bias at $t = 36$s (see figure 4.10 left side). The open-loop estimation of the longitudinal load transfer $TF_{z,lcm} = Fzn + F_{z12} - F_{z21} - F_{z22}$ is illustrated in Figure 4.10. The experiment data has validated the proposed model for estimation of transfer of vertical load. Then the vertical force at each tire was obtained by employing the proposed models, as illustrated in Figure 4.11.

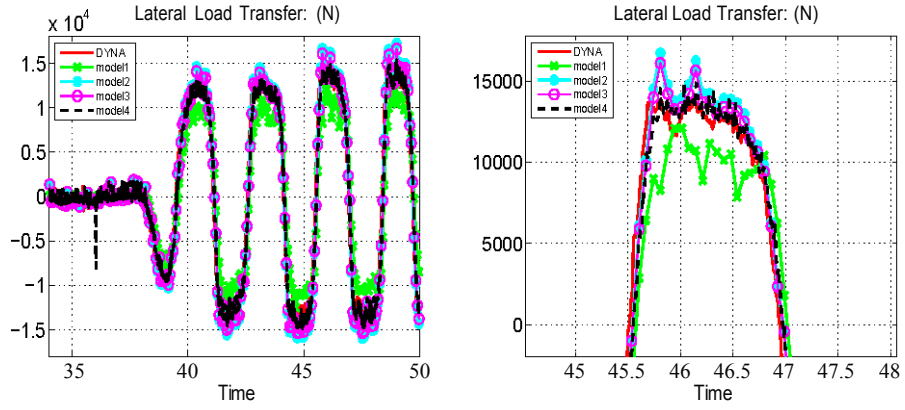

Figure 4.9: Open-loop estimation of lateralload transfer $TFz,lat = Fzn-Fz12+Fz21-Fz22$

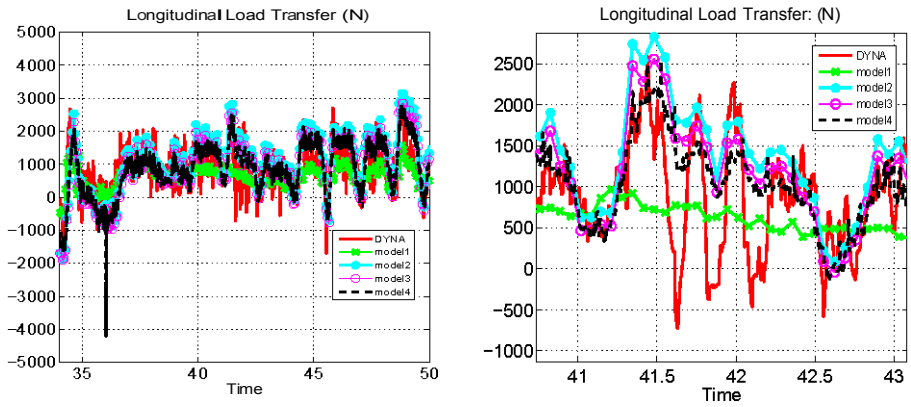

Figure 4.10: Ope n-loop estimation of longitudinal load tra nsfer $TF_{z,lon} = Fzn + F_{z12} - F_{z21} - F_{z22}$

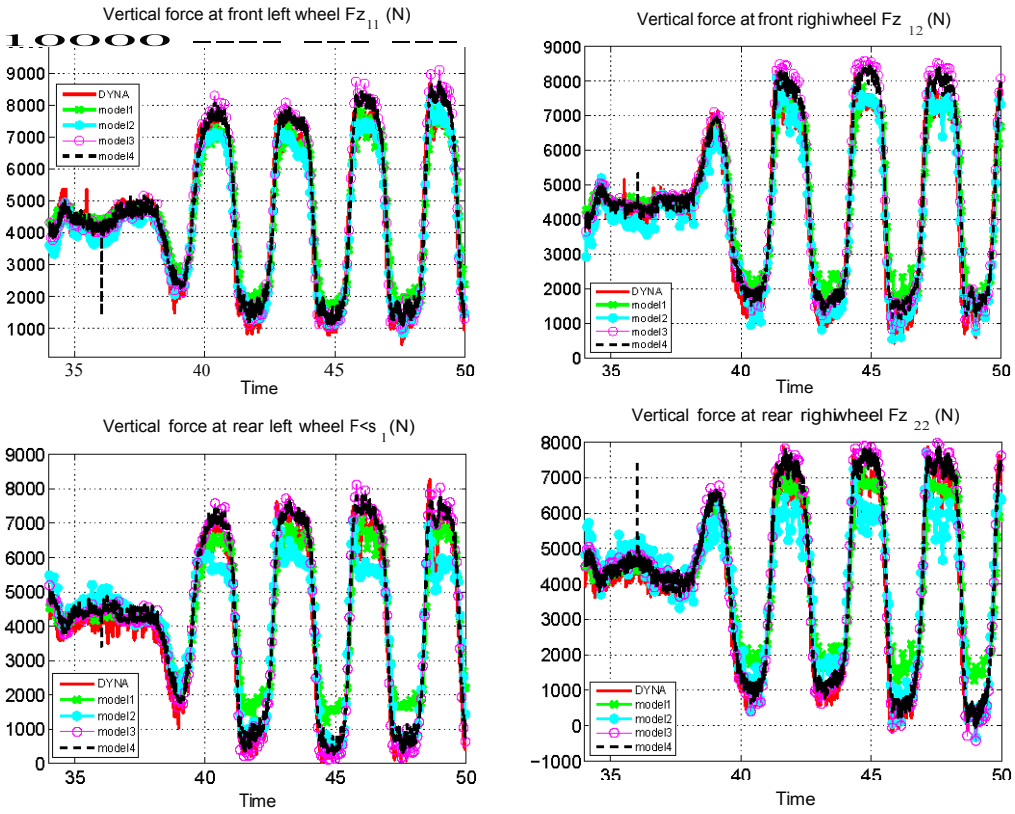

Figure 4.11: Open-loo p estimation of vertical force at each tire

4.3.2 lateral tire force open-loop estimation

The models used for estimating vehicle lateral dynamics are summarized in the Table 4.2. None of the existent models could provide an accurate open-loop estimation of lateral force at each tire, when the sideslip angle is not available. The bicycle model and the double track model are only able to compute the tire forces at each axle but not at each tire. Figure 4.12 illustrates the open-loop estimation of lateral forces at front axles and rear axles. The experiment data validated that the bicycle model can effectively estimate the resultant lateral force at each axle. In our experimental vehicle, the inertial sensors are installed at the rear axle. In order to obtain the acceleration at COG a_{ycog}, the following transformation should be performed,

$$a_{ycog} = a_{yinetial} + L2[/] \tag{4.1}$$

where $a_{yinetial}$ is the measured acceleration by the installed accelerometer.

Table 4.2: Summary of vehicle lateral dynamics models

Model symbol	Model name	equation
$F_{y,model1}$	Tire model	More details in section 2.2 $F_{wy} = C_\alpha \alpha$
$F_{y,model2}$	Bicycle Model	More details in equation 2.78 $\dot{v_x} = \frac{1}{m}(F_{xf}\cos(\delta) - F_{yf}\sin(\delta) + F_{xr})$ $\dot{v_y} = \frac{1}{m}((F_{xf}\sin(\delta) + F_{yf}\cos(\delta) + F_{yr}) - \dot{\psi} v_x$ $\ddot{\psi} = \frac{1}{I_z}[L_1(F_{yf}\cos(\delta) + F_{xf}\sin(\delta)) - L_2 F_{yr}]$
$F_{y,model3}$	Double track model	More details in equation 2.82 $F_{yf}\sin(\delta) = F_{y11}\sin(\delta_{11}) + F_{y12}\sin(\delta_{12})$ $F_{yf}\cos(\delta) = F_{y11}\cos(\delta_{11}) + F_{y12}\cos(\delta_{12})$ $F_{yr} = F_{y21} + F_{y22}$
$F_{y,model4}$	The proposed model	More details in equation 2.86 $F_{y11} - F_{y12} = \frac{T_{Fz,f}}{F_{zf}} F_{yf} + a_1 \delta F_{zf} + a_2 \ddot{\psi} v_x$ $F_{y21} - F_{y22} = \frac{T_{Fz,r}}{F_{zr}} F_{yr} + a_3 \ddot{\psi} v_x$

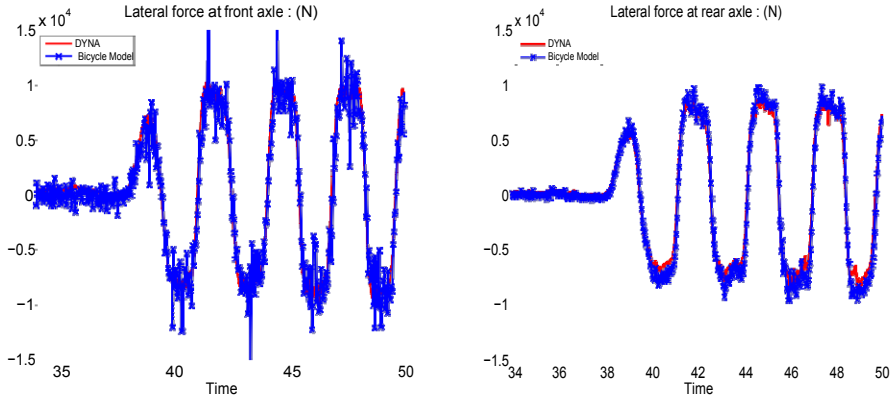

Figure 4.12: Open-loop estimation of resultant lateral force at front axle $F_{y,f} = F_{y11} + F_{y12}$ and at rear axle $F_{y,r} = F_{y21} + F_{y22}$

After getting the lateral forces at each axle, the challenging problem is to calculate the difference between the left wheel and right wheel, which is called the transfer of lateral force in this thesis. In the literature [Doumiati, 2009], the authors propose to firstly calculate the slip angle at each wheel and then employ the tire model to calculate the tire forces. The shortcoming of this approach is that the estimation process is complicate and it needs an observer to provide the value of slip angle. In this thesis, we propose a new model to directly calculate the transfer of lateral force. Figure 4.13 illustrates the open-loop estimation results of the transfer of lateral force at front axle and at rear axle. Experimental results have validated that the proposed model could be used to compute the value of $F_{y11} - F_{y12}$ and $F_{y21} - F_{y22}$.

Then the lateral force at each tire can be obtained by combining the results in Figure

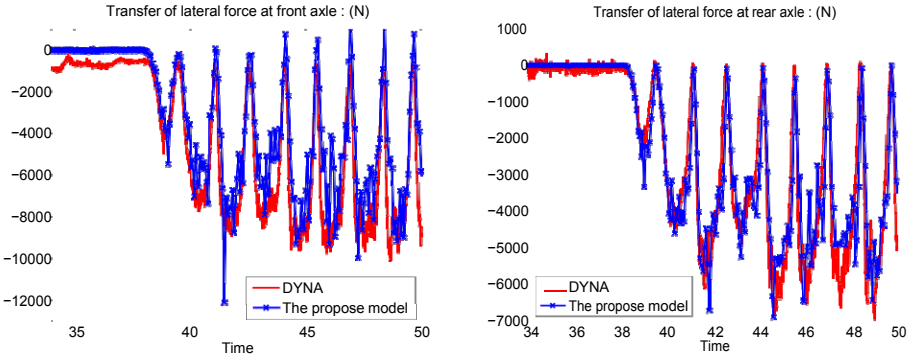

Figure 4.13: Open-loop estimation of transfer of lateral force at front axle $T_{Fy,f} = F_{y11} - F_{y12}$ and at rear axle $T_{Fy,r} = F_{y21} - F_{y22}$

4.12 and 4.13. To make a comparison with the proposed model, the lateral forces at each wheel is also calculated with the bicycle model by supposing that $F_{y11} = F_{y12}$, $F_{y21} = F_{y22}$. Figure 4.14 illustrates the open-loop estimation result of lateral force at each tire. The red lines are the measurement data of force transducer. The blue lines are the open-loop estimation result based on the proposed model. The green lines are results based on the assumption $F_{y11} = F_{y12}$, $F_{y21} = F_{y22}$. The proposed models of transfer of lateral force make it possible to estimate the tire lateral force without the information of the sideslip angle.

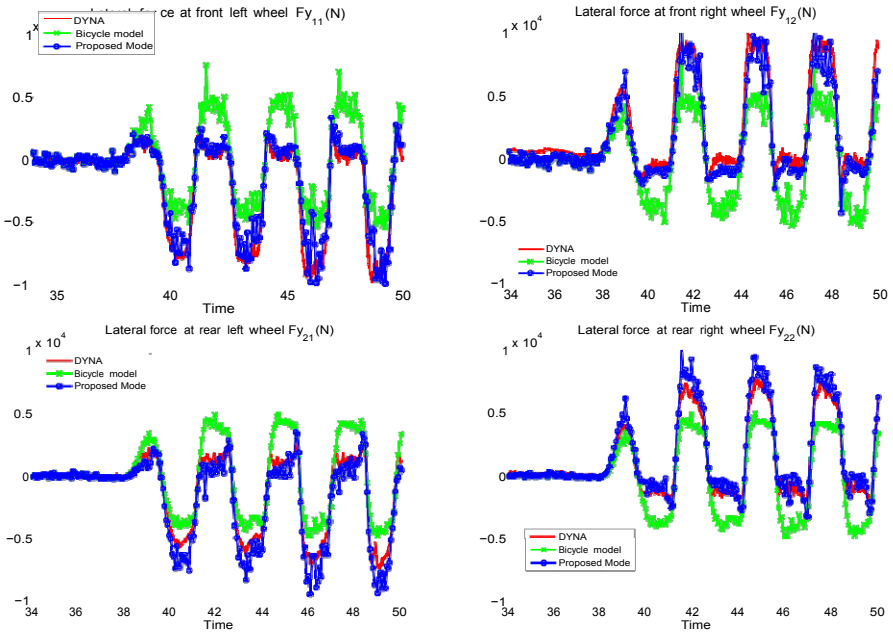

Figure 4.14: Open-loop estimation of lateral force at each tire

Table 4.3: Summary of vehicle longitudinal dynamics models

Model symbol	Model name	equation
$F_{x,model1}$	Tire model	More details in section 2.2 $F_{wy} = C_s s$
$F_{x,model2}$	Bicycle Model	More details in equation 2.78 $\dot{v}_x = \frac{1}{m}(F_{xf}\cos(\delta) - F_{yf}\sin(\delta) + F_{xr})$ $\dot{v}_y = \frac{1}{m}(F_{xf}\sin(\delta) + F_{yf}\cos(\delta) + F_{yr}) - \psi v_x$ $\dot{\psi} = \frac{1}{I_z}[L_1(F_{yf}\cos(\delta) + F_{xf}\sin(\delta)) - L_2 F_{yr}]$
$F_{x,model3}$	Engine torque model	More details in equation 2.97 $F_{wxij} = \frac{T_{ij} - T_b - M_{resis} - I_{wij}\dot{\omega}_{ij}}{R_{eff}}$
$F_{x,model4}$	The proposed model	More details in Equation 2.99 $F_{y11} - F_{y12} = c_3\frac{\omega_z}{v_x} + c_4 a_y + c_5\delta_{steering}$ $F_{x21} - F_{x22} = c_1\frac{\omega_z}{v_x} + c_2$

4.3.3 longitudinal tire force open-loop estimation

The longitudinal tire force could be computed with tire slip ratio s [Pacejka, 2006] or the wheel torque [Altmannshofer et al., 2016]. However, our objective is to estimate the tire forces with only low-cost sensors which are available in a standard vehicle. Due to this limitation, the longitudinal tire forces at each wheel are usually regarded as inaccessible information during the development of ADAS system. In order to solve this challenging problem, we propose a new model for the estimation of longitudinal tire forces. The existent models for estimation of vehicle longitudinal forces are summarized in table 4.3.

To begin with, we present the experimental data about the resultant longitudinal tire forces at front axle and at rear axle in Figure 4.15. The red lines are the measurement of force transducer. The blue lines are the estimation based on the bicycle model. From the Figure 4.15, we can validate that the bicycle model can provide a good estimation of the longitudinal forces at each axle. The experimental data also showed that it is reasonable to approximate the longitudinal force at rear axle by a constant value.

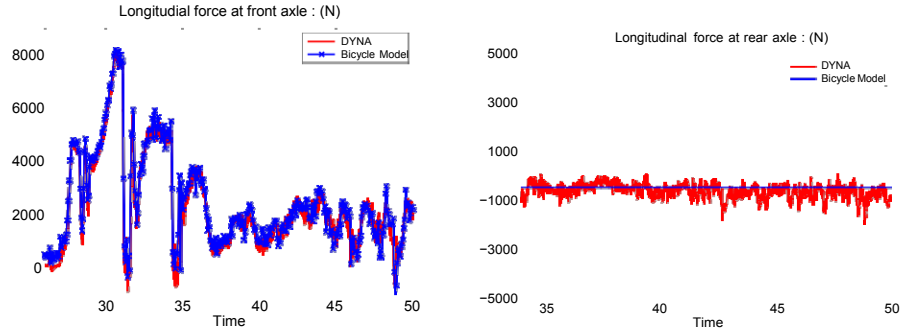

Figure 4.15: Open-loop estimation of resultant longitudinal force at front axle $F_{x,f} = F_{x11} + F_{x12}$ and at rear axle $F_{x,r} = F_{x21} + F_{x22}$

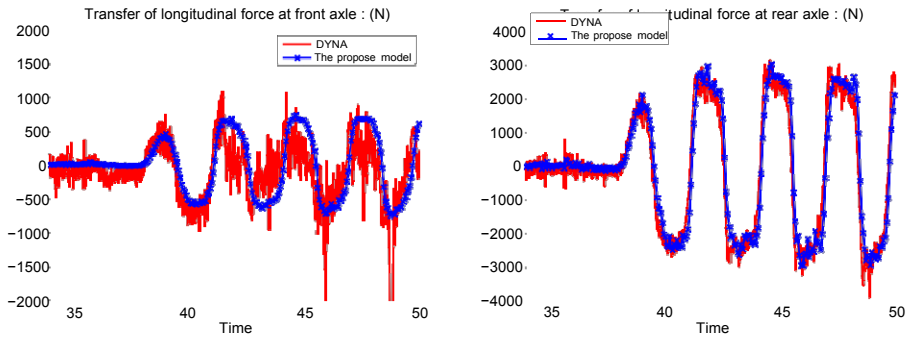

Figure 4.16: Open-loop estimation of transfer of longitudinal force at front axle $T_{Fx,f} = F_{x11} - F_{x12}$ and at rear axle $T_{Fx,r} = F_{x21} - F_{x22}$

The open-loop estimation results of transfer of the longitudinal force are illustrated in Figure 4.16. The proposed model has accurately estimated the transfer of longitudinal force at rear axle. However, it is less accurate at the front axle. It can be explained by the fact that the front wheels are the drive wheels. The drive wheels are controlled by the engine and the steering system. In order to reduce the model errors at drive wheels, further development of model will be realized in our future work.

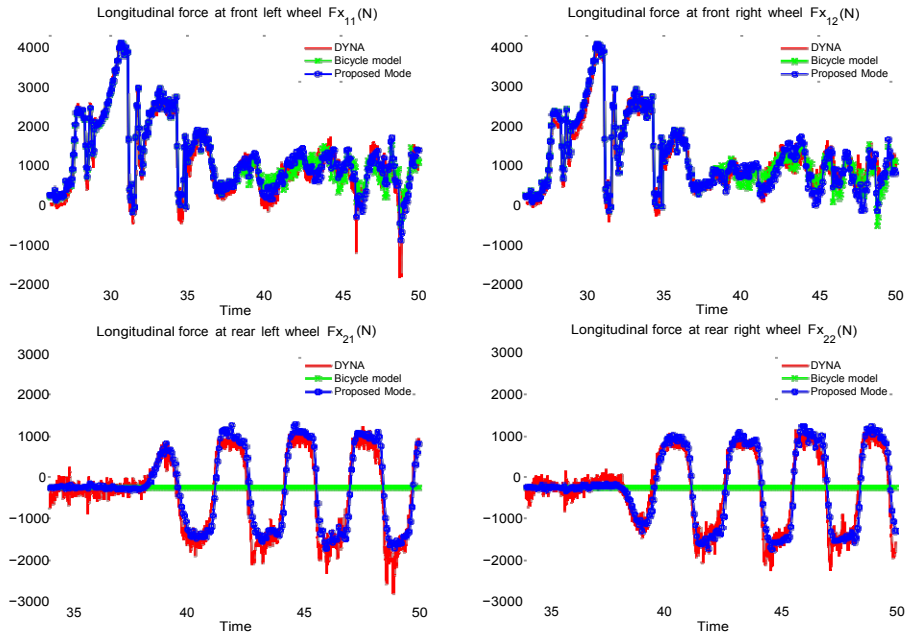

Figure 4.17: Open-loop estimation of longitudinal force at each tire

The open-loop estimation result of longitudinal force at each tire is illustrated in Figure 4.17. The green lines are the estimation result obtained based on the bicycle model and the assumption that $F_{x11} = F_{x12}$, $F_{x21} = F_{x22}$. The blue lines represents the estimation obtained through the proposed models, which has tightly followed the

real data. Figure 4.17 has also demonstrated the importance of estimating longitudinal forces. In many literature, the longitudinal force at rear wheels are regarded as zero. However, we can see that when the vehicle is turning, the rear wheels could generate considerable longitudinal forces.

4.3.4 Sideslip angle open-loop estimation

In the literature, the side slip angle is usually estimated based on the bicycle model and linear tire model, described in equation 4.2.

$$\begin{bmatrix} \ddot{\psi} \\ \dot{\beta}_{cog} \end{bmatrix} = \begin{bmatrix} \frac{L_1C_f+L_2C_r}{I_z} & \frac{L_2C_r-L_1C_f}{I_z} \\ -1+\frac{L_2C_r-L_1C_f}{m_v v_x^2} & -\frac{C_f+C_r}{m_v v_x} \end{bmatrix} \begin{bmatrix} \dot{\psi} \\ \beta_{cog} \end{bmatrix} + \begin{bmatrix} \frac{L_1C_f}{I_z} \\ \frac{C_f}{m_v v_x} \end{bmatrix} \delta + cov(noise) \tag{4.2}$$

where β_{cog} is the sideslip angle at center of gravity, C_f, C_r are cornering stiffness of front tires and rear tires.

In open-loop method, to simplify the computation, we assume $\dot{\beta}_{cog} = 0$. Then we can get the sideslip angle at steady state, expressed by

$$\beta_{cog} = \frac{L_2C_r - L_1C_f - m_v v_x^2}{v_x(C_f + C_r)}\dot{\psi} + \frac{C_f}{C_f + C_r}\delta \tag{4.3}$$

The sideslip angle can also be obtained through steering geometry, expressed by

$$\beta_{cog} = \frac{L_2}{L_1 + L_2}\delta + \alpha_r \tag{4.4}$$

where α_r is the average tire slip angle at rear axle.

In our experimental car, the optic sensor is installed at the middle of the rear axle to directly measure the average tire slip angle at rear axle. Then the measured sideslip angle at center of gravity $\beta_{cog,m}$ is obtained by

$$\beta_{cog,m} = \frac{L_2\dot{\psi}}{v_x} + \beta_{r,m} \tag{4.5}$$

where $\beta_{r,m}$ is the tire slip angle measured by the optic sensor.

The models for estimation of vehicle sideslip angle are summarized in table 4.4. In order to better present the performance of each model, we conducted two different tests. The first test is the steady turning test, where the vehicle is turning with a constant

steering angle (30°) and a low speed (10*km/s*). The second test is the slalom test at speed of 45*km/h*. The experimental result of open-loop estimation is illustrated in the

Table 4.4: Summary of Vehicle longitudinal dynamics models

Model symbol	Model name	Equation
$\beta_{cog,1}$	Integration model	$\beta_{cog,1} = \int (\frac{a_y}{v_x} - \dot{\psi})dt$
$\beta_{cog,2}$	Steady state model	More details in equation 4.3 $\beta_{cog,2} = \frac{L_2 C_r - L_1 C_f - m_v v_x^2}{v_x (C_f + C_r)} \dot{\psi} + \frac{C_f}{C_f + C_r} \delta$
$\beta_{cog,3}$	Kinematic model	More details in equation 2.80,2.81 $\beta_{cog,3} = \delta - \frac{L_1 \dot{\psi}}{v_x} + \frac{F_{yf}}{2C_f}$ $\beta_{cog,4} = \frac{L_2 \dot{\psi}}{v_x} + \frac{F_{yr}}{2C_r}$
$\beta_{cog,5}$	Steering geometry	More details in equation 4.4 $\beta_{cog,5} = \frac{L_2}{L}\delta + \frac{F_{yr}}{2C_r}$

Figure 4.18 and 4.19. By comparing the performance of each model in the two tests, we can find that each of these models has its own advantages. The model $\beta_{cog,2}$ and $\beta_{cog,5}$ are close to the measurement $\beta_{cog,m}$ in the test of steady turning. These models are more accurate at less dynamics situation. In Figure 4.19, the integration method has successfully followed the variation of the sideslip angle, but it has accumulated the model errors causing a large shift from the real value. The kinematic model $\beta_{cog,3}$ and $\beta_{cog,4}$ provided a better performance at the slalom test than at the steady turning test. The best strategy to estimate the sideslip angle is to combine all these models. In the subsequent section, we will present the observers we developed for the purpose of robust estimation at different driving condition.

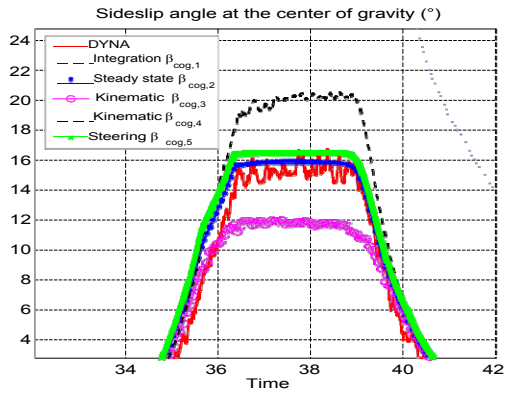

Figure 4.18: Open-loop estimation of sideslip angle during steady turning test

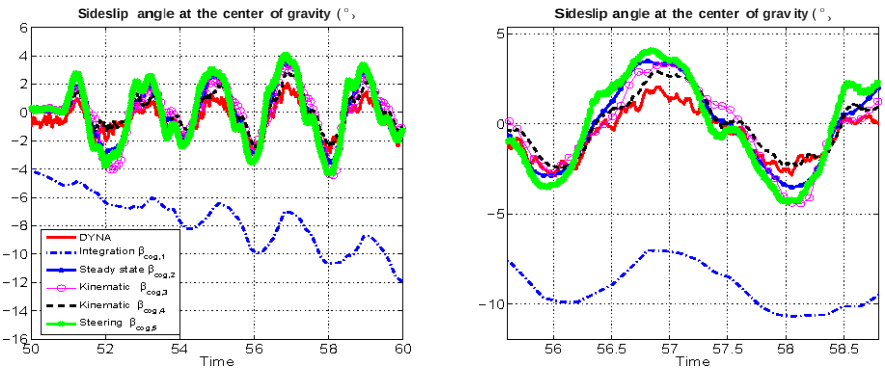

Figure 4.19: Open-loop estimation of sideslip angle during slalom test

4.4 Observer Design

This section presents a description of the observer devoted to tire forces (vertical, lateral and longitudinal forces) and sideslip angle. The need of observers is motivated by the fact that the open-loop estimation is greatly influenced by the sensor noises and model errors. In orcier to minimize the inevitable errors and providing the optimal estimation, observe r techniques are employed. Generally, the role of the observer is to provide a platform where the different models can be incorpor ated to provide the best estimation. In the observer, the estimation of different models are attributed with different weights. The more accurate the model is, the more weights the model will have. The observers we proposed are based on the algorithm of Kalman Filter. The classic Kalma n filter is already well develo ped and widely accepted by the researchers as an effective method to deal with the linear estimation problems. The gener al algorithm is expressed by equation 4.6. In orcier to adapt to the non-linear estimation problem, the EKF, UKF and PF are proposed in the literature. More details can be found in Chapte r 3.

$$
\begin{aligned}
&\textit{Prediction with models}: \\
&\dot{x}_{k+1|k} = A x_{k,k} + B u_{k+1} \\
&P_{k+1|k} = A P_{k|k} A^T + Q_{k+1|k} \\
&K_{k+1} = P_{k+1|k} H^T (H P_{k+1|k} H^T + R_{k+1|k})^{-1}
\end{aligned}
\tag{4.6}
$$

$$
\begin{aligned}
&\textit{Update with measurements}: x_{k+1|k+1} = \\
&x_{k+1|k} + K_{k+1}(z_{k+1} - H x_{k+1|k}) \; P_{k+1|k+1} = \\
&(I - K_{k+1} H) P_{k+1|k}
\end{aligned}
$$

The gener al theo ry of observer technique is already well develo ped in the literature. The observer theory can ens ure that the final estimation result is the mathematically optimal estimation based on the give n models. For a specifie estimation task, the performance of the observer is mainly decided by the quality of the models. In the previous chapte r,

we have already developed adequate models to describe the dynamics behaviors of vehicle's motion. The most challenging problem in this chapter is to design the structure of the observer in order to become robust and accurate in presence of unpredictable disturbances. The most simple but not the best method to construct an observer is to develop one single huge KF observer, which estimate all the unknown variables. That is to say, all the dynamics models will be substituted into one state space representation. This one single observer method has mainly two shortcomings:

1. the observer will probably encounter the problem of observability.
2. it is difficult to explain the estimation result when the estimation errors occur. The single observer works like a black box, difficult to find out which model is responsible for the errors.

4.4.1 Cascaded Kalman observers for estimation of vehicle dynamics states

Due to the reasons explained above, we propose to divide the entire estimation process into four blocks, as shown in Figure 4.20. Each of the four observers will concentrate at one estimation target. The first observer is an Kalman filter to estimate the vertical forces at each wheel. The estimation result of the first block will be regarded as a measurement in other blocks. The second observer is an non-linear filter to estimate the lateral forces at each tire. Both EKF, UKF and PF are employed to minimize the errors caused by the high non-linearity of tire's nature. The third observer is for the estimation of the longitudinal forces at each tire. The last observer is for the estimation of side slip angle. The strategy of using cascaded observers allows us to avoid the observability problems, as in each small observer we can ensure the observation matrix is full rank. Furthermore it can enable the estimation process to be carried out in a simple and practical way.

Observer for tire's vertical force O_{Fz}:

The state space representation of the vertical dynamics system is given by

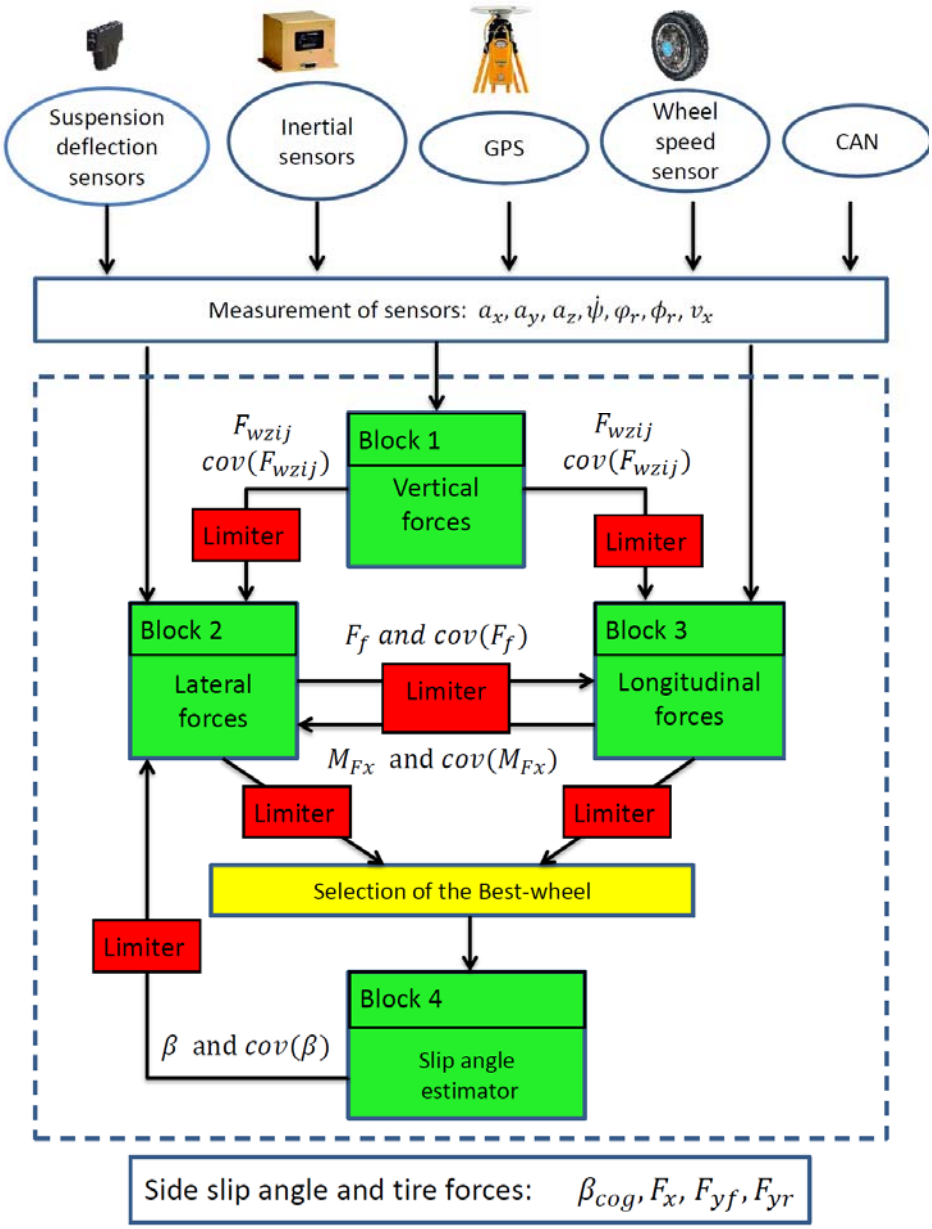

Figure 4.20: Overall algorithm of the estimation of vehicle dynamics states

$$\begin{bmatrix} \dot{F}_{z11} \\ \dot{F}_{z12} \\ \dot{F}_{z21} \\ \dot{F}_{z22} \end{bmatrix} = \frac{1}{\tau_1}\left(\begin{bmatrix} F_{z11,model2} \\ F_{z12,model2} \\ F_{z21,model2} \\ F_{z22,model2} \end{bmatrix} - \begin{bmatrix} F_{z11} \\ F_{z12} \\ F_{z21} \\ F_{z22} \end{bmatrix} \right) + w_{Fz}$$

$$\begin{bmatrix} ma_z \\ F_{z11,model4} \\ F_{z12,model4} \\ F_{z21,model4} \\ F_{z22,model4} \end{bmatrix} = \begin{bmatrix} 1 & 1 & 1 & 1 \\ 1 & 0 & 0 & 0 \\ 0 & 1 & 0 & 0 \\ 0 & 0 & 1 & 0 \\ 0 & 0 & 0 & 1 \end{bmatrix} \begin{bmatrix} F_{zw11} \\ F_{zw12} \\ F_{zw21} \\ F_{zw22} \end{bmatrix} + v_{Fz} \tag{4.7}$$

where $F_{zwij,model2}$ is obtained by equation 2.60, $F_{zwij,model4}$ is obtained by equation 2.69. τ_1 is the time coefficient that the suspension need to develop the vertical force. The accelerations and pitch-roll angle are regarded as available measurement, the parameters of vehicle are supposed to be constants. w_{Fz} is the errors of time update model, v_{Fz} is the error of observation model. We assume that the errors follow the Gaussian distribution: $w_{Fz} \sim N(0,\ Q_1)$, $v_{Fz} \sim N(0,\ R_1)$.

Observer for tire's lateral force O_{Fy}

Due to the non-linearity of tire's nature, the lateral dynamics system cannot be represented with the state space representation. We employed the EKF algorithm to adapt to the non-linear system. However, the linearization process in EKF will introduce additional errors. In order to improve the estimation of non-linear system, the UKF is also employed in this thesis. The detailed algorithm of UKF is introduced in Section 3.3.3. The time update models and observation models for the proposed EKF and UKF observers are identical, represented by the following equation

$$\begin{bmatrix} \dot{F}_{yw11} \\ \dot{F}_{yw12} \\ \dot{F}_{yw21} \\ \dot{F}_{yw22} \\ \dot{\beta}_{cog} \end{bmatrix} = \frac{1}{\tau_2} \begin{bmatrix} f_{Tire,y}(\alpha_{11},\ F_{wz11}) - F_{yw11} \\ f_{Tire,y}(\alpha_{12},\ F_{wz12}) - F_{yw12} \\ f_{Tire,y}(\alpha_{21},\ F_{wz21}) - F_{yw21} \\ f_{Tire,y}(\alpha_{22},\ F_{wz22}) - F_{yw22} \\ 0 \end{bmatrix} + w_{Fy}$$

$$\begin{bmatrix} ma_x - F_{xf}\cos\delta \\ ma_y - F_{xf}\sin\delta \\ I_z\ddot{\psi} - M_{Fx} - L_1\sin\delta F_{xf} \\ T_{Fy,f} \\ T_{Fy,r} \\ \beta_{est} \end{bmatrix} = \begin{bmatrix} -\sin\delta & -\sin\delta & 0 & 0 & 0 \\ \cos\delta & \cos\delta & 0 & 0 & 0 \\ L_1\cos\delta & L_1\cos\delta & -L_2 & -L_2 & 0 \\ 1 & -1 & 0 & 0 & 0 \\ 0 & 0 & 1 & -1 & 0 \\ 0 & 0 & 0 & 0 & 1 \end{bmatrix} \begin{bmatrix} F_{yw11} \\ F_{yw12} \\ F_{yw21} \\ F_{yw22} \\ \beta_{cog} \end{bmatrix} + u_{Fy}$$

(4.8)

where τ_2 is the time coefficient that the tire need to develop the lateral force. $f_{Tire,y}(\alpha, F_{wz})$ is the static lateral tire forces calculated by Dugoff model. The detailed expression of Dugoff's model can be found in Section 2.2. $T_{Fy,f}$ and $T_{Fy,r}$ are the transfer of lateral force at front axle and rear axle respectively. They are obtained by the models originally proposed in the thesis, expressed by equation 2.86. $\ddot{\psi}$ is the change rate of yaw speed. M_{Fx} is the moment caused by the longitudinal tire forces, defined as $M_{Fx} = \frac{E}{2}(F_{x12} + F_{x22} - F_{x11} - F_{x11})$. M_{Fx} is provided by the observer of longitudinal dynamics O_{Fx}. β_{est} is the sideslip angle provided by the observer of sideslip angle O_β. w_{Fy} and v_{Fy} are the model errors and measurement errors respectively. We assume that the errors follow the Gaussian distribution: $w_{Fy} \sim N(0, Q_2)$, $v_{Fy} \sim N(0, R_2)$.

Observer for tire's longitudinal force O_{Fx}

In this thesis, the longitudinal tire force is not obtained by the function of tire slip ratio. Instead, the force at each tire is computed with the transfer of longitudinal forces $T_{Fx,f}$, $T_{Fx,r}$, as explained in section 4.3.3. In order to develop a Kalman filter, the longitudinal dynamics models are transferred into the state space representation form, expressed by

$$\begin{bmatrix} \dot{F}_{xw11} \\ \dot{F}_{xw12} \\ \dot{F}_{xw21} \\ \dot{F}_{xw22} \\ \dot{M}_{Fx} \end{bmatrix} = \begin{bmatrix} 0 & 0 & 0 & 0 & 0 \\ 0 & 0 & 0 & 0 & 0 \\ 0 & 0 & 0 & 0 & 0 \\ 0 & 0 & 0 & 0 & 0 \\ 0 & 0 & 0 & 0 & 0 \end{bmatrix} \begin{bmatrix} F_{xw11} \\ F_{xw12} \\ F_{xw21} \\ F_{xw22} \\ M_{Fx} \end{bmatrix} + w_{Fx}$$

$$\begin{bmatrix} \frac{(ma_x + F_{yf}\sin\delta)}{\cos\delta} \\ F_{xr} \\ T_{Fx,f} \\ T_{Fx,r} \\ 0 \end{bmatrix} = \begin{bmatrix} 1 & 1 & 1 & 1 & 0 \\ 0 & 0 & 1 & 1 & 0 \\ 1 & -1 & 0 & 0 & 0 \\ 0 & 0 & 1 & -1 & 0 \\ \frac{E}{2} & -\frac{E}{2} & \frac{E}{2} & -\frac{E}{2} & 1 \end{bmatrix} \begin{bmatrix} F_{xw11} \\ F_{xw12} \\ F_{xw21} \\ F_{xw22} \\ M_{Fx} \end{bmatrix} + v_{Fx} \tag{4.9}$$

where F_{yf} is the resultant lateral force at front axle, which is provided by the former observer O_{Fy}. F_{xr} is the resultant longitudinal force at rear axle. For a front drive car, F_{xr} is regarded as a constant value when it is not braking. We also assume that the model errors follow the Gaussian distribution: $w_{Fx} \sim N(0, Q_3)$, $v_{Fx} \sim N(0, R_3)$.

Observer for vehicle's sideslip angle O_β

As presented in the section of open-loop estimation, section 4.3.4, the sideslip angle at center of gravity can be obtained by five different equations. The integration model is used as the time update model. The other models are used as the observation model. Then the state space representation of the sideslip angle is given by

$$\begin{bmatrix} \ddot{\beta}_{cog} \\ \dot{\beta}_{cog} \\ \dot{v}_y \end{bmatrix} = \begin{bmatrix} 0 & 0 & 0 \\ 0 & -\frac{C_f+C_r}{m_v v_x} & 0 \\ 0 & 0 & 0 \end{bmatrix} \begin{bmatrix} \dot{\beta}_{cog} \\ \beta_{cog} \\ v_y \end{bmatrix} + \begin{bmatrix} 0 \\ \frac{C_f+C_r}{m_v v_x} \\ 0 \end{bmatrix} \beta_{cog,2} + w_\beta$$

$$\begin{bmatrix} \beta_{cog,3} \\ \beta_{cog,4} \\ \beta_{cog,5} \\ a_y - g\sin\phi_r \\ v_x - \dot{\psi} \\ 0 \end{bmatrix} = \begin{bmatrix} 0 & 1 & 0 \\ 0 & 1 & 0 \\ 0 & 1 & 0 \\ 1 & 0 & 0 \\ 0 & v_x & -1 \end{bmatrix} \begin{bmatrix} \dot{\beta}_{cog} \\ \beta_{cog} \\ v_y \end{bmatrix} + v_\beta \tag{4.10}$$

where ω_β, v_β are the noises of the models and measurements and follow the Gaussian distribution $w_\beta \sim N(0, Q_4)$, $v_\beta \sim N(0, R_4)$. The $\beta_{cog,2}$-$\beta_{cog,5}$ are introduced in Table 4.4. Note that the needed lateral forces are provided by the former observer O_{Fy}.

4.4.2 Filter settings

The setting of Kalman filter parameters can greatly influence the observer's performance. The covariance matrix can be viewed as the representation of the model's uncertainty. By setting the covariance as a small value, we actually attribute more weights to the corresponding models. Generally, the estimation process based on Kalman filter can be expressed as

$$X_{est} = \frac{R}{R+Q} X_{pred} + \frac{Q}{R+Q} X_{meas} \tag{4.11}$$

where X_{pred} is the prediction of state according to the process model with covariance Q. X_{meas} is the measurement of the state with variance R. The Kalman gain is a subtle mix between process and observation noises covariance.

From the above equation, it is clear that the final estimation result is not only dependent on the quality of the models but also dependent on the value of $Q_{1\cdots4}$ and $R_{1\cdots4}$, which are the process noise covariance matrix and the observation noise covariance matrix. The basic strategy of setting the value of $Q_{1\cdots4}$ and $R_{1\cdots4}$ is to correspond to the uncertainty of the model. The situation we have to avoid is that the wrong measurement is attributed with a small covariance. In the literature, in order to reduce the complexity of the problem, $Q_{1\cdots4}$ and $R_{1\cdots4}$ are usually regarded as constant values and configured according to the average uncertainty. In real experiments, due to the variation of road condition, tire property and other unpredictable factors, the covariance of the model noises may vary along the journey. Therefore, to improve the accuracy of the estimation, we propose to change the covariance Q and R according to the vehicle driving condition. Note that we consider $Q_{1\cdots4}$ and $R_{1\cdots4}$ as diagonal matrix.

For observer O_{Fz}:

The model $F_{z,model4}$ is accurate when the transfer of load is obvious, therefore, when $|a_y| > 2m/s^2$, R_1 will be set as small. The model $F_{z,model2}$ is accurate when the vehicle is static. Then we configure Q_1 with a small value when $v_x < 1m/s$.

For observer O_{Fy}:

The tire model is more accurate when the vertical load is significant. The proposed models ($T_{Fy,f}$, $T_{Fy,r}$), are less accurate when the yaw speed change abruptly. Therefore, the values of Q_2 and R_2 are configured with the following equation.

$$\begin{aligned} Q_2 &= 100000diag([f_1(F_{z11}), f_1(F_{z12}), f_1(F_{z21}), f_1(F_{z22}), 10^{-7}]) \\ R_2 &= 100000diag([10, 1, 1, f_2(\ddot{\psi}), f_2(\ddot{\psi}), 10^{-8}]) \end{aligned} \tag{4.12}$$

where

$$f_1(F_z) = \begin{cases} 1 & if\ F_z > 5000N \\ 100 & if\ F_z < 5000N \end{cases} \quad f_2(\ddot{\psi}) = \begin{cases} 1 & if\ \ddot{\psi} < 1rad/s^2 \\ 100 & if\ \ddot{\psi} > 1rad/s^2 \end{cases} \tag{4.13}$$

For observer O_{Fx}:

The model of $T_{Fx,f}$ is less accurate when the vehicle is accelerating. It is because the front wheels are the drive wheels. During accelerating, the drive wheel's force is mainly controlled by engine. Thus $R_3(3, 3)$ is relatively big when $a_x > 1m/s^2$.

For observer O_β:

The model $\beta_{cog,2}$ is used to describe the static steering dynamics and thus is accurate when $\ddot{\psi}$ is small. $\beta_{cog,5}$ is more accurate while the vehicle is moving slowly. To the contrary, the model $\beta_{cog,3}$ and $\beta_{cog,4}$ are more accurate when the speed is high. We also designed the best-wheel selection algorithm to select the wheel with the least tire slip and high tire load. When the rear tires are skidding, the vehicle is over-turning $|\delta| - \frac{L\dot{\psi}}{v_x} < 0$. When the front tires are skidding, the vehicle is under-turning $|\delta| - \frac{L\dot{\psi}}{v_x} > 0$. With this criterion, we can choose the best wheel to calculate the sideslip angle. The value of the Q_4 and R_4 are configured with equation 4.14.

$$\begin{aligned} Q_4 &= diag([1, f_3(\ddot{\psi}), 1]) \\ R_4 &= diag([4f_4(v_x), f_4(v_x), 1 - f_4(v_x), 1, 1]) \end{aligned} \tag{4.14}$$

where

$$f_3(\ddot{\psi}) = \begin{cases} 0.01 & if\ \ddot{\psi} < 0.5rad/s^2 \\ 1 & if\ \ddot{\psi} > 1rad/s^2 \end{cases} \quad f_4(v_x) = \begin{cases} 0.1 & if\ |v_x| < 5m/s \\ 0.01 & if\ |v_x| > 5m/s \end{cases} \tag{4.15}$$

4.4.3 Communication between the four observers

Our strategy of estimation is to divide the whole estimation into four observers, and clearly define the *"responsibility"* of each observer. For instance, O_{Fz} is developed for vertical force, O_{Fy} is developed for lateral force. In each observer, only the targeting states are regarded as the internal variables, all other parameters or variables are regarded as external information. In this way, we can reduce the complexity of modeling. Meanwhile, the four observers are not completely independent. The estimation results of each observer are communicated to other observers to enhance the accuracy of the final estimation. In this way, the interaction between tire forces in different directions could be taken into account. Nevertheless, the communication between observers could possibly transmit the fatal estimation errors from one observer to another. In order to solve this problem, the algorithm of selective communication is designed.

Selective Communication by employing a limiter

According to the Kalman filter algorithm, the estimation result of an observer could be represented by a Gaussian distribution $X_{k+1} \sim N(\hat{X}_{k+1|k+1}, P_{k+1|k+1})$. If this estimation result is correct, we use the estimation result $\hat{X}_{k+1|k+1}$ as the measurement (z_{k+1}) in another observer , the covariance of z_{k+1} could be set as $P_{k+1|k+1}$ (to emphasize the uncertainty of z_{k+1}, we set the covariance as $2P_{k+1|k+1}$). However, the estimation could be wrong, which means the $N(\hat{X}_{k+1|k+1}, P_{k+1|k+1})$ cannot represent the real distribution of X_{k+1}. In this situation, if we continue to use the $\hat{X}_{k+1|k+1}$ as the measurement in other observers, the wrong estimation will cause the malfunction of the latter observer. To avoid this from happening, we designed a limiter to diagnose whether the former observer has fatal errors. A fatal error is detected, if the following criterion is satisfied.

$$\left\| \hat{X}_{k+1|k+1} - \hat{X}_{k|k} \right\| > \varepsilon \tag{4.16}$$

where ε is the threshold value of the variation of the state.

When the fatal error is detected, the limiter behaves as a switch, as illustrated in Figure 4.21. When it has detected the fatal errors from the former observer, the estimation result will not be accepted as measurement in the latter observer. Instead, a rough estimation with large covariance will be sent to the latter observer. In this way the fatal errors will be filtered out. The rough estimation is given by the equation 4.17.

$$\begin{aligned}
F_{z11} = F_{z12} &= mgL_2/(2L) \\
F_{z21} = F_{z22} &= mgL_1/(2L) \\
F_{x11} = F_{x12} &= m_v a_x/2 \\
F_{x21} = F_{x22} &= 0 \\
F_{y11} = F_{y12} &= m_v(a_y + L\ddot{\psi})L_2/(2L) \\
F_{y21} = F_{y22} &= m_v a_y L_1/(2L) \\
\beta_{cog} &= \delta L_2/L
\end{aligned} \tag{4.17}$$

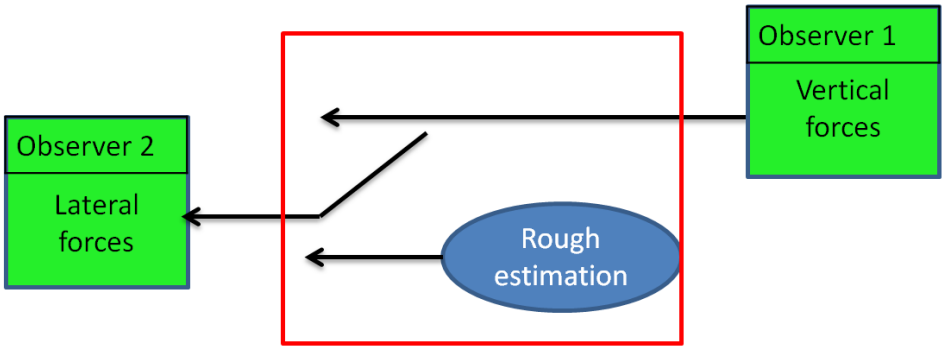

Figure 4.21: Selective communication between the four observers

With the selective communication mechanism, the four observers are connected but relatively independent. The whole estimation system will not collapse even one observer is completely failed. The advantages of our proposed observers will be discussed in the analysis of experimental validation tests.

4.4.4 Particle filter based observer

Among the four observers we proposed in the previous section, only the observer for lateral tire forces O_{Fy} is highly non linear. As explained above, the EKF can introduce errors of linearization when dealing with high nonlinear system. For this reason we proposed to use the Unscented Kalman Filter to construct the observer for lateral tire force, O_{FyUKF}. The UKF supposes the model noises follow a Gaussian distributions. In order to generalize our observer to a larger extend, we propose to use the Particle filter (PF) to process the nonlinear vehicle dynamics model, noted as O_{FyPF}. The Particle filter provides a direct approximation of the posterior distribution with the weighted sample points. It doesn't assume the white errors. The detailed algorithm of Particle Filter was introduced in Section 3.3.4. The models we employed to develop the PF observer are the same as the models used for Unscented Kalman Filter, expressed by equation 4.8. The particle number is set as 50.

4.5 Experimental Validation Of The Observers

In this section, we will focus on the experimental validation of the above-mentioned observers. The input measurements of our observers are obtained from CAN bus, accelerometer, gyrometer and laser distance sensors. The force transducers and Correvit are used as ground truth. The complete description of the function of sensors and the entire architecture of the acquisition system is introduced in section 4.2.In order to bet-

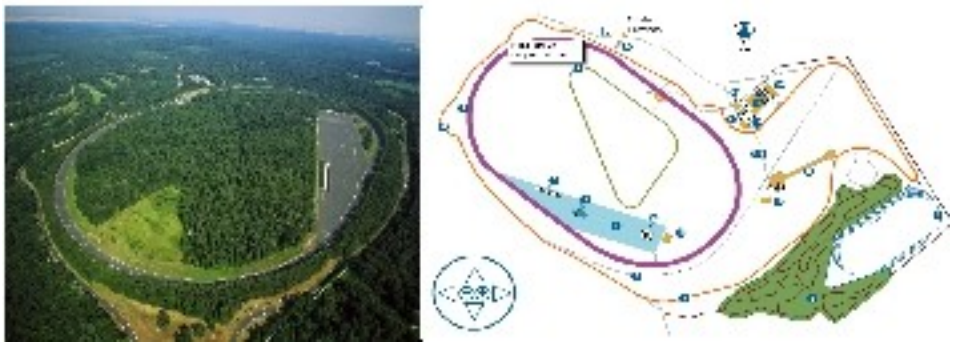

Figue 4.22: The traj..,t,cny of rood circuit an plén

ter pr"'ent the penœmél1Ce of our oœer,.,rs in different oanditions, we wwld like to perlœm seven tests with different rœd oanditians Md different speeds. The se"'n tests include:

1. intense slélom test at. SO krnfh at. le,.,gl'Ollnd;
2. rnoderat.e sWan ta.t at. 30 krn/h at. leve! grwnd;
3. stélldéld chicone ta.! at. 20 krn/h at. leve! grwnd;
4. stélldéld chicone ta.! at. 100 krn/h at. leve! gl'Ollnd;
5. circling test at. 40 krn/h at. leve! gl'Ollnd;
6. slélorn t"'t at. 40 krn/h at. slippery rœd;
7. slélorn t"'t at. 140 krn/h at. bênked rood.

Ali th"'e tests oze perbrned with our experirnent "'hicle DYNA an the Mortefantéine Au<>mobile 'll!sting élld R.Eseozch Centre (CER.AM - Centre d'E'.sséis et de Recherche Autanobile de Mortefœtoine), es sho.vn in Figure 4.22. ln eoch test, we will pr"'ent the "'tirnat.ion ra.ults of "'rticêl tire boa., tudinél tire forces, s&lip onde ond thelat.erél tire boa.. The a.tirnatiœ r"'ults of the proposed new oŒervers ozend.ed *os* *OFx,N.OF>;f<* · *O* , · For thelat.erél boa.,we developed three different nœ-lin= observers by ernp]cying EKF, UKF értd PF élg:nithrns, noted es *O KF. OJ!>:J,UKF. OF>,PF·* Th rnoke a,o::nnpel'io:m with the cbservers in the literai.ure, we élso developed observers besed an the canrnœùy used bicycle rnodels. 'Iheir estimation r"'ults .,,. noted *os* *OFx,OF>;O* . Fùrtherrnore, to dernanstrat.e the o:mtributiœ â this **thesis *at(:!t* thê pl'QYious wark in our lé.baré.tary, wa élso presant thE! estîmâtian results** of the observers developed in (Wong. 2013), noted és *OF9> OF,...., 0..... O—.*

4.5.1 Intense slalom test at 50 km/h at level ground

Firstly, an extreme intense slalom test was performed. The test track was well paved and set to be dry ($\mu = 1$). The maneuver time history is illustrated in Figure 4.23.

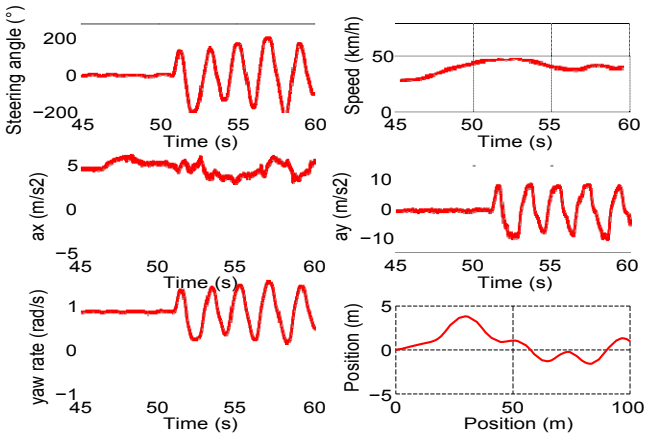

Figure 4.23: Maneuver time history of Test 1: Intense slalom test

During this test, the maximum lateral acceleration reached to $0.9g$, average speed of the slalom test was about $50km/h$. The steering wheel angle changed from 200° to -200° in one second, which could cause the extreme variation of the dynamics states. The slalom test is usually considered as a difficult maneuver from the estimation viewpoint, but it can better reveal the potential of the observer's performances.

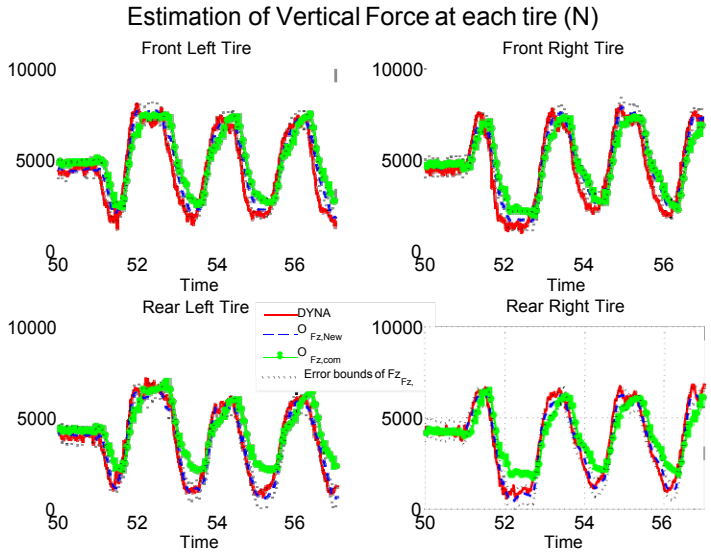

Figure 4.24: Test 1 (intense slalom test): Estimation of vertical force at each tire

Figure 4.24 demonstrates the estimation results of the vertical forces at each tire. The red lines correspond to the ground truth measured by the wheel transducer. Blue lines represent the results of the new observer that we proposed in section 4.4. The black dashed lines are used to illustrate the error bounds of the estimation. The value of the black dashed lines are equal to $Fz_{est} \pm \sqrt{P}$, where P is the covariance obtained by Kalman filter. Green lines are the results of the observers based on the commonly used model, corresponding to the $F_{z,model1}$ in the table 4.1. During the slalom maneuver, the vertical tire forces changed quickly, but our observer can follow tightly with the measurement. Almost all the red data can be included in the error bounds $[Fz_{est} - \sqrt{P},\ Fz_{est} + \sqrt{P}]$. The advantage of our proposed observer is obvious at the moment of each peak turning. In the Figure 4.24, we can see the blue line is close to the red line even at the peak points, while the green line is less accurate. It can be explained as the the pitch-roll motion based models are more sensitive to the variation of vertical force.

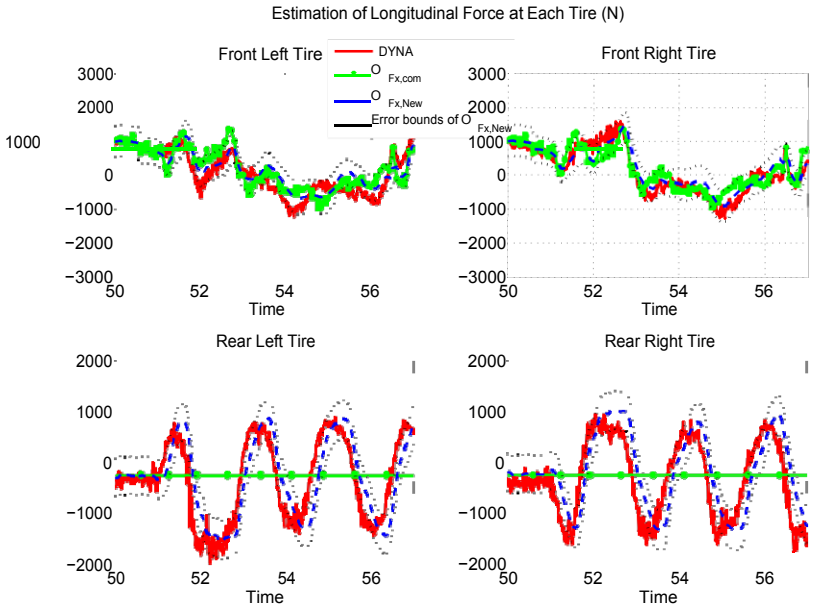

Figure 4.25: Test 1 (intense slalom test): Estimation of longitudinal force at each tire

Figure 4.25 demonstrates the estimation results of the longitudinal forces at each tire. The red lines correspond to the measurement of the wheel transducer. Blue lines represent the results of the new observer that we developed in section 4.4. The black dashed lines represent the error bounds of our observer. The Green lines are the results based on the bicycle model and the assumption that $F_{x11} = F_{x12}$, $F_{x21} = F_{x22}$. During the slalom test, the longitudinal force at front tires seems unrelated to the undulation of steering angle, while the longitudinal force at rear wheel appears a typical “slalom” characteristic. That could be explained by the fact that the experimental car is a front-

drive car. The front tire forces are mainly controlled by the engines. The rear tire forces are mainly affected by the turning behaviors, as explained in the section 2.4.3. The estimation provided by our new observer can tightly follow the variation of the longitudinal forces.

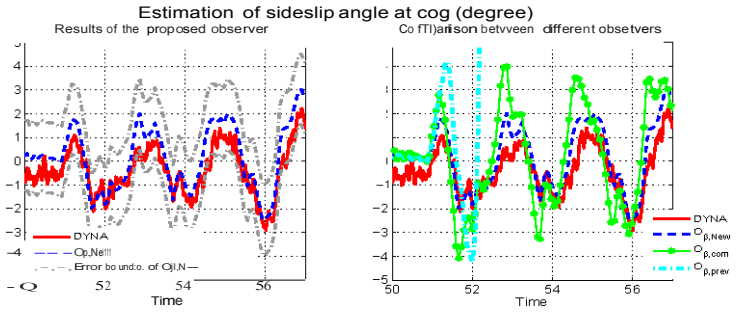

Figure 4.26: Test 1 (intense slalom test): left) Results and error bounds of the new observer for estimation of sideslip angle at CoG; right) Comparison of the estimation results of sideslip angle at CoG obtained by different observers

Figure 4.26 demonstrates the estimation result of the sideslip angle at center of gravity. The result of the proposed observer O_{13} and its error bounds are illustrated in the left side of Figure 4.26. The comparison between different observers is illustrated in the right side of Figure 4.26. Note that the reference data in this figure is not directly measured but obtained through the transformation presented in equation 4.5. The blue lines represent the results of the new observer O_{13}. The green lines are the results of the commonly used observer represented by equation 4.2, which is based on the linear tire model and bicycle model. The cyan lines are the results of EKF observers developed in the previous work of our laboratory [Wang, 2013], noted as $OF_{y,prev}$. There are three remarks about the previous observer $OF_{y,prev}$: (i), the Dugoff's non-linear tire model is employed to estimate the lateral tire force; (ii), the observer is based on the EKF algorithm; (iii), the sideslip angle, longitudinal tire force and the lateral tire force are estimated by one single observer. In this extreme intensive slalom test, the estimation result of $OF_{y,prev}$ was obviously wrong. The huge errors of $OF_{y,prev}$ in this test can be explained by the high non-linearity of Dugoff's tire model in presence of intensive transfer of verticalload. The linearization process in the EKF algorithm has caused significant errors and made the estimation of slideslip angle unstable.

In our new observer, the sideslip angle is estimated by five different models. The influence of the Dugoff's model is limited, as other models will correct the errors in every iteration. Furthermore, the estimation of lateral forces and sideslip angle are realized by two separate observers. The excessive errors will not be communicated to each other.

In orcier to validate our observer in a more convincing way, we transformed the es-

timated β_{3cog} into the sideslip angle at rear axle β_{3r} and compared with the direct measurement of CORREVIT, as illustrated in Figure 4.27. It is clear that our observer has accurately estimated the sideslip angle at rear axle.

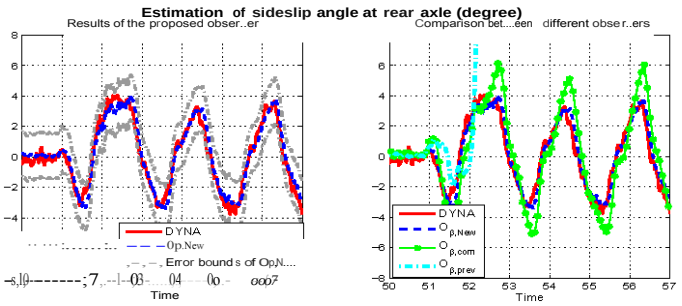

Figure 4.27: Test 1 (intense slalom test): left) Results and error bounds of the new observer for estimation of sideslip angle at rear axle; right) Comparison of the estimation results of sideslip angle at rear axle obtained by different observers

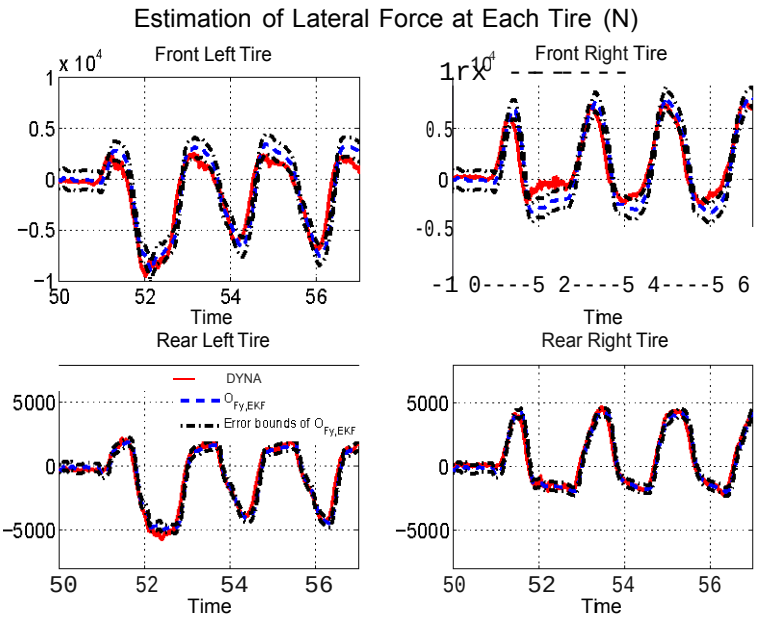

Figure 4.28: Test 1 (intense slalom test): Results and error bounds of the new observer for estimat ion of lateral forces at each tire

Figure 4.28 demonstrates the estimation results of the lateral forces at each tire with the new EKF observer, $O_{Fy,EKF}$. The red lines are the real data acquired by DYNA. The blue lines are the estimation result of the new EKF observer $O_{Fy,EKF}$. The black

lines are the error bounds. From Figure 4.28, we can find that the new observer showed higher accuracy at rear tires than at front tires. It is due to the model errors caused by intense slalom behavior. In this intense slalom test, the lateral forces at front tire are also greatly influenced by the steering torque, which is not considered in our model. Figure 4.29 illustrates the comparison between the results of different observers, including the previous EKF observer $O_{Fy,prev}$, the proposed new EKF observer $O_{Fy,UKF}$, the PF observer $O_{Fy,PF}$ and the UKF observer $O_{Fy,UKF}$.

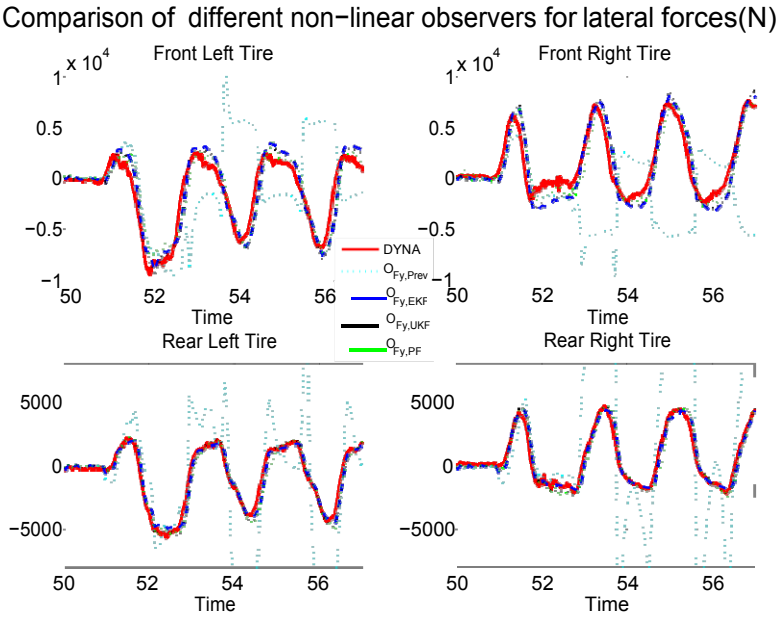

Figure 4.29: Test 1 (intense slalom test): Comparison of the estimation results of tire lateral forces obtained by different observers

The estimation of $O_{Fy,prev}$ is completely wrong in this test. The reason is already explained in the previous paragraph. During intense slalom test, the tire model is quite non-linear. The linear approximation in EKF observer brings fatal errors to the estimation. However, the EKF observer developed in this thesis provided good performance. It is mainly because that we employed the proposed model, the transfer of lateral forces T_{Fy}. With this new model, the estimation of tire force is not only dependent on the Dugoff's tire model. Furthermore, the cascaded structure makes the observer more robust. The UKF and PF observer have also provided good performance. UKF has an obviously advantage that it doesn't need the calculation of Jacobian matrix. Furthermore, the UKF is more efficient than the PF observer, as much fewer sample points are needed.

4.5.2 Moderate slalom test at 30 km/h at level ground

This test is designed to validate the performance of our observers at a slower slalom test. The test track was also level and dry ($\mu = 1$). The maneuver time history is illustrated in Figure 4.30. During this test, the maximum lateral acceleration was about $0.3g$, much smaller than the first slalom test, and therefore it is called a moderate slalom test. The average speed of the slalom test was about $30km/h$. The changing rate of the steering wheel angle is also smaller than the intense slalom test.

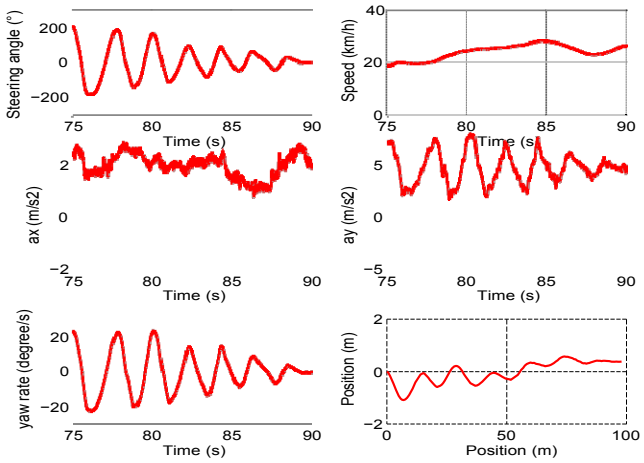

Figure 4.30: Maneuver time history of Test 2: Moderate slalom test

Figure 4.31 demonstrates the estimation result of the vertical forces at each tire. Similar to the test of intense slalom test, our proposed observer can tightly follow the variation of the vertical forces. At each peak points, the proposed observer provided a better estimation than the commonly used observer.

Figure 4.32 demonstrates the estimation result of the longitudinal forces at each tire. The measured data once again proved that during the turning the rear wheels would generate considerable longitudinal forces. Our observers (the blue lines) provided a good estimation of F_x at rear left and right tires. In the estimation result at front left and right tires, the green lines are approximately coinciding with the blue lines. This demonstrats that for the front drive cars, the value of $T_{Fx,f}$ is not significant during moderate driving operation.

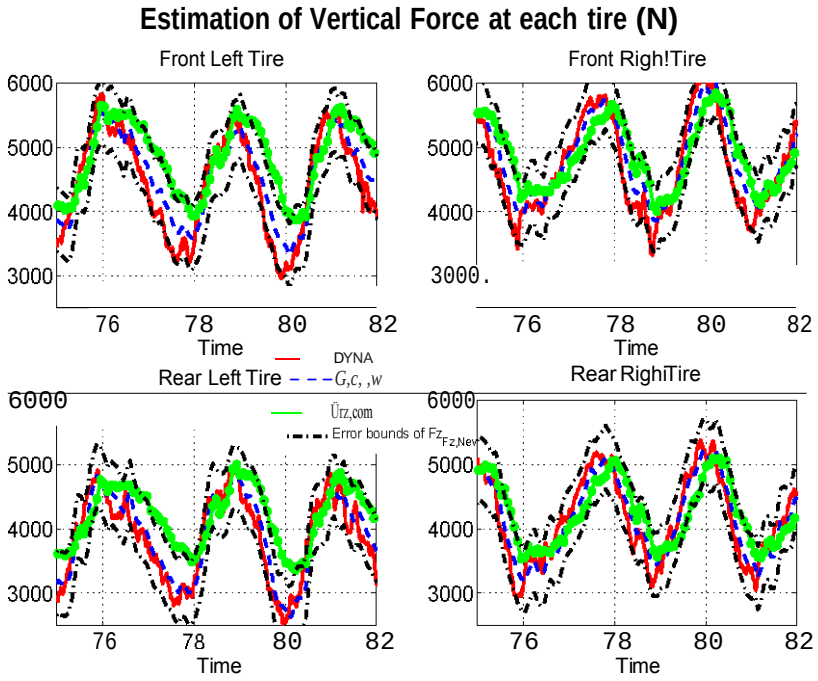

Figure 4.31: Test 2 (moderate slalom): estimation results of vertical force at each tire

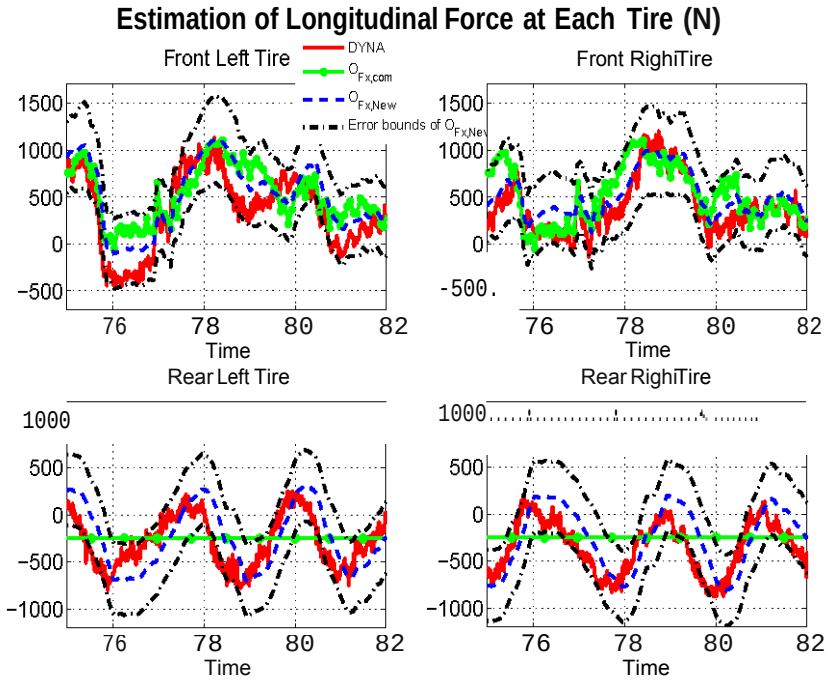

Figure 4.32: Test 2 (moderate slalom): estimation results of Fx at each tire

Figure 4.33 demonstrates the estimation result of the sideslip angle at center of gravity by different observers. The cyan lines are the estimation results of the observer $O_{Fy,prev}$. We remind that in the intense slalom test (Test 1), the results of observer $O_{Fy,prev}$ was totally wrong. However, in this moderate slalom test, the $O_{Fy,prev}$ could work normally. It is due to the transfer of vertical load in this test is small and the Dugoff's tire model is operating around the linear region. Furthermore, we can also find the green lines are close to the ground truth, which proves that during the moderate slalom test, the linear tire model can successfully describe the tire dynamics. Figure 4.34 demonstrates the estimation result of the sideslip angle at rear axle. Our observer provided a better performance than the observer $O_{Fy,prev}$.

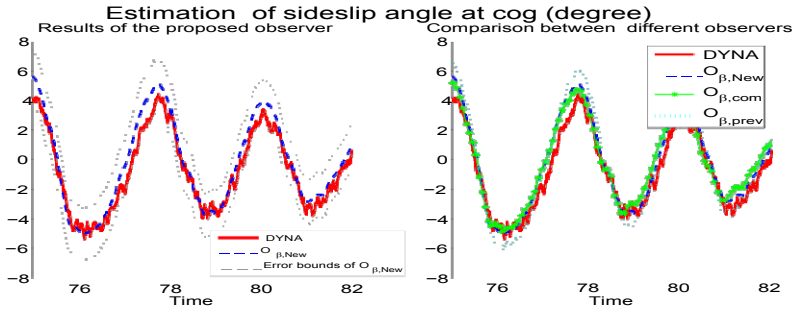

Figure 4.33: Test 2 (moderate slalom test): left) Results and error bounds of the new observer for estimation of sideslip angle at CoG; right) Comparison of the estimation results of sideslip angle at CoG obtained by different observers

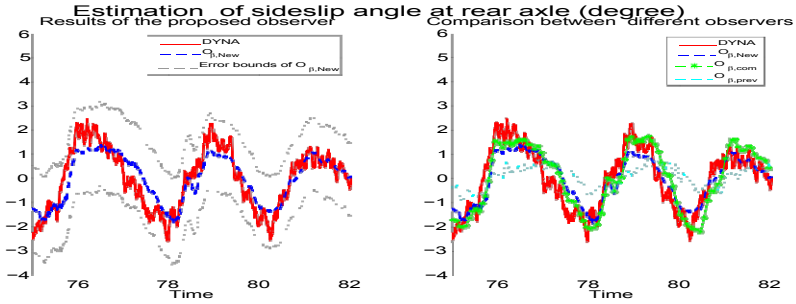

Figure 4.34: Test 2 (moderate slalom test): left) Results and error bounds of the new observer for estimation of sideslip angle at rear axle; right) Comparison of the estimation results of sideslip angle at rear axle obtained by different observers

Figure 4.35 demonstrates the estimation results of the lateral forces at each tire obtained by our new observer. Figure 4.36 compares the estimation results of different non-linear observers. The previously developed observer $O_{Fy,prev}$ provided good estimation of lateral tire force in this test. The new observer had a better performance, as

it combined different lateral force models (the new proposed model *TFy* and the classic double track model).

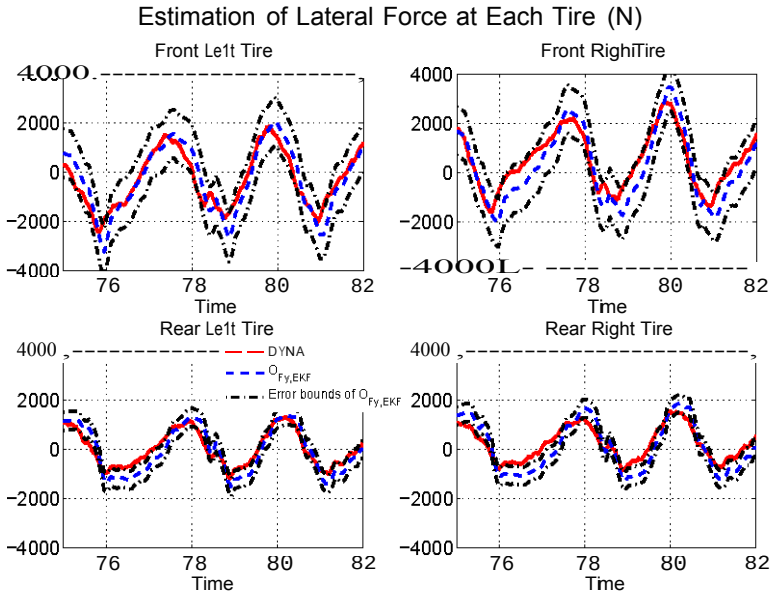

Figure 4.35: Test 2 (moderate slalom test): Results and error bounds of the new observer for estimation of lateral tire forces

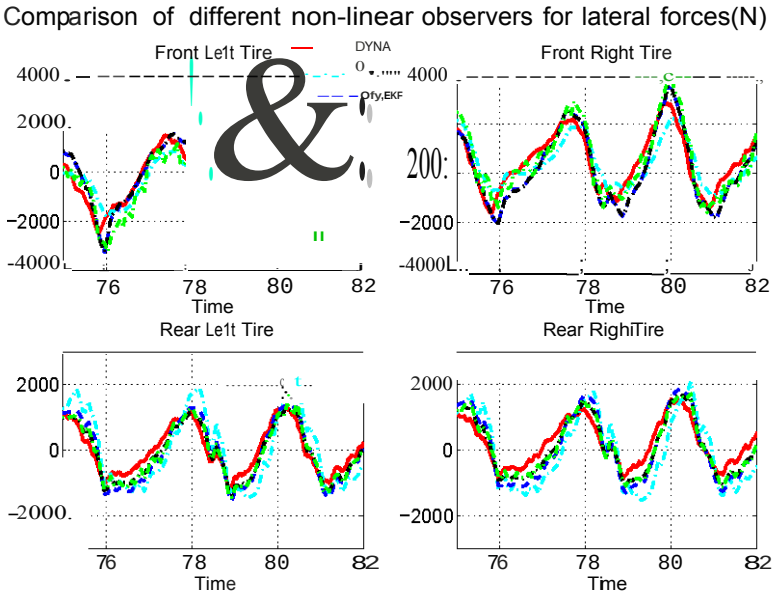

Figure 4.36: Test 2 (moderate slalom test): Comparison of different observers for the estimation of lateral tire forces

4.5.3 Chicane test at 20 km/h at level ground

This test is designed to validate the performance of our observers at a low-speed chicane test. The chicane test can be viewed as a standard lane changing behavior, which is a common driving behavior in the real life. The test track was also level and dry ($\mu = 1$). The maneuver time history is illustrated in Figure 4.37.

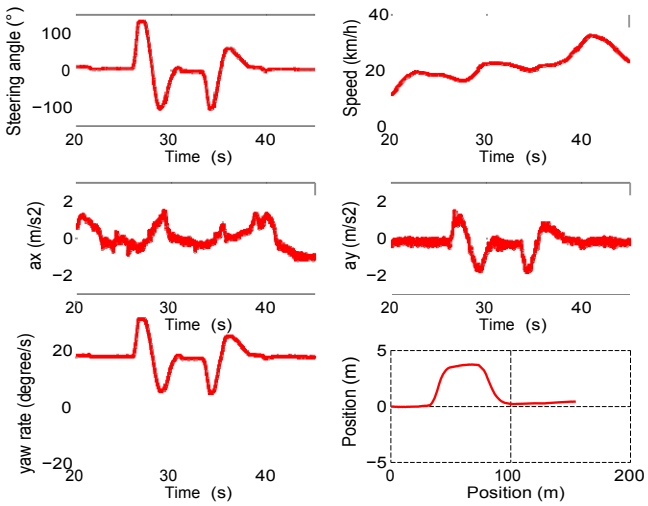

Figure 4.37: Maneuver time history of Test 3: Low-speed chicane test

The estimation result of the vertical forces and longitudinal forces at each tire are illustrated in Figure 4.38 and 4.39 respectively. The performance of the proposed observer was quite satisfactory. It is mainly due to the proposed models are accurate in slow chicane maneuver. The estimation results of sideslip angle at CoG and at rear axle are demonstrated in Figure 4.40 and 4.41. Then Figure 4.42 demonstrates the estimated lateral forces and error bounds at each tire with the proposed EKF observer. In Figure 4.43, we compared the estimation results of different non-linear observers. As we could see in Figure 4.38-4.43, generally all the different observers could provide good estimation close to the real data. In slow chicane test, the linear model and bicycle model are accurate enough to describe vehicle behavior. However, the advantage of our observer is obvious in Figure 4.41. The previous observer $O_{Fy,prev}$ (cyan dotted lines) had less accurate estimation of β_r. Our proposed observer could accurately estimate both the β_{cog} and β_r. The estimation result in this test demonstrated the importance of distinguishing β_{cog} and β_r. In normal driving condition (no excessive tire slip happens), the β_{cog} is mainly dominated by vehicle's steering angle ($\beta_{cog} \approx \frac{L_2}{L}\delta$). In order to estimate the tire slip state, the sideslip angle at rear axle, β_r, is more interesting for us.

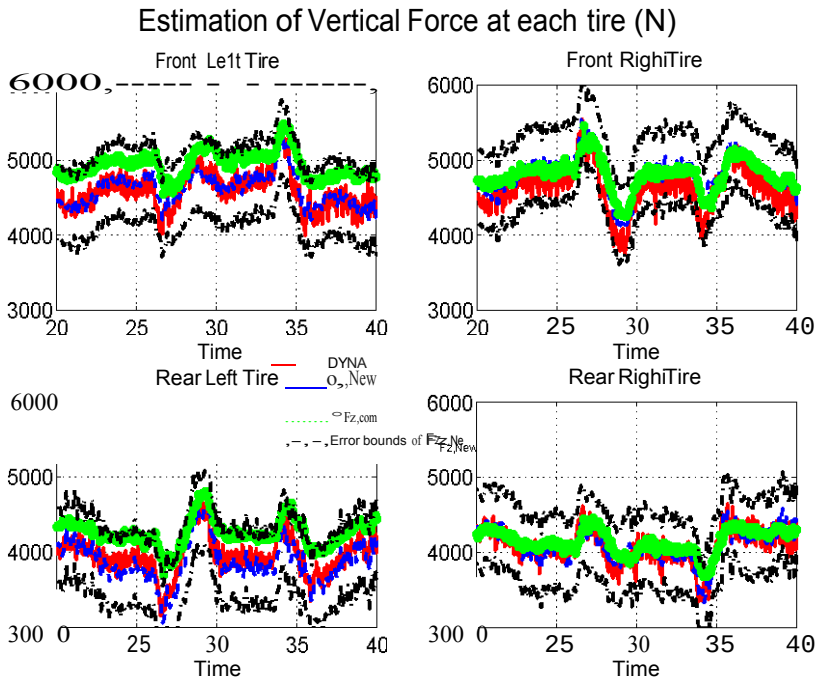

Figure 4.38: Test 3 (low speed chicane test): Comparison of the estimation results of vertical force at each tire

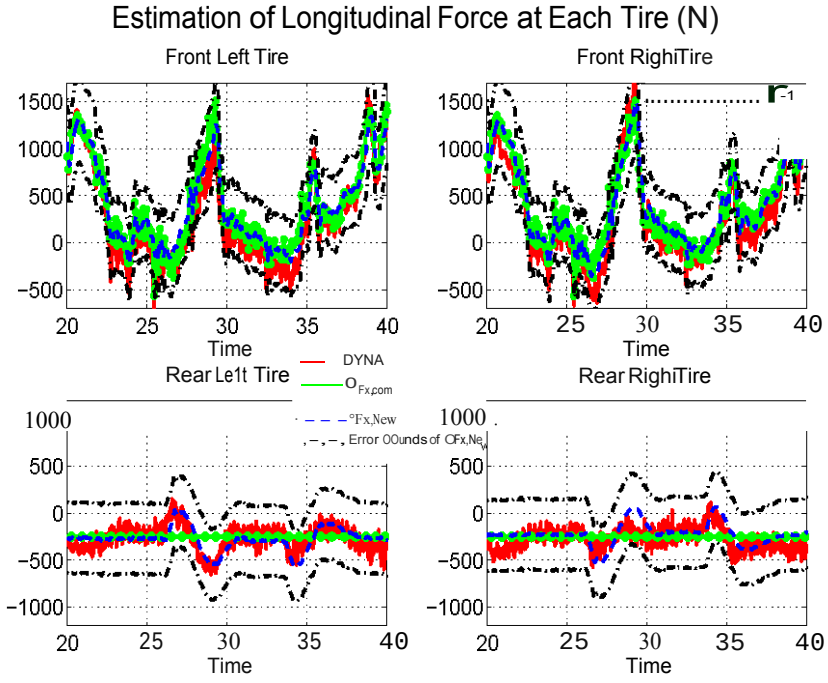

Figure 4.39: Test 3 (low speed chica ne test): Comparison of the estimation results of longitudinal force at each tire

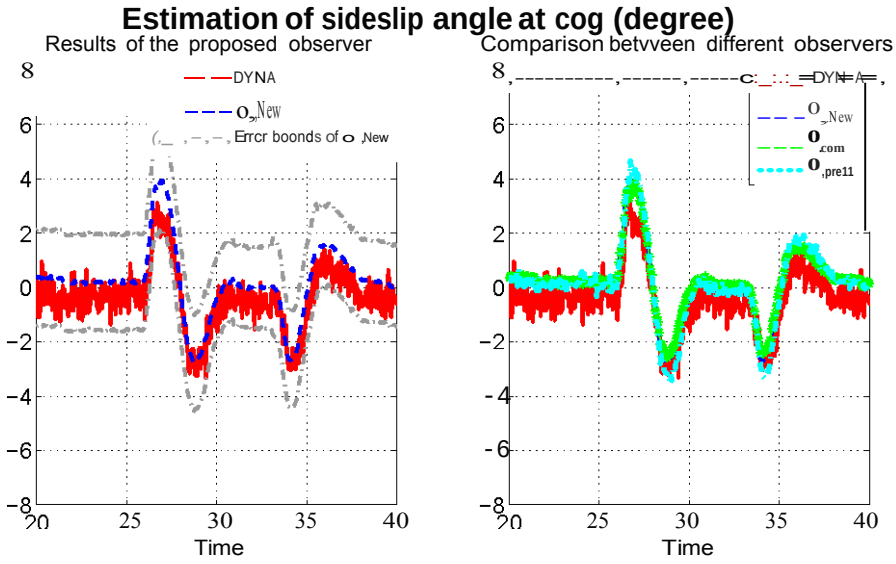

Figure 4.40: Test 3 (low speed chicane test): left) Results and error bounds of the new observer for estimation of sideslip angle at CoG; right) Comparison of the estimation results of sideslip angle at CoG obtained by different observers

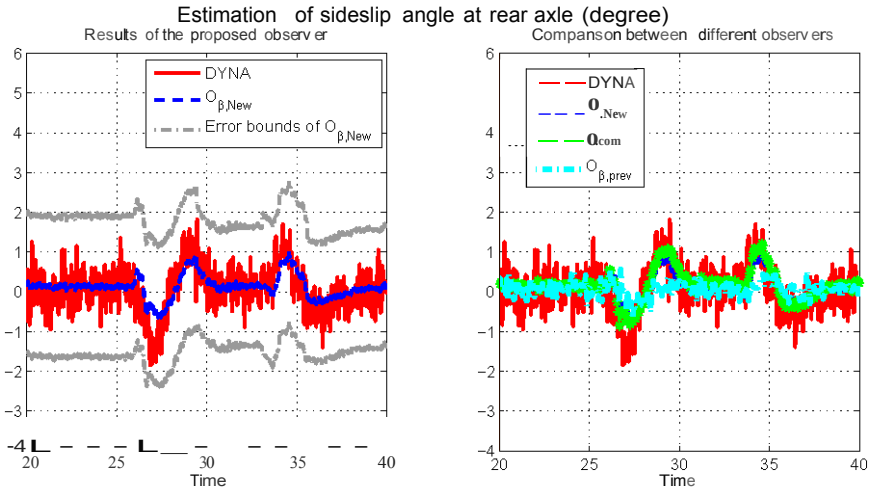

Figure 4.41: Test 3 (low speed chicane test): left) Results and error bounds of the new observer for estimation of sideslip angle at rear axle; right) Comparison of the estimation results of sideslip angle at rear axle obtained by different observers

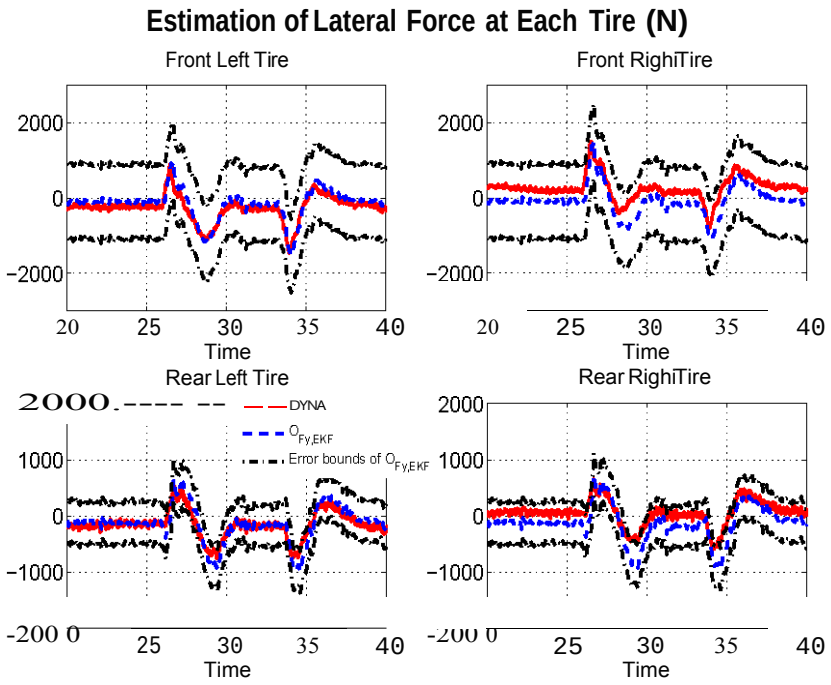

Figure 4.42: Test 3 (low-speed chicane test): Results and error bounds of the new observer for estimation of lateral forces at each tire

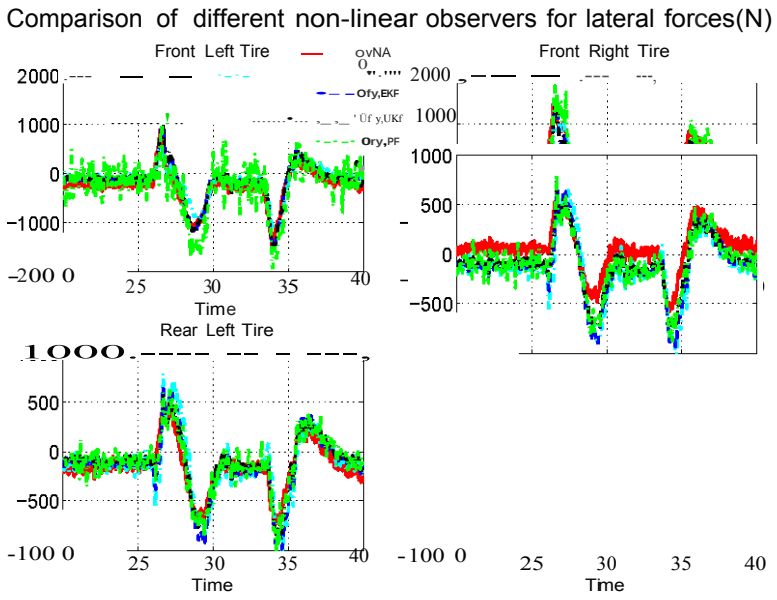

Figure 4.43: Test 3 (low-speed chicane test): Comparison of the estimation results of tire lateral forces obtained by different observers

4.5.4 Chicane test at 100 km/h at level ground

This test is designed to validate the performance of our observers at a high-speed chicane test. The maximum speed reached to 100 km/h. It can be viewed as a sudden lane-changing behavior, which could generate dangerous situation. The test track was also level and dry ($\mu = 1$). The maneuver time history is illustrated in Figure 4.44.

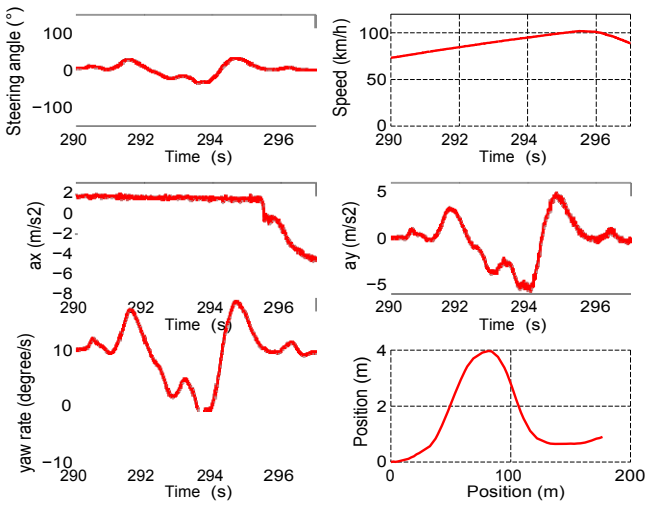

Figure 4.44: Maneuver time history of Test 4: High-speed chicane test

The estimation result of the vertical forces and longitudinal forces at each tire are illustrated in Figure 4.45 and 4.46 respectively. The experimental data has proved that our proposed models, T_{Fz}, T_{Fx} were accurate even in high speed chicane test. In Figure 4.46, the errors of estimation at the time period [295s, 297s] were caused by the braking behavior. In our model, we consider the rear wheels are rotating freely without brakes. The estimation results of sideslip angle at CoG and at rear axle are demonstrated in Figure 4.47 and 4.48. Compared with the previous observer $O_{Fy,prev}$, our new observer had much better performance in the estimation of β_{cog} and β_r. In Figure 4.47, the proposed observer was less accurate at peak points, which can be explained by that the sideslip angle in this test was too small ($-1° < \beta_{cog} < 1°$), many other un-modeled factors could dominate its value. Then Figure 4.49 demonstrates the estimated lateral forces and error bounds at each tire with the proposed EKF observer. In Figure 4.50, we compared the estimation results of different non-linear observers. The PF, EKF and UKF provided equally good performance.

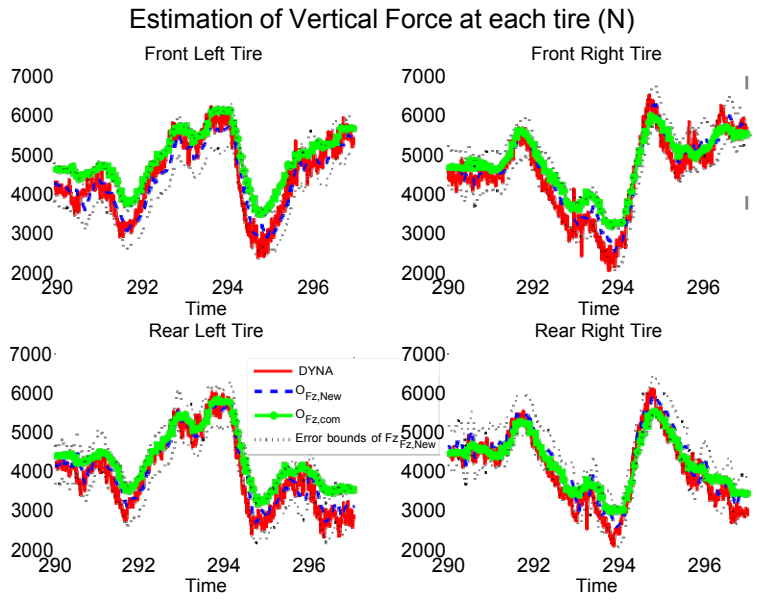

Figure 4.45: Test 4 (high speed chicane test): Comparison of the estimation results of vertical force at each tire

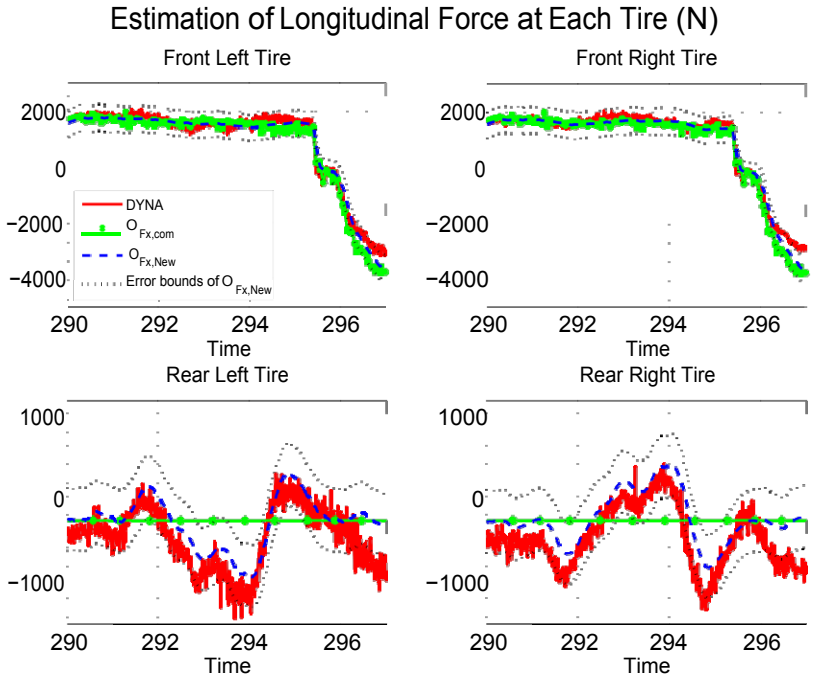

Figure 4.46: Test 4 (high speed chicane test): Comparison of the estimation results of longitudinal force at each tire

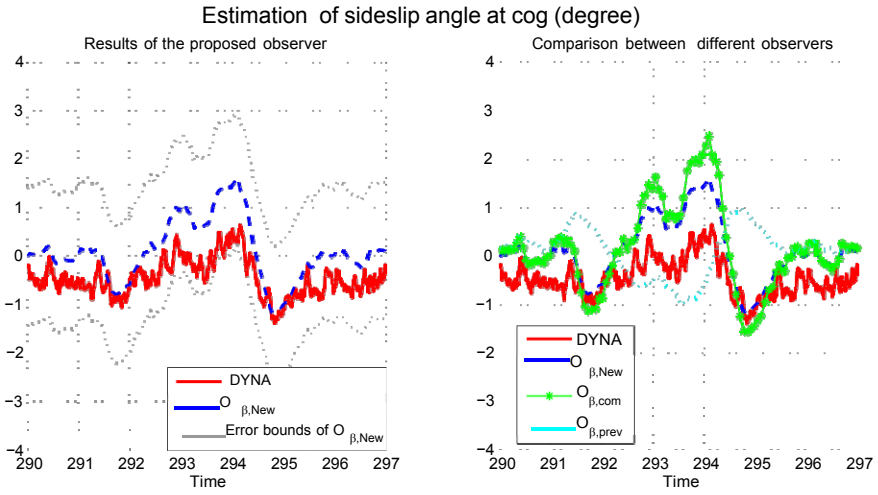

Figure 4.47: Test 4 (high speed chicane test): left) Results and error bounds of the new observer for estimation of sideslip angle at CoG; right) Comparison of the estimation results of sideslip angle at CoG obtained by different observers

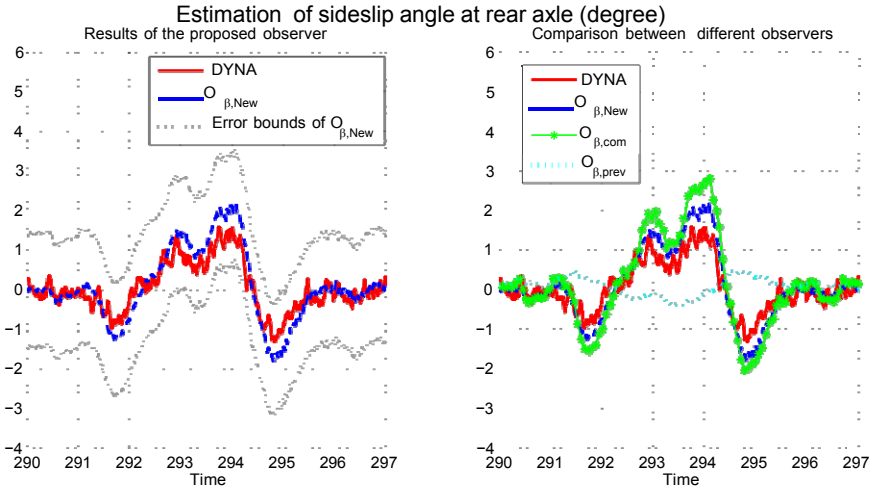

Figure 4.48: Test 4 (high speed chicane test): left) Results and error bounds of the new observer for estimation of sideslip angle at rear axle; right) Comparison of the estimation results of sideslip angle at rear axle obtained by different observers

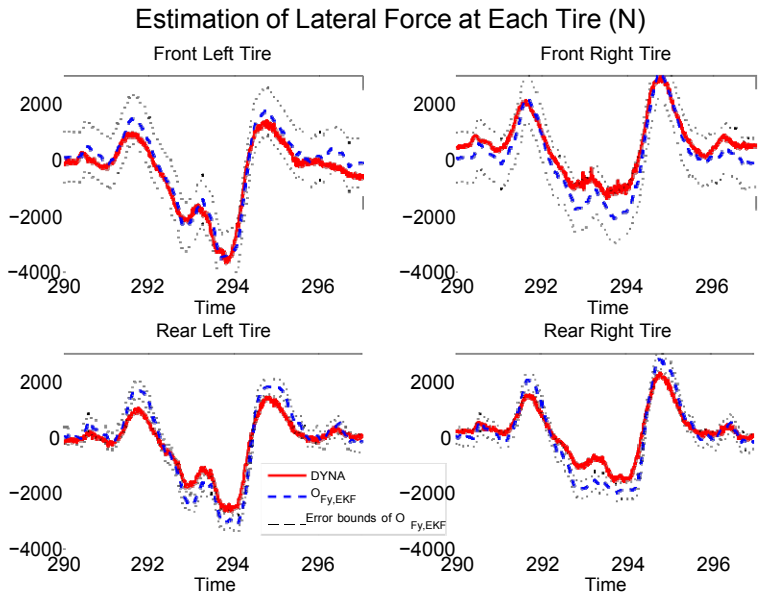

Figure 4.49: Test 4 (high speed chicane test): Results and error bounds of the new observer for estimation of lateral forces at each tire

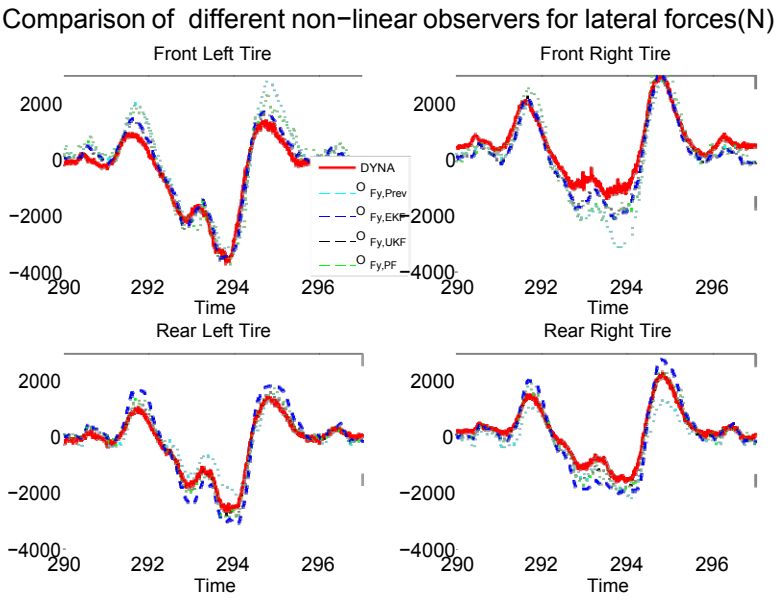

Figure 4.50: Test 4 (high-speed chicane test): Comparison of the estimation results of tire lateral forces obtained by different observers

4.5.5 Circling test at 40 km/h at level ground

This test is designed to validate the performance of our observers during circling behavior. The steering wheel angle was a constant value (around 50°) during the test. The maximum speed reached to 40 km/h. The test track was also level and dry ($\mu = 1$). The maneuver time history is illustrated in Figure 4.51.

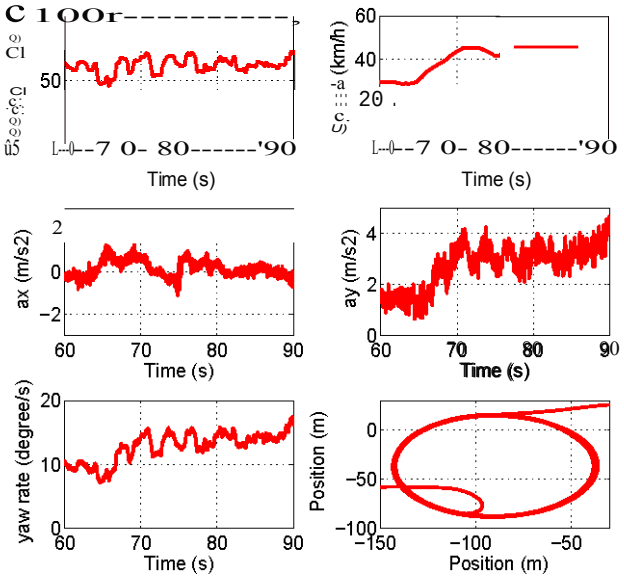

Figure 4.51: Maneuver time history of Test 5: Circling test

Figure 4.52 demonstrates the estimation result of the vertical forces at each tire. The vertical at left wheels were much smaller than that of the right wheels, as the left wheels were the inner wheels during this circling test.

Figure 4.53 demonstrates the estimation result of the longitudinal forces at each tire. The measurement of DYNA once again confirmed that the longitudinal force at rear left and right wheels are different during turning. The model of transfer of longitudinal force TF_x has successfully computed this difference. That's why our proposed observer could accurately estimate the longitudinal force at each tire.

Figure 4.54 demonstrates the estimation result of f_{3cog} by different observers. Figure 4.55 demonstrates the estimation result of f_{3r}. Our new observer provided an accurate estimation. Our estimation is based on the fusion of five different models, summarized in Table 4.4.

Figure 4.56 demonstrates the estimation results of the lateral forces at each tire obtained by our new observer. In Figure 4.57, we compared the estimation results of lateral forces obtained by different non-linear observers. The performance of EKF and UKF

were equally satisfactory. However, the UKF observer is more simple as it doesn't need to compute the Jacobian matrix.

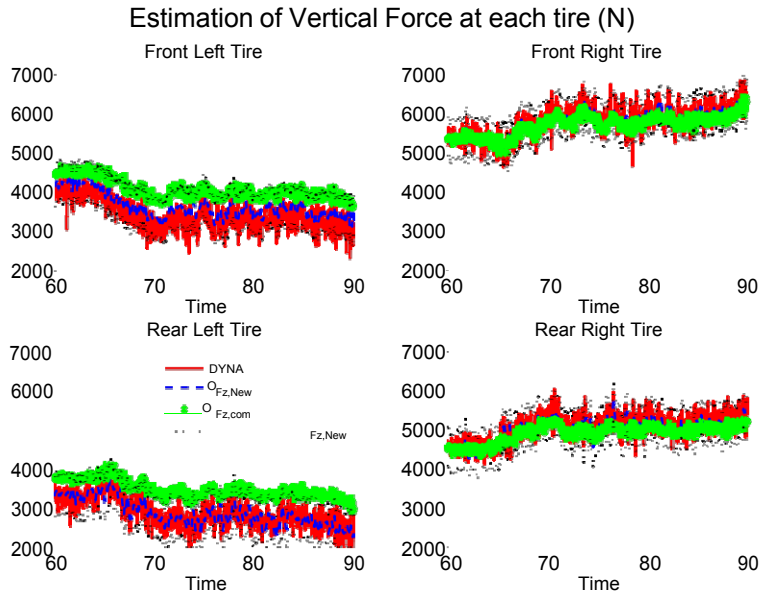

Figure 4.52: Test 5 (circling test): Comparison of the estimation results of vertical force at each tire

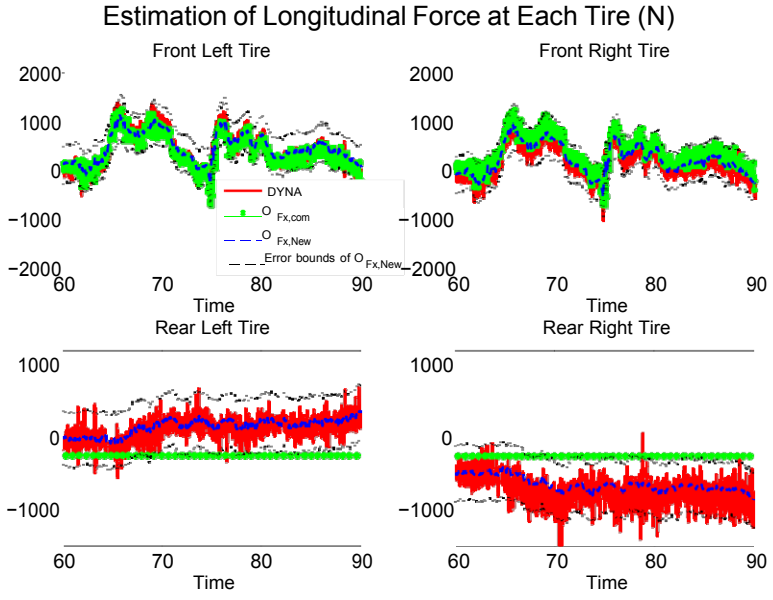

Figure 4.53: Test 5 (circling test): Comparison of the estimation results of longitudinal force at each tire

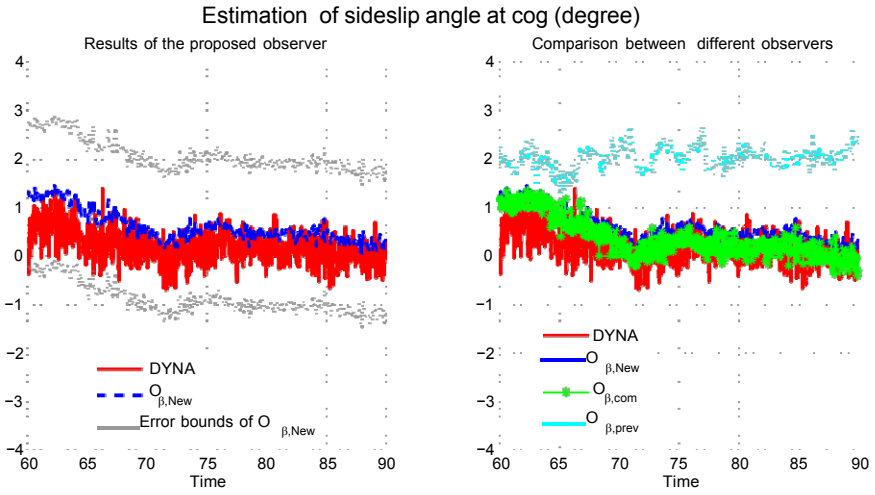

Figure 4.54: Test 5 (circling test): left) Results and error bounds of the new observer for estimation of sideslip angle at CoG; right) Comparison of the estimation results of sideslip angle at CoG obtained by different observers

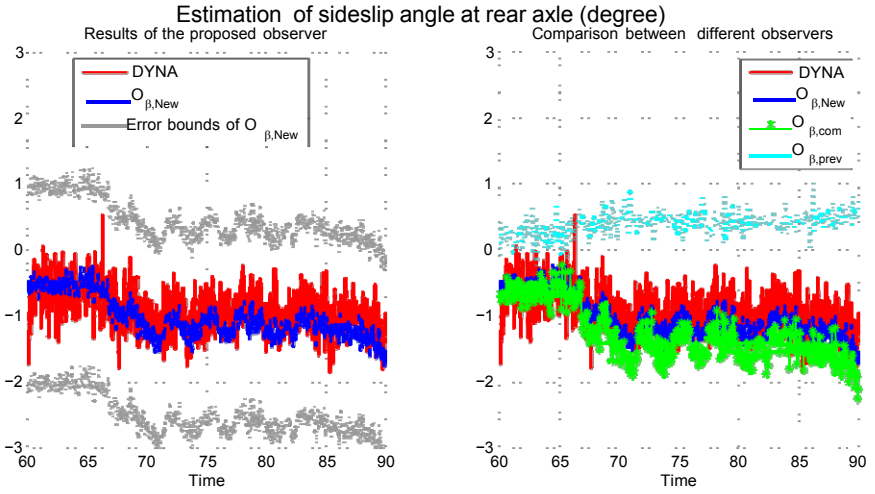

Figure 4.55: Test 5 (circling test): left) Results and error bounds of the new observer for estimation of sideslip angle at rear axle; right) Comparison of the estimation results of sideslip angle at rear axle obtained by different observers

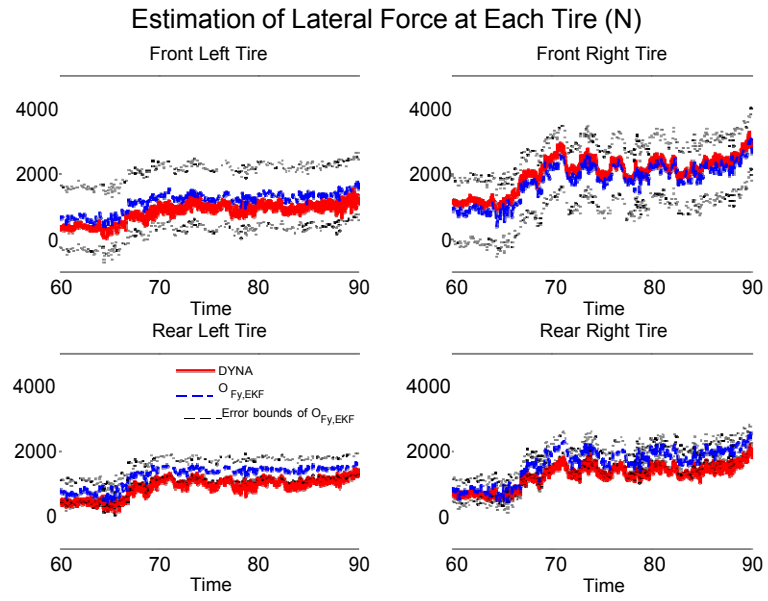

Figure 4.56: Test 5 (circling test): Results and error bounds of the new observer for estimation of lateral forces at each tire

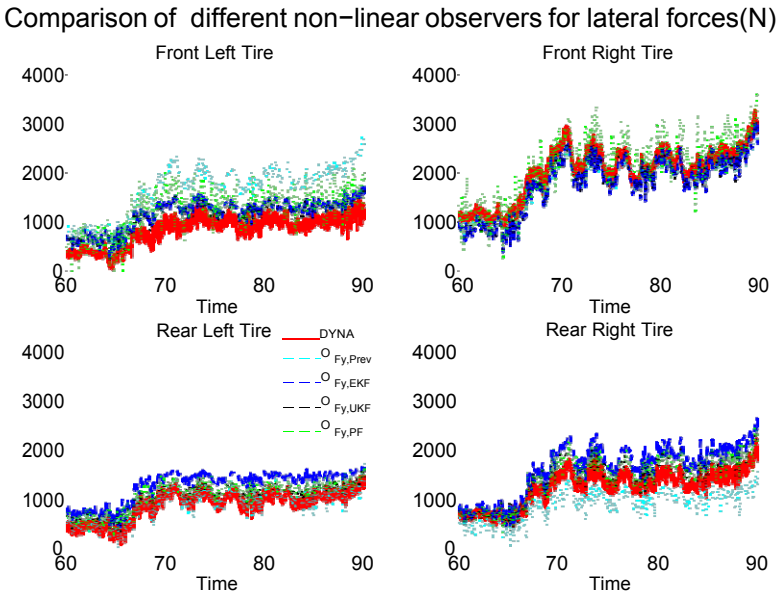

Figure 4.57: Test 5 (circling test): Comparison of the estimation results of tire lateral forces obtained by different observers

4.5.6 Slalom test at 40 km/h at slippery road

This test is designed to validate the performance of our observers at low adhesion condition. The test track was paved with marble tiles and the surface was covered by a layer of water. The maneuver time history is illustrated in Figure 4.58.

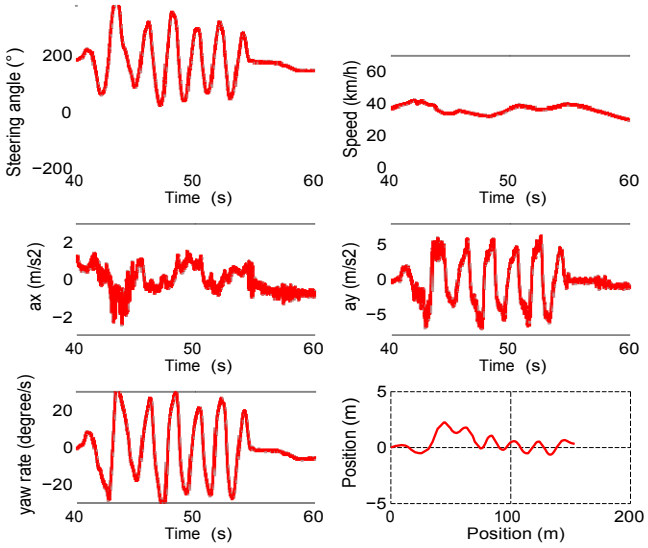

Figure 4.58: Maneuver time history of Test 6: Low adhesion slalom test

Figure 4.59 demonstrates the estimation result of the vertical forces at each tire. The observer of vertical force is not influenced by the road adhesion condition, and therefore provided good performance.

Figure 4.60 demonstrates the estimation result of the longitudinal forces at each tire. The proposed model of T_{Fxr} is accurate even at low adhesion road.

Figure 4.61 demonstrates the estimation result of the sideslip angle at center of gravity by different observers. Figure 4.62 demonstrates the estimation result of the sideslip angle at rear axle. Our estimation could tightly follow the variation of real data but was less accurate at peak points. This error is caused by the wrong configuration of cornering stiffness. The cornering stiffness is an important parameter which could influence the estimation of sideslip angle.

Figure 4.63 demonstrates the estimation results of the lateral forces at each tire obtained by our new observer. In Figure 4.64, we compared the estimation results of lateral forces obtained by different non-linear observers. We can find the estimation result is less accurate compared with the former tests. As we explained in equation 2.86, the transfer of lateral force is influenced by the road friction coefficient. The variation of road condition has increased the model errors and leaded to the estimation errors in the peak points in Figure 4.63.

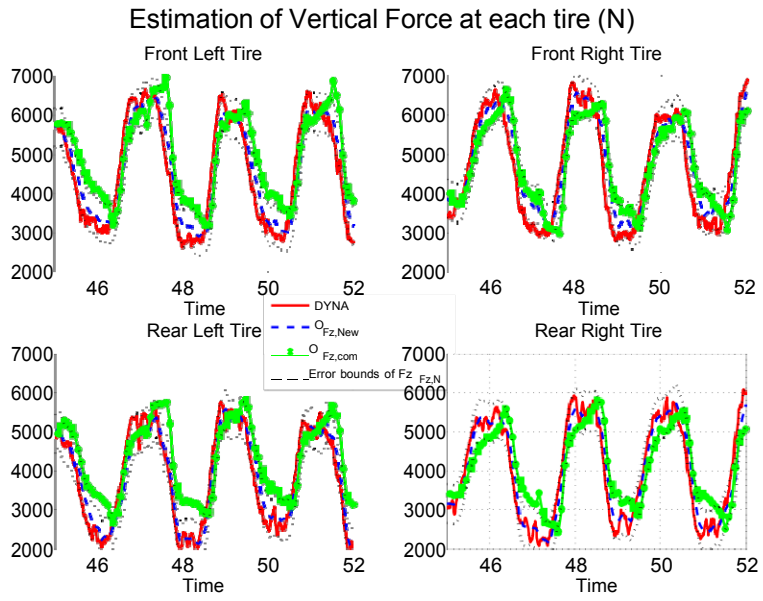

Figure 4.59: Test 6 (low adhesion slalom test): Comparison of the estimation results of vertical force at each tire

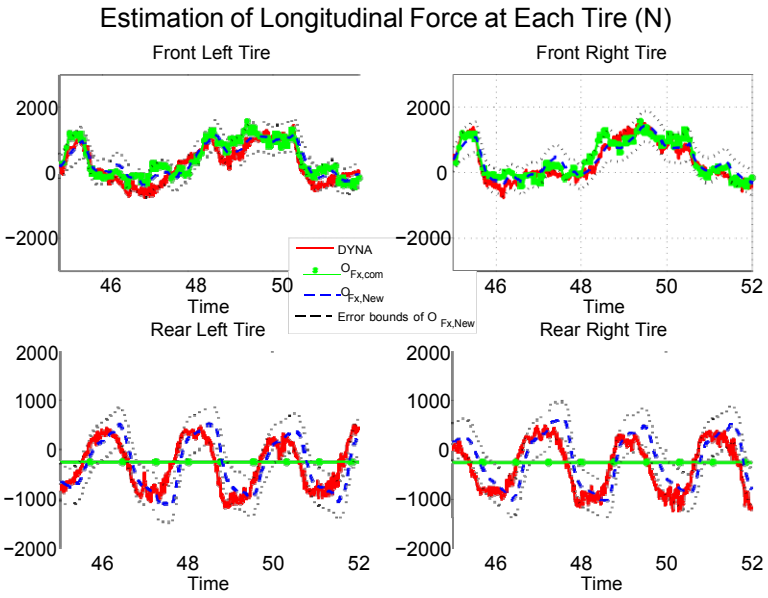

Figure 4.60: Test 6 (low adhesion slalom test): Comparison of the estimation results of longitudinal force at each tire

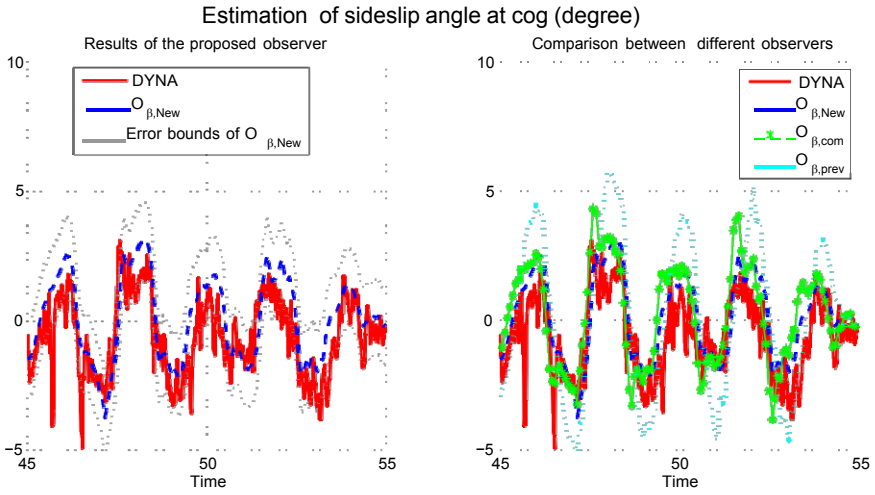

Figure 4.61: Test 6 (low adhesion slalom test): left) Results and error bounds of the new observer for estimation of sideslip angle at CoG; right) Comparison of the estimation results of sideslip angle at CoG obtained by different observers

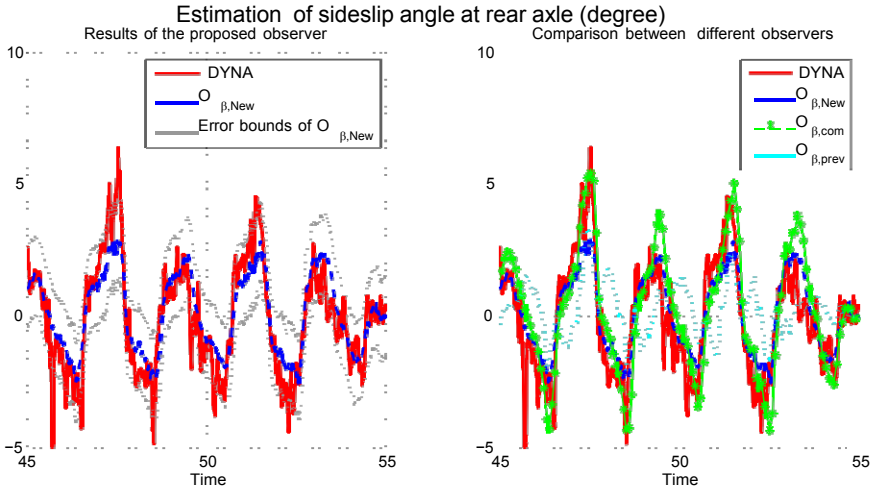

Figure 4.62: Test 6 (low adhesion slalom test): left) Results and error bounds of the new observer for estimation of sideslip angle at rear axle; right) Comparison of the estimation results of sideslip angle at rear axle obtained by different observers

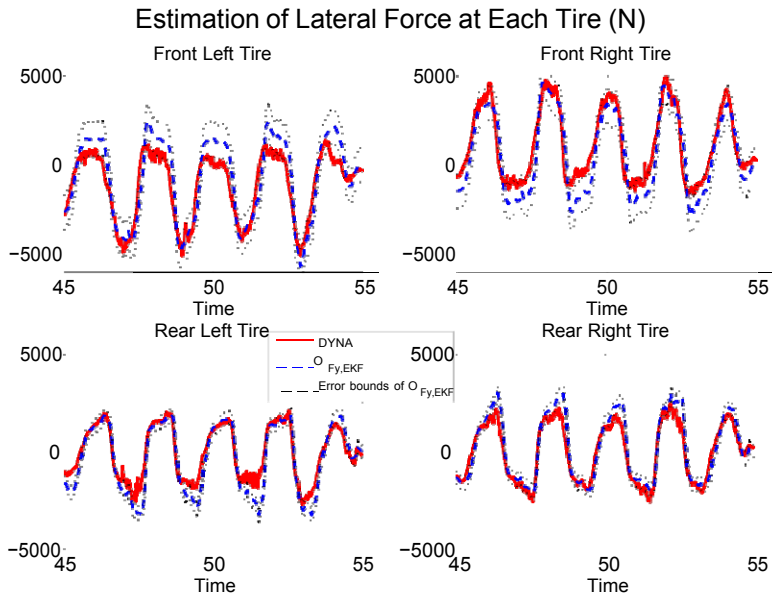

Figure 4.63: Test 6 (low adhesion slalom test): Results and error bounds of the new observer for estimation of lateral forces at each tire

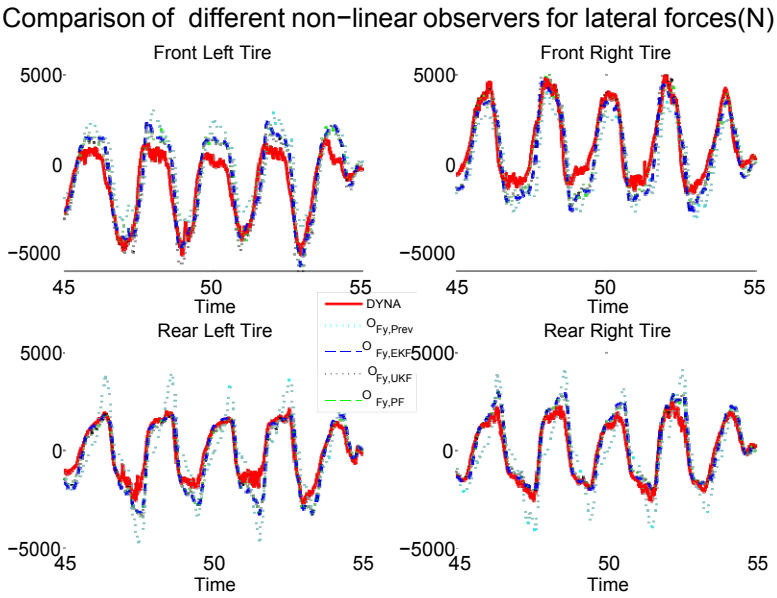

Figure 4.64: Test 6 (low adhesion slalom test): Comparison of the estimation results of tire lateral forces obtained by different observers

4.5.7 Slalom test at 140 km/h at banked road

This test is designed to validate the performance of our observers at banked road. The test track was banked and dry ($\mu = 1$). The maneuver time history is illustrated in Figure 4.65. In the CERAM test center, there are three tracks: the bank angles at low track, middle track, and high track were 15°, 30° and 40° respectively. During the test, the vehicle was continuously changing from the high track to the low track.

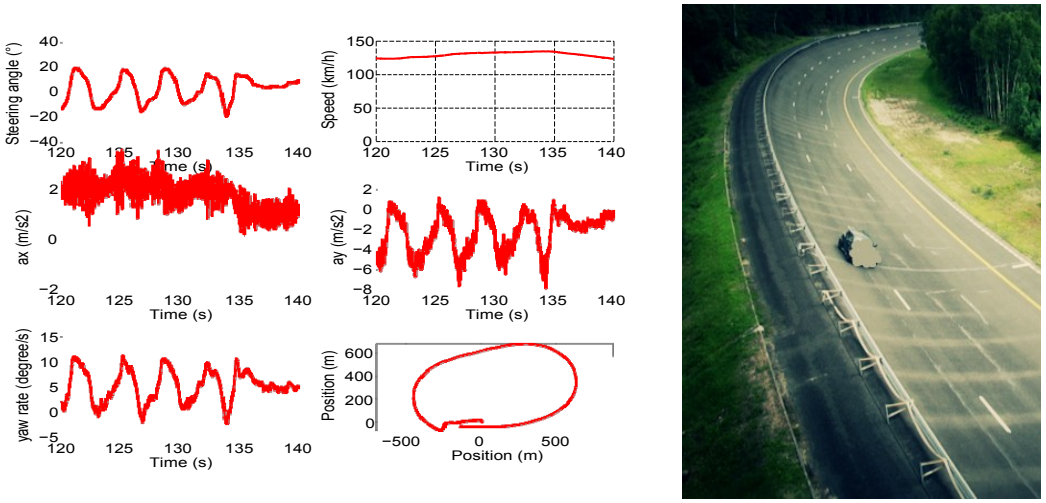

Figure 4.65: Maneuver time history of Test 7: Banked road slalom test

Figure 4.66 demonstrates the estimation result of the vertical forces at each tire. The bank angle of the road can cause the additional transfer of vertical load. However, the measured acceleration already contained the gravity component in lateral direction. As a result, the common model could also provide a good estimation of vertical force at banked road. However, our proposed model was more accurate, as the roll and pitch motion of suspension was taken into account.

Figure 4.67 demonstrates the estimation result of the longitudinal forces at each tire. At such a high speed (140 *km/h*), even the direct measurement of force transducer was coupled with large noises. However, our observer provided a robust estimation about the longitudinal force, which proved the accuracy of the proposed model, T_{Fx}, at banked road.

Figure 4.68 and Figure 4.69 demonstrate the estimation results of β_{cog} and β_r. The estimation of observer $O_{\beta,com}$ and $O_{\beta,prev}$ were not accurate in this test. It is due to the road bank angle has greatly influenced the lateral dynamics. In our modified vehicle dynamics model (equation 2.56), the vehicle's 3D motion is considered. The errors caused by road angle is eliminated. The road angle is used as available information in this chapter, the method of estimating road angle is introduced in section 5.3.

Figure 4.70 demonstrates the estimation results of the lateral forces at each tire ob-

tained by our new observer. In Figure 4.71, we compared the estimation results of lateral forces obtained by different non-linear observers. The proposed models, *TFyf* and *TFyr*, are insensitive to the variation of road angles, which makes our new observer robust in the banked road.

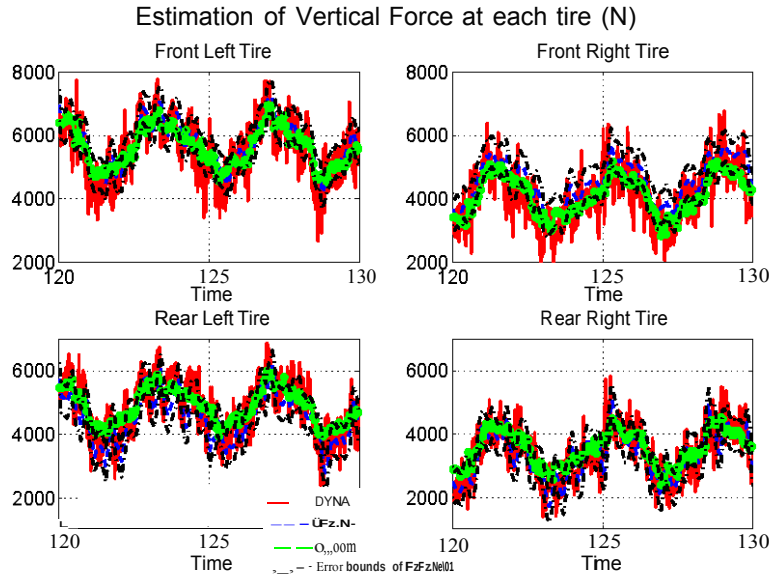

Figure 4.66: Test 7 (banked road slalom test): Comparison of the estimation results of vertical force at each tir e

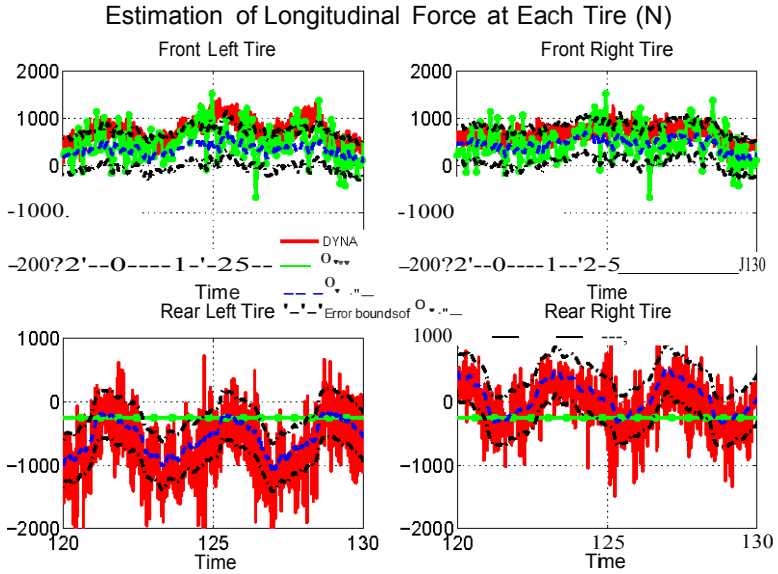

Figure 4.67: Test 1 (banked road slalom test): Comparison of the estimation results of longitudinal force at each tire

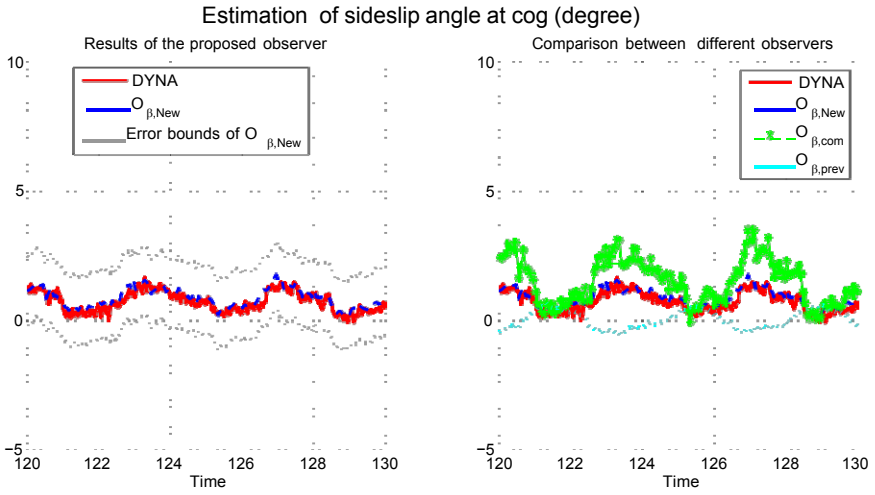

Figure 4.68: Test 7 (banked road slalom test): left) Results and error bounds of the new observer for estimation of sideslip angle at CoG; right) Comparison of the estimation results of sideslip angle at CoG obtained by different observers

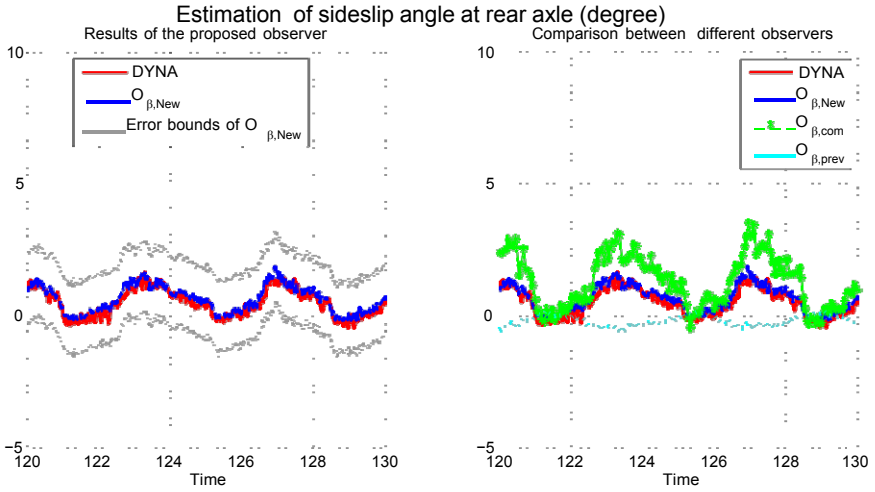

Figure 4.69: Test 7 (banked road slalom test): left) Results and error bounds of the new observer for estimation of sideslip angle at rear axle; right) Comparison of the estimation results of sideslip angle at rear axle obtained by different observers

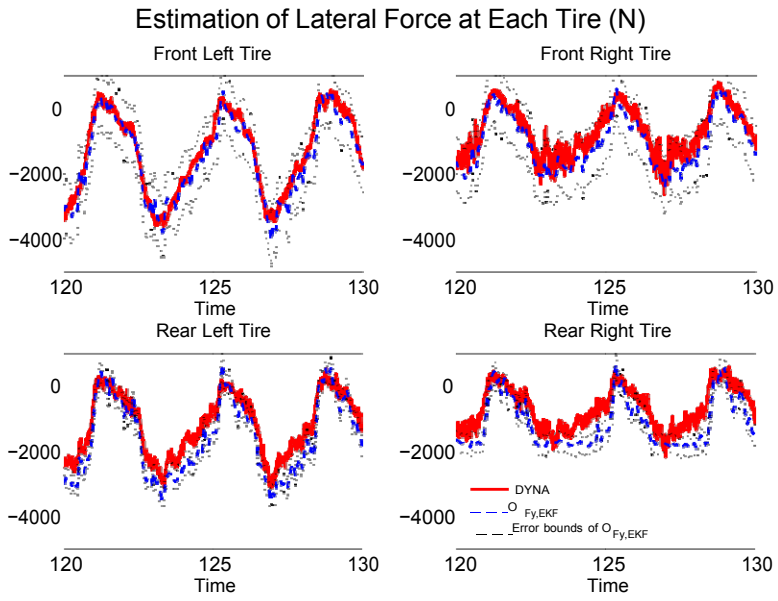

Figure 4.70: Test 7 (banked road slalom test): Results and error bounds of the new observer for estimation of lateral forces at each tire

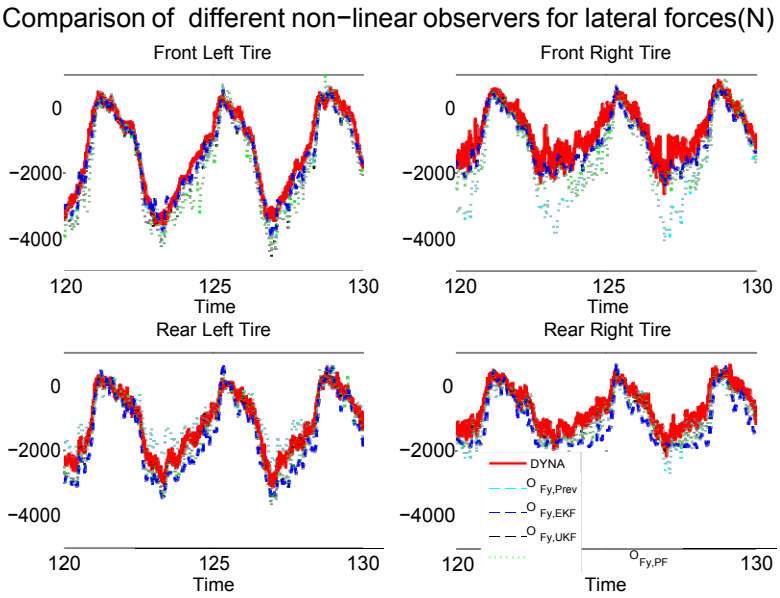

Figure 4.71: Test 7 (banked road slalom test): Comparison of the estimation results of tire lateral forces obtained by different observers

4.6 Conclusion

This chapter presents the new observers we developed for the estimation of the tire forces in three directions and the sideslip angle. We firstly introduced the implementation of our experimental vehicle. Then based on the experimental data, we validate and compare the qualities of different models through the open-loop estimation method. Among all the models validated in this chapter, there are three models originally proposed in this thesis:

1, the model for computing the transfer of vertical load by employing the roll and pitch angle;

2, the model for computing the transfer of lateral force;

3, the model for computing the transfer of longitudinal force.

The open-loop estimation is greatly influenced by the sensor errors. In order to further improve the accuracy of estimation, we employed the observer techniques. We propose to develop four observers to estimate the vertical force, longitudinal force, lateral force and the sideslip angle respectively. In each observer, only the targeting variables are estimated, which could greatly reduce the complexity of modeling. In the observer of vertical force O_{Fz}, the linear Kalman Filter is employed. The vertical force is obtained by incorporating the suspension deflection and the acceleration. In the observer O_{Fx}, the estimation is also realized by employing linear Kalman Filter algorithm. In the observer of sideslip angle O_{β}, five models are combined together to provide the best estimation through the KF algorithm. The observer of lateral force O_{Fy} is more complicate due to the non-linearity of tire's nature. To adapt to the non linear tire model, we employed the non-linear observer techniques. In order to make a comparison and choose the best estimation methods, the EKF observer, UKF observer and PF observer were developed for estimation of lateral forces. All the three observation techniques could provide satisfactory estimation results.

The four observers are not working individually but are connected in a cascaded way. The estimation results of one observer will be communicated to other observers and regarded as the measurement. However, the communication between observers could possibly transfer the fatal errors in the estimation. Therefore, an algorithm to filter out the fatal errors is developed.

Seven critical tests are performed to evaluate the performance of our new observers in different conditions. The observers generally provide satisfactory estimation results at all the tests. The estimation in this chapter is based on the condition that all the vehicle parameters are known. However, in real situation, these parameters are difficult to be measured. In the subsequent chapter, we will focus on the estimation of vehicle's parameters.

5 Adaptive Estimation In Presence Of Parameter Variation

5.1 Introduction

In the previous chapter, we have already developed observers based on low-cost sensors to estimate the non-measured dynamics states. These observers are developed based on two assumptions which has simplified the problem. Firstly, the vehicle's physical parameters are assumed to be constants, which is not true in real condition. The changes in the vehicle's mass, the position of CoG and the road grade angle will bring errors to the estimation. Secondly, we assume the available measurement about vehicle dynamics (the longitudinal speed, accelerations, yaw rate) is reliable. However, those available measurement are always coupled with noises and errors. The errors in these basic information would greatly influence the performance of the whole observer system.

The major contribution of this chapter, is taking into account the variation of vehicle parameters and the unpredictable sensor errors in the estimation process. The vehicle's physical parameters and other basic dynamics parameters are considered as unknown variables and estimated through the fusion of different vehicle dynamics models and different sensors. Another important issue in this chapter is to propose a novel approach to employ the digital map to enhance road safety. The digital map contains information about the road geometry, which could be used to improve the estimation of vehicle dynamics. The digital map and the inertial sensors should be incorporated to evaluate vehicle's safety. The performance of this algorithm is tested and compared with real experimental data.

This chapter is organized as follows. Section 5.2 presents the methods for improving the sensor measurement. Section 5.3 introduces the method of estimating vehicle's physical parameters. Then, the use of digital map is presented in Section 5.4. In each section, the experimental data is presented to validate the proposed algorithm.

5.2 Improvement Of Sensor Measurement

The task of measurement becomes challenging when we consider the occurrence of sensor errors. Sensor errors can be caused by many reasons, such as high temperature or low

battery or software bug. In real experiments, undesired sensor errors could happen at any moment and could possibly cause serious consequence. In order to solve this problem, we propose to use multiple models and sensors to estimate each dynamics states. In this way, the estimation become less sensitive to the error of one sensor, as the error is corrected by the fusion of multiple sensors. In the section 5.2.1, we introduce the different models we developed for the calculation of vehicle's kinematic and dynamics variables. Then in section 5.2.2, we present the whole state observer exploiting the measurement redundancy.

5.2.1 Multiple measurement models

Measurement of longitudinal velocity

Vehicle longitudinal speed is usually regarded as wheel speed. When rear wheels are rotating without longitudinal slip, the relationship between wheel speed and vehicle longitudinal velocity can be written as equation 5.1.

$$\begin{aligned} v_{x,rl} &= \Omega_{21} R_{eff} + \tfrac{E}{2}\dot{\psi} + noise \\ v_{x,rl} &= \Omega_{22} R_{eff} - \tfrac{E}{2}\dot{\psi} + noise \end{aligned} \tag{5.1}$$

where $v_{x,rl}$ and $v_{x,rr}$ are vehicle's longitudinal speed computed with the rear left and right wheel, R_{eff} is the effective tire radius, Ω_{21} and Ω_{22} are the angular velocities of rear left and right wheels respectively, E is the vehicle track width, the *noise* represents model error.

Nevertheless, wheel speeds could become unrelated to the vehicle velocity when driving in slippery conditions. In this situation, we could use the integration method to obtain the vehicle longitudinal speed, as shown in equation 5.2.

$$v_{x,inter} = \int a_x - g\sin\theta_r \, dt + noise \tag{5.2}$$

where θ_r is the slope angle of the road.

In addition, the vehicle speed can also be obtained by a GPS sensor and it is written as equation 5.3.

$$v_{x,GPS} = v_{gps}\cos\beta_{cog} + noise \tag{5.3}$$

where v_{gps} is the velocity measured by GPS, β_{cog} is the sideslip angle at the center of gravity, the estimation of the sideslip angle is introduced in the previous chapter.

As a conclusion, we have four sensors to measure the vehicle speed: two wheel sensors, the accelerometer and the GPS.

Measurement of yaw velocity

Similar to the longitudinal velocity, the yaw velocity could also be observed by multiple sensors. We propose four models for estimation of yaw velocity. First of all, the yaw velocity could be measured by gyroscope sensors ($\dot{\psi}_m$), written as equation 5.4.

$$\dot{\psi}_{inertial} = \dot{\psi}_m + noise \tag{5.4}$$

In addition, the yaw rate can be computed by the difference between the speed of rear left and right wheels, as we can see in equation 5.5.

$$\dot{\psi}_{wheel} = \frac{\Omega_{22}}{E} \frac{-\Omega_{21}}{} R_{eff} + noise \tag{5.5}$$

Moreover, during slow turning, the yaw rate can be obtained according to the steering geometry:

$$\dot{\psi}_{steer} = v_x(\tan \delta_f - \tan \beta_r)/L + noise \tag{5.6}$$

where δ_f is the steering angle at front wheel, β_r is the sideslip angle at rear wheel, L denotes the distance between front and rear axle.

Another method to estimate yaw velocity is to differentiate the yaw angle, as shown in equation 5.7:

$$\dot{\psi}_{diff} = (\psi_{gps,t} - \psi_{gps,t-1})/\ t + noise \tag{5.7}$$

where ψ_{gps} is the direction angle measured by GPS, t is the step time.

Measurement of Roll and Pitch Angle

The roll angle can be calculated by integrating the roll rate measured by accelerometer. However, the sensor bias will also be integrated, leading to large calculation error. In this study, the roll angle and pitch angle are obtained via suspension deflection sensors [Hac et al., 2004].

$$\begin{aligned} \phi_v &= \frac{\sigma_{11} - \sigma_{12} + \sigma_{21} - \sigma_{22}}{2E} \\ \theta_v &= \frac{\sigma_{11} + \sigma_{12} - \sigma_{21} - \sigma_{22}}{2L} + \theta_s \end{aligned} \tag{5.8}$$

where σ_{ij} is the measured suspension deflection at corner of the vehicle, θ_s is vehicle's pitch angle when the vehicle is empty and static.

Measurement of accelerations

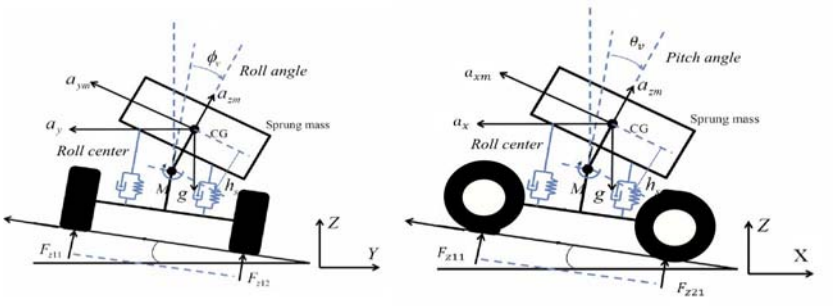

Figure 5.1: Roll and pitch movement of vehicle body

The accelerometer measures directly the sum of accelerations caused by the vehicle's motion and gravity, as illustrated in Figure 5.1. In the vehicle dynamics model, the direction of acceleration should be parallel to the road. Thus a transformation should be realized, as expressed by equation 5.9.

$$\begin{bmatrix} a_{xequ} & a_{yequ} & a_{zequ} \end{bmatrix}^T = R_\theta R_\varphi \begin{bmatrix} a_{xm} & a_{ym} & a_{zm} \end{bmatrix}^T \tag{5.9}$$

where the rotation matrices are:

$$R_\theta = \begin{bmatrix} 1 & 0 & 0 \\ 0 & \cos\theta_v & -\sin\theta_v \\ 0 & \sin\theta_v & \cos\theta_v \end{bmatrix}, R_\varphi = \begin{bmatrix} \cos\varphi_v & 0 & \sin\varphi_v \\ 0 & 1 & 0 \\ -\sin\varphi_v & 0 & \cos\varphi_v \end{bmatrix} \tag{5.10}$$

where θ_v and φ_v are the pitch and roll angle of the vehicle chassis. a_{xm} a_{ym} a_{zm} are the measured accelerations by the accelerometer installed at the vehicle body.

The measured acceleration is also influenced by the vehicle vibration, especially in the vertical direction. The vehicle vibration could cause significant noises in the measurement. In order to filter out the noises, we introduce the following process model:

$$\begin{bmatrix} \dot{a}_x & \dot{a}_y & \dot{a}_z \end{bmatrix}^T = \begin{bmatrix} 0 & 0 & 0 \end{bmatrix}^T + noise \tag{5.11}$$

The physical meaning of this process model is that the change rate of acceleration is close to zero. It actually works as a low-pass filter smoothing the direct measurement.

5.2.2 Observer design

The process for improving sensor measurement is presented by Figure 5.2.

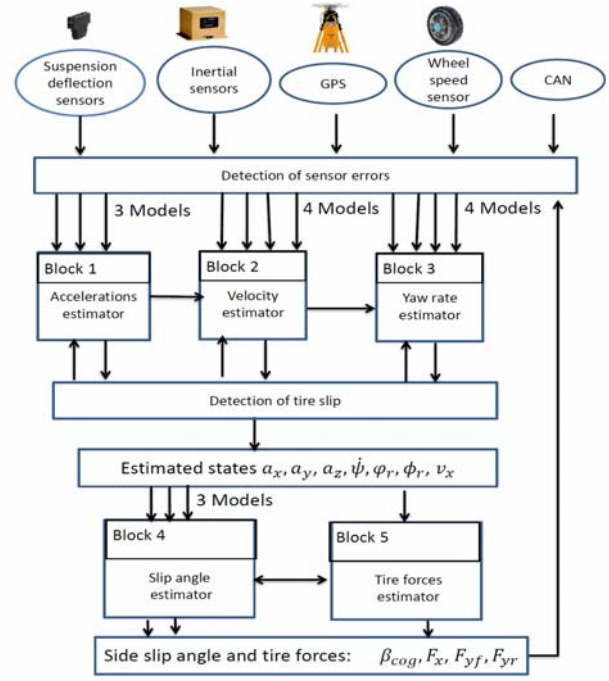

Figure 5.2: Algorithm overview: Estimation based on the fusion of multiple sensors

The estimation procedure is divided into 5 blocks. Each block of estimation is based on the Kalman filter algorithm. The advantage of using 5 Kalman filters is to ensure the observability of each block and simplify the calculation of Kalman gain. The block of estimating the sideslip angle and tire forces is already introduced in the previous chapter. In this chapter we focus on the estimation of vehicle speed, acceleration, yaw rate.

Estimation of vehicle longitudinal speed

A linear Kalman filter is developed for estimation of vehicle longitudinal speed, expressed as the following equations:

$$\begin{bmatrix} \dot{v}_x \end{bmatrix} = \begin{bmatrix} 0 \end{bmatrix} \begin{bmatrix} v_x \end{bmatrix} + (a_{xm} - g\sin\theta_r) + cov(noise)$$

$$\begin{bmatrix} v_{x,rl} \\ v_{x,rr} \\ v_{x,GPS} \end{bmatrix} = \begin{bmatrix} 1 \\ 1 \\ 1 \end{bmatrix} v_x + cov(noise) \tag{5.12}$$

where $v_{x,rl}$ and $v_{x,rr}$ are obtained by equation 5.1. $v_{x,GPS}$ is obtained by equation 5.3.

Estimation of accelerations

A linear Kalman filter is developed for estimation of accelerations, expressed as the following equations:

$$\begin{bmatrix} \dot{a}_x \\ \dot{a}_y \\ \dot{a}_z \end{bmatrix} = 0^{3\times 3} \begin{bmatrix} a_x \\ a_y \\ a_z \end{bmatrix} + cov(noise)$$

$$\begin{bmatrix} a_{xequ} \\ a_{yequ} \\ a_{zequ} \\ g\cos\phi_r\cos\theta_r \end{bmatrix} = \begin{bmatrix} 1 & 0 & 0 & 0 \\ 0 & 1 & 0 & 0 \\ 0 & 0 & 1 & 0 \\ 0 & 0 & 1 & 0 \end{bmatrix} \begin{bmatrix} a_x \\ a_y \\ a_z \end{bmatrix} + cov(noise) \tag{5.13}$$

Estimation of yaw speed

We used 4 models for computing yaw rate, represented by equation 5.4-5.7. Then the four models are combined in the Kalman filter to estimate the yaw rate, expressed as equation 5.14.

$$\begin{bmatrix} \dot{\delta} \\ \ddot{\psi} \\ \dot{\psi} \end{bmatrix} = \begin{bmatrix} 0 & 0 & 0 \\ 0 & 0 & 0 \\ 0 & 1 & 0 \end{bmatrix} \begin{bmatrix} \delta \\ \dot{\psi} \\ \psi \end{bmatrix} + cov(noise)$$

$$\begin{bmatrix} \delta_{CAN} \\ \psi_{gps} \\ \dot{\psi}_{inertial} \\ v_{y,rear} \\ \dot{\psi}_{wheel} \end{bmatrix} = \begin{bmatrix} 1 & 0 & 0 \\ 0 & 0 & 1 \\ 0 & 1 & 0 \\ v_x & -L & 0 \\ 0 & 1 & 0 \end{bmatrix} \begin{bmatrix} \delta \\ \dot{\psi} \\ \psi \end{bmatrix} + cov(noise) \tag{5.14}$$

where δ_{CAN} represents the steering angle obtained from CAN bus, ψ_{GPS} is the heading angle measured by GPS sensor, $\dot{\psi}_{inertial}$ represents the yaw rate measured by inertial sensor, $\dot{\psi}_{wheel}$ is the yaw rate obtained from wheel speed sensor, $v_{y,rear}$ is the lateral speed at rear axle, and is approximated to zero.

It is noted that the vehicle direction measured by GPS, ψ_{GPS}, is within the range of$[0, 2\pi]$. Every time when it passes 2π, it will dramatically drop to 0. The rapid change of ψ will cause errors in the estimation of yaw rate. In order to eliminate this effect, we regard ψ_{GPS} as invalid measurement only when $\psi_{GPS} \in \left[\frac{71}{36}\pi, 2\pi\right) \cup \left[0, \frac{1}{36}\pi\right]$, represented by equation 5.15.

$$R_{yaw}(2,2) = \begin{cases} 1000000 & \textit{if } \psi_{GPS} \in \left[\frac{71}{36}\pi, 2\pi\right) \cup \left[0, \frac{1}{36}\pi\right] \\ 0.1 & \textit{otherwise} \end{cases} \tag{5.15}$$

where R_{yaw} is the covariance matrix of observation model. $R_{yaw}(2,2)$ is the variance of measurement ψ_{GPS}.

5.2.3 Experimental validation

A slalom test is conducted with our experimental vehicle (DYNA) to validate the performance of the observers developed in section 5.2.2. During this slalom test, the speed was about 60km/h, the maximal lateral acceleration was beyond 10m/s^2, as shown in Figure 5.3.

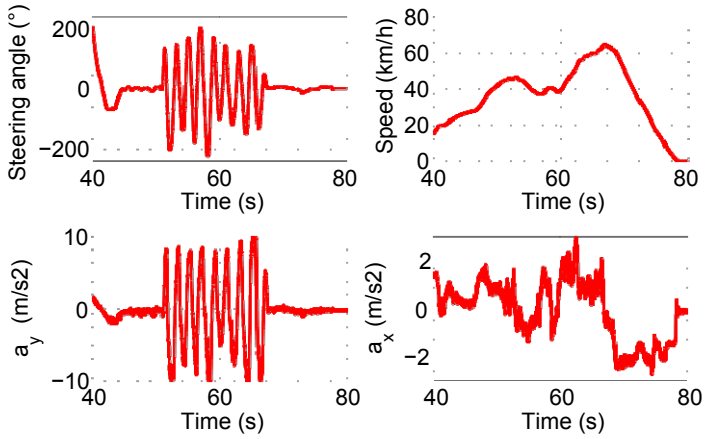

Figure 5.3: Description of slalom test

5.2.3.1 Validation of different kinematic models

Before presenting the results of the fusion of multiple models, we would like to validate the accuracy of each kinematic model introduced in section 5.2.1. The four models for computing vehicle speed ($v_{x,rl}$, $v_{x,rr}$, $v_{x,inter}$, $v_{x,GPS}$) are compared in Figure 5.4.

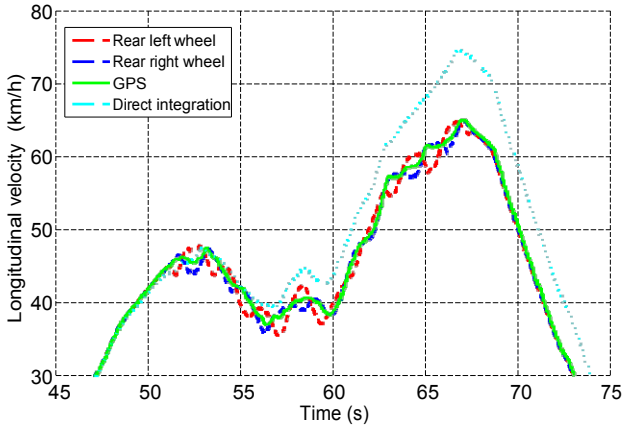

Figure 5.4: Validation of four models for estimating longitudinal velocity: "Rear right wheel" refers to $v_{x,rr}$, "Rear left wheel" refers to $v_{x,rl}$,"GPS" refers to $v_{x,GPS}$

The speed obtained by GPS ($v_{x,GPS}$) is regarded as the reference data, represented by the green lines. The direct integration method ($v_{x,inter}$), represented by cyan dotted lines, showed less accuracy than the other models due to the accumulated errors. Before and after the slalom behavior ($t < 52s$ and $t > 67s$), we can see the results of $v_{x,rl}$ and $v_{x,rr}$ were identical with the reference data. It proves that during normal driving behavior (with small tire slip), the wheel speed can be regarded as the vehicle's longitudinal speed. However, during the slalom behavior, $v_{x,rl}$ and $v_{x,rr}$ were different with the reference data. The difference is caused by the excessive tire slip during slalom behavior. The GPS measurement has the advantage of being accurate regardless of the tire slip , but it has the problem of signal lost in real driving scenarios. The motivation of the fusion of the four models is to filter out the errors of each model.

Similarly, we also compared the four models ($\dot{\psi}_{inertial}$, $\dot{\psi}_{wheel}$, $\dot{\psi}_{steer}$,$\dot{\psi}_{diff}$) for estimating yaw rate in Figure 5.5. Taking the measurement of gyroscope ($\dot{\psi}_{inertial}$) as a reference, we can see yaw rate computed by wheel speed model ($\dot{\psi}_{wheel}$) is close to the real data. The small time delay between the $\dot{\psi}_{inertial}$ and $\dot{\psi}_{wheel}$ is caused by the tire slip. The yaw rate computed by steering model (equation 5.6) was less accurate in this intense slalom test. During slalom behavior, vehicle's heading angle didn't change a lot, therefore, the derivative of heading angle was a rough estimation of yaw rate.

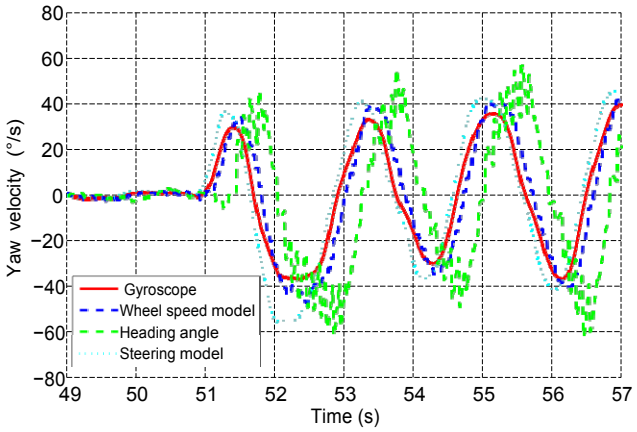

Figure 5.5: Validation of four models for estimating yaw rate: "Gyroscope" represents direct measurement, "Wheel speed model" refers to equation 5.5, "Steering model" refers to equation 5.6, "Heading angle model" refers to equation 5.7

The roll angle obtained by integration method and suspension deflections are compared in Figure 5.6. The integration method will accumulate considerable errors, as shown by the green line. In contrast, the suspension deflections method shows more accurate results. The fusion of the two model also provided good accurate estimation.

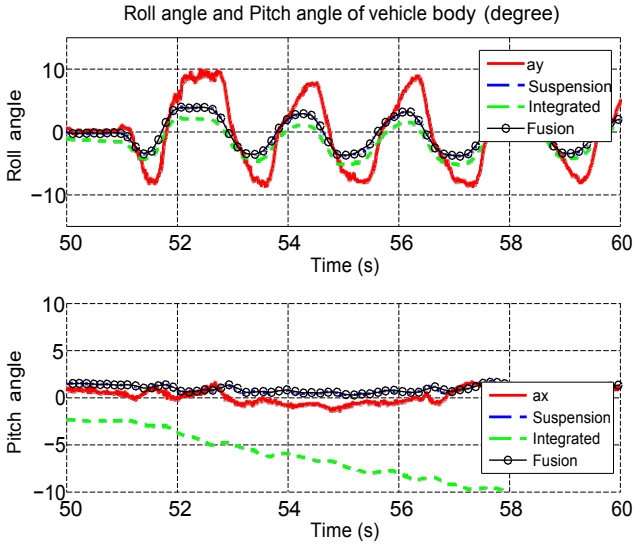

Figure 5.6: Estimation of vehicle roll and pitch angle. In this figure, the red lines are vehicle's accelerations which could indicate the roll and pitch motion of vehicle. "Fusion" represents the results obtained by the fusion of integration method and suspension method.

5.2.3.2 Fusion of multiple models to correct sensor errors

The advantage of fusion of multiple models is the ability to stay robust in presence of sensor errors. Even when the GPS and gyroscope are not working, we can still estimate the vehicle speed and yaw rate, as shown in Figure 5.7. The data of GPS and gyroscope was used only as reference.

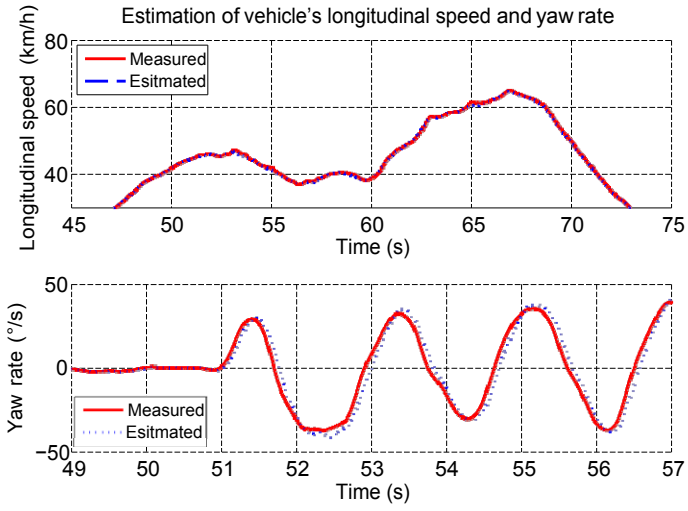

Figure 5.7: Estimation of vehicle longitudinal speed and yaw rate based on sensor fusion.

5.3 Vehicle Physical Parameters

This section describes the mathematical models used to identify the value of vehicle parameters. In real driving condition, the vehicle parameters can vary a lot, such as the weight of vehicle, the cornering stiffness of tire. In chapter 4, the Test 6 and Test 7 (tests at slippery road and banked road) have demonstrated that the knowledge of cornering stiffness and road angle is important to the good performance of observer. For this reason, we proposed to regard these physical parameters as unknown variables and estimate these parameters in real time. The parameters we will estimate in this chapter are listed in Table 5.1.

Table 5.1: parameters of the vehicle

	parameters		parameters
m_v	vehicle weight	φ_r	bank angle of the road
L_1	position of COG	θ_r	incline angle of the road
C_β	cornering stiffness		

5.3.1 Parameters and models

Vehicle mass

Nowadays, many modern vehicle suspensions are equipped with relative position sensors to measure suspension deflections σ_{ij} at each corner. At a passive suspension with linear spring characteristics, a variation of sprung mass at each corner, m_{sij}, changes the spring deflection.

$$m_{sij} = \frac{k_s \sigma_{ij} + F_{internal}}{a_z} \tag{5.16}$$

where σ_{ij} is the spring deflection, k_s is the stiffness of suspension, $F_{internal}$ is the internal forces between each quarter of the body, which could be introduced by the lateral and longitudinal accelerations. The total mass of the vehicle could be obtained by the deflection of suspension, expressed by:

$$m_v = m_e + \frac{k_s}{a_z} \sum \sigma_{ij} \tag{5.17}$$

where m_e is the mass of empty vehicle.

In our vehicle, the suspension deflection is not directly measured. The installed laser sensors actually measure the distance between the road surface and the vehicle body, h_{ij}. Therefore, the variation of vehicle mass could be obtained by

$$mg = a_1 \sum h_{ij} + a_2 \tag{5.18}$$

where $a_1$and a_2 are empirical parameters, they represent the stiffness of the suspension. We set them as $a_1 = -24464$, $a_2 = 23603$.

Position of CoG

The position of CoG, L_1, refers to the distance between the front axle and the center of gravity. The larger the L_1 is, the more load the rear axle will have. It could be explained by the moment balance with respect to pitch axis, as expressed by equation 5.19.

$$Fz_f * L_1 - Fz_r * (L - L_1) = -m_v h a_{xm} \tag{5.19}$$

where Fz_f and Fz_r are the vertical load at front and rear axle respectively.

In the literature, the position of COG is seldom discussed and normally considered as a known constant. In this thesis, we employed the suspension deflection to identify this parameter. At static situation, the vertical load at each tire can be obtained by the suspension deflection, as introduced in section 2.4.1.2. Then the position of CoG is expressed as

$$L_1 = \frac{n_1(\sigma_{21} + \sigma_{22}) + n_2}{n_3(\sigma_{ij}) + n_4} L - \frac{h a_{xm}}{a_{zm}} \tag{5.20}$$

where h is the height of CoG, $n_{1\cdots4}$ are the empirical parameters determined by experiments.

When the vehicle is parking on a level road, the calculation is further simplified as

$$L_1 = \frac{n_1(h_{21} + h_{22}) + n_2}{n_3(h_{ij}) + n_4} L \tag{5.21}$$

In our experiment, the parameters are configured as $n_1 = -23014$, $n_2 = 16302$, $n_3 = -24464$, $n_4 = 38723$.

Cornering stiffness

Cornering stiffness, also called sideslip stiffness, is the key parameter to employ the linear tire model and Dugoff's tire model. It can reflect the ability of a tire to generate lateral forces. Normally, the cornering stiffness is supposed to be proportional to the road friction coefficient. $C_\beta \propto \mu$. To some degree, estimating the cornering stiffness is equal to estimate the road friction coefficient. In [Ahn et al., 2012], the authors present four methods to estimate the friction coefficient based on four different excitation conditions: medium lateral excitation, large lateral excitation, small longitudinal excitation, and large longitudinal excitation. In this work, both tire forces and steering torques are used as inputs to estimate the road friction. In this thesis, the estimation is only based on the low-cost sensors and linear tire model. To simplify the problem, we only consider

the the medium lateral excitation condition. The cornering stiffness is estimated only when the vehicle is undergoing a slalom test.

According to linear tire model and bicycle models, the lateral tire forces at each axle can be approximated by the following equations:

$$\begin{aligned} Fy_f &= -2C_f(\beta + \omega L_1/v_x - \delta_f) \\ Fy_r &= -2C_r(\beta - \omega L_2/v_x) \\ Fy_f + Fy_r &= m_v(a_{ym} + L_2\dot{\omega}) \\ I_z\dot{\omega} &= L_1 Fy_f - L_2 Fy_r \end{aligned} \tag{5.22}$$

To eliminate the β in (5.22), we assume the cornering stiffness of front and rear wheels are identical, $C_f = C_r = C_\beta$. Then we have the estimation model for cornering stiffness as follows:

$$2(\omega L - v_x\delta_f)C_\beta = v_x m_v \frac{L_1 - L_2}{L}(a_{ym} + \dot{\omega} L_2) - 2\frac{I_z\dot{\omega}}{L}v_x \tag{5.23}$$

Road grade angles

As mentioned in section 4.5.7, the negligence of road angles could cause significant errors in the estimation of sideslip angle. In this thesis, we use the inertial sensors to get a rough estimation of the road angle. The road angles can be extracted from the measured acceleration with equation 5.24.

$$\begin{aligned} \theta_r &= (a_{xm} - \dot{v}_x)/g \\ \varphi_r &= (a_{ym} + v_x\dot{\psi})/g \end{aligned} \tag{5.24}$$

5.3.2 Observer Design

For the purpose of simplification, we employed the recursive least squares (RLS) algorithm to estimate these constant parameters, shown in equation 5.25.

$$y(t) = \phi^T(t)\theta(t) \tag{5.25}$$

where the estimated parameter $\theta(t)$, input regression $\phi^T(t)$, and measured output $y(t)$ are given as

$$\theta(t) = [m_v, L1, C_\beta, \theta_r, \phi_r]^T$$

$$\phi^T(t) = diag[g, n_3(\sum^{2:} h_{ij}) + n_4, 2(\omega L - v_x\delta_f), g, g]$$

$$y(t) = \begin{bmatrix} \sum^{2:} h_{ij} + a_2 + m_e g \\ n_1(h_{21} + h_{22})L + n_2 L \\ v_x m_v \frac{L_1 - L_2}{L}(a_{ym} + \dot{\omega} L_2) - 2\frac{I_z\dot{\omega}}{L}v_x \\ a_{xm} - \dot{v}_x \\ a_{ym} - v_x\dot{\psi} \end{bmatrix}$$

The recursive process of the RLS algorithm, in a Kalman filter interpretation, is described as [Nam et al., 2013]:

$$\begin{aligned} \hat{\theta}(t+1) &= \hat{\theta}(t) + K(t+1) \cdot \varepsilon(t+1|\hat{\theta}(t)) \\ \varepsilon(t+1|\hat{\theta}(t)) &= y(t+1) - \phi^T(t+1)\hat{\theta}(t) \\ K(t+1) &= P(t)\phi(t+1)[\lambda I + \phi^T(t+1)P(t)\phi(t+1)]^{-1} \\ P(t+1) &= \frac{1}{\lambda}[I - K(t+1)\phi^T(t+1)]P(t) \end{aligned} \tag{5.26}$$

where I is the identity matrix, $\varepsilon(t)$ is the prediction error, $K(t)$ and $P(t)$ are the Kalman gain and covariance matrices, respectively, λ is the forgetting factor. The smaller λ is, the less weight is assigned to the older data. In our test, $\lambda = 0.99$.

5.3.3 Experimental Validation

Estimation of vehicle mass:

To validate our algorithm of estimating vehicle's mass, we changed the number of passengers (including the driver) from 0 to 3. During the test, the vehicle was parked on a well paved road. At the beginning, the vehicle was empty. Then during $130s < t < 180s$, there were three passengers in the car, one sitting on the rear right seat and the other two sitting on the front seats. When $180s < t < 200s$, there was only one passenger sitting on the front right seat. When $200s < t < 260s$, there were three passengers. When $260s < t < 320s$, there were two passengers sitting on the front seats. Figure 5.8 shows the comparison between measured and estimated value of vehicle's total weight. The The experimental results validated that the deflection of suspension could effectively represent the variation of vehicle's mass.

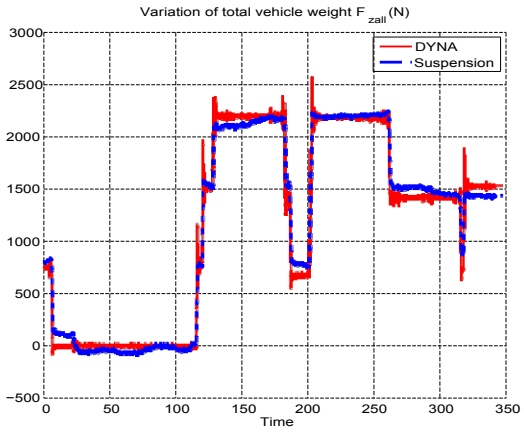

Figure 5.8: Comparison of the estimated variation of vehicle weight with real data. "suspension" corresponds to the estimated value by suspension deflection.

Estimation of position of COG:

During the same test, we also validated the algorithm for estimation of position of CoG. In Figure 5.9, the blue lines illustrated the estimation results of the RLS estimator. When the vehicle was empty, the position of CoG is at a distance of 1.22m from the front axle. When there were one or two passengers sitting on the front seats, the CoG moved closer to the front axle. When there was passenger sitting on the rear seat, the CoG moved closer to the rear axle. The proposed estimator provided a good estimation of position of CoG.

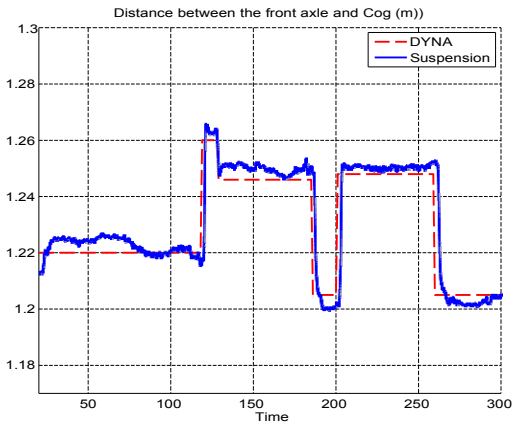

Figure 5.9: Experimental results of the estimator for position of CoG. “suspension” corresponds to the value estimated with suspension deflection.

Estimation of cornering stiffness:

The model for estimating cornering stiffness (equation 5.23) is only valid under considerable lateral acceleration, therefore the estimation is activated only at slalom test. We use the data of two different slalom test to validate our algorithm.

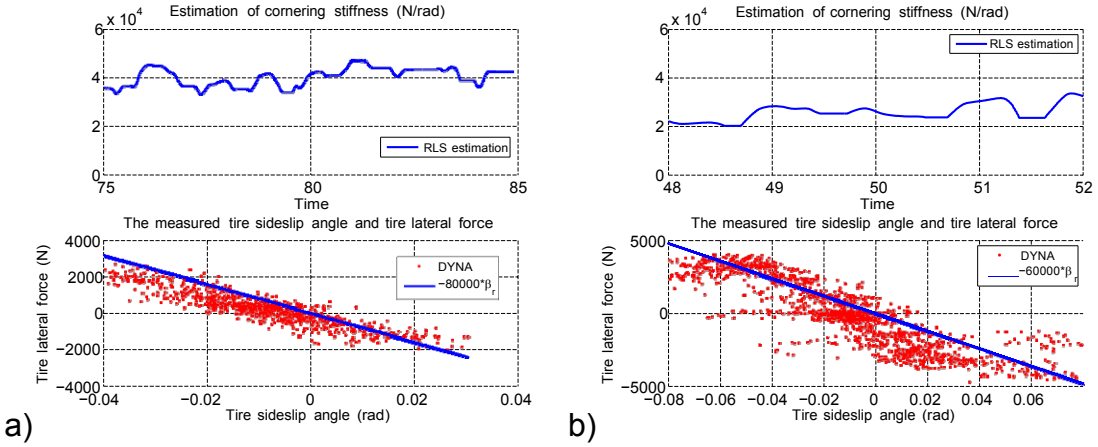

Figure 5.10: Estimation results of the cornering stiffness: a) slalom test at dry road; b) slalom test at wet slippery road

The first test is the Test 2 in section 4.5.2, a slalom test at dry road. The estimated cornering stiffness is illustrated in Figure 5.10.a). The estimated value, C_β, was varying in the range of $(3.6 \sim 4.4) \times 10^4$. The proposed algorithm is only capable of providing a rough estimation due to the simple model we used. Accurate estimation of cornering stiffness is a very challenging task. Recent works can be found in [Ahn et al., 2012]. The final estimation result of cornering stiffness is about 4×10^4 *N/rad*. To evaluate the estimated cornering stiffness, we also illustrate the tire forces and the tire sideslip angle obtained by direct measurement in Figure 5.10.a). The results showed that our estimated cornering stiffness could generally fit these points.

The second test is the Test 6 in section 4.5.6. The slalom test was conducted at a slippery road. The proposed RLS algorithm could also roughly estimate the cornering stiffness. The estimated value of C_β is about 3×10^4 *N/rad*. Comparing Figure 5.10.a) and 5.10.b), we can find that the estimator has successfully detected the drop of cornering stiffness.

Estimation of road angle:

The algorithm for estimation of road angle is validated by Test 7: a slalom test at banked road. The maneuver time history is illustrated in Figure 4.65. The bank angles at high, middle and low track were about 40 degree, 30 degree and 15 degree respectively. The estimated road angles are presented in Figure 5.11. We can find the proposed algorithm has successfully estimated the road angles.

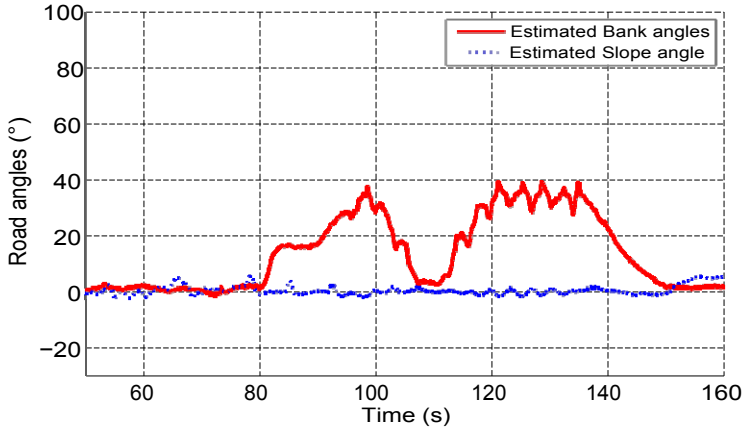

Figure 5.11: Estimation results of the road angles

5.4 Prediction Based On The Use Of OpenStreetMap

5.4.1 Introduction

This section presents a novel approach for estimating and predicting vehicle dynamics states by incorporating digital road map and vehicle dynamics models. In Chapter 4, we presented different observers to estimate vehicle dynamics states. However, these observers are only capable of estimating vehicle dynamics states at a current instant but not to predict the potential dangers in a future instant. In order to make time for correcting drive behaviors, especially when driving at high speed, it seems very appealing for us to predict an impending dangerous event and react before the danger occurs.

In order to predict the accidents, the knowledge of the upcoming road is necessary. In [Wang, 2013], the author proposed to use the infrastructure to communicate the road curvature information to the vehicle. Then based on the road information, the vehicle would decide whether the current speed is safe to pass through the upcoming corner. Inspired by this work, we would like to develop an active safety system to warn the drive about the potential accidents based on the digital map.

It is very meaningful to put useful information into the digital map, such as the road curvature, road angle and even road coefficient. Then by using the digital map, we could not only predict the vehicle's safety at future instant but also improve the estimation of vehicle dynamics states at current instant. After the prediction of vehicle dynamics states, the evaluation of accidents risk is also a challenging work. In the literature, various methods are presented to develop accidents risk assessments. In [Bouton et al., 2007], a rollover indicator is proposed to predict the vehicle rollover phenomenon of light all terrain vehicles. Some other vehicle rollover prediction method can be equally found in [Imine and Dolcemascolo, 2007] for heavy vehicles. [Sentouh et al., 2006] proposes an algorithm for the curve speed prediction which addresses control loss due to excessive speed in curves. In this thesis, we propose to use the tire forces to evaluate vehicle's safety.

The main contribution of this section is to incorporate the digital-map and inertial sensors to estimate and predict the safety of vehicle. The method of how to read the road information from the digital map is presented in Section 5.4.2. Then section 5.4.3 introduces the risk assessment index. In Section 5.4.4, the whole estimation algorithm is presented. The results of experimental validation is illustrated in Section 5.4.5.

5.4.2 Road Geometry Estimation

The digital map we used is the OpenStreetMap(OSM). OSM [http://openstreetmap.fr] is a free editable map capable of describing a variety of information about roads. Typically, the OSM data is stored in a xml file. The OSM data model consists of three basic

Table 5.2: Tags attributed to Critical Points

Longitude Position	Latitude Position	Altitude
x	y	h
Road Direction	Curvature	Vertical curvature
ψ_r	κ	ρ
Road Friction	Bank Angle	Slope Angle
μ	ϕ	θ
ID in OSM	Number of lanes	Number of roads
Id_{osm}	N_{lane}	N_{road}

Table 5.3: Tags attributed to Corridors

Id of Beginning CP	Id of Ending CP	Length of Corridor
Id_0	Id_n	L_{corr}
Id of corridor	Curve or Line	Stop or Not
Id_{way}	$R_{curve} = \{0, 1\}$	$R_{stop} = \{0, 1\}$

geometric elements: 1,*Node*, which defines points in space. Each node comprises at least an id number and a pair of coordinates. 2,*Way*, which represents linear features and area boundaries and is defined by an ordered list of nodes. 3, *Relation*, which is used to explain how other elements work together. Each element can be attributed to multiple tags to represent different road information.

Road geometry description

The first problem we encountered is how to describe the road geometry with a digital map. Currently, there is no available digital map which has already contained the information about road curvature, road angle and road coefficient. Therefore, we would like to create a new map database. The OSM is a good tool to create new map database. We firstly measured the road curvature, road bank angle and road coefficient [Ghandour, 2011]. Then we put these information in the OSM. In OSM, a road is represented by intensive and consecutive way points. It is unpractical to attribute road information to every way point, due to the huge amount of work needed. We only attribute road information to the points where the road condition changes a lot. These points are called as Critical Point (CP), as critical situation could happen here (roundabout, slippery region or traffic light stop). After the CPs are defined, the vehicle path could be represented by the CPs and the corridors between two CPs [Victorino et al., 2003]. The list of tags we attributed to each CP is illustrated in the Table 5.2. Then the corridors can be obtained by connecting two CPs, as illustrated in Table 5.3.

It is noted that the connections between two CPs can be straight lines or curves.

In order to simplify the representation of the vehicle's travel path, the CPs should be selected carefully and the following assumption is made.

- Hypothesis 1: The CPs are carefully selected so that each corridor is represented by a straight line or a clothoid, defined by equation 5.27;
- Hypothesis 2: The length of each corridor is known;
- Hypothesis 3: The road condition is linearly distributed along the whole length of the corridor, as explained by equation 5.28.

The clothoid is widely used in urban road construction for representing curved road [Kühn, 2013]. They are defined by their begin curvature κ_0 and a constant curvature change rate κ_1 and their total length l. The current curvature of a clothoid after length l_c can be obtained by equation 5.27.

$$\kappa(l_c) = \kappa_0 + \kappa_1 \cdot l_c \tag{5.27}$$

The road information stored in the CPs is manually attributed, then the road information of the point between two CPs is obtained through the linear interpolation method.

$$State_{current} = (1 - \frac{L}{L_{corr}})State_{CP0} + \frac{L}{L_{corr}}State_{CPn} \tag{5.28}$$

where $State$ means the road geometry information listed in Table 5.2, $State = [x\ y\ h\ \mu\ \kappa\ \theta\ \phi\ \rho\ \psi_r]$, the index "*current*" means the current point, "CP_0" represents the beginning point of the corridor and "CP_n" corresponds to the ending point, L is the length between the current position and CP_0.

Vehicle localization

The vehicle location is measured by a differential GPS sensor. However, the GPS has the problem of signal lost. Therefore, the Extended Kalman filter algorithm is employed to incorporate the direct measurement and the integration of speed. The continuous state equations and measurement models are given by equation 5.29.

$$\text{Process model}\quad \begin{bmatrix} \dot{X} \\ \dot{Y} \\ \dot{v}_x \\ \dot{\psi} \\ \ddot{\psi} \end{bmatrix} = \begin{bmatrix} \sin(\psi)\cdot v_x \\ \cos(\psi)\cdot v_x \\ a_x - g\sin\theta \\ \dot{\psi} \\ 0 \end{bmatrix} + noise$$

$$\text{Observation model}:\quad \begin{bmatrix} X_{gps} \\ Y_{gps} \\ v_{gps} \\ \psi_{gps} \\ v_{wheel} \\ \dot{\psi}_{gyro} \end{bmatrix} = \begin{bmatrix} 1 & 0 & 0 & 0 & 0 \\ 0 & 1 & 0 & 0 & 0 \\ 0 & 0 & 1 & 0 & 0 \\ 0 & 0 & 0 & 1 & 0 \\ 0 & 0 & 1 & 0 & 0 \\ 0 & 0 & 0 & 0 & 1 \end{bmatrix} \begin{bmatrix} X \\ Y \\ v_x \\ \psi \\ \dot{\psi} \end{bmatrix} + noise \tag{5.29}$$

where X_{gps}, Y_{gps}, v_{gps}, v_{wheel}, ψ_{gps}, $\dot{\psi}_{gyro}$ are the measurement of GPS receiver and inertial units, ψ is the clockwise angle between the north and the vehicle direction. In this equation, we suppose the lateral speed is negligible in the calculation of displacement.

Map matching

When using the CPs and corridors to represent the path, we have simplified the map matching problem into a one-dimension localization problem, as illustrated in Figure 5.12.

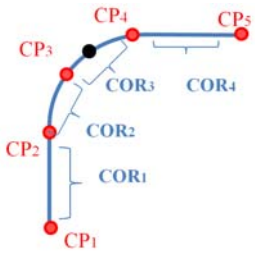

Figure 5.12: Topological representation of vehicle path

The map matching process can be divided into two steps: firstly searching for the corresponding corridor and secondly localizing the vehicle's position in the corridor. In the one-dimension localization problem, the most important information is the total travel length, l_{total}. When the vehicle is at the initial position, the total travel distance (l_{total}) equals to zero. Then the travel distance can be calculated with the Kalman filter

expressed in equation 5.30.

$$\begin{bmatrix} \dot{l}_{total} \end{bmatrix}_{\text{Process model}} = 0 \times [l_{total}] + [v] + noise$$
$$[l_{map}]_{\text{Observation model}} = [l_{total}] \tag{5.30}$$

where v is the speed of the vehicle, l_{map} is the travel distance read from the map, which is explained later by equation 5.33.

Based on the calculated travel distance , the criterion for matching the corridor of number n is given by equation 5.31.

$$\sum_{i=1}^{n-1} L_{corr,i} < l_{total} < \sum_{i=1}^{n} L_{corr,i} \tag{5.31}$$

where $L_{corr,i}$ is the length of the ith corridor.

To further confirm the matching result obtained by equation 5.31, the estimated vehicle current location ($P_{current}$) is used to check whether the vehicle is really within the located corridor. If the following equation is satisfied, then the corridor is regarded as the current corridor. Otherwise the nearby corridors will be checked.

$$dis(P_{current},\ corridor_n) < \varepsilon \tag{5.32}$$

where $dis(\cdot,\cdot)$ means the function to calculate the distance between two points or a point and a straight line, ε is the threshold to decide whether the point is within the corridor.

After the current corridor, $corridor_n$, is identified, we can calculate the travel distance with the information in the map, as expressed in equation 5.33. Then the travel distance obtained from map (l_{map}) is used to correct the accumulated errors in the integration of speed.

$$l_{map} = \frac{dis(P_{current}, CP_{sta})}{dis(P_{current}, CP_{sta}) + dis(P_{current}, CP_{end})} L_{corr,n} + \sum_{i=1}^{n-1} L_{corr,i} \tag{5.33}$$

where CP_{sta} and CP_{end} are the starting and ending points of $corridor_n$, we can find that every time the vehicle passes a CP, the travel distance l_{total} will be calibrated by the map information.

Map Reading

We remember that the reading of the map is based on the travel distance, as previously explained in equation 5.28.

For the reading of current road information, $L = l_{total} - \sum_{i=1}^{n-1} L_{corr,i}$.

For the reading of the future road information, $L = l_{fut} + l_{total} - \sum_{i=1}^{n-1} L_{corr,i}$. where l_{fut} is the distance before vehicle's current position.

After reading these information from the map, we can predict the kinematic parameters of the vehicle with equation 5.34.

$$\begin{aligned} ax_{osm} &= dv_x/dt + g\sin\theta_{osm} \\ ay_{osm} &= v_x^2\kappa_{osm} + g\sin\phi_{osm} \\ az_{osm} &= v_x^2\rho_{osm} + g\cos\theta_{osm}\cos\phi_{osm} \\ \dot{\psi}_{osm} &= v_x\kappa_{osm} \\ \delta_{osm} &= L_v\kappa_{osm} \end{aligned} \tag{5.34}$$

where θ_{osm} and ϕ_{osm} are the slope and bank angle of the road, ρ_{osm} is the vertical curvature of the road, κ_{osm} is the road curvature.

The most important information from the map is the curvature of road, κ_{osm}. If the vehicle follows the road curve, κ_{osm} could be regarded as the curvature of vehicle's trajectory. The lane changing behavior can be viewed as a noise of the κ_{osm}. The noise variance of κ_{osm} is set as 0.03^2. When κ_{osm} is the curvature at current point, equation 5.34 is an redundant resource of current dynamics states. When κ_{osm} is the curvature at future point, the obtained accelerations and yaw rates are used to anticipate the tire forces.

5.4.3 Risk assessment

In order to evaluate vehicle's safety, we employ three risk assessment indexes: load transfer ratio (LTR) and lateral skid ratio (LSR), and the stopping distance (SD) [Imine and Dolcemascolo, 2007]. These risk assessments are based on the awareness of tire forces. The estimation of vertical and lateral tire forces and slip angle are already explained in Chapter 4. The lateral load transfer ratio LTR is defined by using four wheel vertical forces as in equation (5.35).

$$LTR = \frac{F_{z11} - F_{z12} + F_{z21} - F_{z22}}{F_{z11} + F_{z12} + F_{z21} + F_{z22}} \tag{5.35}$$

The lateral skid ratio LSR represents the loss of adhesion resulting in the lateral drift. The lateral skid ratio is defined by road friction coefficient and tire forces, as in equation 5.36.

$$\begin{aligned} LSR_{ij} &= 1 - \frac{\mu_{max} - \mu_{ij}}{\mu_{max}} \\ \mu_{ij} &= \frac{F_{yij}}{F_{zij}} \end{aligned} \tag{5.36}$$

where μ_{max} is the threshold of safe friction, it should be smaller than the real friction coefficient.

The stopping distance (SD) refers to the distance needed to stop the vehicle. We assume that during the stopping process, the braking acceleration is a constant value a_{xmax}. The a_{xmax} is defined as to ensure the comfort of passengers. The stopping distance can be obtained by equation 5.37.

$$SD = \frac{1}{2a_{xmax}} v_x^2 + v_x t_e \tag{5.37}$$

where t_e is driver's response time delay.

5.4.4 Prediction Algorithm

The overall prediction process can be expressed by the Figure 5.13.

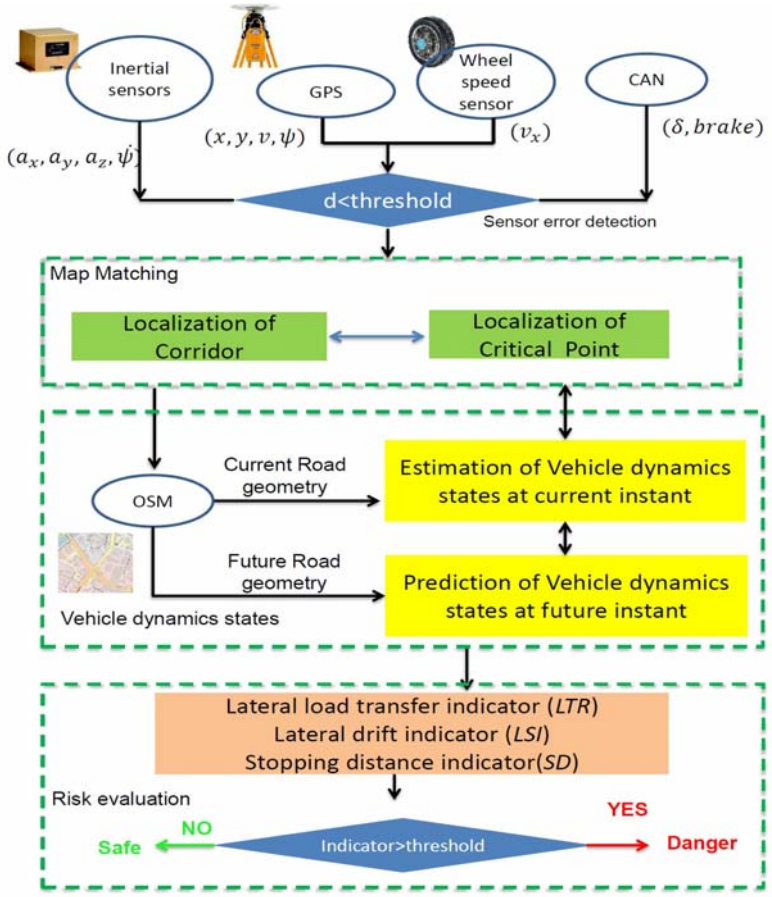

Figure 5.13: Overall structure of vehicle safety prediction system

The sensor measurements are used to locate the vehicle's position and identify the corresponding corridors and CPs. Then CPs can provide information about road friction coefficient which can improve the the estimation of current states. Moreover, by extracting the upcoming CPs, the estimator could anticipate the potential variation of

dynamics states. Then the dynamics states of current instant and future instant will be evaluated by three indicators of safety, introduced in the above section. To simplify the prediction process, the vehicle keeps the current speed during the coming road. The prediction system will perform the risk assessment for the coming 300m road. If a potential danger is detected, the system will warn the driver to slow down.

5.4.5 Experimental Validation

Our current map database only contains the information about the road near our school, as shown in Figure 5.14. In the experiment, the vehicle has followed the trajectory indicated in this figure. The prediction algorithm was implemented in Matlab and validated by using the experimental data from this test.

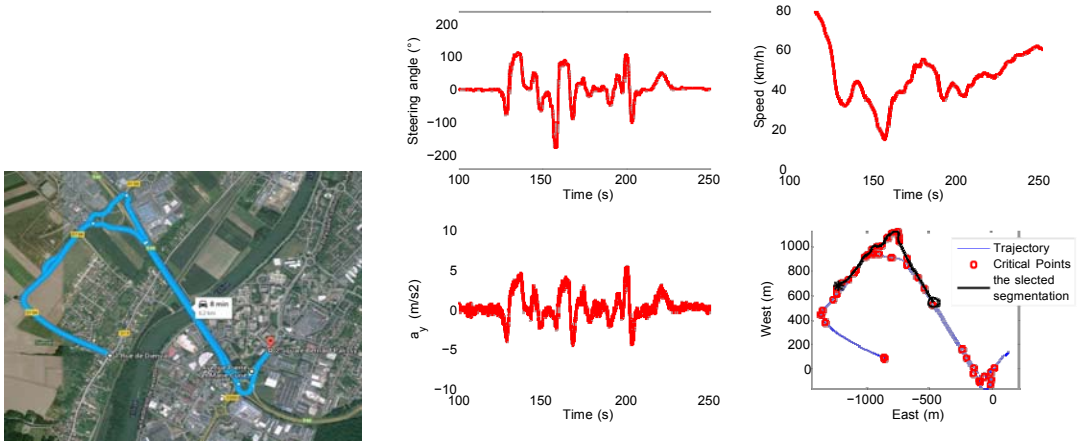

Figure 5.14: Vehicle's trajectory and maneuver time history: at $t = 150s$, the vehicle is at the point of black circle, $t = 250s$, the vehicle is at the point of black star.

In total, 53 critical points and 52 corridors were defined to describe the trajectory. More CPs were defined around the sharp turning and road intersection in order to better describe the road. Some examples of CPs and corridors are demonstrated in Table 5.4. A segmentation of data ($150 < t < 250s$) is selected due to the successive turning behaviors in this period, represented by the black line in Figure 5.14. The maneuver time history are presented by red lines in Figure 5.14. The average speed is about 50 km/h. The curvature at each critical point is illustrated by red spots in Figure 5.15. As we can see in this figure, the interpolation method (represented by red lines) was a simplification of real road geometry and was not always accurate. However, it effectively represented the main characteristic of the road. In the bottom of Figure 5.15, we also demonstrated the result of localization. We have successfully estimated the travel distance, and therefore we were able to read the geometry information about the road.

CP ID	x(m)	y(m)	h(m)	ψ_r(-)	κ	ρ	μ_{max}	ϕ(-)	θ(-)
:	:	:	:	:	:	:	:	:	:
7	-717.7	986.7	52.6	333.3	0	0	1	0	5
8	-748.1	1066.1	56.8	2.1	-0.031	0	1	0	0
9	-743.6	1103.3	57.0	343.7	0.046	0	1	0	0
:	:	:	:	:	:	:	:	:	:

Corridor Id	Id_0	Id_n	L_{corr}(m)	R_{curve}	R_{stop}
:	:	:	:	:	:
5	5	6	690	0	0
6	6	7	270	0	0
7	7	8	85	1	1
:	:	:	:	:	:

Table 5.4: The construction of Critical points and corridors

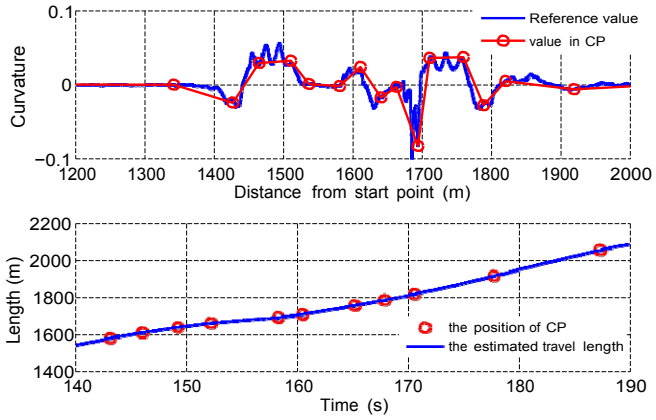

Figure 5.15: The value of curvature stored in each Critical Point

The obtained curvature was used to compute the value of accelerations and yaw rate with equation 5.34. The comparison between inertial sensor measurement and digital map based (OSM) estimation was illustrated in Figure 5.16. Then two data are incorporated to provide a robust estimation about the basic dynamics parameters, as represented by the green lines in the same figure. The obtained kinematic parameters were used to estimate the tire forces and sideslip angle with the observers developed in chapter 4. The estimation results of tire forces are compared with the measurement of force transducer in Figure 5.17. The red lines are the measurement data. The green lines represented the estimation result based on inertial sensors. The blue lines correspond to the estimation result based on the OSM. The accuracy of the OSM method depends on the intensity of critical points and map quality. Moreover, it is also based on the

condition whether the vehicle has successfully followed the planned path.

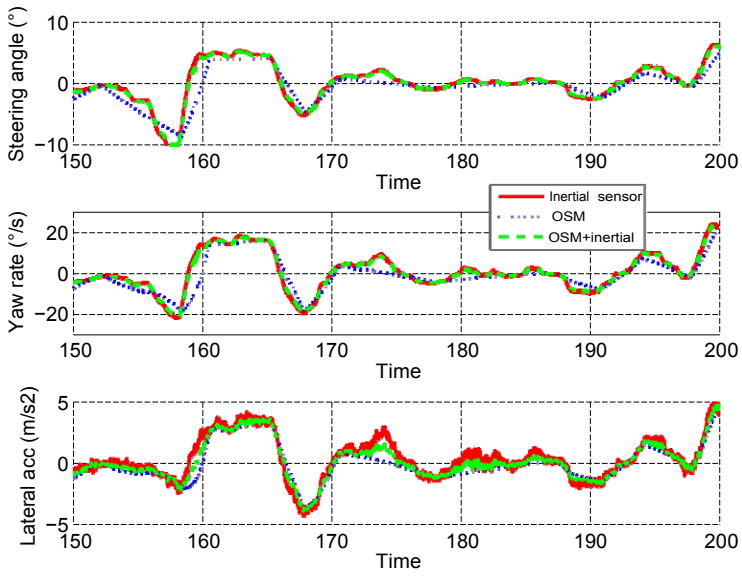

Figure 5.16: Comparison of lateral dynamics states estimated by inertial sensors and OSM

At $t = 175s$, the driver did a lane changing behavior, which was not in the planning and caused some errors. As demonstrated by the experimental result, the inertial sensor based method can better follow the vertical force variation, while, the OSM based estimation method is accurate when the vehicle is following the curve. Fusion of these two estmation provides a better estimation of vertical force, as expressed by solid black lines in the Figure 5.17.a). The similar situation can be found in the estimation of lateral force. The advantage of OSM is obvious in the estimation of sideslip angle. The OSM method could get the correct C_r from the digital map. It is clear that the combined method provided a better estimation of sideslip angle.

Every time we localized the vehicle's position, we also got the curvature of the following 300 meters ahead of the vehicle's current position. Then these information was used to predict the vehicle dynamics states with equation 5.34. And the vehicle's safety was evaluated with the index introduced by equation 5.35-5.37. Figure 5.18 illustrated the prediction of vehicle's safety situation in the following 300 meters at instant $t = 160\,s$ and $t = 180\,s$. The results showed at instant t=180s, the algorithm detected potential dangers in the upcoming path.

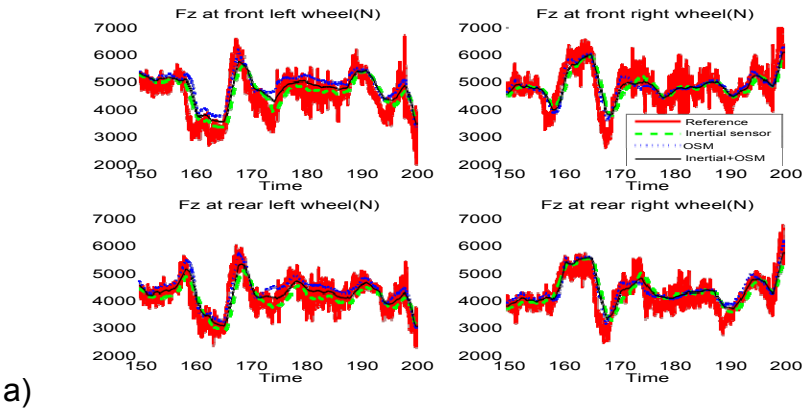

a)

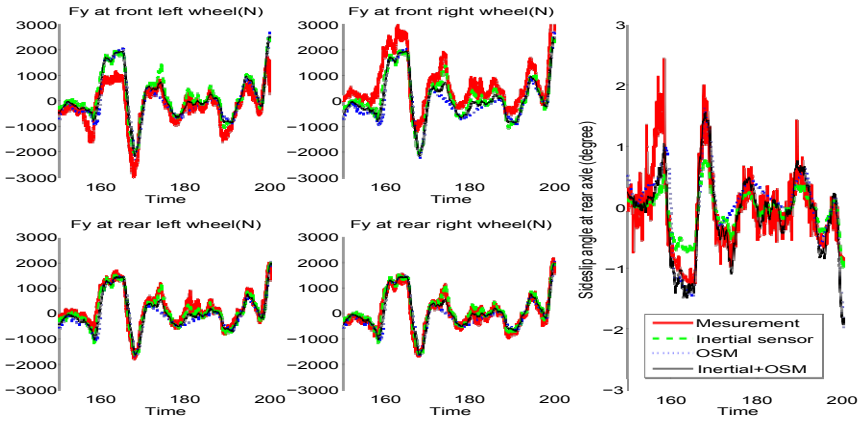

b)

Figure 5.17: a) Estimation of of vertical forces at each tire; b) Estimation of lateral forces at each tire: comparison between sensor measurement and estimation

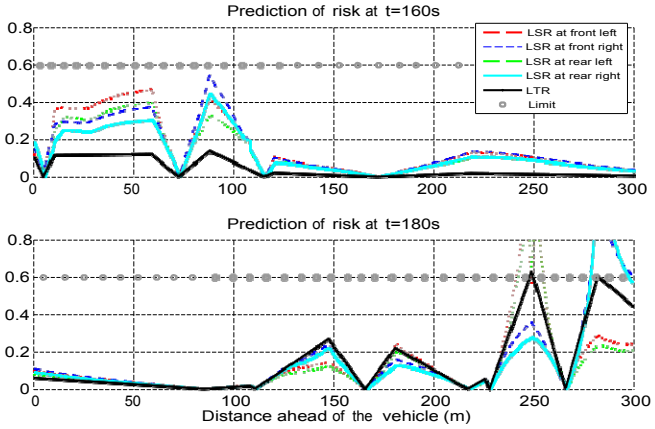

Figure 5.18: Prediction of vehicle safety in the following 300 meters road

5.5 Conclusion

This chapter considers the estimation problem in a more challenging and realistic context, which is to consider the presence of sensor errors and the variation of vehicle parameters. The vehicle speed, accelerations, yaw rate and other basic sensor measurements are usually regarded as available from the sensors. In real driving scenario, it is quite possible that these sensors may contain fatal errors resulting in the malfunction of observers. In order to make the observers robust even in presence of sensor errors, we propose to use the Kalman filter to improve the accuracy of these basic measurements. In this thesis, these basic vehicle dynamic states are estimated with different models. Besides the errors of sensors, the variation of vehicle physical parameters could also introduce significant errors in the estimation. The vehicle mass and the position of CoG are the key parameters to estimate vertical forces at each tire. The sideslip stiffness and the road grad angle have great impact on vehicle's lateral dynamics. These physical parameters are usually regarded as constant values. In this chapter, we proposed several models to calculate these parameters. Then the RLS algorithm is employed to improve the estimation of parameters.

Another contribution presented in this chapter is to propose an algorithm to improve the estimation and prediction of vehicle's dynamics states by incorporating the knowledge of the environment around the vehicle, provided by a digital map. The current and future road information was obtained from the digital map after the localization process. Then the vehicles models and map data are combined to evaluate the safety of the vehicle, from the evaluation of the risk indicators in a diagnosis algorithm. Experimental results validated the proposed algorithm. The future work will focus on the improvement of map quality and localization accuracy.

6 Conclusion And Perspectives

6.1 Conclusions

More and more intelligent vehicle safety systems have been developed in the university laboratories and research centers. To reduce the complexity of problem, many intelligent systems can only work in a limited speed and a simplified scenario. Expansion of these intelligent systems from the early-stage development into the real application requires an accurate estimation of the vehicle dynamics states in uncertain environments. This requirement mainly involves three challenging problems: 1, extract useful information about the immeasurable dynamics states from the limited measurements; 2, stay robust and accurate against the uncertain disturbances caused by the sensors or the environment; 3, provide state estimation and risk prediction in real time. Specifically, the mentioned immeasurable dynamics states include the tire forces and the sideslip angle. Current and future vehicle control systems would benefit from knowledge of these fundamental variables of the vehicle's handling. In this thesis, our solution to the three challenging problems can be briefly concluded as one word: **Observer**. However, construction of an observer which could provide satisfactory performance at all condition is never simple. It requires: 1, accurate and efficient models; 2, a well-developed estimation algorithm; 3, more sources of reliable information. As motivated by these requirements, this dissertation was organized to present our contribution in three aspects: vehicle dynamics modelization, observer design and multi-sensor fusion.

Chapter 2 reviewed the state of the art in the field of vehicle dynamics modeling and proposed some novel models to reduce the model errors caused by the road condition. The role of modelization is to find the relationship between the unmeasured states and the measured states. It is the fundamental step to extract information from the available measurements. The existent models are obtained by simplifying the vehicle motion as a planar motion. In the proposed models, we described the vehicle motion as a 3D motion and considered the effects of road inclination. We also proposed to incorporate the suspension deflection to calculate the transfer of vertical load as suspension is more sensitive to the variation of vertical load. For the lateral dynamics, we proposed the model of transfer of lateral forces to describe the force difference between left wheel and right wheel. With this new model, the lateral force at each tire can be calculated without sideslip angle. Moreover, this model is insensitive to the variation of road angles.

Similarly, we have also proposed the model of transfer of longitudinal forces to calculate the longitudinal force at each tire.

Chapter 3 reviewed the basic concepts in estimation theory. The estimation theory is to minimize the estimation errors in a statistical way. The dissertation is started by the estimation of constant parameters. The Minimum Variance Unbiased estimator and Minimum Mean Square estimator were introduced and compared. In order to realize real-time estimation, the sequential estimation algorithm was also presented. Then we introduced the technique for estimation of time-varying parameters, which is called the observer technique. The algorithms of Kalman Filter, Extended Kalman filter, Unscented Kalman Filter and Particle Filter were reviewed and compared in this chapter. In order to be more intuitive, we provided a new interpretation of these observer techniques based on the Bayesian philosophy.

Chapter 4 presented the details about the observers we developed for the estimation of tire forces and sideslip angle. The construction of observers was based on the models and observer techniques introduced in the former chapters. The main contribution of this chapter is the design of the overall structure of the observer system. The tire forces in three direction and the sideslip angle are observed by four individual observers while connected in a cascaded way. The selective communication mechanism has prevented the fatal errors of one observer from being transferred to other observers. Furthermore, we designed an algorithm to change the covariance of model noises according to the road condition and driving maneuvers. Another difficulty of the estimation is to consider the non-linearity of lateral dynamics. We developed three different non-linear observers for estimation of lateral forces by employing EKF, UKF and PF respectively. These observers were programmed in C++ as a real-time application and embedded in our experimental vehicle DYNA. Then experimental data in several critical tests was presented to compare and validate the performance of our observers.

Chapter 5 presented the algorithms to further improve the accuracy of estimation in the context of disturbance caused by parameter variation and sensor errors. The key to filter out sensor errors is to find another source of reliable information, which could be an additional sensor or a new model. In this thesis, we preferred to use as less sensors as possible. Therefore, we proposed many models to compute each kinematic state with different sensors. Then information obtained through different models and sensors was incorporated to obtain the optimal estimation. The fusion of multiple sensors was more robust than the measurement of one sensor. In addition, we have also proposed the models to estimate the vehicle parameters, such as the vehicle mass, position of CoG, road angle and so on. However, these models are only valid in several simplified scenarios. In order to get road information more easily, we proposed to take advantage of the digital map. The road angle, road surface condition and road curvature was extracted from the digital map and was used for the estimation and prediction of tire forces. A risk prediction system was developed based on the predicted tire forces to

evaluate potential risk. It is highlighted that the use of digital map enables the system to anticipate the vehicle dynamics in the future instant and avoid the potential accidents. Experimental data was presented to validate our algorithm.

6.2 Future work

The following points are quite interesting for the future work:

- Improvement of the models of transfer of lateral forces (T_{Fy}) and transfer of longitudinal forces (T_{Fx}). The classic tire models concentrate on the single tire-road characteristics. In reality, the four tires are not moving freely but connected with the vehicle body. The motion and forces of each tire are highly interdependent. To study the interaction between the four tires is quite meaningful for understanding the behavior of a driving car. The model of T_{Fx} and T_{Fy} proposed in this thesis is our attempt to describe the interaction between left tire and right tire. However, these models are a simplification of the real problem. We suppose the interaction between tires is only determined by the load transfer, the steering angle and the acceleration. In order to improve the accuracy of estimation, further development of the models describing tire interaction is needed.
- Utilization of the data of the past. All efforts in this dissertation is devoted to the real-time estimation of vehicle dynamics. All the observers developed in this thesis is based on sequential estimation algorithm. However, some useful information can be extracted in an off-line way. For example, employing the machine learning to extract the road friction or the driver's habits.
- Incorporation of the information obtained through computer vision. The difficulty of estimating the sideslip angle is mainly caused by the lack of information about vehicle's lateral speed. However, it is possible to detect the lateral motion of vehicle with the cameras. Furthermore, the vision-based method to estimate the road angles is also proposed in the literature. It is believed that the fusion of camera could enhance the accuracy of the estimation.
- Improvement of the accuracy of localization. The localization is the fundamental step to use a digital map. The passed trajectory and the data of vision should be combined to improve the map matching and localization.
- Application of these observers in the vehicle motion control. This relates to another huge topic, the design of controllers. The various information provided by our observers could help the controllers make a better decision in order to ensure the stability and safety of the vehicle.

Bibliography

[Ahn et al., 2012] Ahn, C., Peng, H., and Tseng, H. E. (2012). Robust estimation of road friction coefficient using lateral and longitudinal vehicle dynamics. *Vehicle System Dynamics*, 50(6):961–985.

[Aitken, 1936] Aitken, A. C. (1936). Iv.âon least squares and linear combination of observations. *Proceedings of the Royal Society of Edinburgh*, 55:42–48.

[Altmannshofer et al., 2016] Altmannshofer, S., Endisch, C., Martin, J., GerngroÃ, M., and Limbacher, R. (2016). Robust estimation of vehicle longitudinal dynamics parameters. In *Intelligent Vehicles Symposium (IV), 2016 IEEE*. IEEE.

[Andrieu et al., 2011] Andrieu, C., Jasra, A., Doucet, A., Del Moral, P., et al. (2011). On nonlinear markov chain monte carlo. *Bernoulli*, 17(3):987–1014.

[Baffet, 2007] Baffet, G. (2007). *Développement et validation expérimentale d'observateurs des forces du contact pneumatique/chaussée d'une automobile*. PhD thesis, Université de Technologie de Compiègne.

[Batavia, 1999] Batavia, P. H. (1999). *Driver-adaptive lane departure warning systems*. PhD thesis, Carnegie Mellon University.

[Beadle and Djuric, 1997] Beadle, E. R. and Djuric, P. M. (1997). A fast-weighted bayesian bootstrap filter for nonlinear model state estimation. *Aerospace and Electronic Systems, IEEE Transactions on*, 33(1):338–343.

[Bevly et al., 2001] Bevly, D. M., Sheridan, R., and Gerdes, J. C. (2001). Integrating ins sensors with gps velocity measurements for continuous estimation of vehicle sideslip and tire cornering stiffness. In *Proceedings of the 2001 American Control Conference*, volume 1, pages 25–30. IEEE.

[Bouton et al., 2007] Bouton, N., Lenain, R., Thuilot, B., and Fauroux, J.-C. (2007). A rollover indicator based on the prediction of the load transfer in presence of sliding: application to an all terrain vehicle. In *Proceedings 2007 IEEE International Conference on Robotics and Automation*, pages 1158–1163. IEEE.

[Boyden and Velinsky, 1994] Boyden, F. D. and Velinsky, S. A. (1994). Dynamic modeling of wheeled mobile robots for high load applications. In *Robotics and*

Automation, 1994. Proceedings., 1994 IEEE International Conference on, pages 3071–3078. IEEE.

[C. and M., 2007] C., O. and M., G. (2007). Selection of the most similar image in a database for critical structures segmentation. In *Proceedings of the 10th Int. Conf. on Medical Image Computing and Computer-Assisted Intervention - MICCAI 2007, Part II*, volume 4792 of *LNCS*, pages 203–210. Springer Verlag.

[Candy, 2007] Candy, J. V. (2007). Bootstrap particle filtering. *IEEE Signal Processing Magazine*, 24(4):73–85.

[Chen and Hsieh, 2008] Chen, B. C. and Hsieh, F. C. (2008). Sideslip angle estimation using extended kalman filter. *Vehicle System Dynamics*, 46(S1):353–364.

[Cheng et al., 2011] Cheng, Q., Victorino, A., and Charara, A. (2011). Nonlinear observer of sideslip angle using a particle filter estimation methodology. In *IFAC World Congress, Milan, Italy*.

[Cho et al., 2010] Cho, W., Yoon, J., Yim, S., Koo, B., and Yi, K. (2010). Estimation of tire forces for application to vehicle stability control. *Vehicular Technology, IEEE Transactions on*, 59(2):638–649.

[Clark, 1981] Clark, S. K. (1981). *Mechanics of pneumatic tires*. US Department of Transportation, National Highway Traffic Safety Administration.

[Cramér, 1947] Cramér, H. (1947). Mathematical methods of statistics.

[Cunha et al., 2011] Cunha, F., Victorino, A., Ghandour, R., and Charara, A. (2011). Vehicle dynamics prediction based on state observers entries anticipation. In *IFAC World Congress*, volume 18, pages 2260–2265.

[Dahmani et al., 2013] Dahmani, H., Chadli, M., Rabhi, A., and El Hajjaji, A. (2013). Vehicle dynamic estimation with road bank angle consideration for rollover detection: theoretical and experimental studies. *Vehicle System Dynamics*, 51(12):1853–1871.

[Dahmani et al., 2010] Dahmani, H., Chadli, M., Rabhi, A., and Hajjaji, A. (2010). Fuzzy uncertain observer with unknown inputs for lane departure detection. In *2010 American Control Conference (ACC)*, pages 688–693.

[Dakhlallah et al., 2008] Dakhlallah, J., Glaser, S., Mammar, S., and Sebsadji, Y. (2008). Tire-road forces estimation using extended kalman filter and sideslip angle evaluation. In *American Control Conference, 2008*, pages 4597–4602.

[Dherbomez et al., 2013a] Dherbomez, G., Monglon, T., Crubillé, P., Wang, B., Victorino, A. C., and Charara, A. (2013a). Dyna, véhicule expérimental pour la dynamique du véhicule. *Quatrièmes Journées des Démonstrateurs en Automatique*.

[Dherbomez et al., 2013b] Dherbomez, G., Monglon, T., Crubillé, P., Wang, B., Victorino, A. C., and Charara, A. (2013b). Dyna, véhicule expérimental pour la dynamique du véhicule. *Quatrièmes Journées des Démonstrateurs en Automatique*.

[Ding et al., 2006] Ding, E., Massel, T., and Ding, S. (2006). Estimation of vehicle pitch angle. *ATZ worldwide*, 108(2):22–24.

[Ding and Taheri, 2010] Ding, N. and Taheri, S. (2010). A modified dugoff tire model for combined-slip forces. *Tire Science and Technology*, 38(3):228–244.

[Douc and Cappe, 2005] Douc, R. and Cappe, O. (2005). Comparison of resampling schemes for particle filtering. In *Proceedings of the 4th International Symposium on Image and Signal Processing and Analysis*, pages 64–69.

[Doucet et al., 2001] Doucet, A., De Freitas, N., and Gordon, N. (2001). An introduction to sequential monte carlo methods. In *Sequential Monte Carlo methods in practice*, pages 3–14. Springer.

[Doumiati, 2009] Doumiati, M. (2009). *Estimation embarquée des effors verticaux et latéraux d'un véhicule pour le diagnostic du comportement sur route*. PhD thesis, Université de Technologie de Compiègne.

[Doumiati et al., 2008] Doumiati, M., Victorino, A., Charara, A., Baffet, G., and Lechner, D. (2008). An estimation process for vehicle wheel-ground contact normal forces. *IFAC Proceedings Volumes*, 41(2):7110–7115.

[Doumiati et al., 2009] Doumiati, M., Victorino, A., Charara, A., and Lechner, D. (2009). Lateral load transfer and normal forces estimation for vehicle safety: experimental test. *Vehicle System Dynamics*, 47(12):1511–1533.

[Doumiati et al., 2010] Doumiati, M., Victorino, A., Lechner, D., Baffet, G., and Charara, A. (2010). Observers for vehicle tyre/road forces estimation: experimental validation. *Vehicle System Dynamics*, 48(11):1345–1378.

[Dugoff et al., 1969] Dugoff, H., Fancher, P. S., and Segel, L. (1969). *Tire performance characteristics affecting vehicle response to steering and braking control inputs*.

[Eckermann, 2001] Eckermann, E. (2001). World history of the automobile. *Training*, 2011:04–20.

[Eric Tseng et al., 2007] Eric Tseng, H., Xu, L., and Hrovat, D. (2007). Estimation of land vehicle roll and pitch angles. *Vehicle System Dynamics*, 45(5):433–443.

[Fischer and Isermann, 2004] Fischer, D. and Isermann, R. (2004). Mechatronic semi-active and active vehicle suspensions. *Control engineering practice*, 12(11):1353–1367.

[Fukada, 1999] Fukada, Y. (1999). Slip-angle estimation for vehicle stability control. *Vehicle System Dynamics*, 32(4-5):375–388.

[Gadola et al., 2014] Gadola, M., Chindamo, D., Romano, M., and Padula, F. (2014). Development and validation of a kalman filter-based model for vehicle slip angle estimation. *Vehicle System Dynamics*, 52(1):68–84.

[Ghandour, 2011] Ghandour, R. (2011). *Diagnostic et évaluation anticipée des risques de rupture d'itinéraire basés sur l'estimation de la dynamique du véhicule*. PhD thesis, Université de Technologie de Compiègne.

[Ghandour et al., 2011] Ghandour, R., da Cunha, F. H., Victorino, A., Charara, A., and Lechner, D. (2011). A method of vehicle dynamics prediction to anticipate the risk of future accidents: Experimental validation. In *2011 14th International IEEE Conference on Intelligent Transportation Systems (ITSC)*, pages 1692–1697. IEEE.

[Gilks et al., 1995] Gilks, W. R., Best, N., and Tan, K. (1995). Adaptive rejection metropolis sampling within gibbs sampling. *Applied Statistics*, pages 455–472.

[Glaser et al., 2007] Glaser, S., Nouveliere, L., and Lusetti, B. (2007). Speed limitation based on an advanced curve warning system. In *Intelligent Vehicles Symposium, 2007 IEEE*, pages 686–691.

[Gordon et al., 1993] Gordon, N. J., Salmond, D. J., and Smith, A. F. M. (1993). Novel approach to nonlinear/non-gaussian bayesian state estimation. *IEEE Proceedings on Radar and Signal Processing*, 140(2):107–113.

[Grip et al., 2009] Grip, H. F., Imsland, L., Johansen, T. A., Kalkkuhl, J. C., and Suissa, A. (2009). Vehicle sideslip estimation. *IEEE Control Systems*, 29(5):36–52.

[Gruber, 1997] Gruber, M. H. (1997). Statistical digital signal processing and modeling. *Technometrics*, 39(3):335–336.

[Gruber et al., 2012] Gruber, P., Sharp, R. S., and Crocombe, A. D. (2012). Normal and shear forces in the contact patch of a braked racing tyre. part 2: development of a physical tyre model. *Vehicle System Dynamics*, 50(3):339–356.

[Guermah et al., 2008] Guermah, S., Djennoune, S., and Bettayeb, M. (2008). Controllability and observability of linear discrete-time fractional-order systems. *International Journal of Applied Mathematics and Computer Science*, 18(2):213–222.

[Guimond et al., 2000] Guimond, A., Meunier, J., and Thirion, J. P. (2000). Average brain models: A convergence study. *Computer Vision and Image Understanding*, 77(2):192–210.

[Guldner et al., 1996] Guldner, J., Tan, H.-S., and Patwardhan, S. (1996). Analysis of automatic steering control for highway vehicles with look-down lateral reference systems. *Vehicle System Dynamics*, 26(4):243–269.

[Hac, 2004] Hac, A. (2004). Influence of active chassis systems on vehicle propensity to maneuver-induced rollovers. *PROGRESS IN TECHNOLOGY*, 101:60–67.

[Hac et al., 2004] Hac, A., Brown, T., and Martens, J. (2004). Detection of vehicle rollover. *Vehicle Dynamics & Simulation*.

[Haklay and Weber, 2008] Haklay, M. and Weber, P. (2008). Openstreetmap: User-generated street maps. *IEEE Pervasive Computing*, 7(4):12–18.

[Haykin et al., 2001] Haykin, S. S. et al. (2001). *Kalman filtering and neural networks*. Wiley Online Library.

[Hentschel and Wagner, 2010] Hentschel, M. and Wagner, B. (2010). Autonomous robot navigation based on openstreetmap geodata. In *Intelligent Transportation Systems (ITSC), 2010 13th International IEEE Conference on*, pages 1645–1650. IEEE.

[Hermann and Krener, 1977] Hermann, R. and Krener, A. J. (1977). Nonlinear controllability and observability. *IEEE Transactions on automatic control*, 22(5):728–740.

[Heydinger et al., 1991] Heydinger, G. J., Garrott, W. R., and Chrstos, J. P. (1991). The importance of tire lag on simulated transient vehicle response. Technical report, SAE Technical Paper.

[Hol et al., 2006] Hol, J. D., Schon, T. B., and Gustafsson, F. (2006). On resampling algorithms for particle filters. In *2006 IEEE Nonlinear Statistical Signal Processing Workshop*, pages 79–82.

[Holmes and Stone, 1969] Holmes, K. and Stone, R. (1969). Tyre forces as functions of cornering and braking slip on wet road surfaces. In *Handling of vehicles under emergency conditions.*

[Hsu and Chen, 2009] Hsu, L. Y. and Chen, T. L. (2009). Vehicle full-state estimation and prediction system using state observers. *IEEE Transactions on Vehicular Technology*, 58(6):2651–2662.

[Imine and Dolcemascolo, 2007] Imine, H. and Dolcemascolo, V. (2007). Rollover risk prediction of heavy vehicle in interaction with infrastructure. *International Journal of Heavy Vehicle Systems*, 14(3):294–307.

[Imine and Dolcemascolo, 2008] Imine, H. and Dolcemascolo, V. (2008). Sliding mode observers to heavy vehicle vertical forces estimation. *International Journal of Heavy Vehicle Systems*, 15(1):53–64.

[Jiang et al., 2015] Jiang, K., Victorino, A. C., and Charara, A. (2015). Adaptive estimation of vehicle dynamics through rls and kalman filter approaches. In *2015 IEEE 18th International Conference on Intelligent Transportation Systems*, pages 1741–1746. IEEE.

[Jun et al., 2010] Jun, L., Sumei, W., Ke, P., Jun, X., Yun, W., and Tao, Z. (2010). Research on on-line measurement and prediction for vehicle motion state. In *2010 International Conference on Digital Manufacturing and Automation (ICDMA)*, volume 2, pages 247–250.

[Kalman et al., 1960] Kalman, R. E. et al. (1960). A new approach to linear filtering and prediction problems. *Journal of basic Engineering*, 82(1):35–45.

[Kawashima et al., 2010] Kawashima, K., Hori, Y., Uchida, T., and Sehoon, O. (2010). Robust bank angle estimation for rolling stability control on electric vehicle. In *2010 11th IEEE International Workshop on Advanced Motion Control*, pages 448–453.

[Khalil, 2002] Khalil, H. K. (2002). *Nonlinear systems*, volume 3. Prentice hall Upper Saddle River.

[Kiencke and Nielsen, 2005] Kiencke, U. and Nielsen, L. (2005). *Automotive Control Systems For Engine, Driveline, and Vehicle*. Springer.

[Kim, 2009] Kim, J. (2009). Identification of lateral tyre force dynamics using an extended kalman filter from experimental road test data. *Control Engineering Practice*, 17(3):357–367.

[Kitagawa, 1996] Kitagawa, G. (1996). Monte carlo filter and smoother for non-gaussian nonlinear state space models. *Journal of computational and graphical statistics*, 5(1):1–25.

[Klomp et al., 2014] Klomp, M., Gao, Y., and Bruzelius, F. (2014). Longitudinal velocity and road slope estimation in hybrid electric vehicles employing early detection of excessive wheel slip. *Vehicle System Dynamics*, 52(sup1):172–188.

[Kühn, 2013] Kühn, W. (2013). *Fundamentals of road design*, volume 20. WIT Press.

[Lechner, 2002] Lechner, D. (2002). *Analyse du comportement dynamique des véhicules routiers légers: développement d'une méthodologie appliquée à la sécurité primaire*. PhD thesis, Ecole Centrale de Lyon.

[Leung et al., 2011] Leung, K. T., Whidborne, J. F., Purdy, D., and Barber, P. (2011). Road vehicle state estimation using low-cost gps/ins. In *Mechanical Systems and Signal Processing*, volume 25, pages 1988–2004.

[Li et al., 2008] Li, K., Tan, H. S., Misener, J. A., and Hedrick, J. K. (2008). Digital map as a virtual sensor–dynamic road curve reconstruction for a curve speed assistant. *Vehicle System Dynamics*, 46(12):1141–1158.

[Li et al., 2014a] Li, L., Jia, G., Ran, X., Song, J., and Wu, K. (2014a). A variable structure extended kalman filter for vehicle sideslip angle estimation on a low friction road. *Vehicle System Dynamics*, 52(2):280–308.

[Li et al., 2010] Li, L., Li, H., Zhang, X., He, L., and Song, J. (2010). Real-time tire parameters observer for vehicle dynamics stability control. *Chinese Journal of Mechanical Engineering*, 23(5):620–626.

[Li et al., 2014b] Li, X., Song, X., and Chan, C. (2014b). Reliable vehicle sideslip angle fusion estimation using low-cost sensors. *Measurement*, 51:241–258.

[Liu and Ye, 2011] Liu, C. and Ye, T. J. (2011). Run-off-road crashes: an on-scene perspective. Technical report.

[Mammar et al., 2006] Mammar, S., Glaser, S., and Netto, M. (2006). Time to line crossing for lane departure avoidance: a theoretical study and an experimental setting. *IEEE Transactions on Intelligent Transportation Systems*, 7(2):226–241.

[Manwaring, 1966] Manwaring, L. A. (1966). *The Observer's Book of Automobiles (12th ed.)*. Library of Congress.

[Menhour, 2010] Menhour, L. (2010). *Synthse de commandes au volant d'une automobile pour le diagnostic de rupture d'un itinéraire. Développement et validation expérimentale*. PhD thesis, Université de Technologie de Compiègne.

[Menhour et al., 2011] Menhour, L., Lechner, D., and Charara, A. (2011). Steering control and road bank angle estimation to evaluate the vehicle behaviour under high dynamic loads: Experimental evaluation. In *Proceedings of the 18th World Congress of the International Federation of Automatic Control (IFAC WC 2011), Milano, Italy*.

[Milanese et al., 2004] Milanese, M., Novara, C., Mastronardi, F., and Amoroso, D. (2004). Experimental modeling of vertical dynamics of vehicles with controlled suspensions. In *SAE world congress,*, Detroit, Michigan.

[Milliken et al., 2003] Milliken, D. L., Kasprak, E. M., Metz, L. D., and Milliken, W. F. (2003). *Race car vehicle dynamics*. SAE International.

[Nam et al., 2013] Nam, K., Oh, S., Fujimoto, H., and Hori, Y. (2013). Estimation of sideslip and roll angles of electric vehicles using lateral tire force sensors through rls and kalman filter approaches. *IEEE Transactions on Industrial Electronics*, 60(3):988–1000.

[NHTSA, 2013] NHTSA (August 2013). Early estimate of motor vehicle traffic fatalities for the first quarter of 2013.

[Nilsson and Lingefelt, 2011] Nilsson, A. and Lingefelt, H. (2011). Estimation of vehicle roll angle.

[Oakes, 1999] Oakes, D. (1999). Direct calculation of the information matrix via the EM algorithm. *J. R. Statistical Society*, 61(2):479–482.

[Oh and Choi, 2013] Oh, J. and Choi, S. B. (2013). Vehicle roll and pitch angle estimation using a cost-effective six-dimensional inertial measurement unit. *Proceedings of the Institution of Mechanical Engineers, Part D: Journal of Automobile Engineering*, 227(4):577–590.

[ONISR, 2015] ONISR (2015). La sÃ➞curitÃ➞ routiÃšre en france. bilan de l'accidentalitÃ➞ de l'annÃ➞e 2015, www.securite-routiere.gouv.fr. Technical report.

[Otso et al., 2016] Otso, J., Yi, X., Niskanen, A., and Tuononen, A. (2016). Energy harvesting system for intelligent tyre sensors. In *Intelligent Vehicles Symposium (IV), 2016 IEEE*. IEEE.

[Ouahi et al., 2013] Ouahi, M., Stéphant, J., and Meizel, D. (2013). Simultaneous observation of the wheelsâ torques and the vehicle dynamic state. *Vehicle System Dynamics*, 51(5):737–766.

[Pacejka, 2006] Pacejka, H. B. (2006). *Tire and Vehicle Dynamics*. SAE International, second edition.

[Pacejka et al., 1987] Pacejka, H. B., Bakker, E., and Nyborg, L. (1987). Tyre modelling for use in vehicle dynamics studies. *SAE paper*, 870421.

[Pacejka and Sharp, 1991] Pacejka, H. B. and Sharp, R. S. (1991). Shear force development by pneumatic tyres in steady state conditions: a review of modelling aspects. *Vehicle system dynamics*, 20(3-4):121–175.

[Phanomchoeng, 2011] Phanomchoeng, G. (2011). *State, Parameter, and Unknown Input Estimation Problems in Active Automotive Safety Applications*. PhD thesis, University of Minnesota.

[Popp and Schiehlen, 2010] Popp, K. and Schiehlen, W. (2010). *Ground Vehicle Dynamics*. Springer.

[Rajamani, 2012] Rajamani, R. (2012). *Vehicle Dynamics and Control*. Springer.

[Rajamani et al., 2006] Rajamani, R., Piyabongkarn, D., Lew, J. Y., and Grogg, J. A. (2006). Algorithms for real-time estimation of individual wheel tire-road friction coefficients. In *American Control Conference*.

[Ray, 1997] Ray, L. R. (1997). Nonlinear tire force estimation and road friction identification: Simulation and experiments. *Automatica*, 33(10):1819 – 1833.

[Reza, 2007] Reza, N. J. (2007). *Vehicle Dynamics Theory and Application*. Springer.

[Ryu and Gerdes, 2004a] Ryu, J. and Gerdes, J. C. (2004a). Estimation of vehicle roll and road bank angle. In *American Control Conference, 2004. Proceedings of the 2004*, volume 3, pages 2110–2115. IEEE.

[Ryu and Gerdes, 2004b] Ryu, J. and Gerdes, J. C. (2004b). Estimation of vehicle roll and road bank angle. In *Proceedings of the 2004 on American Control Conference*, volume 3, pages 2110–2115 vol.3.

[Ryu et al., 2002] Ryu, J., Rossetter, E. J., and Gerdes, J. C. (2002). Vehicle sideslip and roll parameter estimation using gps. In *Proceedings of AVEC 2002 6th International Symposium of Advanced Vehicle Control*.

[Savitski et al., 2015] Savitski, D., Hoepping, K., Ivanov, V., and Augsburg, K. (2015). Influence of the tire inflation pressure variation on braking efficiency and driving comfort of full electric vehicle with continuous anti-lock braking system. *SAE International Journal of Passenger Cars-Mechanical Systems*, 8(2015-01-0643):460–467.

[Schiehlen, 2009] Schiehlen, W. (2009). *Dynamical Analysis of Vehicle Systems*. Springer.

[Schindler, 2013] Schindler, A. (2013). Vehicle self-localization with high-precision digital maps. In *Intelligent Vehicles Symposium (IV), 2013 IEEE*, pages 141–146. IEEE.

[Sentouh et al., 2006] Sentouh, C., Glaser, S., and Mammar, S. (2006). Advanced vehicle–infrastructure–driver speed profile for road departure accident prevention. *Vehicle System Dynamics*, 44(sup1):612–623.

[Shiang-Lung et al., 2004] Shiang-Lung, K., Han-Shue, T., and Tomizuka, M. (2004). Nonlinear tire lateral force versus slip angle curve identification. In *Proceedings of the 2004 on American Control Conference*, volume 3, pages 2128–2133 vol.3.

[Smith and Starkey, 1995] Smith, D. E. and Starkey, J. M. (1995). Effects of model complexity on the performance of automated vehicle steering controllers: Model development, validation and comparison. *Vehicle System Dynamics*, 24(2):163–181.

[Smith, 2004] Smith, N. D. (2004). Understanding parameters influencing tire modeling. *Department of Mechanical Engineering, Colorado State University*.

[Song, 2013] Song, R. T. (2013). Estimation of vehicle's vertical and lateral tire/road forces with non-zero road bank angle. Master's thesis, Université de Technologie de Compiègne.

[Stéphant, 2004] Stéphant, J. (2004). *Contribution à l'étude et à la validation expérimentale d'observateurs appliqués à la dynamique du véhicule*. PhD thesis, Université de Technologie de Compiègne.

[Svendenius, 2007] Svendenius, J. (2007). *Tire modeling and friction estimation*. PhD thesis, Lund University.

[Tan, 2012] Tan, Z. (2012). Monte carlo integration with acceptance-rejection. *Journal of Computational and Graphical Statistics*.

[Taylor et al., 1999] Taylor, C. J., Košecká, J., Blasi, R., and Malik, J. (1999). A comparative study of vision-based lateral control strategies for autonomous highway driving. *The International Journal of Robotics Research*, 18(5):442–453.

[Thomas, 1997] Thomas, D. G. (1997). *Fundamentals of Vehicle Dynamics*. SAE International.

[Tseng, 2001] Tseng, H. E. (2001). Dynamic estimation of road bank angle. *Vehicle System Dynamics*, 36(4-5):307–328.

[Tsourapas et al., 2009] Tsourapas, V., Piyabongkarn, D., Williams, A. C., and Rajamani, R. (2009). New method of identifying real-time predictive lateral load transfer ratio for rollover prevention systems. In *American Control Conference, 2009. ACC'09.*, pages 439–444.

[Van der Horst and Hogema, 1994] Van der Horst, R. and Hogema, J. (1994). Time-to-collision and collision avoidance systems. *VERKEERSGEDRAG IN ONDERZOEK*.

[Van Zanten, 2002] Van Zanten, A. T. (2002). Evolution of electronic control systems for improving the vehicle dynamic behavior. In *Proceedings of the 6th International Symposium on Advanced Vehicle Control*, pages 1–9.

[Victorino et al., 2003] Victorino, A. C., Rives, P., and Borrelly, J.-J. (2003). Safe navigation for indoor mobile robots. part ii: exploration, self-localization and map building. *The International Journal of Robotics Research*, 22(12):1019–1039.

[Von Vietinghoff et al., 2005] Von Vietinghoff, A., Hiemer, M., and Kiencke, U. (2005). Nonlinear observer design for lateral vehicle dynamics. In *Proc. 16th IFAC World Congress*.

[Wan and Van der Merwe, 2000] Wan, E. A. and Van der Merwe, R. (2000). The unscented kalman filter for nonlinear estimation. In *The IEEE 2000 Adaptive Systems for Signal Processing, Communications, and Control Symposium*, pages 153–158.

[Wang, 2013] Wang, B. (2013). *State observer for diagnosis of dynamic behavior of vehicle in its environment*. PhD thesis, Université de Technologie de Compiègne.

[Wang et al., 2012] Wang, B., Cheng, Q., Victorino, A. C., and Charara, A. (2012). Real-time experimental validation of nonlinear observer for vehicle dynamics parameters estimation: A laboratory vehicle description. In *Vehicular Electronics and Safety (ICVES), 2012 IEEE International Conference on*, pages 72–77. IEEE.

[Wang et al., 2013] Wang, B., Correa Victorino, A., Charara, A., Augsburg, K., and Höpping, K. (2013). Assessment of rollover stability based on risk indicator. In *Symposium Series on Computational Intelligence, 2013 IEEE*.

[Wenzel et al., 2006] Wenzel, T. A., Burnham, K. J., Blundell, M. V., and Williams, R. A. (2006). Dual extended kalman filter for vehicle state and parameter estimation. *Vehicle System Dynamics*, 44(2):153–171.

[Wong, 2008] Wong, J. Y. (2008). *Theory of Ground Vehicles*. John Wiley & Sons Ltdringer.

[Xu and Tseng, 2007] Xu, L. and Tseng, H. E. (2007). Robust model-based fault detection for a roll stability control system. *IEEE Transactions on Control Systems Technology*, 15(3):519–528.

[Yu et al., 2013] Yu, G. Z., Wang, D., Li, Q., Wang, P. W., and Wang, Y. P. (2013). Road bank estimation for bus rollover prediction. *Appl. Math*, 7(5):2027–2034.

[ZANTEN, 2000] ZANTEN, A. T. V. (2000). Bosch esp systems: 5 years of experience. In *SAE Technical Paper*, volume 109, pages 428–436, New York, NY, ETATS-UNIS.

[Zhan et al., 2000] Zhan, W. Z., Lin, Y., Shi, G. B., and Wang, L. G. (2000). Study on non-linear dynamic characteristic of vehicle suspension rubber component. In *International ADAMS User Conference*.

[Zhang et al., 1998] Zhang, Y. L., Hong, D. H., Chung, J. H., and Velinsky, S. A. (1998). Dynamic model based robust tracking control of a differentially steered wheeled mobile robot. In *Proceedings of the 1998 American Control Conference*, volume 2, pages 850–855 vol.2.

[Zhu et al., 2011] Zhu, X., Qiu, C., Guo, L., and Zhang, Y. (2011). New method for slip and tire force estimation of wheeled mobile robot on inclined terrain. In *2011 IEEE International Conference on Robotics and Biomimetics*, pages 2264–2269.